The Dissertation Committee for Elena Rodriguez-Pin Certifies that this is the approved version of the following dissertation:

Grain-Scale Mechanisms of Particle Retention in Saturated and Unsaturated Granular Materials

Committee:

Steven L. Bryant, Supervisor

Matthew Balhoff

David DiCarlo

Chun Huh

Douglas R. Lloyd

Grain-Scale Mechanisms of Particle Retention in Saturated and Unsaturated Granular Materials

by

Elena Rodriguez-Pin, B.S.; M.S.

Dissertation

Presented to the Faculty of the Graduate School of

The University of Texas at Austin

in Partial Fulfillment

of the Requirements

for the Degree of

Doctor of Philosophy

The University of Texas at Austin

December, 2010

Dedication

To my family

Acknowledgements

I would like to express my gratitude to Dr. Bryant for all his support during my years as a graduate student. Without his guidance and encouragement this work would not have been possible. Special thanks Dr. Prodanović for taking great interest into my research and sharing her knowledge. Her participation played a very important role in the completion of this dissertation.

I would like to extend my appreciation to the members of my dissertation committee, Dr. Balhoff, Dr. DiCarlo, Dr. Huh, and Dr. Lloyd for their helpful comments during my proposal and final defense.

I would also like to acknowledge my colleagues Siyavash Motealleh and Javad Behseresht, for our helpful technical discussions, and Matthew Roberts and Haiyang Yu for performing the experimental work shown in this dissertation.

Finally I would like to thank Joanna Castillo for helping me with the format of this dissertation, and Roger Terzian and Tim Guinn for being available every time that I had a computer or software problem.

This material is based upon research supported by the National Institute of Food and Agriculture, U.S. Department of Agriculture, under Agreement No. 2007-35102-18162 and the Advanced Energy Consortium (BP America Inc., Baker Hughes Inc., ConocoPhillips, Halliburton Energy Services Inc., Marathon Oil Corp., Occidental Oil and Gas, Petrobras, Schlumberger, Shell, and Total). Any opinions, findings, conclusions, or recommendations expressed in this publication are those of the author and do not necessarily reflect the view of the U.S. Department of Agriculture or the Advanced Energy Consortium.

Grain-Scale Mechanisms of Particle Retention in Saturated and Unsaturated Granular Materials

Publication No._____

Elena Rodriguez-Pin, Ph.D.

The University of Texas at Austin, 2010

Supervisor: Steven L. Bryant

The phenomenon of particle retention in granular materials has a wide range of implications. For agricultural operations, these particles can be contaminants transported through the ground that can eventually reach to aquifers, consequently contaminating the water. In oil reservoirs, these particles can be clays that get detached from the rock and migrate with the flow after a change of pressure, plugging the reservoir with the consequent reduction in permeability. These particles can also be traceable nanoparticles, introduced in the reservoir with the purpose of identifying bypassed oil. For all these reasons it is important to understand the mechanisms that contribute to the transport and retention of these particles.

In this dissertation the retention of micro and nano size particles was investigated. In saturated model sediments (sphere packs), we analyzed the retention of particles by the mechanism of straining (size exclusion). The analysis focused on experiments reported in the literature in which particles smaller than the smallest pore throats were retained in the sediment. The analysis yields a mechanistic explanation of these observations, by

indentifying the retention sites as gaps between pairs of sediment grains. A predictive model was developed that yields a relationship between the straining rate constant and particle size in agreement with the experimental observations.

In unsaturated granular materials, the relative contributions of grain surfaces, interfacial areas and contact lines between phases to the retention of colloidal size particles were investigated. An important part of this analysis was the identification and calculation of the length of the contact lines between phases. This estimation of contact line lengths in porous media is the first of its kind. The algorithm developed to compute contact line length yielded values consistent with observations from beads pack and real rocks, which were obtained independently from analysis of high resolution images. Additionally, the predictions of interfacial areas in granular materials were consistent with an established thermodynamic theory of multiphase flow in porous media. Since there is a close relationship between interfacial areas and contact lines this supports the accuracy of the contact line length estimations. Predictions of contact line length and interfacial area in model sediments, combined with experimental values of retention of colloidal size particles in columns of glass beads suggested that it is plausible for interfacial area and contact line to contribute in the same proportion to the retention of particles.

The mechanism of retention of surface treated nanoparticles in sedimentary rocks was also investigated, where it was found that retention is reversible and dominated by attractive van der Waals forces between the particles and the rock's grain surfaces.

The intricate combination of factors that affect retention makes the clear identification of the mechanism responsible for trapping a complex task. The work presented in this dissertation provides significant insight into the retention mechanisms in relevant scenarios.

Table of Contents

List of Tables

List of Figures

Chapter 1: Introduction

1.1. Problem Statement

Colloids are particles with effective diameters between 0.01 and 10 μm that are naturally present in the subsurface. Their nature can be organic (humic materials), inorganic (silicate clays and mineral precipitates), or biologic (viruses and bacteria). The colloids themselves can be contaminant (bacteria and viruses) or they can act as carriers of contaminants such as pesticides or heavy metals (McCarthy and Zachara, 1989). The presence and transport of colloids in the subsurface strongly affect ground water quality. The transport mechanisms of these particles are of specific interest in quantifying water quality with respect to pathogen transport (e.g. E. coli, Cryptosporidium) between the source (e.g. farms) and human users.

On the other hand, inorganic colloids, such as clay particles, can cause problems in oil reservoirs, affecting the reservoir properties of sandstones. Kaolinite and illite are two common colloidal clays naturally present in most reservoirs and the petroleum literature refers to them as a "fines". These fine particles can move within the reservoir due to drag forces during oil and gas production. This phenomenon is known as fines migration and consist of the release of the fines from the porous media, their movement with the flow of permeate, and eventually their capture within the porous medium or their path out of the medium. Migration and capture in oil reservoirs can cause a reduction in permeability and therefore a decline in oil production.

Smaller than colloids are nanoparticles, which are between a few nm to a few hundred nm in diameter. Engineered nanoparticles have properties potentially useful for oil recovery processes and formation evaluation. For example, nanoparticles with magnetic properties can act as sensors to detect bypassed oil (Prodanović *et al.*, 2010) Although nanoparticles are small enough to pass through the pore throats of conventional

reservoirs they can also be trapped in rock, typically by the phenomenon of classical deep-bed filtration which involves attractive and repulsive forces between the nanoparticle and the surface of the rock (Lecoanet and Wiesner, 2004; Li *et al*., 2008; Wang *et al*., 2008b). In order to develop field applications of nanoparticles it is essential first to understand the nature of the interaction between rock and nanoparticle.

The transport of both colloidal and nano size particles through sediments is a complex process, where the retention of particles within the sediment play a key role. The mechanisms that govern the transport and retention of these particles in the saturated and unsaturated zone of soils are still poorly understood, because of the complexity of processes that occur at the pore scale.

Two types of retention are commonly identified in saturated granular media: filtration and straining (McCarthy and Zachara, 1989). Filtration refers to the attachment/detachment of particles to the surfaces of sediment grains due to electrostatic and Van der Waals forces. Straining is a purely geometric mechanism that occurs when colloids arrive at constrictions in pore space too small to admit them. Even though straining is a conceptually simple mechanism, the current understanding of the phenomenon is inadequate. The classical retention theories (Yao *et al.* 1971) consider physicochemical filtration as the only mechanism responsible for retention. As discussed in more depth in section 1.3, these theories occasionally underestimate colloid retention. In particular, the retention of particles much smaller than the smallest pore throat in porous media under conditions that minimize retention by attachment/detachment was observed in several independent studies over the course of the years (Gruesbeck and Collins, 1982; Baghdikian *et al*., 1989; Marlow *et al.*, 1991; Geilikman *et al*., 2005).

For nanoparticles, retention is unlikely to occur in typical pore throats because the particles are typically much smaller than the throats. In this case the mechanism of retention is probably similar to the classical phenomenon of deep bed filtration, which can be explained in terms of attraction and repulsion between the nanoparticle and the surface of the reservoir rock grains. As discussed in section 1.3, the literature related to transport and retention of nanoparticles is limited to one phase experiments that use dilute, aqueous suspensions in unconsolidated porous materials. However, concentrated solutions of nanoparticles may be employed for oil reservoir applications and it will be also necessary to investigate how the presence of fluid/fluid interfaces will affect retention.

In the unsaturated zone of the sediments, particles can be retained at the interfaces between air, water, and grain. This retention is in addition to straining at pore throats and constrictions of smaller or equivalent size. Because of the complexity of processes at the pore scale, the mechanisms that govern retention in the unsaturated zone are still poorly understood. Theories competing to explain this mechanism claim that retention can be caused by adhesion at the air-water-interface (AWI) between sediment grains (Wan and Tokunaga, 1997) or by straining at the air-water-solid (AWS) contact line (Crist *et al*. 2004) (see Figure 1.1 for a illustration of AWI and AWS in porous media).

Currently, there are no established methods for the estimation of particle retention in unsaturated media because of the intricate influence of AWI and AWS on transport and retention. Reliable quantitative estimates of the specific interfacial area are still difficult to obtain: measurements with interfacial tracers typically include contribution from wetting films in drained pores, and direct observation (e.g. from epoxy-filled sections (Morrow, 1970) or from high-resolution X-ray images (Cullingan *et al*., 2004; Kumar *et al*., 2009) is tedious to acquire. No estimates of lengths of AWS have been

reported. What is clear is that the geometric configuration and connectivity of the aqueous phase is an important factor in unsaturated transport. Another factor that makes the particles susceptible to retention at these interfaces is their affinity for the aqueous phase and therefore the water saturation. Also important are factors like pH or ionic strength of the particle solution.

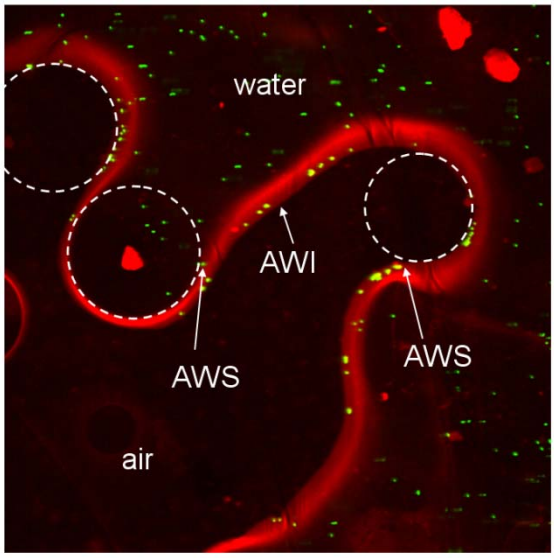

Figure 1.1: Carboxylated colloids (in green) of 1μm size in a capillary duct packed with 200 μm glass beads. The colloids are shown retained at the air-water interface. AWI denotes air-water interface and AWS denotes air-water-solid line (courtesy of Dr. Yan Jin from The University of Delaware). White dashed lines outline where the glass beads are.

1.2. OBJECTIVES

The primary objectives of this dissertation are the following:

a) In saturated sediments, investigate the mechanism of straining to determine the reason that causes the retention of particles in granular materials to exceed the level predicted by current theories.

b) In unsaturated sediments, quantify the air/water interface (AWI) and air/water/solid contact line (AWS) in simple geometries and in granular materials to later estimate their relative contribution to retention of particles.

c) Investigate the mechanisms of interaction between nanoparticles and reservoir rocks as a first step before designing processes that use nanoparticles for oil enhanced oil recovery purposes.

1.3. LITERATURE REVIEW

1.3.1. Straining of Colloids in Saturated Systems

Different experiments performed by independent research groups (referenced in the next paragraphs) have shown that particles too small to be trapped by straining according to classical theories are nevertheless retained. Thus, the behavior of these particles does not fit clearly into the filtration versus straining classification discussed in section 1.1.

Hall (1957) observed retention of particles 3 to 9 times smaller than pore throats in sand filters. In a clean-bed experiment, Yao *et al.* (1971) observed that the retention of colloids between 0.3 to 3 μm was more efficient than predicted from filtration theory. Gruesbeck and Collins (1982) reported retention of colloids three to six times smaller than estimated pore throat diameters in their sand pack. Baghdikian *et al.* (1989)

observed significant retention of particles an order of magnitude smaller than pore throats. Marlow *et al.* (1991) observed retention of colloids sixteen times smaller than pore throats. The retention of the same size particles was almost complete when throat size was reduced by a third by reducing grain size. The sensitivity to grain size is much greater than theoretically expected for filtration.

Geilikman *et al.* (2005) measured a reduction in the permeability of sandstone cores when the diameter of fine particles was up to 3 times smaller than the smallest throats, achieving the maximum reduction when fines are about 12 times smaller than the average sandstone grain.

Sharma and Yortsos (1987c) developed a straining theory for retention of particles whose size is comparable to the size of pore throats and where size exclusion is the dominant mechanism of particle trapping. The model relates trapping probability to pore scale flow rate distribution and yields a definition for the straining rate constant. Implicit in this theory is the assumption that the probability of a particle entering a constriction and being strained is proportional to the flow rate into that constriction.

Bradford *et al*., (2002) observed that retention was strongly dependent on colloid size in a saturated glass bead pack under conditions in which filtration would have been relatively insignificant. Similar behavior was observed in sand packs. They showed that a straightforward application of filtration theory could not account for their observations and concluded that straining must have contributed to retention, though the colloids were much smaller than the theoretical thresholds for straining. In an attempt to fit the experimental data to a empirical equation, Bradford *et al.* (2003) defined a constant for straining (k_{str}) that follows a power-law relationship with the size of the colloids (d) and the average size of the sediment grains (D). Many years before, Hall (1957) presented an analogous straining model based in purely geometric considerations of the pore space.

The experiments of Tufenkji and Elimelech (2004) conducted under conditions in which physicochemical filtration is negligible, indicated straining as an important capture mechanism of bacteria. Foppen *et al.* (2005) demonstrated that straining in dead end pores dominates bacteria breakthrough in fine grained sediment (0.06-0.2 mm). Later, Bradford and Bettahar (2006) modified the previous empirical equation (Bradford *et al*., 2003) by adding an inverse dependence of straining with porosity.

Xu *et al*. (2006) extended the range of particle sizes tested by Bradford *et al.* (2003) using latex microspheres as colloids in sand quartz columns. It was shown that retention by straining is negligibly small for $d/D < 0.008$ and above that threshold the rate constant varies linearly with d/D. The absolute value of the straining rate constant inferred from these experiments is considerably smaller than the one reported by Bradford *et al*. (2003).

In these straining theories, pore throats, the void spaces between three neighboring grains, are considered the location where retention occurs. Rodriguez and Bryant (2007) proposed that the reason why the trapping of particles exceeds the predictions from classical theories is that retention by straining can take place in small gaps between pairs of grains besides pore throats. In this work, the Sharma and Yortsos (1987c) theory was applied to gaps in order to get a correlation between the ratio of particle to grain size and the straining rate constant. The results indicated that considering retention by straining to depend only on the flow through the constriction cannot explain experimental observations of straining.

1.3.2. Retention of Colloids in Unsaturated Systems

Because of the complexity of processes at pore scale, the mechanisms that govern retention in the unsaturated zone are still poorly understood (Bradford and Torkzaban, 2008). There are no established models for colloid retention in unsaturated media because of the intricate influence of AWI and/or AWS on water flow and colloid attachment. Theories regarding colloid retention are based on the filtration theory of Tufenkji and Elimelech (2004) for colloidal dispersions in single phase flow where spherical particles are attached to the spherical collector's surface.

The studies dedicated to unsaturated systems are relatively new compared with what has been done in saturated systems. Saiers and Lenhart (2003) proposed a model for the transport of silica colloids in unsaturated sand columns based on the one-dimensional form of the advection-dispersion equation. The unknown parameters are the concentrations of colloids in pore water, fraction of immobile water in narrow conduits (gaps), area of immobile air-water interface, and immobile solid-water interface respectively. This equation is coupled with kinetics expressions for the unknown parameters and then solved numerically using a finite difference scheme.

There is an unsettled discussion about the relative contributions of AWI and AWS to retention which started several years ago (Wan and Tokunaga 2005; Steenhuis *et al*. 2005). There are two theories competing to explain the retention of particles in unsaturated media: retention by adhesion at the air-water-interface (AWI) between sediment grains (Wan and Tokunaga, 1997; Wan and Tokunaga, 2005) versus retention by straining at the air-water-solid (AWS) contact line (Crist *et al*., 2004; Steenhuis *et al*., 2005). These theories are reviewed in the paragraphs to follow.

Several experimental works were performed in order to elucidate the dominant mechanism of retention of colloids in the unsaturated zone. Experiments with hydrophobic and hydrophilic colloids in unsaturated chromatographic columns filled with quartz sand (Wan and Wilson, 1994) showed that colloids are retained preferentially on the air-water interface rather than on the grain surface and more of the hydrophobic colloids were retained on the interface than the hydrophilic. Other investigators (Wan and Tokunaga, 1997) introduced a "film-straining theory" based on the observation that thin water films on solid surfaces can hinder the transport of hydrophilic colloids in unsaturated media, suggesting that AWI is the dominant mechanism for retention of colloids. The sorption of viruses in polypropylene (hydrophobic) and glass (hydrophilic) vessels was also investigated (Thompson *et al.,* 1998), concluding that the viruses attach more effectively to the air-water-solid line even though the air-water interface still plays an important role in the retention.

Experiments with silica colloids in unsaturated quartz sand columns (Lenhart and Saiers 2002) showed that the retention of colloids was inversely proportional to the amount of water in the column. A "dual rate-law model" was proposed that incorporates a first order formulation to account for film straining and a second order formulation to incorporate the effect of air-water interfaces. The effects of the pore water chemistry in the retention of colloids were also investigated (Saiers and Lenhart, 2003) concluding that as the ionic strength of the colloid suspension increased the removal mechanism changes from straining to air-water interface trapping to grain attachment.

Crist *et al.* (2004) developed a visualization technique in order to clearly distinguish between air-water interface and air-water–solid line. Using quartz sand as porous medium and hydrophilic colloids, the AWS was presumed to be predominant factor in colloid retention. Crist *et al.* (2005) further showed that both hydrophilic and

hydrophobic colloids attached preferentially to menisci associated with the AWS contact line in a chamber filled with either hydrophilic or weakly hydrophobic sand. Wan and Tokunaga (2005) criticized this work (Crist *et al*., 2004; Crist *et al*., 2005) arguing that the experiments were performed in devices open to the atmosphere and subject to evaporation. According to them, the AWS contact lines are "artifacts caused by evaporation" and a thin film existed at the place of the AWS. Steenhuis *et al*. (2005) replied to these critics explaining that the constant flow of water used in the experiments of Crist *et al.* (2004, 2005) was enough to make evaporation insignificant and that these works only attempted to improve the pioneering experiments of Wan and Wilson (1994).

In an experimental work also related to the AWS line (Zevi *et al.*, 2005) the retention was attributed specifically to the region where the grain water menisci diminish to a thin water film and define a new region within the AWS, the air-water meniscus-solid contact line or AWmS. Hydrophobic colloids showed more retention at this interface than hydrophilic. In a later work Zevi *et al.* (2006) showed that the quantification of colloids trapped at the AWS contact was well defined by Langmuir isotherms. An important factor to consider in colloid attachment is the ionic strength. While total colloid attachment was shown to increase with the increase in ionic strength, the attachment to the AWmS was reduced on behalf of the attachment to the SWI (Zevi *et al*., 2009).

Torkzaban *et al.* (2006) investigated the factors that control the attachment to the AWI in column experiments using solutions of bacteriophages at different pH and ionic strengths. The experiments showed that retention at AWI and SWI increased as the pH decreased and that electrostatic interactions were more important than hydrophobicity regarding attachment to the AWI.

On the other hand, Gao *et al.* (2008) credit capillary and friction forces rather than electrostatic (DLVO) forces to be responsible for the retention of colloids at the AWmS.

Recently, Bridge *et al.* (2009) studied the movement of colloids during drainage in quartz sands and observed colloid mobilization by AWI while the AWS contact plays the part of fixing the colloids to the SWI.

1.3.3. Transport and Retention of Nanoparticles

The transport of engineered nanoparticles in reservoir rock for oil recovery applications has been little studied to date. Research regarding transport of nanoparticles is being carried out by environmental engineers to investigate the impact of nanoparticles unintentionally introduced into sediments (Brant *et al*., 2007; Bradford and Torkzaban 2008). These studies characterize the retention of nanoparticles by the mechanisms applicable to colloidal particles, i.e., the clean-bed filtration theory (Elimelech *et al.*, 1995; Tufenkji and Elimelech, 2004; Bradford *et al*., 2003; Wang *et al*., 2008a; Wang *et al.*, 2008b; Li *et al*., 2008) where nanoparticle deposition is described as the particle transport to the vicinity of the soil grain surface followed by attachment. The van der Waals attractive force is believed to be the governing force for attachment to the grain surfaces and interaction energies are calculated using DLVO theory for the case of a flat plate (surface of porous medium) and a sphere (nanoparticle) (Guzman *et al.*, 2006; Hoek and Agarwal, 2006). Attractive forces are also responsible for the aggregation of nanoparticles in suspension, with the aggregate being able to reach the size of a colloidal particle (Brant *et al*., 2007). Aggregation was observed to occur faster at higher ionic strengths (Kallay and Žallac, 2002; Kobayashi *et al*., 2005).

A background on experiments related to transport and retention of nanoparticles is shown in Chapter 4, since this chapter will be an introduction to the application of nanoparticles to oil recovery.

1.4. SUMMARY OF CHAPTERS

In Chapter 2 the problem of the retention by straining of colloidal size particles in saturated granular materials is investigated. The granular materials are computer generated packs of spheres. A relationship between straining rate and ratio of particle size to grain size analogous to the empirical relationship proposed by Bradford *et al*. (2003) is sought in this chapter. A series of hypotheses regarding the relation between straining rate, flow and geometric characteristic of the granular materials are tested with the objective of explain the mechanism of straining.

Chapter 3 focuses on the problem of retention of particles in the unsaturated zone of the sediments. The objective here is to quantify the contact line length and interfacial areas in different granular materials. A method based on the level set technique, that can be applied to any type of porous media as long as the detailed geometry is available, is used for this purpose. This is the first comprehensive report on contact line measurement for fluid configurations in porous media.

Chapter 4 focuses on the problem of nanoparticle transport and retention in sedimentary rocks. Background regarding nanoparticle transport and retention experiments is presented here, as well as detailed explanation and discussion of the results of several experiments of transport of nanoparticle solutions through sedimentary rocks.

In Chapter 5 the calculations of contact line and interfacial areas presented in Chapter 3 are applied to estimate the amount of particles trapped per unit length and unit length square in columns packed with glass beads of different hydrophobicity, using experimental results of particle (viruses) trapping found in the literature.

Chapter 6 presents the application of the level set method estimation of interfacial areas to evaluate a thermodynamic theory (Morrow, 1970; Hassanizadeh and Gray, 1990; 1993) that relates capillary pressure to interfacial areas. The contribution of the interfacial areas and the system free energy to the capillary pressure of the system is estimated in this chapter.

Concluding remarks for this dissertation and future work recommendations are presented in Chapter 7.

Chapter 2: Trapping of Colloids by Anomalous Straining in Porous Media

2.1. INTRODUCTION

As discussed earlier in Chapter 1, the transport of colloids in saturated granular media presents two types of retention, that is, filtration and straining (McCarthy and Zachara, 1989). For colloid removal, retention theories consider only filtration as the mechanism of trapping, since the retention by straining is considered insignificant because of the small size of the colloids when compared with pore throats. However, filtration theories have been consistently underestimating the extent of retention for a particular size range of particles (Hall, 1957; Yao *et al*. 1971; Gruesbeck and Collins, 1982; Baghdikian *et al*. 1989).

The retention by straining of colloidal size particles in saturated granular materials is studied in this chapter in order to determine the reason behind the anomalous straining behavior. The size of the colloids considered is in the range of sizes of the particles that underwent anomalous straining in several experiments, being trapped when they were not expected because of their small size. The granular materials are computer generated packs of dense, disordered spheres of the same size.

We begin by reviewing existent theories for filtration and straining, before stating the objective and hypothesis that will lead the analysis of straining. More detailed information about the mechanism of retention of small particles in porous media and the intervening forces can be found in Appendix A. This information is also relevant to the material shown in Chapter 4 regarding nanoparticle retention in porous media.

2.2. PARTICLE RETENTION THEORIES

2.2.1. Filtration Theory

Filtration refers to a complex interaction of physical and chemical phenomena leading to the attachment and detachment of particles to the surfaces of the sediment's grains. For colloidal dispersions in single phase flow, the filtration equation describes the variation of particle concentration with time and space as (Tufenkji *et al*., 2004):

$$\frac{\partial C}{\partial t} + \mathbf{v} \cdot \nabla C = \mathscr{D} \nabla^2 C - \nabla \cdot \left(\frac{\mathscr{D}\, \mathbf{F}}{kT} C \right) \qquad (2.1)$$

where C is the particle concentration in flowing phase, $\mathscr{D}$ is the particle diffusion coefficient, $\boldsymbol{v}$ is the particle velocity vector induced by fluid flow, k is the Boltzmann constant, T is the absolute temperature, and $\boldsymbol{F}$ is the external force vector that causes particle retention on a solid surface. Equation (2.1) is a form of the convection-diffusion equation where the sink term represents the mechanism of particle retention.

The external forces for particle retention in filtration theories are the summation of van der Waals and electric double layer interactions that operate between particles and collector surfaces at short distances plus the gravitational forces. Elimelech (1994) solved equation (2.1) numerically using boundary conditions in agreement with the classical filtration model of Happel (1958). This model assumes the medium to be made of spherical collectors of radius d_p each, surrounded by a spherical cell of fluid of radius d_c. Each collector has a removal efficiency η, which is the product of the collector contact efficiency η_0 and attachment efficiency α, introduced to account for the fact that a particle does not necessarily attach to the collector surface when it reaches the collector (Elimelech *et al*., 1995).

Once the concentration distribution of particles around the collector *C* was determined numerically (Elimelech, 1994), the perpendicular flux of particles at the collector surface and consequently the overall rate of particle collisions with the collector *I* could be calculated. The latter parameter can be used to estimate the theoretical single collector contact efficiency η_0, as:

$$\eta_0 = \frac{I}{\pi a_c^2 U C_0} \tag{2.2}$$

where a_c is the radius of the spherical collector, *U* is the approaching velocity of the fluid, and C_0 is the bulk fluid concentration. The denominator of equation (2.2) represents the convective transport of upstream particles towards the projected area of the collector. This contact efficiency is inversely proportional to the approach velocity of the fluid. These collector contact efficiencies can be regarded as a dimensionless deposition rates.

In this filtration theory, there is not a contribution for the size exclusion mechanism (straining) for trapping particles within the external force vector *F*.

2.2.2. Straining Theory

Retention by straining occurs when colloids arrive at a constriction in pore space too small to allow their passage. There are not many models that account explicitly for straining, as colloid retention is usually described by the classical filtration theory described above. The theories discussed next consider straining as an irreversible process with a first order dependence on the concentration of particles.

In 1957, Hall provided a simple geometric argument for the observed dependence of rate of retention by straining on particle size. His study of the crevice between two

spheres in point contact yielded a straining rate constant k_{str} that scales with the power of the ratio between the size of the trapped particle d and the size of the sediment grain D with a scaling exponent of 1.5.

Sharma and Yortsos (1987c) developed a straining theory for particles whose size is comparable to the size of pore throats and where size exclusion is the dominant mechanism of particle trapping. The dimensionless population balance for the suspended particles is expressed as:

$$\frac{\partial C_D}{\partial t_D} + \frac{\partial C_D}{\partial x_D} = -\frac{1}{M}\frac{I(d/D)}{I(\infty)}C_D \tag{2.3}$$

where C_D is the dimensionless concentration of particles, t_D is the dimensionless time, x_D is the dimensionless distance, M is the ratio of the length of the pore throat to the length of the porous medium, $I(d/D)$ is the cumulative flow in all the throats that can trap a particle of a given size d and $I(\infty)$ is the cumulative flow in all the pores. Thus, this model relates trapping probability to pore scale flow rate distribution. The model yields a definition for the straining rate constant that can be extracted from equation (2.3) as the ratio of the two cumulative flows:

$$k_{str} = \frac{I(d/D)}{I(\infty)} \tag{2.4}$$

Note that the rate constant depends on the size d of the particle being strained, as in Hall's geometric theory, but the power-law for this dependence is not explicit.

Implicit in this theory is the assumption that the probability of a particle entering a constriction and being strained is proportional to the flow rate into that constriction. No

further relation between the straining constant and the ratio of particle to grain size was estimated in this theory.

More recently, Bradford *et al.* (2002; 2003) developed a model for particle straining and attachment by including two sink terms in the convection-diffusion equation, one for particle attachment by physicochemical forces, and another one for particle straining. The convection – diffusion equation is expressed now as:

$$\frac{\partial C}{\partial t} + \mathbf{v} \cdot \nabla C = \mathscr{D} \nabla^2 C - E_{Sw}^{att} - E_{Sw}^{str} \tag{2.5}$$

where E_{Sw}^{att} and E_{Sw}^{str} are the mass transfer terms between the aqueous phase and the solid due to colloid attachment and straining respectively. The straining term is then defined as:

$$E_{Sw}^{str} = \theta_w k_{str} \psi_{str} C \tag{2.6}$$

where θ_w is the volumetric water content, k_{str} is the straining coefficient (with units of reciprocal time) and ψ_{str} is a dimensionless parameter that depends on the distance from the porous medium inlet where straining is being evaluated.

The experiments of Bradford *et al*. (2003) consisted of the injection of suspensions of four different sized fluorescent particles with negatively charged surface in columns of various sieve sizes of Ottawa sand. The observed concentration of colloids at the effluents was fitted to equation (2.5). Three cases were considered, one assuming that particle retention occurs by both attachment and straining, and another two assuming that retention occurs exclusively by attachment or straining, respectively. The following

relationship between the ratio of particle sizes to grain size and the straining rate constant was found:

$$k_{str} = 269.7\left(\frac{d}{D}\right)^{1.42} \tag{2.7}$$

This scaling exponent of 1.42 for the straining rate constant is very close to the 1.5 value that Hall (1957) found based only on geometric considerations.

These particle straining models do not include other factors that will probably affect straining, such as the uniformity of the soil grain size, the particle surface charge, the water content and the experimental scale, but they show that particle size has a first order effect on the straining threshold and the straining rate.

This dissertation examines the mechanism of straining without consideration of any physicochemical mechanism for trapping. The hypothesis regarding the anomalous straining behavior of colloidal size particles is stated in the next section.

2.3. HYPOTHESIS FOR ANOMALOUS STRAINING BEHAVIOR

An important observation in straining theories is that pore throats (void spaces between three neighboring grains) are considered as the location where retention occurs. We hypothesize that straining also occurs in small "gaps" between pairs of grains in addition to the pore throats between triplets of nearest-neighbor grains

Pore throats are the constrictions between triplets of nearest neighbor grains and they connect two larger pore volumes. Gaps are the void spaces between the centers of two neighboring grains and they are the smallest constrictions in the "corners" of a pore throat (Figure 2.1). Pore throat size is usually measured as the diameter of the biggest

circumference that can be inscribed in a pore throat. Gap widths are given by the distance between the centers of the pair of grains less the radii of the grains.

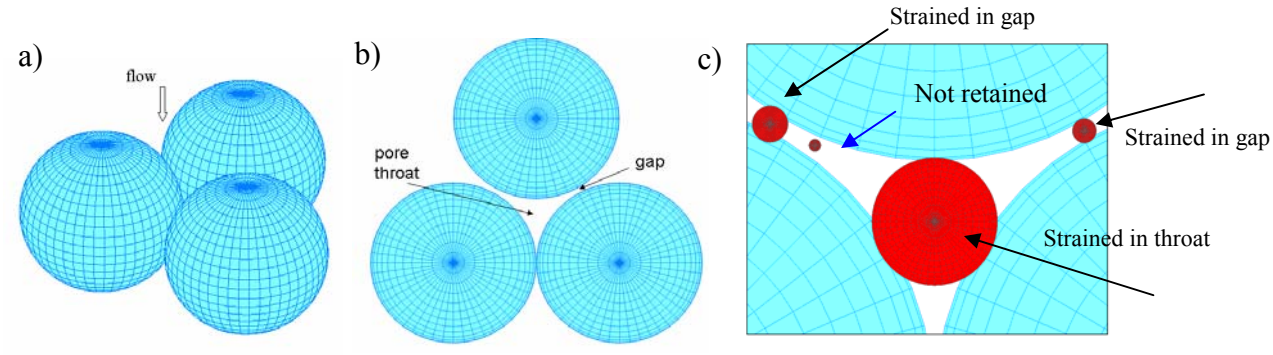

Figure 2.1: Gaps and throats in porous media. a) Three spheres in 3D space representing sediment grains. The arrow indicates the local direction of the flow. b) Plan view of the three spheres showing the location of a gap and the pore throat. c) Retention of particles in pore throats and gaps. The particles retained in the gaps would pass through the pore throat and would not be trapped according to classical straining theories.

This hypothesis will be tested by applying the Sharma and Yortsos (1987c) theory for straining, discussed above, to particles of the size range of interest that are being trapped in gaps, instead of in pore throats. The porous medium used to test this hypothesis will be a model sediment, whose characteristics we will discuss in the next section.

Sharma and Yortsos theory yields a definition for the constant for straining rate that is dependent on the ratio of trapped particle to grain size (d/D) (equation 2.4). The dependence is based on straining rate being proportional to the volumetric flow through the constrictions that can trap the particle of the given size. We will test if the relationship between straining rate constant and particle size obtained by adapting

Sharma and Yortsos theory to gaps is in agreement with the empirical correlations obtained by Bradford *et al*. (2003) (cf. equation (2.7)) and Hall (1957).

Initial testing of the hypothesis (Rodriguez, 2006) arrived at meaningful conclusions, mainly that the assumption that the probability of particle retention in a constriction is proportional to the flow rate through that constriction overestimates the scaling exponent between the constant for straining rate and the size of the strained particles. A more thorough test of the hypothesis is completed in this dissertation.

Important concepts and terminology that will be used during this chapter are defined in the next section.

2.4. TERMINOLOGY

2.4.1. Model Sediments

The geometric analysis of dense disordered periodic packs of equal spheres will be the basis of our study. Disordered sphere packs are used as models for ideal sediments in columns packed with glass beads, in laboratory studies of flow and transport through sands. Even though these smooth mono-dispersed spheres are a simplification of the natural grains occurring in soils, they capture the random spatial arrangement of grains which is a physical feature of the actual soils. Therefore, an ideal sediment is a powerful method to study phenomena that depend on pore geometry.

The first physically representative model for a sediment with a complete description of the geometry of both grain and void space was built by Finney (1970). The pack was made of 25,000 precision ball bearings and Finney mechanically measured the Cartesian coordinates of the centers of 8,000 of them.

Computer generated ideal models of sediments were created by Thane (2006) implementing a version of the cooperative rearrangement method (Cargill, 1984) which allows the use of periodic boundary conditions at the packing edges to eliminate edge effects. The spheres in the front (top) are virtually in contact with the spheres at the back (bottom), eliminating edge effects and thus possible non-randomness in the packing. They contain approximately 4,000 equal spheres (mono-dispersed) and their porosities range from 36% to 38%. For convenience, the original sphere radius of these packs has been normalized to one. Figure 2.2 shows a computer generated packing of 1,000 spheres.

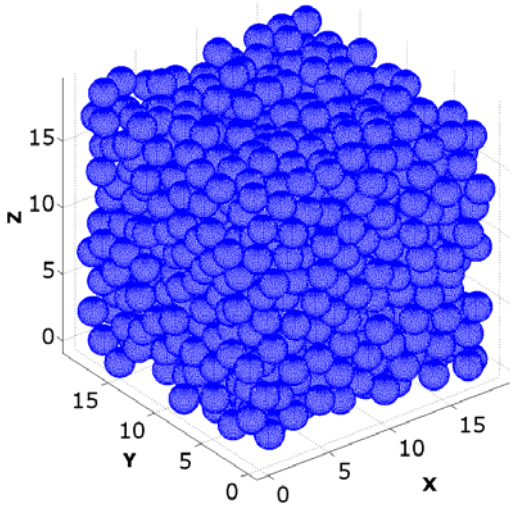

Figure 2.2: Computed generated periodic packing of 1000 spheres of radius 1

2.4.2. Pore Throat Identification

A tessellation is a computational geometric structure created by dividing space into convex polygonal regions. The procedure in 3D is known as Delaunay Tessellation and it divides the space into tetrahedra. When tessellation is applied to the space defined

by the sphere centers in a pack, it will subdivide the pore space by grouping four nearest sphere centers together. The resultant tetrahedra are similar to the one shown in Figure 2.3, where each face corresponds to a pore throat and the center corresponds to the pore body. Depending on whether the spheres are touching or not, each edge of the tetrahedron will correspond to a grain-grain contact or a gap respectively.

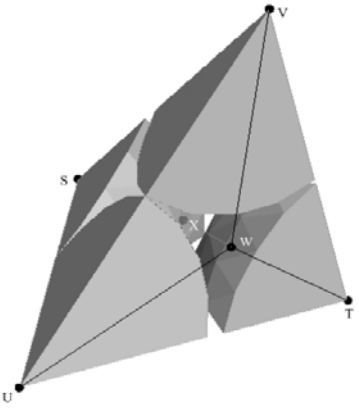

Figure 2.3: Delaunay cell formed by four neighboring spheres. The point W indicates the center of the gap. The point X indicates the center of the pore body. The plane defined by points UVT identifies one of the four pore throats

2.4.3. Size Range of Interest for Particles, Throats and Gaps

The minimum pore throat size in a dense disordered packing of equal spheres, measured as the diameter of the biggest circumference that can be inscribed in a pore throat, is $0.3R$, where R is the grain radius. It occurs when the three spheres are in point contact (touching) and it sets a lower bound on the size of particles that can be trapped in pore throats. However, as stated above, experiments show that particles smaller than this lower bound may nevertheless be strained.

Based on the size of the particles that underwent anomalous straining in the experiments (Hall, 1957; Gruesbeck and Collins, 1982; Baghdikian *et al.*, 1989; Marlow

et al., 1981) we focus on a particle size range of 0.03R to 0.1R, which is common to most of these observations. The range of interest for gap sizes corresponds to all the gaps that can trap particles in the size range of interest. Thus, we will quantify the prevalence and flow characteristics of gaps of width up to 0.1R. This range corresponds to gaps between 1% and 5% of the grain size. Gaps whose width is larger than 0.1R are considered part of the pore throat. Making an analogy with sands, if the average size (diameter) of a sand grain is 0.2 mm (R = 0.1mm), a particle of size 0.1R corresponds to 10 microns and a particle of size 0.03R corresponds to 3 microns.

A detailed geometric and statistical analysis of several model sediments, like the one shown in Figure 2.2, revealed that the number density of gaps in the range of interest for trapping colloidal size particles is large enough to trap a considerable number of colloidal sized particles (Rodriguez, 2006) . The density of gaps whose width is between 0.01R and 0.1R, was found to be 0.15 gaps/R^3; for comparison the density of small pore throats in the computer generated packs is about 0.3 per R^3. The analysis found that each grain in a dense disordered packing of equal spheres will have about one neighbor separated by a gap in the size range of interest. This analysis shows that gaps of the appropriate size range are sufficiently common to account for the observations of anomalous straining and it offers preliminary support for our hypothesis.

2.4.4. Range of Capture

The size of the particle being strained determines the "range of capture" in a gap, and, according to the straining theory of Sharma and Yortsos (1987c), it would be only the flow rate through that range of capture that affects the probability of trapping.

The gap width is the minimum distance between the grain surfaces, at the line joining their centers, as shown in Figure 2.4. A particle of diameter d equal to the gap width w will be strained only if the streamline carrying it passes through its minimum constriction. This event has an infinitesimal probability. However, particles whose diameters are bigger than the gap width will be strained if they pass within some finite distance of the minimum constriction. This distance will be called "range of capture" and represented by a, as shown in Figure 2.4. Its value depends on the particle size d and the gap width w.

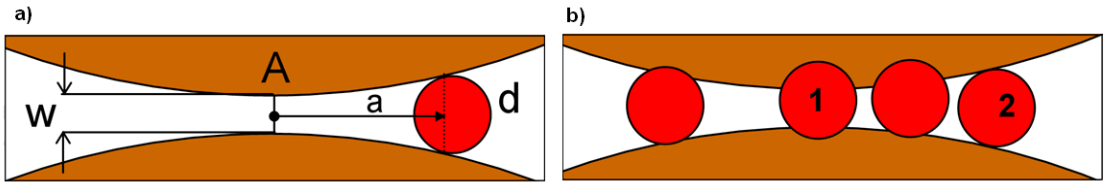

Figure 2.4: a) Zoom of the front view of a gap showing the range of capture a for a particle of size $d > w$. The point A indicates the middle of the gap. b) Zoom of the front view of a gap showing possible locations where a particle of size $d > w$ can be trapped. Particle 2 is trapped at the maximum range of capture. Particle 1 is trapped in the middle of the gap.

The following equation (2.8) is derived from trigonometry (Rodriguez, 2006) and it relates range of capture a with particle, size d, grain size D, and gap width w:

$$\frac{2a}{D} = \sqrt{\left(\frac{d}{D}\right)^2 - \left(\frac{w}{D}\right)^2 + 2\left(\frac{d}{D} - \frac{w}{D}\right)} \tag{2.8}$$

Hence, we identify gaps by their width, w, relative to the grain radius R, but we identify trapped particles by the ratio of their diameter d to the diameter of the grains D where $D = 2R$. For example, a gap of width $0.05R$ will trap particles whose diameter d is

equal to 0.05*R*, equivalently, 0.05×(*D*/2) or higher, since the particle of size 0.025*D* will fit right in narrower part of the gap. The following table indicates the size of particles that can be trapped in gaps of different widths.

Table 2.1: Size (*d/D*) of particles trapped in gaps of different width *w* measured as a function of grain radius *R*.

Gap width,w (*R*)	**Size of particles that can get trapped (*d/D*)**
0.03	≥ 0.015
0.04	≥ 0.02
0.05	≥0.025
0.07	≥ 0.035
0.10	≥0.05

2.5. APPLICATION OF THE SHARMA AND YORTSOS THEORY FOR ESTIMATION OF THE CONSTANT FOR STRAINING RATE

In this section we apply Sharma and Yortsos theory (1987c) to estimate the constant for straining rate for gaps in the size range of interest. As we saw before, the right hand side of equation (2.3) is the straining rate, i.e., the rate of capture of particles in constrictions in the porous medium. From there, the straining rate constant is given by equation (2.4). The cumulative distribution *I* that appears in equation (2.4) is expressed in the Sharma and Yortsos work (1987a) as a function of the pore throat radius, r_p:

$$I(r_s) = \int_0^{r_p} r_p^2 u_R f_p dr_p \qquad (2.9)$$

where u_R is the fluid velocity through a throat of radius r_p, r_s is the radius of the suspended particles, and $f_p\ dr_p$ is the fraction of pore throats of radius r_p. Since the volumetric flow rate through a throat is proportional to $r_p^2 u_R$ we can substitute $r_p^2 u_R$ by q_R in equation (2.9):

$$I(r_s) = \int_0^{r_p} q_R f_p dr_p \tag{2.10}$$

where $I(r_s)$ is the cumulative flow through all the pore throats from size 0 to r_p, that can trap particles of size r_s, therefore $r_s \geq r_p$.

We adapt this theory to gaps by using flow rates through gaps in equation (2.10) instead of flow rates through pore throats, since the particles in the size range of interest are too small to be trapped by straining in the pore throats. Therefore, the integral in equation (2.10) is calculated with respect to gap width w instead of pore throat radius r_p.

$$I(d/D) = \int_0^{w} q_{w\text{-}d/D} f_w dw \tag{2.11}$$

where $I(d/D)$ is the cumulative flow through all the gaps that can trap particles of size d/D, f_w is the frequency of gaps of width w and $q_{w\text{-}d/D}$ is the volumetric flow through a gap of width w specific to the particle of size d/D. In the next section we will see how to calculate this particle specific flow.

2.5.1. Calculation of the Particle Specific Volumetric Flow through a Gap

To estimate the straining rate constant with equation (2.4) we need to calculate the volumetric flow in the gap, specific to the size of the trapped particle. This local flow in gaps was calculated as follows. The gap is approximated as an infinitely wide slit of height equal to the gap width *w* and length equal to twice the range of capture (*2a*) (cf. Figure 2.4). The equation for flow velocity, *u*, through a slit of width *w* is (Bird *et al*., 2001):

$$u = -\frac{w^2}{12}\frac{\nabla P}{\mu} \tag{2.12}$$

where μ is the viscosity of the fluid and ∇P is the pressure gradient in the gap. To determine the pressure gradient in the gap, the approach of Bryant *et al*. (1993), which involves the Delaunay tessellation, was used first to determine the steady state flow in pore throats and the pressures in the center of Delaunay cells. From the geometric analysis of the sphere packs we know that each gap between a pair of spheres is part of four and up to nine Delaunay cells. Simple geometric considerations showed that the centers of those cells are in the same plane; moreover the center of the gap is also in that plane, as shown in Figure 2.5a). We found that the pressures at the pore centers are nearly co-planar when plotted as a function of transformed coordinates x_t and y_t in the plane of the centers. That is, the pressure gradient is approximately constant in the plane containing the gap (Rodriguez, 2006). Figure 2.5b shows the pressure contour in the plane defined by the center of the gap and the center of the Delaunay cells containing the gap. Thus, the pressures can be fit well with an equation of the form $P = Ax_t + By_t + C$ and calculate the magnitude of the pressure gradient as:

$$\| \nabla P \| = \sqrt{A^2+B^2} \tag{2.13}$$

Using the calculated pressure gradient in equation (2.12), the volumetric flow through the gap/slit is then calculated as:

$$q_{w\text{-}d/D} = 2\ a\ w\ u \tag{2.14}$$

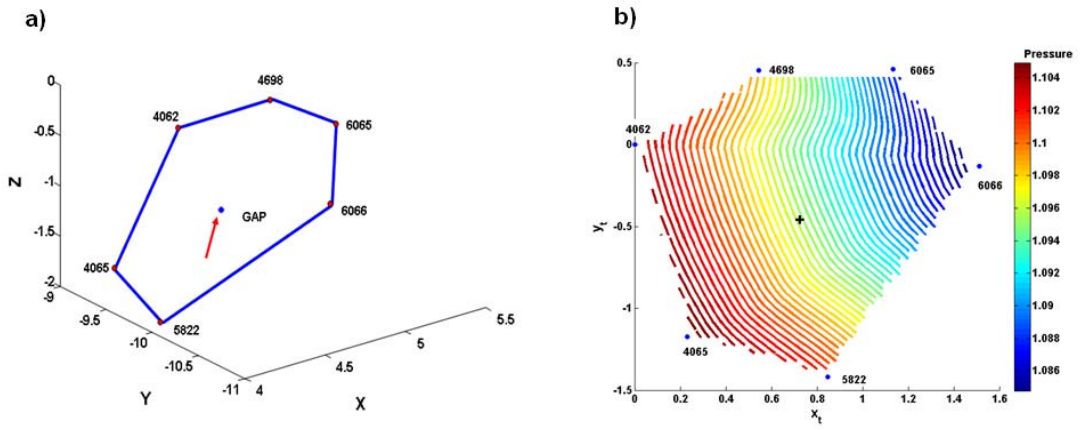

Figure 2.5: a) Plane made by the centers of the six Delaunay cells and center of the gap (indicated by an arrow).b) Contours of pressure in the plane defined by the centers of the Delaunay cells and the center of the gap in a). The coordinates have been transformed so the plane coincides with z=0. The gradient in pressure is approximately constant, and this is found to be true for nearly all gaps in the reference porous medium.

We remark that our treatment of gaps, equations (2.12) and (2.14), gives zero velocity to point contacts since they are gaps of width zero. Consequently, point contacts between grains will not contribute to straining in this version of the theory.

The cumulative flow rate distribution $I(d/D)$ expresses the assumption that the probability of a particle entering a constriction is proportional to the flow rate into that constriction. Therefore, we refer to this straining rate constant as "flow rate weighted". It is of interest to compute several alternative straining rate constants, reflecting different assumptions regarding the probability of a particle of size d/D being trapped in a gap of width w. In the next section we explore some of the alternatives.

2.5.2. Alternative Straining Rate Constants

The opposite limiting case to flow rate weighting is to assume the probability of a particle entering a gap of a certain size depends only on the relative frequency of such gaps. In this case the integral $I(d/D)$ reduces to the frequency distribution of the constrictions that can trap particles of size d/D:

$$I_c(d/D)=\int_0^w f_w dw \tag{2.15}$$

This case we refer to as "geometry weighted," as only the size of the gaps affects the straining rate.

A variation of geometry weighting is to assume that the probability of trapping is proportional to the range of capture, which depends on the gap width and the particle size. In this case the integral expressing the straining rate constant becomes:

$$I_a(d/D)=\int_0^w a(r_p) f_w dw \tag{2.16}$$

The denominator in equation (2.4), $I(\infty)$, is the cumulative flow through all the gaps in the packing. Since this will be a constant for all the particle sizes d/D we are not including it in the calculations. We will solve equations (2.11), (2.15) and (2.16) for different particle sizes d/D. What we are looking for is a relationship between k_{str} and d/D analogous to the one obtained by Bradford *et al*. (2003) and see how the scaling exponents compare. Since $I(\infty)$ is a constant for all particle sizes, its value will not affect the scaling exponent.

2.5.3. Hypothesis of Rebound of Particles

The Sharma and Yortsos (1987c) straining model discussed above assumes that particles will be trapped when they arrive at a constriction of appropriate size. This assumption is consistent with the trapping mechanism in pore throats, where large particles cannot avoid being retained between the three grains. Since gaps are bounded by grain surfaces on two sides but not the third, a permanent retention is not guaranteed.

Instead, a particle may collide with the grains and rebound, and it may be carried into a streamline that passes outside the range of capture, as shown in Figure 2.6, avoiding retention even though it entered a gap of appropriate size. We account for rebound and escape by defining the probability of retention as the product of two independent probabilities. The first is the probability of the particle arriving at the constriction. This corresponds to the flow-rate-weighted model of Sharma and Yortsos and it applies to both pore throats and gaps. We hypothesize that this probability increases as the flow velocity increases and, because of the small size of the particles (< 10 μm), we approximate the dynamics of the system to a simple transport along streamlines, as if the particles had negligible mass. The second is the probability that a

particle is trapped by the constriction, given that it has arrived there. This probability is 100% for throats if $d > d_{throat}$, but remains to be quantified for gaps.

We also assume that the probability of particle rebound and escape increases as the angle of incidence increases. A frontal collision (zero angle) is almost certain to trap the particle but is also rare since the streamline carrying the particle should pass exactly through the center of the gap.

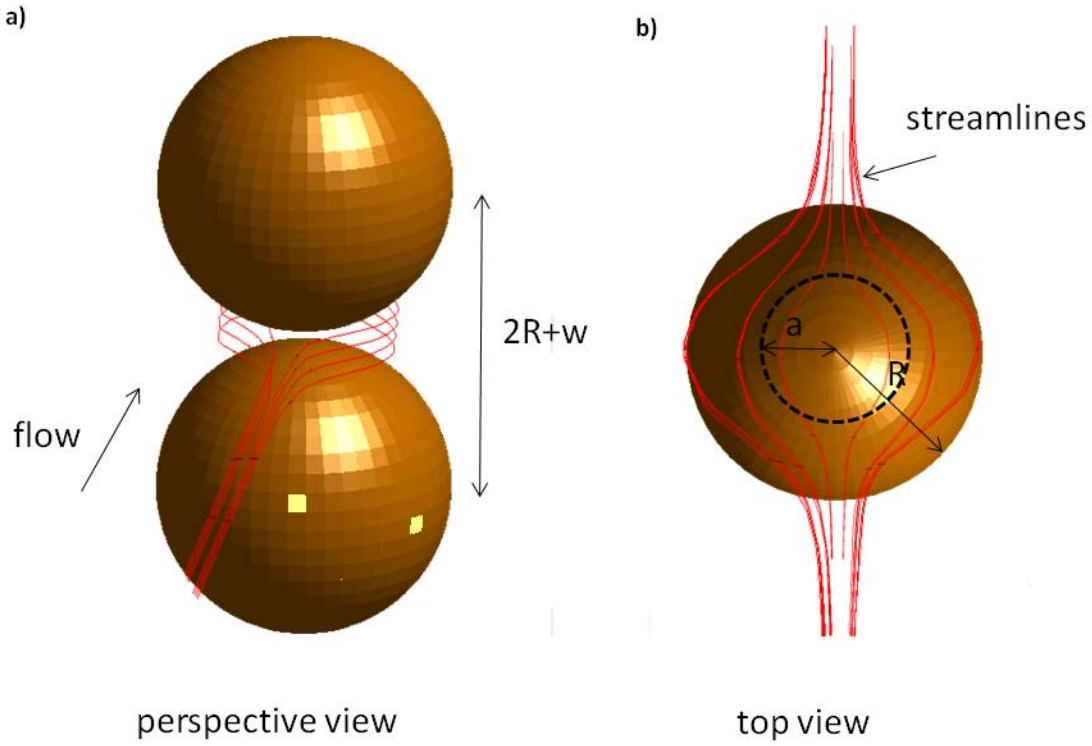

Figure 2.6: Streamlines near a gap between two spheres. a) Perspective view. b) Top view.

We are thus led to consider two more straining rate constants applicable only to gaps. The "momentum weighted" case assumes that the probability of retention is

proportional to the flow rate entering the gap and inversely proportional to the fluid momentum. In this case we revise the numerator of the straining rate constant to be:

$$I_m(d/D) = \int_0^w \frac{q_w}{u_w} f_w dw \tag{2.17}$$

The "kinetic energy weighted" case assumes that the probability of retention is proportional to the flow rate entering the gap and inversely proportional to the square of the fluid velocity. In this case we revise the numerator of the straining rate constant to be:

$$I_k(d/D) = \int_0^w \frac{q_w}{u_w^2} f_w dw \tag{2.18}$$

Having obtained the steady-state flow field in the reference porous medium, evaluating the straining rate constants is a straightforward matter of evaluating the various expressions for $I(d/D)$ in this section.

2.5.3. Results

Reference Porous Medium for Flow Calculations

We obtain a dense disordered packing of equal spheres by placing a periodic packing and its replica side by side. The resulting packing is rectangular of dimensions 0.006×0.006×0.0135 m, containing 10,000 spheres of radius 2.192×10^{-4} m. Flow was imposed in the long direction, and the other boundaries were sealed. The pressure in the pore throats located at the inlet of the packing was set to 1.5×10^5 Pa and the pressure in the pore throats located at the outlet was set to 1.0×10^5 Pa in order to solve a system of

flow equations that yields the pressure in each pore body from the approach of Bryant *et al.* (1993) (recall we need pressures in pore bodies to evaluate equation (2.12). The carrier fluid was given viscosity μ = 0.001 Pa-s. Figure 2.7 shows the variation of volumetric flow in gaps, calculated with equation (2.14), for strained particles of sizes d/D=0.03 and d/D=0.05 respectively. For a given gap width there is a modest increase in the flow rate as the particle size increases. The main influence of increasing the particle size is that more gaps that are larger can trap the particle.

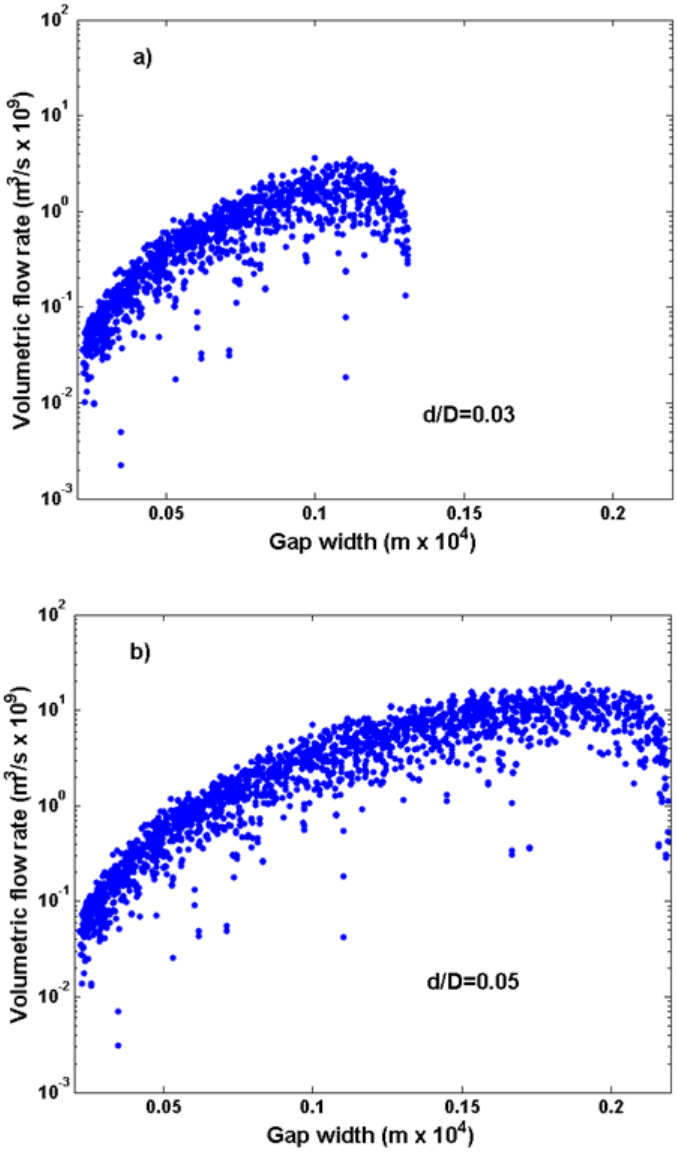

Figure 2.7: Volumetric flow rate through gaps *vs.* gap width for flow through a dense disordered packing of equal spheres. a) Particle size d/D=0.030. b) Particle size d/D=0.050.

Flow Rate Weighted Straining Rate Constant

Figure 2.8 shows the numerical evaluation of equation (2.11) using flow rates in gaps computed from equation (2.14). Each curve corresponds to a different particle size *d/D*. In order to compare with the correlation in Bradford *et al*. (2003), the predicted values of k_{str} have been fitted to a power trend line, yielding:

$$k_{str} = 29.21\left(\frac{d}{D}\right)^{4.03} \tag{2.19}$$

This trendline is plotted along with the other straining rate constants in Figure 2.13 at the end of this section. Also, the value of k_{str} for different particle sizes, according equation (2.19) is presented in Table 2.2 at the end of the section.

The scaling exponent of 4.03 in equation (2.19), about three times bigger than those observed by Bradford. The discrepancy suggests that the flow rate through a gap, as computed above, greatly overestimates the probability of a particle being strained in a gap. The main reason for the large exponent is that as particle size increases, the number of gaps that can retain that particle increases, and the flow rate through a gap is proportional to the cube of the gap width.

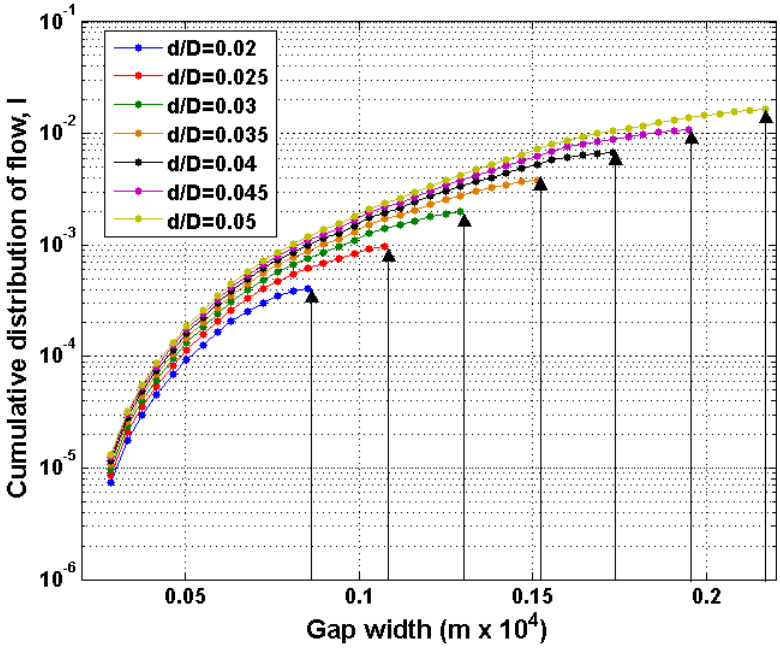

Figure 2.8: Evaluation of the "flow rate weighted" straining rate constant requires integration of the flow rate distribution in the gaps that can trap a given particle. The arrows indicate the value of $I(d/D)$, equation (2.11), for different sizes of strained particles d/D.

Geometry Weighted Straining Rate Constant

For this case we evaluate equation (2.15). Figure 2.9 shows a plot of $I_c(d/D)$ versus gap width for this case. The calculated value of k_{str} is shown in Table 2.2. The correlation between straining constant and the size of the strained particle is:

$$k_{str} = 0.061\left(\frac{d}{D}\right)^{0.88} \tag{2.20}$$

In this case the scaling exponent is about two thirds the size of the empirically obtained exponents. The discrepancy suggests that the number fraction of gaps that can trap a particle underestimates the probability of a particle being strained in those gaps. Evidently the distribution of flow rates among gaps does influence the probability of trapping, though not nearly as much as predicted by the flow-rate-weighted model.

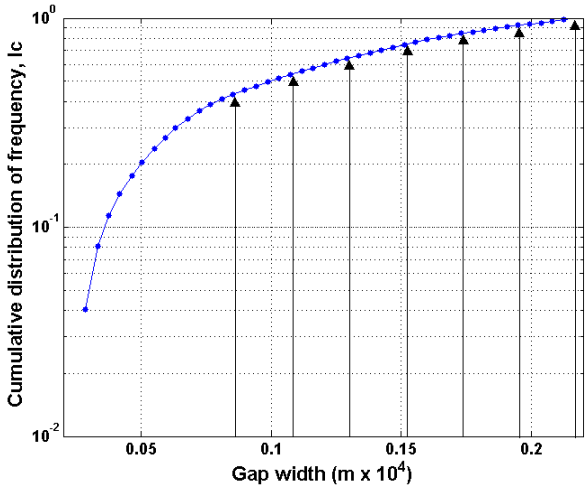

Figure 2.9: Evaluation of the "geometry weighted" straining rate constant requires integration of the frequency distribution of the gaps that can trap a given particle. The arrows indicate the values of I_c, equation (2.15), for different particle sizes in the range of interest

Range of Capture Weighted Straining Rate Constant

Equation (2.16) has been evaluated in this case. Figure 2.10 shows a plot of $I_a(d/D)$ versus gap width. The values for k_{str} are presented in Table 2.2 and are plotted versus the size of the strained particles in Figure 2.13. The correlation between straining constant and the size of the strained particle is:

$$k_{str} = 0.22\left(\frac{d}{D}\right)^{1.55} \qquad (2.21)$$

In this case the scaling exponent is within 25% of the empirical values. The agreement is encouraging, given that equation (2.21) is based entirely on geometry of realistic pore space. On the other hand, equation (2.21) is based on equation (2.16) , which is tantamount to assuming that flow rate does not vary from one gap to the next. This is clearly not the case, as Figure 2.7 showed.

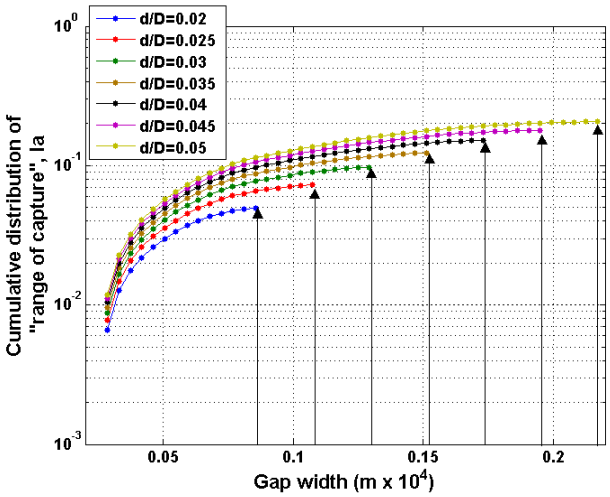

Figure 2.10: Evaluation of the "range of capture weighted" straining rate constant requires integration of the distribution of ranges of capture for the gaps that can trap a given particle. The arrows indicate the values of I_a, equation (2.16), for different particle sizes in the range of interest.

Momentum Weighted Straining Rate Constant

For this case we evaluated equation (2.17). Figure 2.11 shows the corresponding figure. Table 2.2 shows the calculated values for k_{str} and Figure 2.13 shows a plot of k_{str}

versus the size of the strained particles. The correlation between straining constant and the size of the strained particle is:

$$k_{str} = 0.16\left(\frac{d}{D}\right)^{2.25} \tag{2.22}$$

This scaling exponent is much closer to the observed value than the "flow rate weighted" exponent. This supports the hypothesis of particle/grain collisions reducing the probability of retention. However, the momentum-weighting of equation (2.22) still overestimates the influence of particle size.

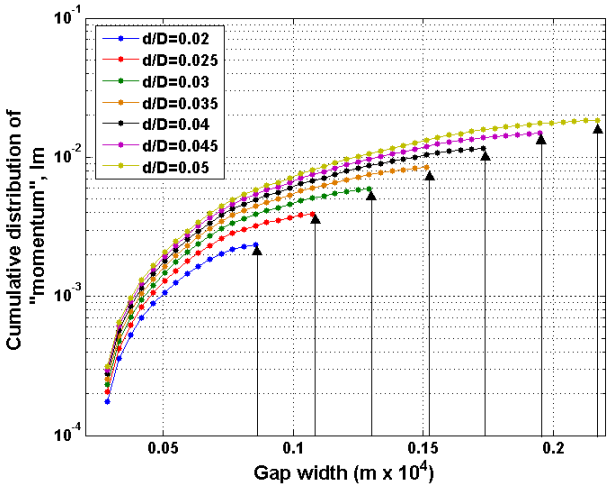

Figure 2.11: Evaluation of the "momentum weighted" straining rate constant requires integration of the ratio of flow rate through a gap to the fluid velocity in that gap, for the gaps that can trap a given particle. The arrows indicate the values of I_m, equation (2.17), for different particle sizes in the range of interest.

Kinetic Energy Weighted Straining Rate Constant

In this case we evaluated equation (2.18). The numerical evaluation is shown in Figure 2.12**.** The values of k_{str} for this case are also shown in Table 2.2 and plotted in Figure 2.13. The correlation between particle size and straining constant is in this case:

$$k_{str} = 0.0016\left(\frac{d}{D}\right)^{1.11} \tag{2.23}$$

The scaling exponent in this case is somewhat smaller than experimentally observed.

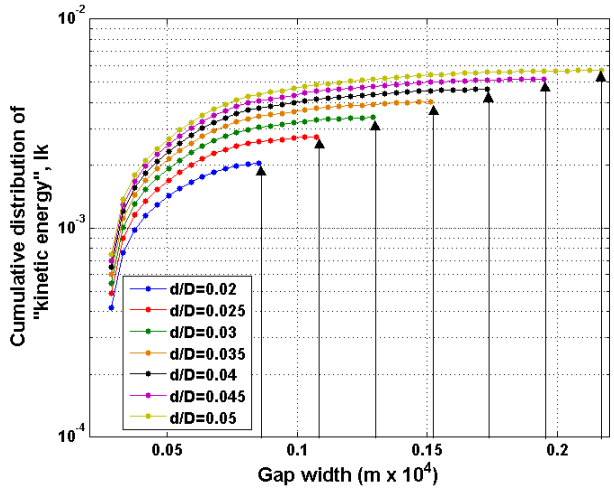

Figure 2.12: Evaluation of the "kinetic energy weighted" straining rate constant requires integration of the ratio of flow rate through a gap to the square of the fluid velocity in that gap, for the gaps that can trap a given particle. The arrows indicate the values of I_k, equation (2.18), for different particle sizes in the range of interest.

Table 2.2: Values of k_{str} for different particle sizes (d/D) calculated by different methods

d/D	Flow Weighted	Geometry	Momentum	Kinetic	Range of Capture
0.020	4.21E-06	1.93E-03	2.37E-05	2.04E-05	5.01E-04
0.025	9.86E-06	2.37E-03	3.95E-05	2.74E-05	7.29E-04
0.030	2.03E-05	2.82E-03	5.98E-05	3.40E-05	9.76E-04
0.035	3.89E-05	3.28E-03	8.50E-05	4.02E-05	1.24E-03
0.040	6.86E-05	3.66E-03	1.16E-04	4.62E-05	1.52E-03
0.045	1.09E-04	3.99E-03	1.49E-04	5.17E-05	1.79E-03
0.050	1.63E-04	4.26E-03	1.85E-04	5.69E-05	2.07E-03

Table 2.3 summarizes the scaling exponents obtained with the five alternatives for estimating probability of retention. Figure 2.13 shows the power trend lines for the five cases considered along with Bradford's correlations.

Table 2.3: Scaling exponents from five different methods

Method	Exponent
Flow weighted	4.03
Geometry	0.88
Range of Capture	1.55
Momentum	2.25
Kinetic	1.11

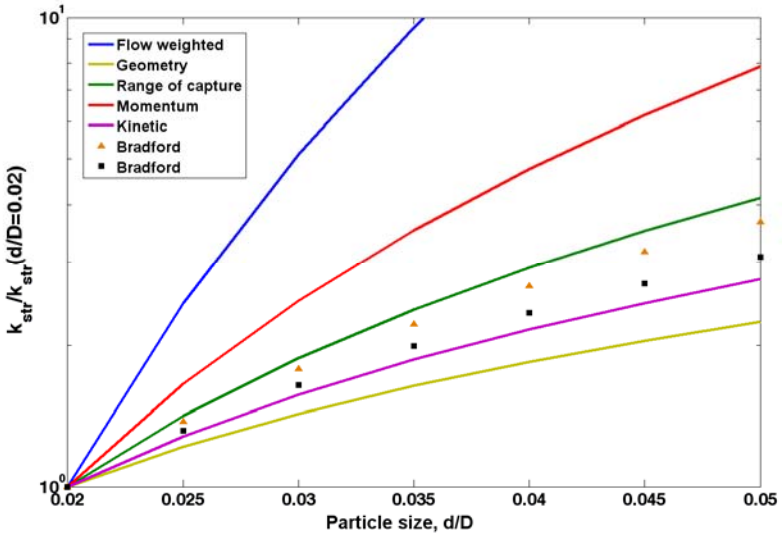

Figure 2.13: Straining rate constant (k_{str}) for different particle sizes, evaluated by introducing different assumptions in the Sharma and Yortsos theory.

Discussion

The flow rate weighted scaling exponent is based on reasoning that is appropriate for pore throats but neglects the possibility of particle/grain collision leading to rebound and escape from a gap. Consequently it is not surprising that it is much larger than the observed scaling exponent for particles smaller than the smallest pore throats. At the other extreme, the geometry weighted scaling exponent assumes that the probability of encountering a constriction is independent of the flow field. This is unlikely to be true, given the wide range of flow velocities within pore space, and it is not surprising that this exponent is much smaller than observed.

The momentum weighted and kinetic energy weighted scaling exponents bracket the observed values much more tightly than the flow rate weighted and geometry weighted exponents. The kinetic energy weighted exponent is fairly close to the empirical

exponent of 1.42 in equation (2.7). This supports the premise on which these exponents are based, namely a nonzero probability of particle escape from a gap that increases with the average velocity of fluid through the gap. On the other hand, our evaluation of the exponents merely postulated a plausible dependence upon relevant hydrodynamic quantities. A more rigorous assessment of particle/grain dynamics in a flow field is needed to verify our interpretation of the behavior.

Interestingly, the range of capture weighted exponent, which assumed straining probability is independent of flow rate, is close to the empirical value of equation (2.7). There is no obvious physical justification for this exponent. It is more likely to be a numerical coincidence. Because it depends only upon geometry of void space, it nevertheless may be useful as a much more easily computed rough estimate of the scaling exponent.

The analysis presented here does not allow for contributions of point contacts to straining. This is because the gap width w is zero at a point contact and equation (2.14) will therefore assign a zero flow rate to them. However, point contacts clearly have a range of capture, just as gaps do, and can be expected to strain particles. Point contacts are five to six times more numerous than gaps, so their influence on the scaling exponent could be significant. We have also neglected multi-particle effects, assuming that particles approach gaps alone and that previously strained particles do not affect the flow dynamics in a gap. Given the reasonable agreement between the kinetic energy weighted exponent and measurements, we anticipate that including these phenomena will refine the agreement rather than change the qualitative behavior.

In the next section we propose and evaluate a method to estimate the straining rate constant based on a detailed calculation of flow in the gaps, rather than considering the gap as a slit.

2.6. Estimation of the Constant for Straining Rate by Calculation of Detailed Flow Field in Pore Throats

In the previous section we conclude that a detailed calculation of the flow distribution within a throat, specifically at gaps and near point contacts, may be needed to get a better agreement between the scaling exponents of the computed constant for straining rate and the one reported in the literature (Hall, 1957; Bradford *et al*., 2003). When applying Sharma and Yortsos theory we used a single value of flow that was calculated for a pair gap-strained particle. Also, our adaptation of Sharma and Yortsos (1987c) theory treats gaps and throats independently. However, pore throats are adjacent with gaps, as was shown in Figure 2.1 and Figure 2.3, and straining in the gap may also depend on the flow through the throat.

In this section we propose a method to calculate the constant for straining rate that accounts for the flow in the throat and also allows the calculation of the straining rate constant in point contacts between spheres. A detailed flow field in gaps and throats will be calculated by solving Navier-Stokes equation with the finite element based tool COMSOL.

2.6.1. Hypothesis

A hypothesis is proposed, stating that the rate of straining of a particle, and therefore the constant for straining, is proportional to the fraction of the total flow

through the throat that passes through the gap in order to trap a particle of a given size. Therefore we define the constant for straining rate k_{str} for a particle of size d/D as:

$$k_{str}(d/D)_{gap} = \frac{flow_{gap}(d/D)}{flow_{\Omega}} \tag{2.24}$$

where $flow_{\Omega}$ is the total volumetric flow in the domain Ω (throat plus gaps) and $flow_{gap}(d/D)$ is the volumetric flow through the portion of the gap that will trap a particle of size d/D. Figure 2.14 shows the a front view of two particles being trapped in a gap and a constriction near a point contact that belong to the same pore throat.

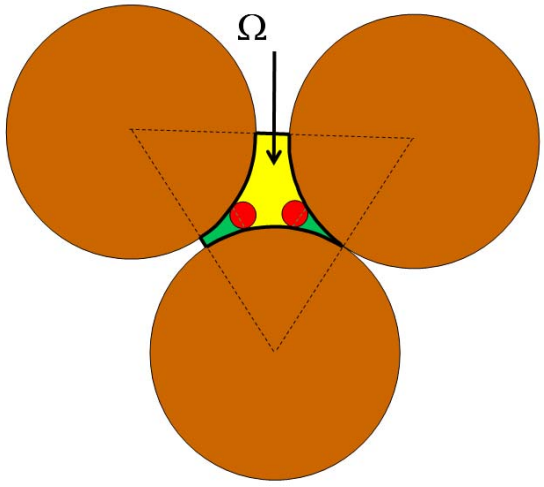

Figure 2.14: Particles (in red) being trapped in a gap and a constriction associated with a pore throat. The constant for straining can be calculated as the ratio of flow through the regions of the throat that would trap the particle (in green) and the total flow through the throat (highlighted with a thicker black line in the figure).

In this fashion, we can calculate the straining rate constant k_{str} for a particle of a given size *d/D* in a given throat configuration if we know the detailed volumetric flow in the throat.

To estimate the relationship between straining rate constant and particle size for a whole pack of spheres, we will use the data of the frequency of gaps in the pack from the statistical analysis of sphere packs (Rodriguez, 2006) and calculate a weighted straining rate constant for each particle in the size range of interest using the following expression:

$$k_{str}\left(d/D\right)_{pack} = \sum_{gap} k_{str}(d/D)_{gap} f_{gap} \tag{2.25}$$

where f_{gap} is the frequency of a gap of size w that can trap a particle of size *d/D* and $k_{str}(d/D)_{gap}$ is the straining rate constant in a gap of size w for a particle of size *d/D* calculated with equation (2.24). The summation is extended to all the gaps in the pack that can trap the particle of the given size *d/D*.

Therefore we can calculate the value of the constant for straining rate $k_{str,gap}(d/D)$ for a particle of size *d/D* in a gap whose width w is adequate to trap the particle using equation (2.24), repeat the procedure for all the gap sizes in the size range of interest that could trap the aforesaid particle, and then use equation (2.25) to "weight" the constant for straining rate in a pack and obtain $k_{str,pack}(d/D)$. Later we will fit $k_{str,pack}(d/D)$ to *d/D* using a power law relationship and check how the scaling exponent compares with the ones reported in the literature (Hall, 1957; Bradford *et al.*, 2003) and with the ones that resulted from our adaptation of Sharma and Yortsos theory (section 2.5.)

2.6.2. Calculation of the Velocity Field in the Gap

To test the previous hypothesis we need to calculate the detailed volumetric flow in the throat and the gaps (cf. equation (2.24)). When adapting Sharma and Yortsos theory for estimating the straining rate constant in section 2.5, we used the actual flow field in the granular medium to calculate the flow through the gaps. But now, gaps of different size as well as point contacts are going to be studied independently. We have to set boundary conditions in the domain of the gap, rather than in the pack, that will allow the calculation of the volumetric flow which will be local to the gap configuration consider in each case.

We used the finite element based software COMSOL to calculate a detailed velocity field in the domain of the gap. We choose the following application module, for incompressible fluids, as is the case for fluids under normal conditions:

Chemical Engineering → Momentum Transport → Laminar Flow → Incompressible Navier-Stokes.

The Navier-Stokes equation being solved is:

$$\rho\left(\frac{\partial \mathbf{u}}{\partial t} + \mathbf{u}\cdot\nabla\mathbf{u}\right) - \mu\nabla^2\mathbf{u} = -\nabla p \qquad (2.26)$$

where ρ is the density of the fluid, μ is the dynamic viscosity, p is the pressure and $\boldsymbol{u}$ is the velocity vector.

We start by defining our domain for the flow field calculation as the 3D pore space between three spheres making the pore throat. This domain is created in COMSOL's "draw mode" as the intersection of a cylinder with three spheres that make the pore throat with the desired configuration, as shown in Figure 2.16a. The next step is to define the domain properties and boundary conditions in the "Physics" mode. We

assume the fluid properties of water (ρ = 1000 kg/m^3 and μ = 0.001 Pa·s) and we set the following boundary conditions:

a) No slip condition on the grain surface, that is, the velocity of the fluid is zero at the grain surface.
b) Symmetry condition on the fluid open boundaries, that is, vanishing shear stresses.
c) Inlet normal stress equal to 2 N/m^2 and no tangential velocities.
d) Outlet normal stress equal to 1 N/m^2 and no tangential velocities.

The boundary conditions are indicated in the domain in Figure 2.15a. The next step is to generate the mesh of the domain in the "Mesh" mode. The mesh is shown in Figure 2.15b.

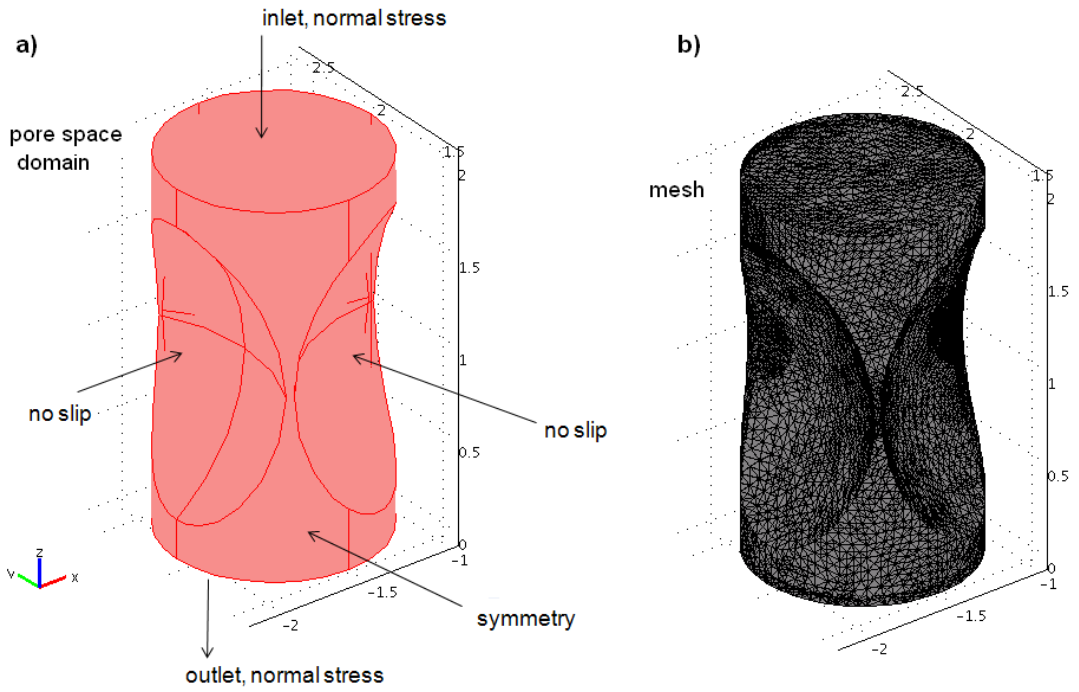

Figure 2.15: a) Domain for detailed velocity field calculation in a throat, obtained as the intersection of a cylinder with the three spheres that make a pore throat. The width of the three gaps between spheres is $0.05D$ and the pore throat diameter is $0.21D$. The boundary conditions used are indicated. b) Mesh of the domain.

After the mesh is generated, we chose the default solver in "Solve" mode (GMRES, Generalized Minimal Residual Method) to solve Navier-Stokes equation in the domain. Figure 2.16 shows a slice of the resultant velocity field between three spheres.

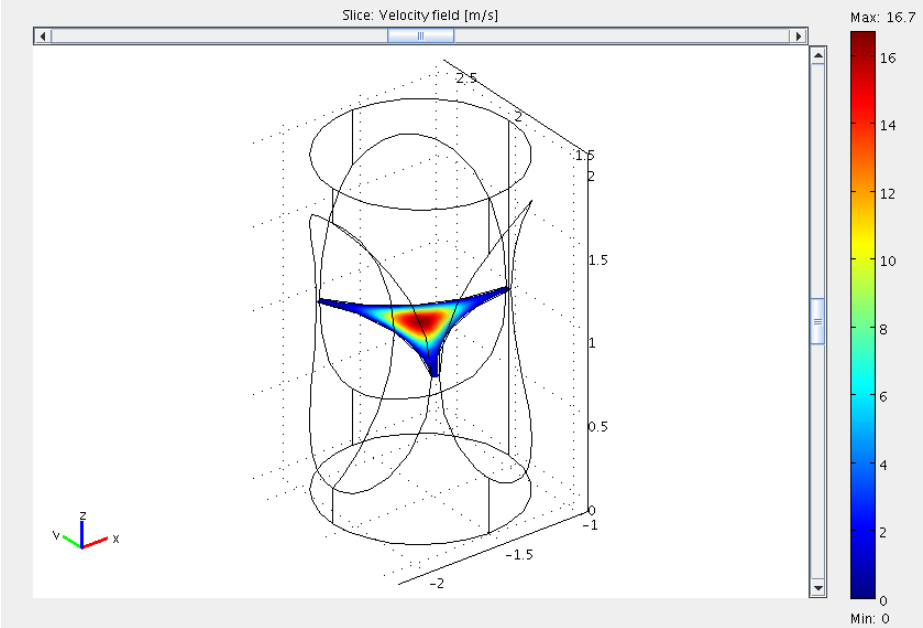

Figure 2.16: Velocity field in a slice of the pore space domain generated by the intersection of three spheres and a cylinder.

The maximum velocity value in the center of the throat between the three spheres is proportional to the difference in normal stresses that we chose as inlet and outlet boundary conditions. Since we are ultimately looking for the scaling exponent between straining rate and particle size, the choice of value for the normal stress will not affect the result as long as it is kept constant for each particle size.

The simulation outputs the value of the velocity in each node of the domain mesh, therefore now we know the distribution of velocity values from the gap to the pore throat rather than single, averaged values for gap and for throat.

The next step is to integrate the velocity values in the vicinity of the gap to get the volumetric flow field that we need for equation (2.24). But we could solve this problem in a less complex domain taking advantage of the symmetry boundaries. We will select a

smaller portion of the system, closer to the gap that will allow for more mesh refinement, and therefore more velocity values in the vicinity of the gap, without increasing computation time. We are going to focus on individual gaps between two spheres and choose a domain for velocity calculation that includes the center of the gap. Figure 2.17 shows an example of the simplified portion of the system that we used for the detailed flow field calculations.

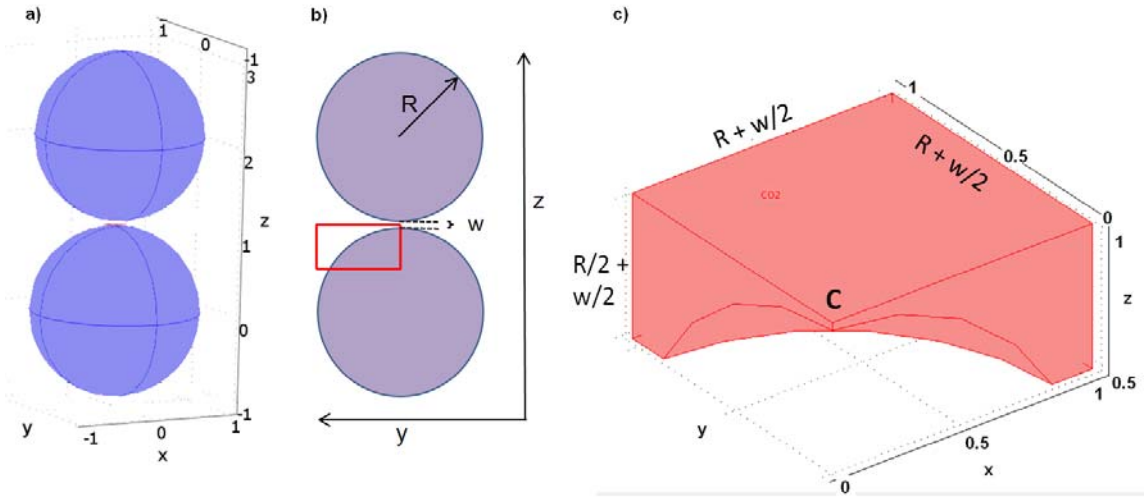

Figure 2.17: Subdomain used for velocity field calculations. a) Two spheres of radius R=1 separated by a gap of width $w = 0.05R$. The flow is in the x direction. b) Front view of the two spheres showing the subdomain (red box) used for the calculation of the flow field. We draw a box of sides (R+w/2) in the x and y directions and (R/2 + w/2) in the z direction whose upper right corner (C) coincides with the center of the gap. c) Subtracting the bottom sphere in a) or b) from the box we get the domain for velocity field calculations shown in part c).

We select boundary conditions for the domain analogous to the ones for the case of three spheres intersected by a cylinder. The surface of the grain has a no-slip boundary, inlet and outlet boundaries have a normal stress of 2 N/m^2 and 1 N/m^2 respectively and the rest of the surfaces have a symmetry boundary. Figure 2.18 illustrates the boundary conditions.

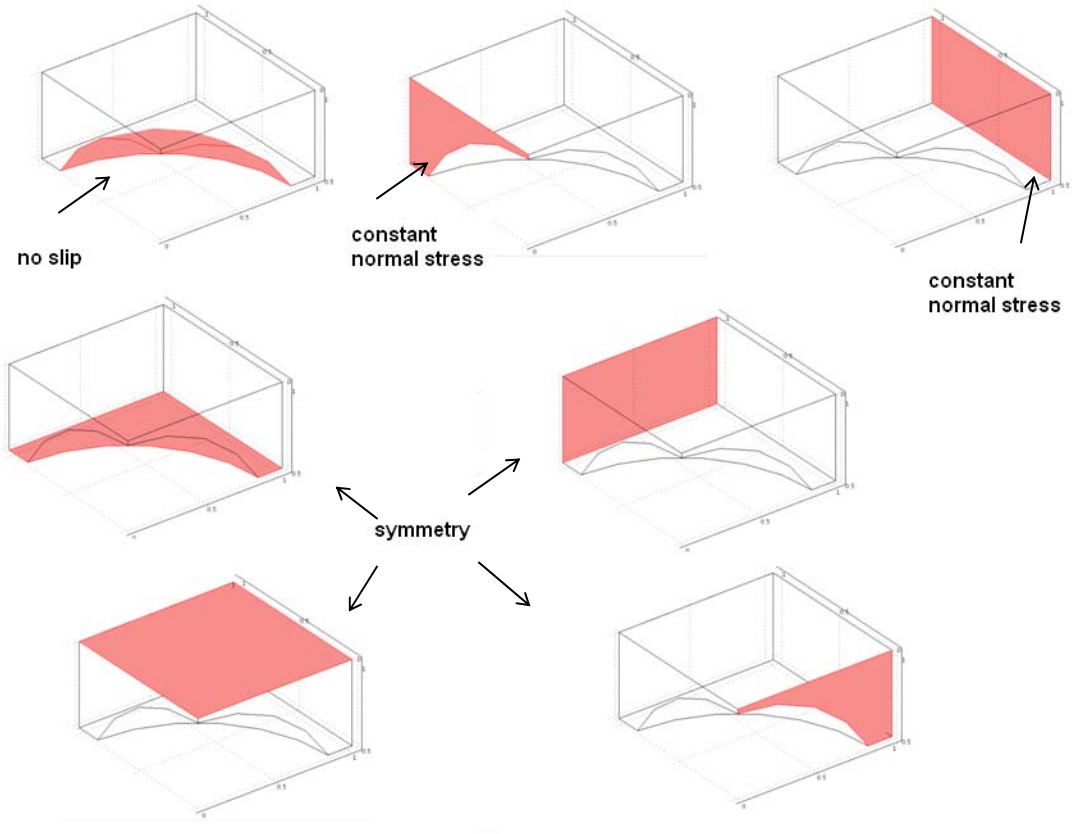

Figure 2.18: Boundary conditions used in the domain to solve the Navier-Stokes equation.

After setting the boundary conditions we create the mesh in the domain with COMOSOL "Mesh" mode. In order to get more mesh elements near the center of the gap

but not elsewhere we use the "Free mesh parameters" option, where we change the default value of "Resolution of narrow regions" to 6. This parameter controls the number of layers of elements that are created in the narrower regions of the subdomain (refer to COMSOL user manual for more information on mesh parameters.)

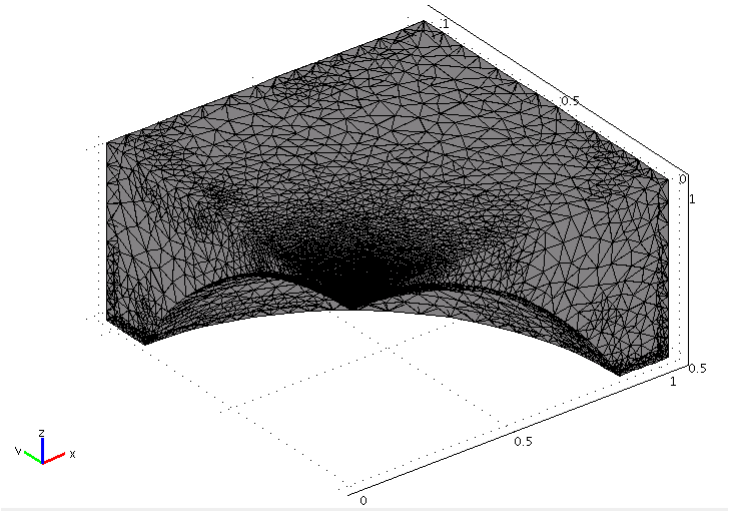

Figure 2.19: Mesh in the domain for velocity field calculation. The domain corresponds to the case of a gap width $w = 0.05R$.

We solve Navier-Stokes equation in COMSOL "Solve" mode using the default solver (GMRES). Figure 2.20a shows the solution of the velocity field from the solution of the incompressible Navier-Stokes model in the vicinity of the gap and Figure 2.20b show the pressure field across the gap. This exercise is repeated for different gap sizes w, i.e., new domains are created by intersection of a sphere of radius R and a box of dimensions $(R + w/2) \times (R + w/2) \times (R/2+w/2)$ as shown in Figure 2.17, where w is in the range of sizes of interest for particle trapping.

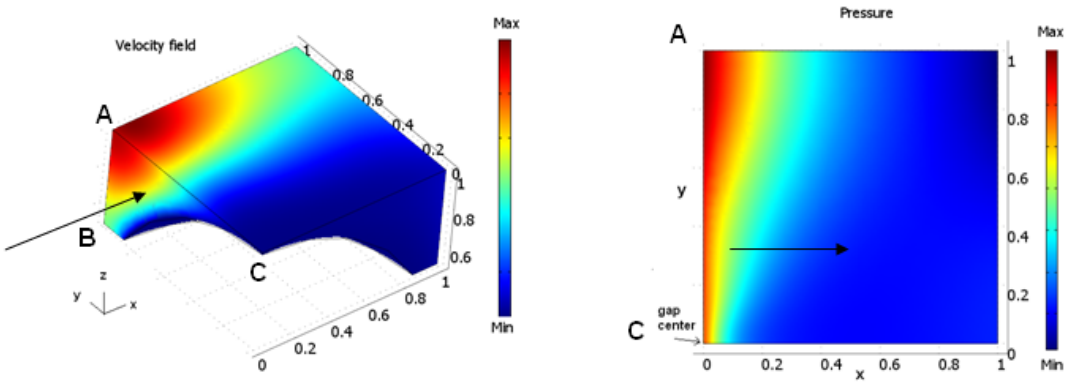

Figure 2.20: a) Detailed velocity flow in the vicinity of a gap situated at (0, 0, 0) (point C). b) x-y view of the pressure field in the plane through the gap. The arrows indicate the direction of the flow.

COMSOL has the option of integrating the velocity field through the boundaries to obtain the volumetric flow field but we are interested in yet another small region of the domain shown in Figure 2.20a. The flow relevant to trap a given particle is enclosed a region that we will call "annulus of capture" and that is shown in Figure 2.21. The figure shows a particle of size d/D = 0.04 being trapped in a gap of size $w = 0.05R$, at the maximum range of capture a (the center of the particle is at a distance equal to the range of capture from the center of the gap). The region from the center of the gap to the inner radius of the annulus (a - $d/2$) is inaccessible to the particle. If the particle were in a streamline leading to that area it will get stuck between the two grains before getting to that zone. If the center of the particle follows a streamline that passes at a distance larger than the range of capture from the center of the gap it will not be trapped. Therefore we are going to consider only the velocities in the annular region between (a - $d/2$) and (a +

d/2) to calculate the flow in the gap relevant to trap the particle. Figure 2.22 shows a sketch of the annulus of capture.

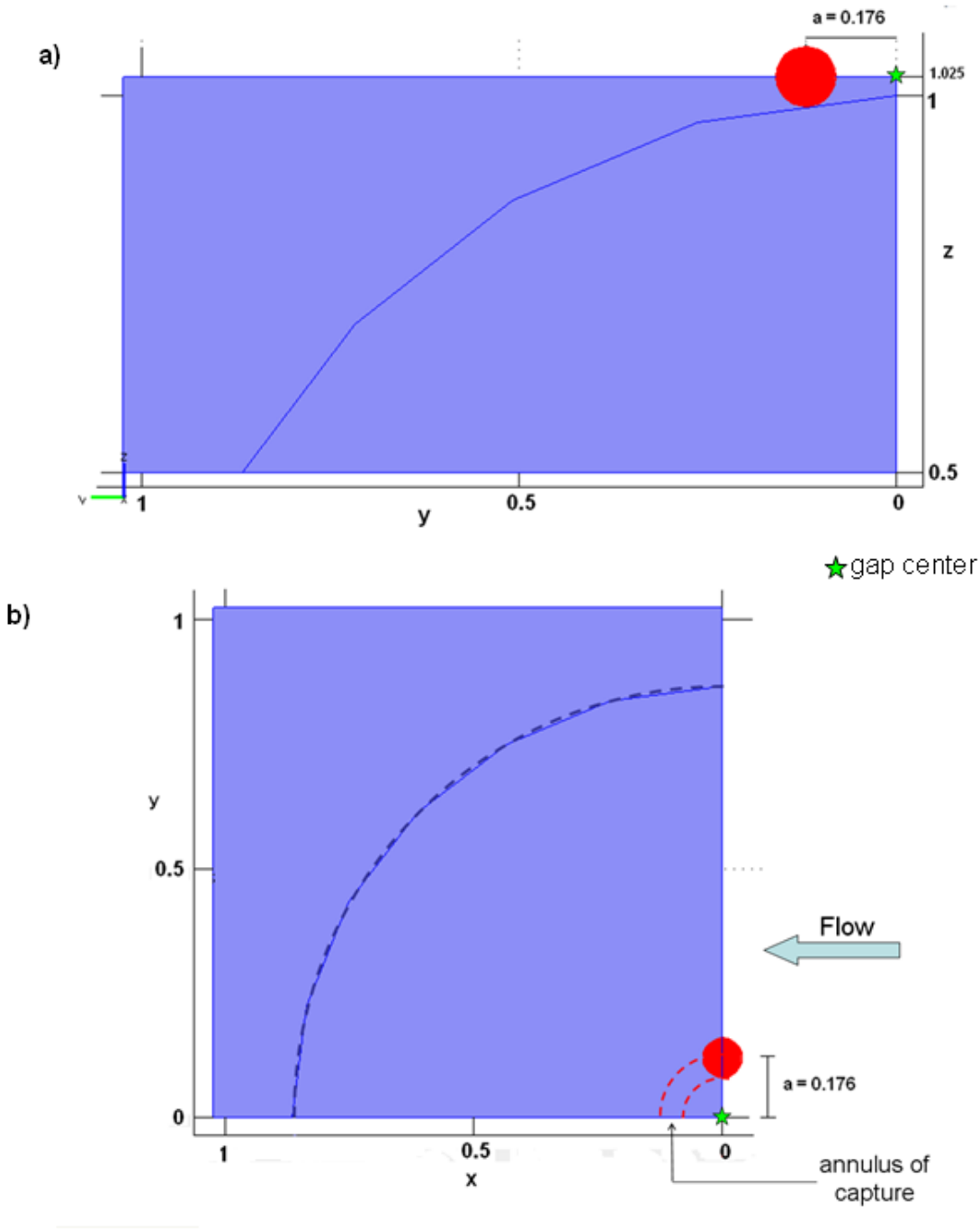

Figure 2.21: a) Particle of size $d/D = 0.04$ being trapped in a gap of size $w = 0.05R$. The flow is perpendicular to the plane of the paper. Shown is the y-z view of the subdomain in Figure 2.17c. b) Top view (x-y) of the subdomain, showing a quarter of the annulus of capture (dashed red line) for the particle in a).

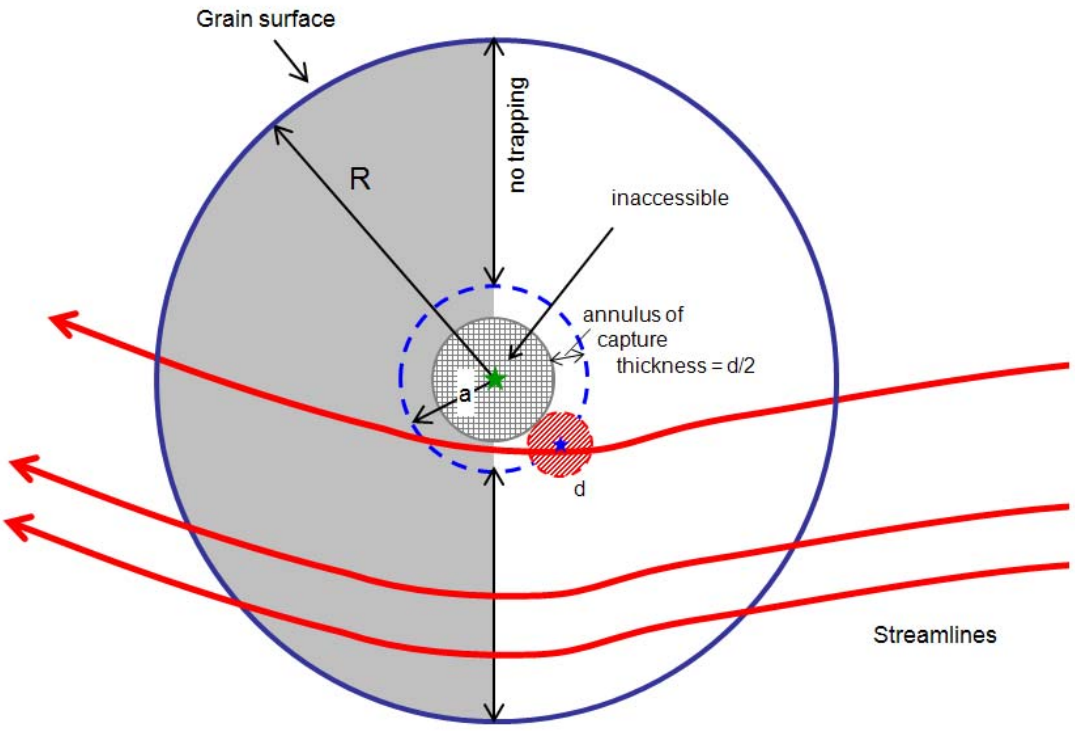

Figure 2.22: Sketch of a top view of the annulus of capture. A particle of diameter *d* (in red) is being trapped in a gap between two spheres at its maximum range of capture *a*. The shaded area in the center is not accessible for the particle. If the particle follows a streamline that passes outside the range of capture *a*, it will not be trapped.

In the following section we describe how we calculated the volumetric flow in the region of the annulus of capture.

2.6.3. Calculation of the Volumetric Flow on the Annulus of Capture

The volumetric flow in the subdomain of the annulus of capture will be calculated by independent integration of the velocity field obtained by solving Navier-Stokes equations in the geometry described in the previous section (cf. Figure 2.17c). The spatial coordinates of every node of the mesh and the value of the velocity field at every node in the domain can be exported from COMSOL post processing data as follows: In the main toolbar go to:

File → Export →Postprocessing Data

A menu populates showing several tabs. In the "General" tab mark "Subdomains" under "Export data from" option. In the same tab, give a name to the file in which the data will be written in the "Export to file" field. Then choose "Coordinates, data" in the "Format of exported data" option. In the "Subdomain" tab, under "Expression to export" choose "Velocity field" under the "Predefined quantities" scroll menu. A text file will be created with four columns of data that corresponds to the x, y, and z coordinates and velocity of each node in the mesh. From here, we will process this file in Matlab to calculate the volumetric flow field in the annulus of capture (relevant code is shown in Appendix B).

Since we know the geometry of the domain, we can easily filter with Matlab the points that belong to the annulus of capture for a given particle size. Remember that the annulus of capture expands from $y = a\text{-}d/2$ to $y = a$ (cf. Figure 2.22) where a is the range of capture (for the given particle in a given gap, equation (2.8)) and d is the diameter of the trapped particle. Figure 2.23 shows the location of the nodes of the 3D mesh created in COMSOL that correspond to the annulus of capture of a particle of size $d/D = 0.09$ in a gap of width $0.1R$. We know the value of the velocity in each of these points.

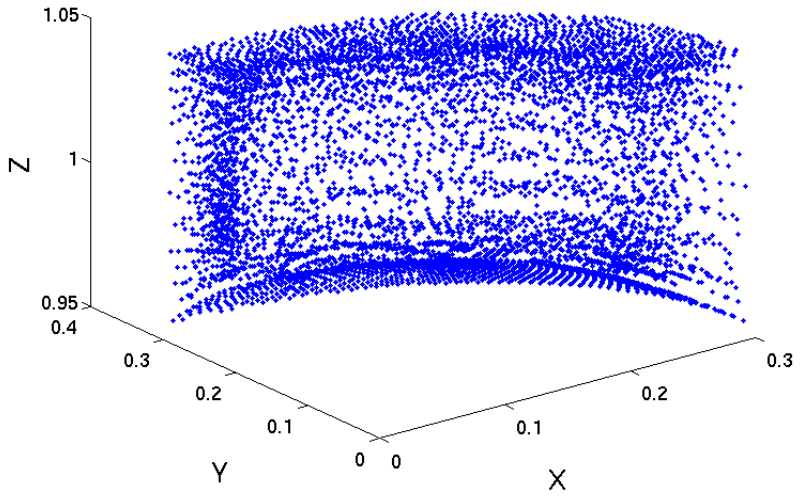

Figure 2.23: Plot of the (x,y,z) location of the nodes in the annulus of capture from which we know the value of the velocity from COMSOL calculations. This annulus corresponds to a gap of width $w = 0.1R$ for a particle of size d/D=0.09.

We have a different set of points for different combinations of gap size and particle size. The flow in the annulus is calculated as a double integral of the velocity v through the y-z plane (recall the fluid flows in the x direction) as shown in the following equation:

$$\text{flow}_{\text{gap}}(\text{d}/\text{D}) = \int_{\Delta y}\int_{\Delta z} \text{v}\,\text{dz}\,\text{dy} \tag{2.27}$$

To solve this integral we divided the velocity points in the annulus of capture into blocks of size $\Delta y \Delta z$ as shown in Figure 2.24. We specifically divided the range of y and z values into 10 increments. We calculated the arithmetic mean of the velocities in each $\Delta y \Delta z$ block. Then we integrate these average values first with respect to z, so we will

have a value of velocity multiplied by length for each Δy. The integration limits for z are given by the surface of the sphere (bottom) and the top plane of the domain.

Finally we integrate with respect to y to get the final volumetric flow in the annulus. This value corresponds to a pair of values for gap size and particle size. We repeat the same procedure for different particle sizes (d/D) in the same gap (w). For each particle size, the maximum value of y will be different, since it corresponds to the range of capture which is particle specific.

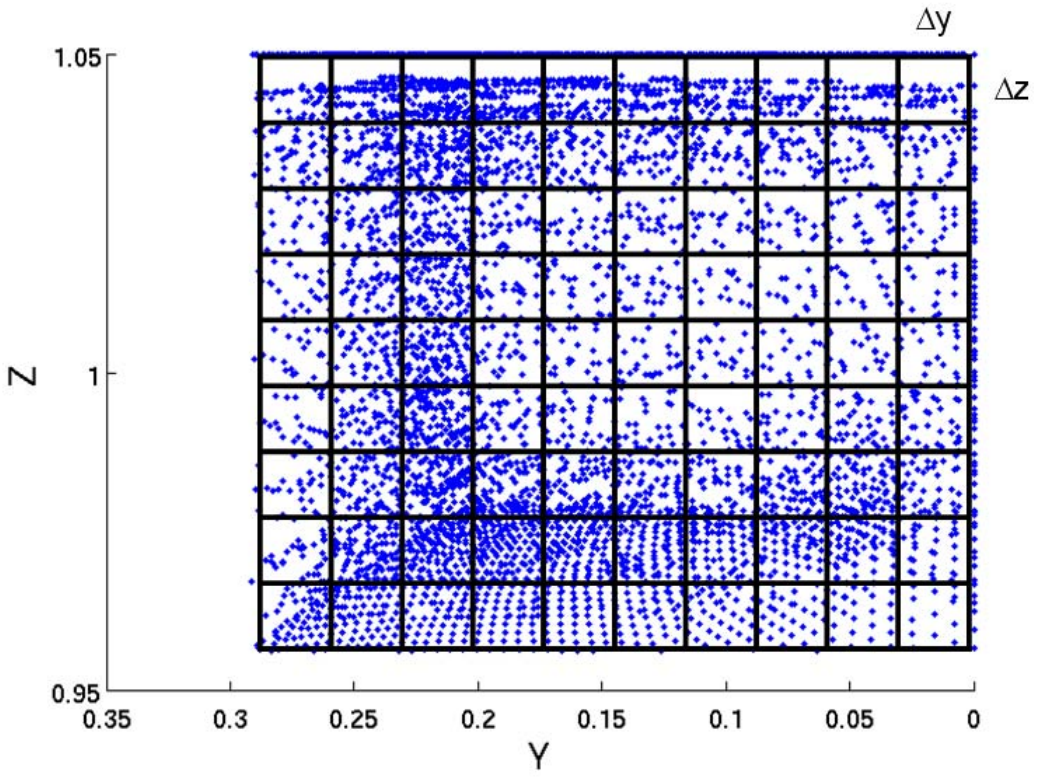

Figure 2.24: Integration grid used to solve the flow in the annulus. First we calculated the arithmetic mean of velocities in each $\Delta y \Delta z$ block. Second, we integrated these values over z to obtain a single value of velocity times length for each Δy. Finally, we integrated with respect to y to obtain the volumetric flow through the annulus of capture.

This procedure for a particle size d/D in a gap of width w gives us the value of the numerator in equation (2.24) $flow_{gap}(d/D)$. The denominator $flow_{\Omega}$ is the total flow in the domain which is calculated directly with COMSOL "Postprocessing" menu using the "Boundary integration" option.

Calculating these volumetric flows for specific gap-particle pairs is the first step towards the calculation of the constant for straining rate in a computer generated pack of spheres. The next steps are described in the following section.

2.6.4. Calculation of the Constant for Straining Rate

In the previous section we showed the procedure to calculate the volumetric flow in a gap specific for a particle size, $flow_{gap}(d/D)$ in equation (2.24). With this equation we can calculate the value of the straining rate constant for a particle of size d/D in a gap of width w, what we called $k_{str}(d/D)_{gap}$.

To calculate the straining rate constant for a particle of size d/D in a pack of spheres, we need the value of $k_{str}(d/D)_{gap}$ in all the gaps that can trap that specific particle. Then each $k_{str}(d/D)_{gap}$ will be multiplied by the frequency of the gap size that it refers to in the pack of spheres. That will give us a single value $k_{str}(d/D)_{pack}$ as indicated in equation (2.25).

This procedure is done for combinations of particles and gaps sizes in the range of interest where anomalous straining was observed, d/D = 0.015 to 0.05 for particles and $w = 0R$ to $0.1R$ for gaps. Notice that in contrast to the situation in section 2.5.1., we now are able to compute a straining rate constant for a point contact, since we are calculating the volumetric flow in an annulus and not in the center of the gap.

Table 2.4 shows the results of the individual $k_{str}(d/D)_{gap}$ from equation (2.24) , the frequency of each gap size in a computer generated dense disordered pack of spheres of the same size and the value of $k_{str}(d/D)_{pack}$ from equation (2.25). The cells shaded in gray correspond to cases where the particles are too small for being trapped in the given gap size, therefore is not possible to calculate a straining rate constant.

Table 2.4: Chart for $k_{str}(d/D)_{gap}$ and $k_{str}(d/D)_{pack}$ calculations

Gap size, w (R)	$\mathbf{f_{gap}}$	**Particle size (d/D)**							
		0.015	0.020	0.025	0.030	0.035	0.040	0.045	0.050
0									
0.01									
0.02									
0.03					$k_{str}(d/D)_{gap}$				
0.04									
0.05									
0.06									
0.07									
0.08									
0.09									
0.1									
$\boldsymbol{k_{str}(d/D)_{pack}}$									

Finally, the values of the constant for straining rate for particle of size *d/D* in the pack $k_{str}(d/D)_{pack}$ are plotted versus *d/D* and fitted to a power law to calculate the scaling exponent between constant for straining rate and particle size. Figure 2.25 shows the results, where the constant for straining rate has been normalized with respect to its value for *d/D*=0.05.

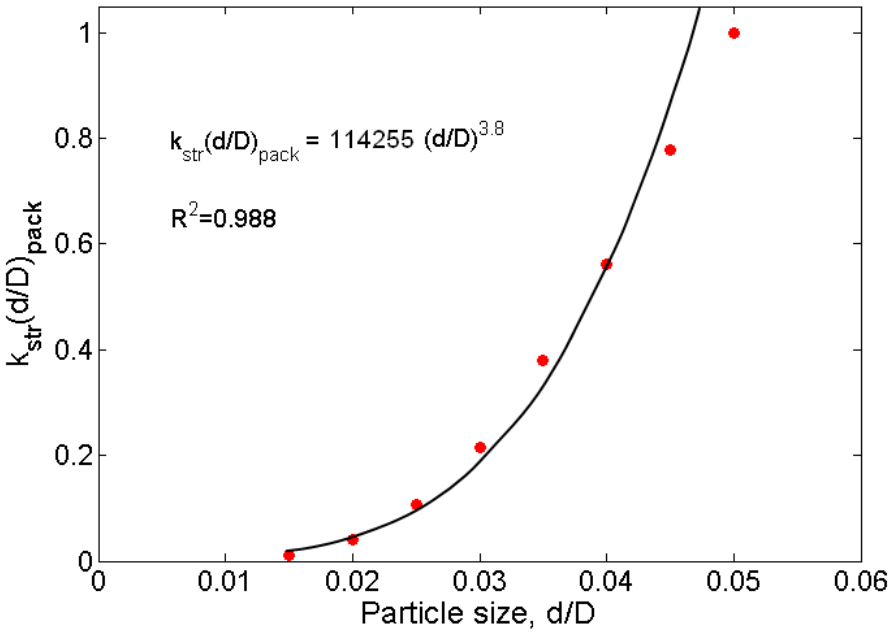

Figure 2.25: Constant for straining rate *vs*. particle size from detailed calculation of the flow field in the vicinity of a gap.

The calculation of the straining rate constant assuming that it is only dependent and directly proportional to the flow through the annulus of capture (using equations (2.24), (2.25) and (2.27)) yielded a scaling exponent of 3.8 as shown in Figure 2.25. This confirms that the assumption that the probability of straining in gaps fully depends on the

flow through the gap overestimates retention, as our adaptation of Sharma and Yortsos theory to gaps revealed.

In the next section we are going to account for the possibility of rebound and escape of particles from the range of capture applying similar logic as we did with the Sharma and Yortsos theory.

2.6.5. Accounting for Rebound and Escape of Particles

The possibility of collision and rebound of colloids when approaching constrictions was considered by assuming that the probability of trapping depends on two factors. The first factor is the angle of incidence of the colloids, the angle between the line that joins the center of the gap and the center of the colloid when it arrives at the trapping position, and the (straight) streamline that passes through the center of the gap, cf. Figure 2.6. An angle of zero corresponds to a "head-on" collision between colloid and the pair of grains. An angle of 90 degrees corresponds to a "grazing" collision in which the colloid contacts the pair of grains at the far lateral edge of the range of capture. Figure 2.26 illustrates the angle of incidence of a particle being trap between two spheres.

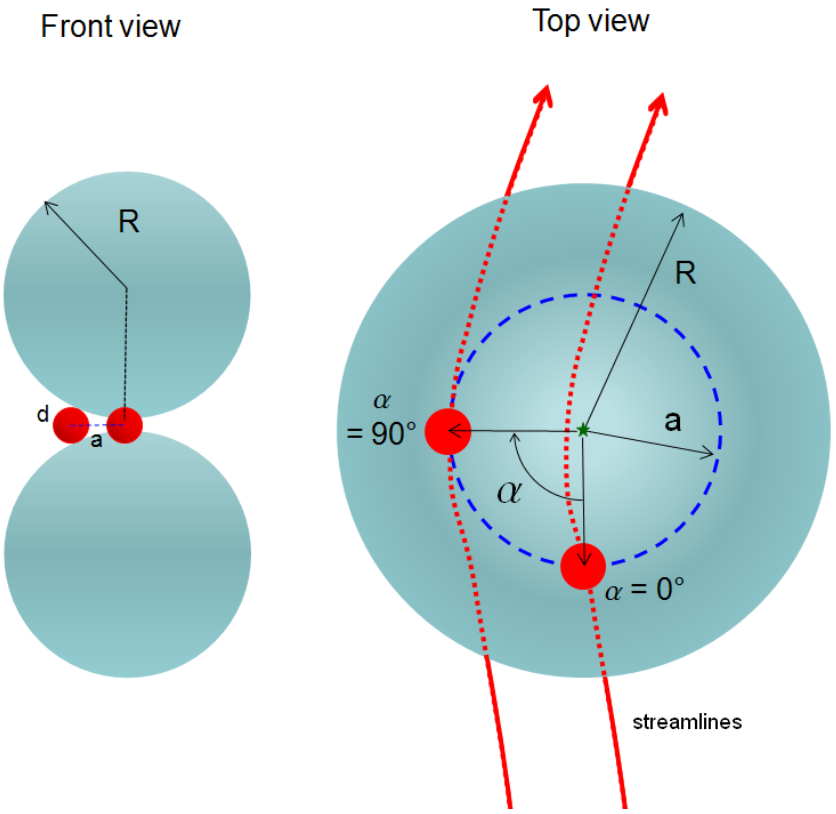

Figure 2.26: Illustration of the angle of incidence in the collision between particles of diameter d (in red) and grains of radius R (in blue), where a is the range of capture for the given particle-grain pair and α is the angle of incidence. In the front view the flow is perpendicular to the plane of the paper. The particle at $\alpha = 90°$ is being trapped at the far lateral edge of the range of capture. (Figure not to scale.)

The second factor is average flow velocity. Consequently we can modify equation (2.27) to account for a dependence of the straining constant with the velocity of the fluid as well as with the angle of incidence.

Now we are going to see how the angle of incidence affects the trapping of a particle by looking at the magnitude of the velocities in the gap. Figure 2.27 shows how the velocity in the gap varies with respect to the distance from the center of the gap, i.e.

along the range of capture. Initially, the original velocity increases rapidly when going away from the center of the gap. However in these outer locations (larger angle of incidence) it is more probable that the particles can rebound and escape by following streamlines of larger velocities, shown as red dots in Figure 2.27. If we multiply the velocity at every node by the cosine of the angle of incidence (in this case the center of the particle in the definition above is replaced by the coordinates of the node in which the velocity was calculated by COMSOL) we see how the weighted values of the velocity along the range of capture (shown as blue dots in Figure 2.27) do not increase as fast as the actual flow velocities with distance from the center of the gap. In fact, at the end of the range of capture some of the velocities become close to zero (because cos(90) = 0). Therefore the multiplication of the velocity by the cosine of the angle of incidence angle accounts for the effect of rebound yielding smaller effective velocities (i.e. the fraction of the flow rate that leads to colloids being trapped) in the outer part of the gap. Therefore we can modify equation (2.27) to use ($v \cdot cos\ \alpha$) instead of v.

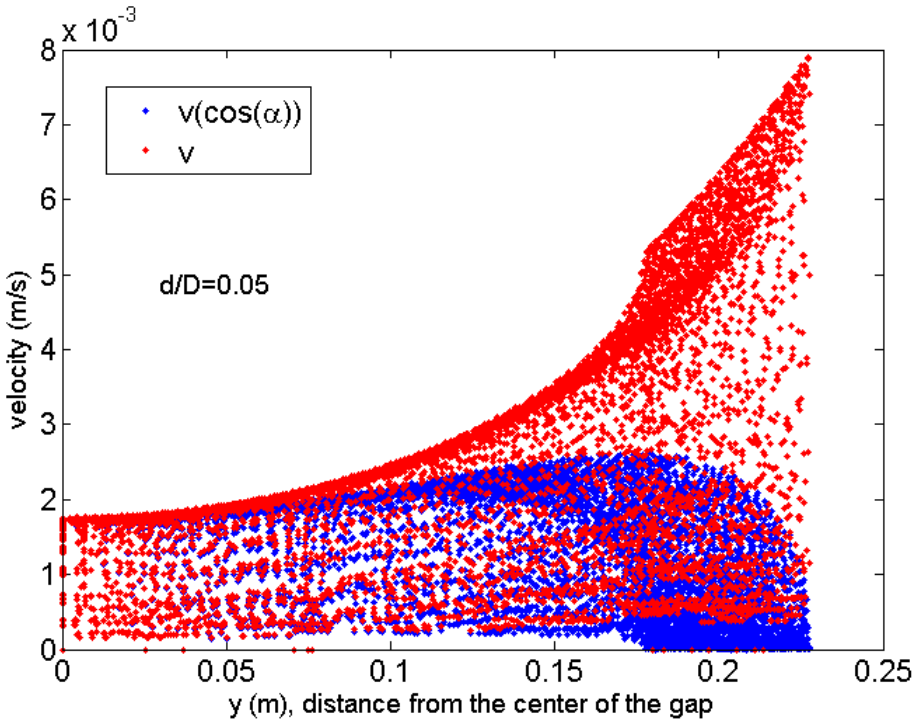

Figure 2.27: Actual velocities in the range of capture (red dots) are multiplied by the cosine of the angle of incidence with respect to the center of the gap to yield weighted velocities (blue dots) which better estimate the probability of trapping colloids at those positions in the gap.

The other effect presumed to affect the straining rate is the momentum of the fluid carrying the particle. We explained before that the higher the velocity of the fluid approaching the gap, the more probable will be for a trapped particle to rebound and escape from the gap. This is especially true for large angles of incidence. To include the dependence of the straining rate constant upon the momentum of the fluid we assume that the straining rate constant is inversely proportional to the velocity of the particle approaching the gap. With these two modifications regarding angle of incidence and momentum, equation (2.27) is modified as follows:

$$\text{flow}_{gap}(d/D) = \iint_{\Delta y} \left(\frac{v \cdot \cos\alpha}{< v_{d/D} >} \right) dz\, dy \qquad (2.28)$$

where α is the angle of incidence and $<v_{d/D}>$ is the average velocity in the annulus (calculated simply as the arithmetic average of all the velocities in the nodes in the annulus) for the given particle size *d/D*. Remember that the size of the annulus is different for different particles sizes, so the average value of the velocity that we use in the denominator of equation (2.28) will be different for each particle size.

Once we applied equation (2.28) for all the possible combinations of gap widths and particle sizes as shown in Table 2.4 we applied equation (2.25) to calculate the integrated straining rate constant for a given particle size in a pack $k_{str}(d/D)_{pack}$.

With the modifications regarding angle of incidence and momentum, the constant for straining rate will be analogous to a weighted area for straining. Figure 2.28 shows the plot of the dimensionless constant for straining rate $k_{str}(d/D)_{pack}$ versus particles size *d/D* also normalized with respect to the value for *d/D* = 0.05. The fitting of the data to a power law trendline yield the following relationship:

$$k_{str} = 106\left(\frac{d}{D}\right)^{1.57} \qquad (2.29)$$

where we can see that the scaling exponent of 1.57 is very close to the one reported experimentally by Bradford *et al*. (2003).

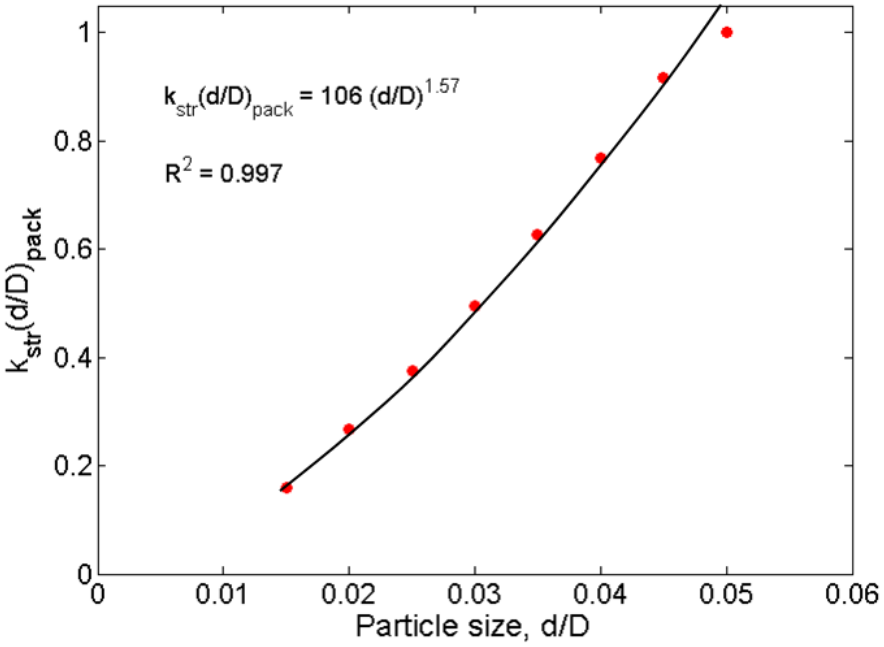

Figure 2.28: Constant for straining rate *vs*. particle size from detailed calculation of the flow field in the vicinity of a gap, assuming dependence of straining with the angle of incidence of the particle.

We have found a method that provides a scaling exponent for the constant of straining rate k_{str} with respect to the ratio of particle to grain size (d/D) in agreement with the exponent reported in the literature. In the next section we will estimate the pre-factor for the straining rate constant.

2.6.6. Calculation of the Prefactor for the Straining Rate Constant

Now that the scaling exponent between the constant for straining rate and the ratio of particle to grain size matches the experiments we will estimate the pre-factor for the straining rate constant in order to compare with the one reported in the literature (cf. equation (2.7), Bradford *et al.*, 2003). We used the Sharma and Yortsos approach, which yield the following expression for the straining rate:

$$\text{Rate of Straining} = \frac{v}{\phi l_p} k_{str} C \tag{2.30}$$

where v is the flow velocity through the constriction, ϕ is the porosity and l_p is the average length of the pore throats (see Appendix C for the derivation of this expression). Therefore:

$$\text{Prefactor} = \frac{v}{\phi\, l_p} \tag{2.31}$$

Notice that the pre-factor has units of reciprocal time. Substituting our expression for the straining rate constant in equation (2.30) we get:

$$\text{rate of straining} = \left[\frac{v}{\phi l_p} \left(\frac{d}{D} \right)^{1.57} \right] C \tag{2.32}$$

Recalling the analogy between Delaunay cells (tetrahedra) and pore bodies and pore throats (cf. Figure 2.3) we can approximate the length of a pore body as the diameter of the insphere in a tetrahedron of edge length D. This will be a lower bound for the length of the pore throat in a pack of identical spheres, since it is equivalent to having the four spheres in the tetrahedron in point contact. From simple geometric considerations we find that:

$$l_p = 2D\sqrt{1/24} \tag{2.33}$$

We calculated this pre-factor for the different type of soils used in Bradford *et al*. (2003), assuming their values for flow rate v, porosity ϕ, and estimated pore length, l_p.

Table 2.5: Estimation of straining rate constant pre-factor for different soils (experimental data from Bradford *et al.* (2003)).

Experimental data					**eq.2.31**
soil type	**d_{50} (mm)**	**l_p(cm) (eq. 2.33)**	**ϕ**	**v (cm/min)**	**Pre-factor, gap v/(ϕ*l_p) (min^{-1})**
2030	0.71	0.05822	0.369	0.1	0.0093
3550	0.36	0.02952	0.342	0.1	0.0198
MIX	0.24	0.01968	0.335	0.11	0.0334
70110	0.15	0.0123	0.348	0.11	0.0514

The typical velocity in pore throats is ~ 0.1 cm/min). Rodriguez (2006) showed that the rate of encountering a gap is smaller than the rate of encountering a throat, since the density of gaps in dense disorder pack of spheres is 0.15 per R^3 versus 0.3 per R^3 for pore throats. Moreover, velocity in the gaps could be as low as three orders of magnitude smaller than the velocity in the surrounding pore throats, Figure 2.29. This leads to prefactors of the order of 10^{-3} to 10^{-2} in Table 2.5.

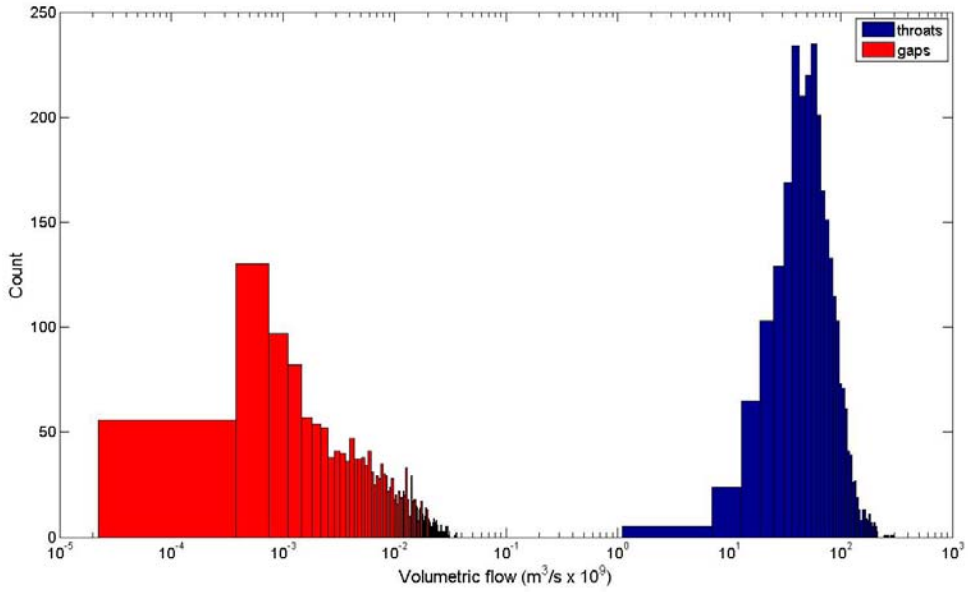

Figure 2.29: Histogram of flow velocities in flows and gaps in a computer generated dense disordered pack of spheres of the same size (radius = 2.19×10^{-4} m)

We also need to calculate the pre-factor for the Bradford *et al*. (2003) results, since the pre-factor reported in equation (2.7) is also a fitting factor, but not the pre-factor for the straining rate term in the convection-diffusion equation. We saw earlier, in section 2.1 the definition of Bradford *et al*. (2003) for the straining term in the convection-diffusion equation, which we repeat here:

$$E_{S_w}^{str} = \theta_w \psi_{str} k_{str} C \tag{2.34}$$

where k_{str} follows equation (2.7), θ_w is the water content of the packing , which equals the porosity for single phase flow, and ψ_{str} is a factor that depends on the depth of the packing. Straining in Bradford's experiments is a strong function of distance being the

more retention for straining found at the column inlet and then decreasing with increasing distance.

The value of ψ_{str} has been taken at the end of the column, since the asymptotic behavior of ψ_{str} in the column will give the appropriate value to use in the field. Also we use small values of ψ_{str} since Sharma and Yortsos (1987c) consider one particle at a time, which is equivalent to a lower bound (diluted solution).

The pre-factor that we calculate with this method will be a lower bound value that applies for the outlet, where straining occurs in smaller amount according to Bradford's observations. The results are shown in Table 2.6.

Table 2.6: Calculation of straining rate constant pre-factor for Bradford *et al.* (2003) experiments.

Soil type	θ_{cw} ($\cong \phi$)	ψ_{str}	**Pre-factor (min^{-1})**
2030	0.369	0.106	0.0391
3550	0.342	0.079	0.0270
MIX	0.335	0.067	0.0224
70110	0.348	0.055	0.0191

These prefactors differ from our estimation in Table 2.5 by a factor that ranges between 2.7 and 4.2. What is interesting to notice is that our prefactor increases when the average grain size decreases whereas the pre-factor estimated for the experiments of Bradford *et al.* (2003) decreases with grain size. We can attribute the discrepancy to the depth dependent factor that decreases with grain size, indicating that less straining would occur in sediments with larger grain sizes. Larger grain sizes are associated to larger pore

sizes, therefore the straining of a given size particle would be smaller. We will have to extend the study to a larger range of soils types to validate this observation.

2.7. CONCLUSIONS

While straining is an important mechanism for the retention of fines at constrictions within a porous medium, classical theories of straining in pore throats cannot account for independently reported observations of anomalous retention: particles smaller than the smallest pore throats were trapped within the medium.

We extend the notion of constrictions to include gaps between pairs of grains, as well as the throats between triplets of grains after analysis of model sediments proved that the occurrence of gaps of the appropriate size range is adequate to account for the observations of anomalous straining.

We extend the existent straining theory of Sharma and Yortsos to include gaps in model granular materials in which the steady-state single-phase flow field can be computed at the pore scale. This theory assumes that the probability of particle retention in a constriction is proportional to the flow rate through that constriction and enables the prediction of the relationship between the constant for straining rate and size of the trapped particle. Our results showed that this theory greatly overestimates the scaling exponent observed in experiments.

We argue that this discrepancy is due to a crucial difference between gaps and pore throats, namely the possibility of particle rebound from a collision with a pair of grains defining the gap, which could avoid the particle from being retained even if it enters a constriction small enough to retain it. We accounted for this phenomena by taking the probability of retention to be proportional to flow rate through the gap and

inversely proportional to the flow velocity or the square of flow velocity in the gap, suggesting that the probability of particle rebound and escape increases with the momentum of the fluid or with the kinetic energy of the fluid, respectively. The scaling exponents between the straining rate constant and the particle size were closer to the experimental observations that the result from the standard "flow rate weighted" theory.

After this analysis we conclude that applying the extended theory to another important class of constrictions, the void space near point contacts between grains will be a good validation for these observations. A more rigorous treatment of particle/fluid dynamics and particle/grain collision is also needed for this purpose.

Therefore we used a finite element based software that allowed the calculation of a detailed flow field in the vicinity of the gap. We defined the straining rate constant as the ratio between the flow in the region of the gap that could trap the given particle and the flow in a larger domain that includes the throat containing the gap. We calculated the constant for straining rate for different combinations of particle size and gap size and then calculating a global constant for straining rate in a pack of spheres using the frequency of the gaps in the size range of interest in the pack.

In the development of this model, we confirmed our previous observation that the straining exponent reported in the literature is overestimated when the straining rate is assumed to be fully dependent on flow rate through the constriction that will trap the colloid. More importantly, we identified the mechanism behind the anomalous straining of colloidal size particles. Straining depends not only on the flow rate through the constriction but also on the angle of incidence of the particle when approaches the gap, and the momentum of the approaching fluid, which accounts for the possibility of rebound and escape of particles that otherwise could be strained.

Chapter 3: Contact Line Extraction and Length Measurements in Model Sediments and Sedimentary Rocks

3.1. INTRODUCTION

In this chapter, we focus on the quantification of the air-water-solid (in general, the non wetting-wetting-solid) contact line in simple geometries and granular materials. Later in Chapter 5 we will relate the contact line measurement with the amount of interfacial area between wetting and non-wetting phases. The comparison will allow us to make a prediction about where the colloidal size particles are trapped when compared with experimental visualizations.

We used a novel computational, level set method based, progressive quasi-static algorithm (LSMPQS) to reveal the configuration of the air-water-solid (AWS) contact lines. LSMPQS tracks the pore scale motion of interfaces assuming capillary forces are dominant. It has been implemented to compute the location of an interface between two immiscible fluids confined by arbitrary solid surfaces. Thus the method implicitly determines the location of contact lines as the intersection of any pair of interfaces (e.g., the intersection of the wetting-non-wetting interface with the wetting-solid interface) as a function of applied capillary pressure. The volume fraction occupied by water, the total interfacial areas, and the contact line length are recorded for each configuration.

While energy, mass and momentum conservation equations for the "common lines" have been developed (Gray and Hassanizadeh, 1998; Gray, 1999) and the importance of contact lines in the modeling of multiphase flow in porous media has been explored, (Held and Celia, 2001; Gray *et al*., 2002) to our knowledge, this is the first comprehensive work on quantifying contact line lengths in disordered porous media.

McClure *et al*. (2007) report the ability to measure contact lines but their focus is primarily on interface areas and curvatures.

The contact lines have been identified and computed in model sediments (random packs of spheres). We validate these computations using fluid configurations extracted from high resolution images of glass beads packs and consolidated rock formations (Fontainebleau sandstone and sucrosic dolomite.) The latter enable a comparison of the magnitudes of the interfacial areas and contact line lengths in sedimentary rocks with those in model sediments.

The effect of spatial configuration and grain size on the contact length has been studied briefly and it is shown in Appendix H.

3.2. METHODOLOGY

3.2.1. Level Set Method

Measuring the contact line length requires detailed knowledge of wetting and non-wetting interface positions in the granular medium under investigation. We use both LSMPQS simulation and microtomography images as a source of such knowledge. LSMPQS method (Prodanović and Bryant, 2006) determines the geometry of capillary controlled fluid configurations and thus readily provides pore scale interfacial areas (wetting/non-wetting, wetting/solid, non-wetting/solid). The fluid interfaces are confined by solid surfaces which correspond to the grains in the porous medium. The contact lines exist at the intersection of these interfaces with grain surfaces. Figure 3.1a shows non-wetting phase (air) displacing wetting phase (water) between two solid grains. The point contacts at the intersection between fluid-fluid interface and solid in the 2D schematic will become contact lines in 3D.

The level set method is a numerical method for propagating interfaces (Osher and Sethian, 1988). The fluid locations are defined by an arbitrary function φ (x,y,z) whose value is zero at the interface between the two fluids, less than zero for the non-wetting phase and larger than zero for the wetting phase. This interface is allowed to move normal to itself with a velocity *F*. Its motion is governed by the following equation:

$$\varphi_t - F|\nabla\varphi| = 0 \tag{3.1}$$

Therefore the physics of the problem are defined by the velocity *F*. In our porous medium application, the driving force for the displacement of one fluid by another is the capillary pressure. This force is counteracted by the interfacial tension at the fluid/fluid interface. Thus *F* is defined as:

$$F = P_c - \sigma\kappa \tag{3.2}$$

where P_c is the capillary pressure, σ is the interfacial tension between fluids and κ is the mean curvature of the interface. The steady-state solution (i.e. the limit at large time) of solving equation (3.1) for different curvatures κ determines the location of the interface.

Another level set function ψ is defined for the solid. This function is stationary, since the solid phase does not move, and it is equal to zero on the interface between solid and pore space and negative in the pore space. The region where the level set functions φ and ψ are both equal to zero correspond to the interface between solid and non-wetting phases; cf. Figure 3.1b. Similarly, the locus of points where φ is positive and ψ is zero corresponds to the interface between solid and wetting phases. The locus of points where φ is zero and ψ is negative corresponds to the interface between non-wetting and wetting

phases. To identify triple contact points more conveniently, we define an auxiliary level set function for the wetting phase φ_w, that will be less than zero where φ is positive and ψ is negative (see Figure 3.1b) and larger than zero elsewhere but at the interface. As a result the triple contact points will be the locations where all three level set functions are equal to zero.

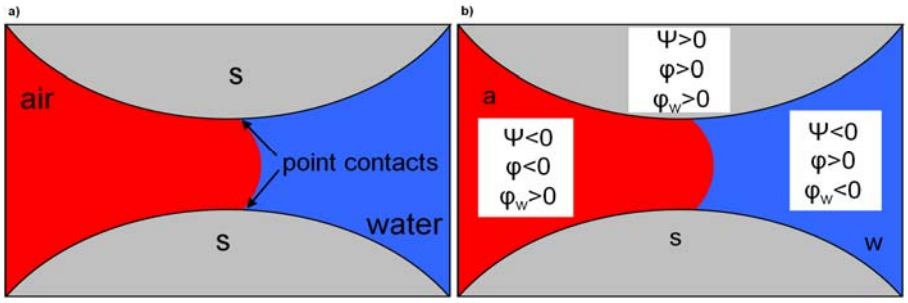

Figure 3.1: a) Displacement of wetting phase (water) by non-wetting (air) in a simple pore throat (s=solid). b) Level set function for the non-wetting fluid (φ), wetting fluid (φ_w) and solid (ψ) phases.

Figure 3.2 shows the result of applying LSMPQS to simulate drainage in a computer generated pack of spheres. The pack is initially assumed to be 100% filled with wetting phase; the final state shown in Figure 3.2b corresponds to a drainage endpoint. The wetting phase (green) is held at contacts between spheres. The red surfaces indicate grains in contact with the non-wetting phase in drained pores.

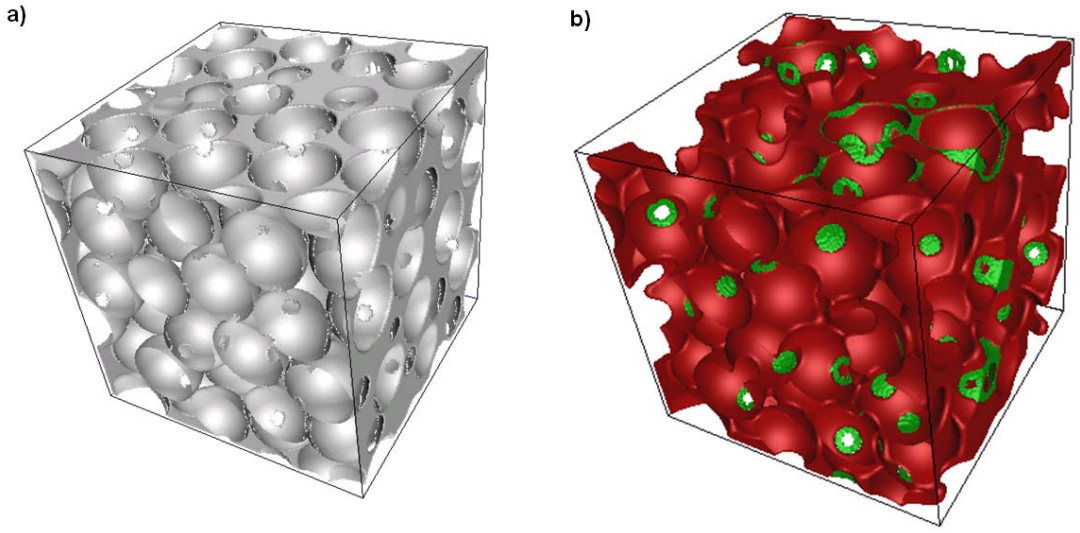

Figure 3.2: a) Computer generated pack of randomly arranged, densely packed spheres of the same size. b) Location of the non-wetting phase at a wetting phase saturation of 7%, red represents the non-wetting phase, and green represents the wetting phase.

3.2.2. Contact Line Length Identification

The procedure to find the point contacts involves the calculation of Heaviside and Dirac delta functions. The Heaviside function *H*, also called unit step function, is a discontinuous function whose value is equal to zero for negative arguments and equal to one for positive arguments. The Heaviside function of the level set function $\varphi(x)$ will be:

$$H\left(\varphi(x)\right)=\begin{cases}0 & \varphi(x)<0\\ 1 & \varphi(x)>0\end{cases} \tag{3.3}$$

To avoid the discontinuity at $\varphi(x=0)$ in the numerical calculations we used the "smoothed" version of equation (3.3), selecting a tolerance ε whose value is of the order of the width of the numerical cell, such that:

$$H\left(\varphi\left(x\right)\right)=\begin{cases}0 & \varphi\left(x\right)<-\varepsilon \\ \frac{1}{2}+\frac{\varphi\left(x\right)}{2\varepsilon}+\frac{1}{2\pi}sin\left(\frac{\pi\varphi\left(x\right)}{\varepsilon}\right) & -\varepsilon<\varphi\left(x\right)<\varepsilon \\ 1 & \varphi\left(x\right)>\varepsilon\end{cases} \tag{3.4}$$

The Dirac delta function is defined as the derivative of the Heaviside function, therefore:

$$\delta\left(\varphi\left(x\right)\right)=H'\left(\varphi\left(x\right)\right)=\begin{cases}0 & \varphi\left(x\right)<-\varepsilon \\ \frac{1}{2\varepsilon}\left(1+cos\left(\frac{\pi\varphi\left(x\right)}{\varepsilon}\right)\right) & -\varepsilon\le\varphi\left(x\right)\le\varepsilon \\ 0 & \varphi\left(x\right)>\varepsilon\end{cases} \tag{3.5}$$

We are interested in finding the locations where our level set function is equal to zero, which now correspond to the interval $-\varepsilon\le\varphi(x)\le\varepsilon$. Therefore, examining equations (3.3) to (3.5), the contact line will exist in the voxels where the three Dirac delta functions (solid, wetting and non-wetting) are positive.

This procedure was written in a C code and added as a new functionality to the LSMPQS software package developed by Dr. Prodanović (Chu and Prodanović, Level Set Method Library (LSMLIB), 2009). Information about the code is shown in Appendix D.

3.2.3. Contact Line Length Measurement

While the contact line position and identification in the porous media is conceptually simple, due to discretization (in simulation) and finite resolution (in imaging), its extraction and precise length measurement are not trivial. We thus first identify rather thick regions of voxels around triple contact lines. Because we smoothed the Heaviside function to avoid a discontinuity in the numerical calculation (see previous section) the Dirac delta function in equation (3.5) identifies as belonging to the contact line the voxels where the value of the level set function $\varphi(x)$ is between the positive and negative values of the specified tolerance ε. This set of voxels is larger than just the voxels where the value of the level set function is equal to zero.

We "thin" these thick regions of voxels using medial axis approach implemented in 3DMA-Rock package (W.B. Lindquist of SUNY Stony Brook). The purpose of the medial axis is to obtain a reduced representation of an object that is easier to analyze. The medial axis of an object can be seen as its skeleton. For this reason, the medial axis of the thick region of voxels should be a very good representation of the contact line, which is a one-dimensional object. The resulting contact line is a collection of digitized links and nodes, and subsequent length measurement is straightforward.

To obtain the skeleton of the digitized object, the object voxels are carefully eroded, layer by layer, while preserving the object topological and geometric properties. A voxel is removed only if its removal does not induce a local change in topology, such as breaking the object in two parts or creating a hole or cavity.

We normalize the computed length in order to be able to compare different systems. We divided the computed contact line length (L_C) by a characteristic length of the system that we choose to be the radius of the grains (R) to obtain a dimensionless contact line length, L_{CD}. Then we divide this magnitude by the total volume of the

domain (or brick volume, V_b), also made dimensionless by dividing its value by the cube of the characteristic length (R^3). Therefore:

$$\text{Normalized specific contact line length} = \frac{L_{CD}}{V_{bD}} \tag{3.6}$$

In this way, we obtain an intrinsic value for the contact line length. This normalized specific contact line length is then independent of, for example, the number or size of spheres in a packing, as we will see later.

3.3. RESULTS

3.3.1. Analytical Test for Contact Line Length Validation

We first simulated drainage in a simple system of two equal size spheres contained in a box as shown in Figure 3.3a, where we can easily determine the contact length analytically and then compare it with the result from simulation. By observation of the last step of drainage, the canonical shape of the contact line has been identified as two circles bounding the pendular ring between the two spheres (Figure 3.3b). Once the pendular ring was completely formed we calculated the length of the contact line as the length of the medial axis obtained with 3DMA-Rock. We compared this length with the analytical result, where pendular ring configuration is assumed to be a toroid (see Appendix E for analytical calculation of the length of the contact line in a pendular ring). Two cases were tested. In one the spheres are in point contact and in the second, the spheres are separated by a gap of width equal to 10% of the radius of the spheres. The curvature used for the calculations does not necessarily reflect the curvature at which most pendular rings are present in sphere packs. The purpose of this exercise is to test the

accuracy of the medial axis for calculating the contact length. Table 3.1 shows the relative error of the calculation for different resolutions (*dx*). The relative error is between 2-10% in all cases. This test gives us confidence that the length calculated by means of medial axis is a fairly accurate measure of the simulated contact line.

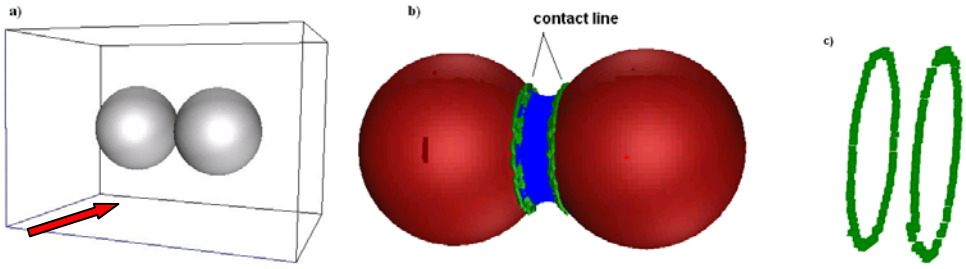

Figure 3.3: a) Two spheres of radius *R* in a box. b) Last step of drainage, where a pendular ring between the two spheres has been formed (red = non-wetting phase in contact with sphere surfaces, blue = wetting phase, green=contact line). c) The two rings that make the medial axis of the contact line.

Table 3.1: Contact line length from analytical test and simulation (via 3DMA*) in two simple cases. The length is measured at a constant curvature for different voxel sizes (*dx*).

Two Spheres in Point Contact Curvature = 1.48 R^{-1}, Analytical Length = 8 R			**Two Spheres with a Gap of 0.1 R Curvature = 2.89 R^{-1}, Analytical Length = 5.63 R**	
dx	**Length, R (3DMA)**	**Relative Error (%)**	**Length, R (3DMA)**	**Relative Error (%)**
0.02	8.36	4.31	5.92	5.15
0.04	8.20	2.50	5.76	2.31
0.05	8.69	8.63	5.12	9.06
0.08	7.56	5.25	5.31	5.68

* The criteria for the 3DMA trimming are as follows: 1) 26 connectivity between voxels is considered (see Appendix F for discussion on connectivity). 2) Isolated voxels, needle eye paths and surface remnants have been removed. 3) Branch leaf paths of less than 20 voxels have been removed to reduce noise effects. See 3DMA documentation for medial axis modification case 4.10 (W.B. Lindquist (1994-2010))

Table 3.1 reports contact line length in units of grain radius for this simple case. In packings of grains, we will report the contact line length per unit bulk volume. This intrinsic value can be used to compare contact line lengths of systems of different sizes.

3.3.2. Contact Line Validation

There are no previous contact line measurements (experimental or numerical) in porous media with which we can compare our results. Analytical solutions are not feasible for disordered packings except at drainage endpoints when all wetting phase is held as pendular rings. For example, a dense disordered packing of equal spheres of radius R has about 6 point contacts per sphere. If the pendular rings are formed at a curvature $C = 1.48\ R^{-1}$, then from Table 3.1, the specific contact line length will be:

$$\text{Specific contact line length} = \frac{8\text{R}}{1\text{ contact}} \times \frac{6\,\text{contacts}}{1\text{ sphere}} \times \frac{1}{2} \times \frac{(1 - \phi)}{\frac{4}{3}\pi\text{R}^3} \tag{3.7}$$

where division by two eliminates double counting the contacts. The normalized value (divide length by R and volume by R^3) is thus 3.7. At $C = 10\ R^{-1}$, the analytical value of the length of the ring is $4.65R$ and therefore we get 2.1. Since this calculation neglects the contribution of menisci, we can expect magnitudes of normalized specific contact line length to be between 1 and 10. This analysis is expanded in section 3.3.5.

Interfacial area measurements are more easily available, however. Since contact lines are the intersection of fluid/fluid interfaces with fluid/solid interfaces, it is reasonable to expect contact line length to correlate with fluid-fluid interfacial area. Thus comparing the simulated interfacial areas with experimental results can provide some confidence in the predicted contact line lengths.

There are two contributions to interfacial area as commonly measured by interfacial tracers. One is the interface of the bulk connected volumes of wetting and non-wetting phases, the other is the film of wetting phase covering the solid surfaces in drained pores. Figure 3.4 shows the sum of these contributions in the LSMPQS simulation of drainage in a pack of random spheres. The experimentally determined interfacial area is subject to variability because of the time limitation for the diffusion of the tracer from the bulk water phase to the interface and hence to the films. This limitation results in smaller interfacial areas. As shown in Figure 3.4, our results for the total wetting-non-wetting interfacial area follow the trend of experimental results obtained from tracer techniques.

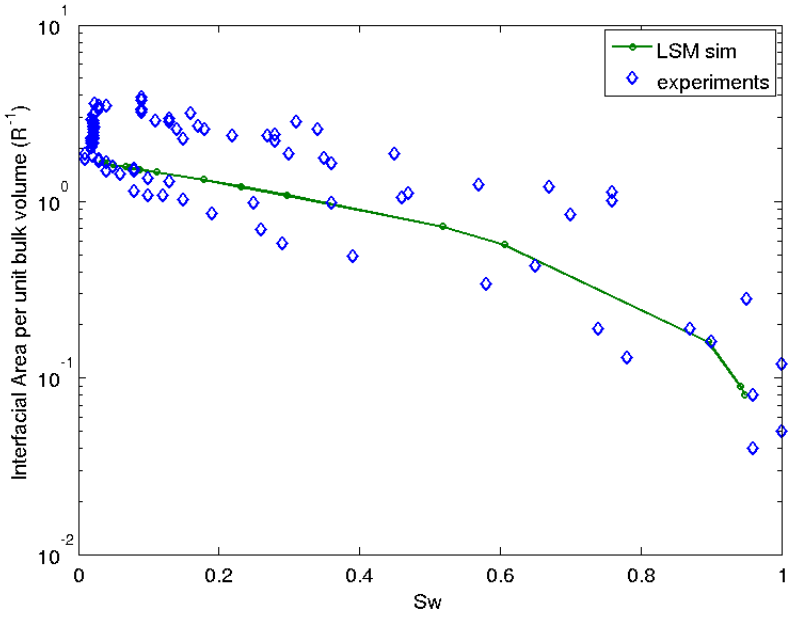

Figure 3.4: Wetting-non-wetting interfacial areas from experimental data and LSMPQS simulation. Experimental measurements extracted from Faisal Anwar *et al.* (2000), Kim *et al.* (1997), Schaefer *et al.* (2000) and Kim *et al.* (1999). Here the simulation accounts for interfaces between bulk wetting and non-wetting phases, and between the surface of grains (presumed to hold wetting phase film) and non-wetting phase in drained pores.

Given the lack of experimental measurements of contact line length, the fact that our simulated interfacial area follows the same trend as the experiments gives us confidence that our estimation of contact line length should be a good approximation.

3.3.3. Results of Contact Line Length in Model Sediments

We simulated drainage and imbibition displacements in two packs of different numbers of randomly arranged, densely packed spheres of the same radius, as the one shown in Figure 3.5a. The spheres are packed into a periodic cubic domain using the cooperative re-arrangement algorithm developed by Thane (2006). The periodicity allows spheres to extend beyond the faces of the cube to avoid boundary artifacts. The curvature

versus saturation plot is shown in Figure 3.5b. In Figure 3.5c we compare normalized specific contact line length during drainage and imbibition. One pack has 91 spheres while the other has 623 spheres, making its volume six times larger, yet the normalized specific length of the contact line does not differ considerably.

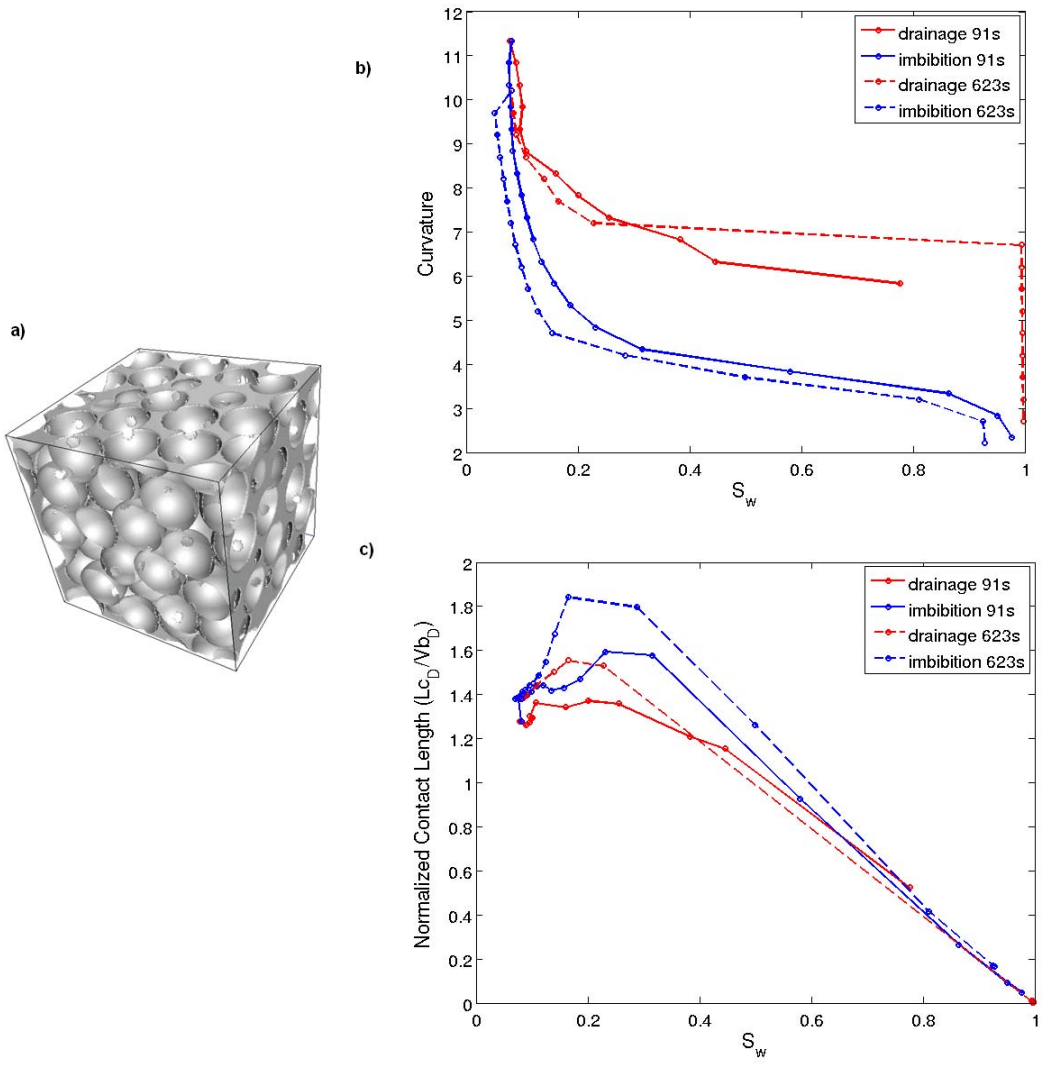

Figure 3.5: a) Periodic cubic pack of randomly distributed spheres of the same size (radius R and voxel size $dx = 0.08R$). b) Curvature *vs*. wetting phase saturation plot for two different cubic packs of same size spheres c) Normalized specific contact line length during drainage and imbibition *vs*. wetting phase saturation for small (91 spheres) and large (623) different packs of same size spheres.

The main parameter affecting the length of the contact line is the resolution or voxel size (dx) used in the simulations. Figure 3.6 shows the normalized contact line

length for the same pack of 91 spheres for two different voxel sizes ($dx = 0.04R$ and $dx = 0.08R$). The length for the smaller dx (better resolution) is considerably larger than for the larger dx, being almost twice as large at the last steps of drainage.

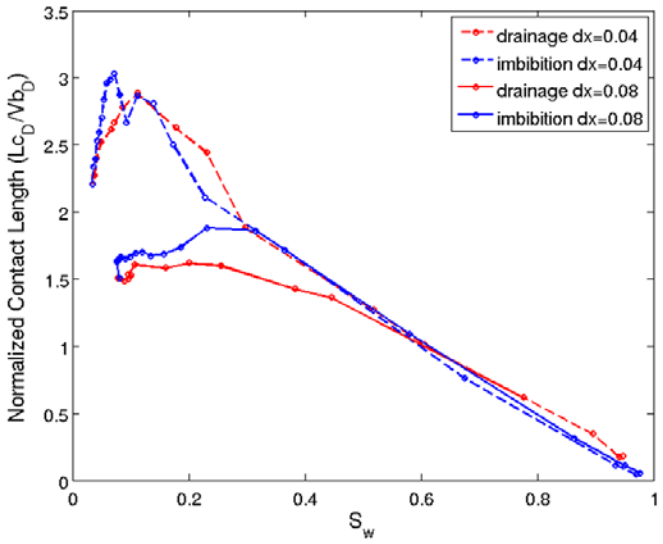

Figure 3.6: Normalized specific contact line length *vs.* wetting phase saturation during drainage and imbibition for the same pack of spheres using two different resolutions (voxel size, dx of 0.04 R and 0.08 R).

This difference can be explained by looking at the representation of contact line for two different resolutions in a single pore throat as shown in Figure 3.7.

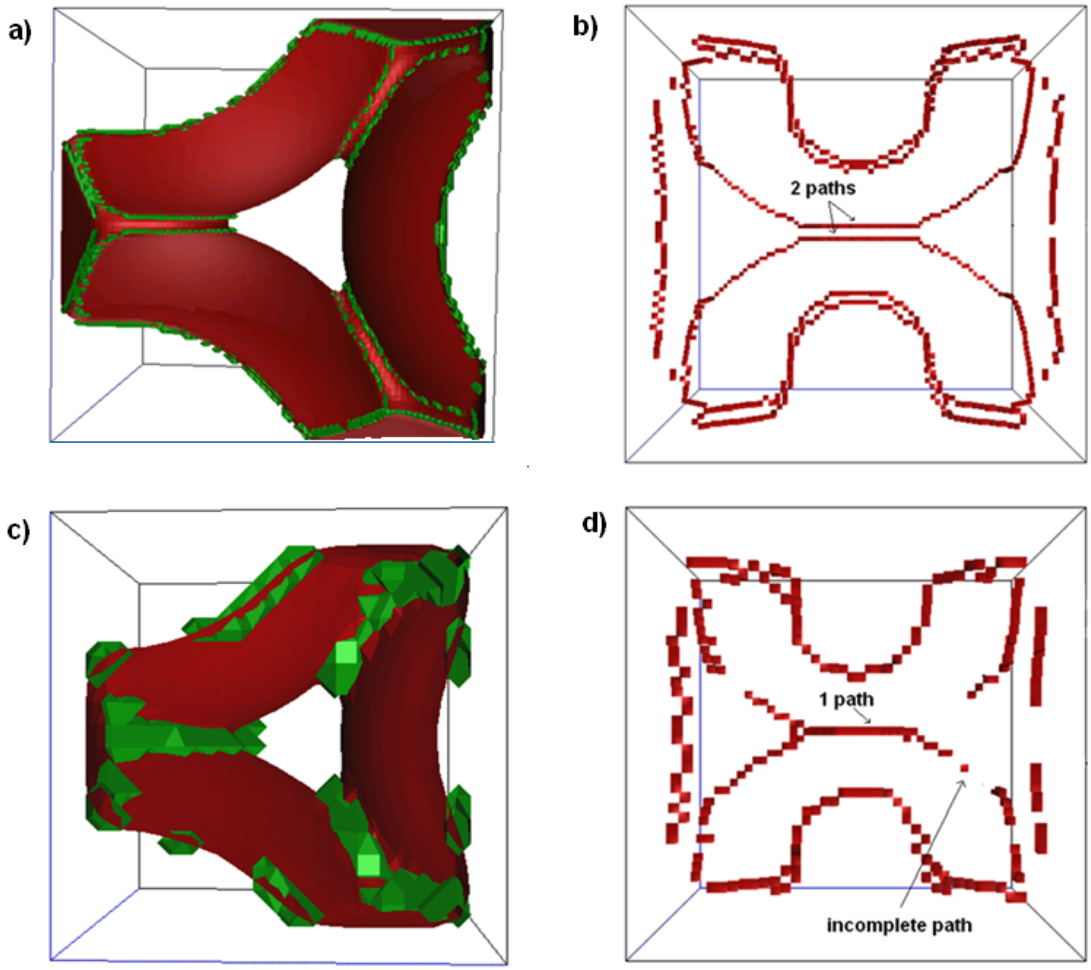

Figure 3.7: Voxel representation of the contact line (green) in a pore throat for two different resolutions (a) $dx = 0.04R$ and (c) $dx = 0.08R$ when dimensionless curvature of the wetting/non-wetting interface = 11. Medial axis representation of the contact line in the same pore throat for (b) $dx = 0.04R$ and (d), $dx = 0.08R$.

Figure 3.7a shows the voxel representation of the contact line for a resolution $dx = 0.04R$ after the pore has been drained and the wetting phase is held as pendular rings between the three grain contacts. Once we calculate the medial axis of the voxel output in Figure 3.7b, we can see two isolated rings of contact line in the center of the picture

corresponding to a single pendular ring. The same ring is at the left of the image in Figure 3.7a. In Figure 3.7c we compute exactly the same state (dimensionless curvature = 11) using a resolution $dx = 0.08R$, and instead of two lines, we see a single thick line of voxels for contact line where the pendular ring is. When we calculate the medial axis in Figure 3.7d we obtain a single contact line. Moreover, we also see incomplete paths of contact line elsewhere on the sphere surfaces at this coarser resolution. Therefore, larger voxel sizes are not able to resolve the contact line associated with pendular rings and lead to an underestimate of the contact length. We computed contact line length accurately previously for a voxel size of $dx = 0.08R$ for the case of a pendular ring between two spheres of radius R (see Table 3.1). The main difference here is the curvature of the wetting-non-wetting interface ($C = 1.5$ in Table 3.1 versus $C = 11$ in Figure 3.7). At larger curvatures, the radius of the ring of contact line decreases, being the ring closer to the location of minimum separation between the two spheres. For coarse resolution we have smaller number of voxels defining the space between the grains and the contact line associated to each sphere can merge into a single line. This effect would be more noticeable as the width of the gap between spheres decreases.

This analysis suggests that the reason why the length is almost twice as large at the last steps of drainage when using larger voxel size (Figure 3.6) is because most of the contact line at these points is associated with pendular rings.

An image of the contact line in the last step of drainage for a pack of 91 spheres for two different resolutions is shown in Figure 3.8. The rings of contact line are easier to distinguish for the finer resolution case on the left.

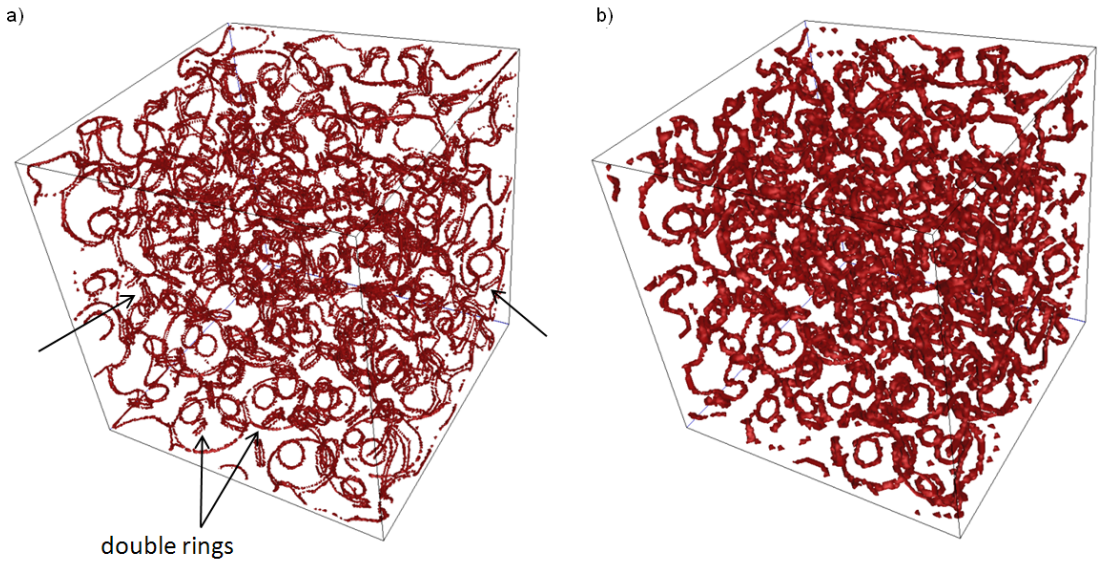

Figure 3.8: Contact line configuration in the last step of drainage in a pack of 91 spheres for two different resolutions (a) $dx = 0.04R$ (b) $dx = 0.08R$.

In Figure 3.6 we observed that the contact line length in these sphere packs increased as saturation decreased until reaching a maximum value at a wetting phase saturation near 20%. Beyond that saturation the contact line length started to decrease until the drainage endpoint. The behavior of the contact line length for imbibition is similar; however in Figure 3.5 and Figure 3.6, the contact line length exhibits some hysteresis from intermediate to small water saturations ($S_w < 0.5$) in the case of coarse resolution ($dx = 0.08R$), being the length for imbibition larger than the length for drainage at a given water saturation. The better resolution simulation suggests no major hysteresis; still the contact line length curves for drainage and imbibition do not completely match.

During imbibition, the decrease in capillary pressure is causing the pendular rings to expand and therefore the length associated to them increases. Recall that the imbibition simulation assumes that all pendular rings are connected via wetting films to the bulk wetting phase and thus can expand in response to a decrease in capillary pressure. If

imbibition starts from a drainage endpoint where most of the wetting phase is present in form of pendular rings (as we saw is the case in these sphere pack cases), the shrinkage of the pendular rings that occurred during the last steps of drainage is reversed in the first steps of imbibition. The fluid/fluid interfaces thus are following reversibly the last steps of drainage and no significant hysteresis in contact line length is expected. A pendular ring will keep expanding with the decrease in curvature until a snapoff event occurs that forms a meniscus. Because imbibition and drainage events of the same pore do not occur at the same curvature we see hysteresis in the curvature-saturation plot, yet we have to see if this translates into hysteresis for the contact line length.

We are going to further investigate hysteresis (of the lack of it) in contact line length by looking at its behavior with curvature (or, equivalently, capillary pressure), rather than saturation. We will keep working with the results from the simulation using the finer resolution ($dx = 0.04R$) since we have shown that the coarser resolution is not representing the contact line length accurately. Figure 3.9 shows the corresponding lines of contact line length versus dimensionless curvature for the same pack of 91 spheres of Figure 3.5a.

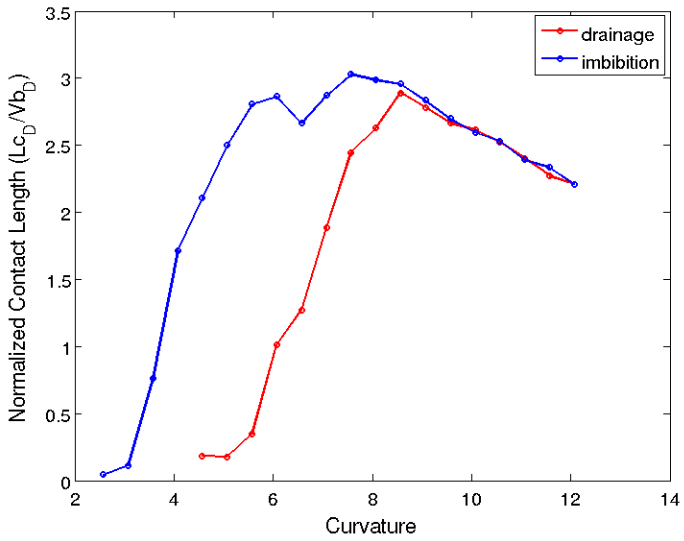

Figure 3.9: Normalized specific contact line length *vs.* dimensionless curvature during drainage and imbibition for a pack of 91 spheres of the same radius R using a resolution $dx = 0.04R$.

Figure 3.9 shows that contact line length does show hysteresis with respect to curvature being the length larger for imbibition for curvatures between 2 and 8. At large curvatures ($8 < C < 12$) corresponding to small wetting phase saturations we do not observe major hysteresis since as we said before the fluid is following the reversible path of the last steps of drainage, and the pendular rings are expanding but not coalescing. Then we reach certain curvature ($C \sim 8$) where contact line length starts to differ. This curvature indicates the point where the fluid stops following the reversible path since irreversible events (drainage of pores) may have happened during drainage or are taking place now during imbibition (snapoff in throats, meniscus merger in pores).

Since interfacial areas and contact lines are closely related we are going to examine the behavior of the interfacial area between wetting and non-wetting phases drainage and imbibition in the same sphere packs to gain some insight in contact line behavior. The curves of interfacial area versus wetting phase saturation in Figure 3.10

show that interfacial area also exhibit hysteresis during imbibition, being larger than the area during drainage at a given wetting phase saturation.

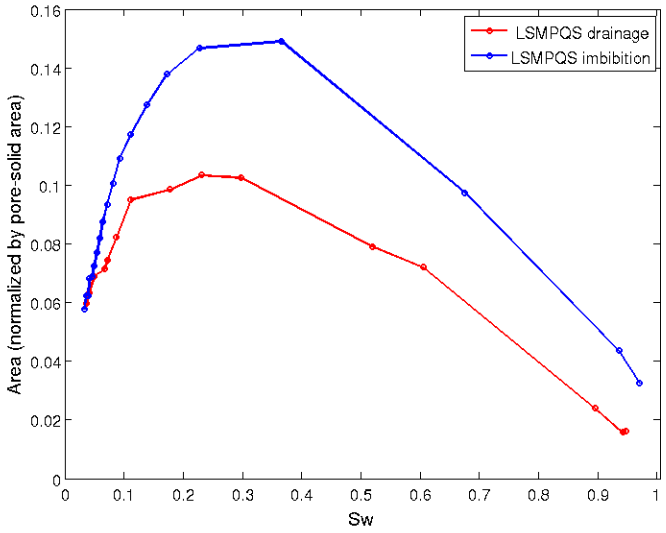

Figure 3.10: Wetting-non-wetting interfacial area *vs.* water saturation for a computer generated pack of 91 spheres of radius R using a resolution $dx = 0.04R$

It could also be instructive to plot interfacial area versus contact line length. The results are shown in Figure 3.11 where we see regions where the increase in contact line length is associated to an increase in interfacial area as well as regions where the increase in contact line length is associated to a decrease in interfacial area. Notice that here we have also calculated a normalized specific interfacial (A_D/V_{bD}) as:

$$\text{Normalized specific area} = \frac{\dfrac{\text{A}_{\text{w-nw}}}{\text{Grain Surface}}}{\dfrac{\text{Bulk Volume}}{(\text{Grain Radius})^3}} \tag{3.8}$$

where grain surface is equal to $4\pi R^2$.

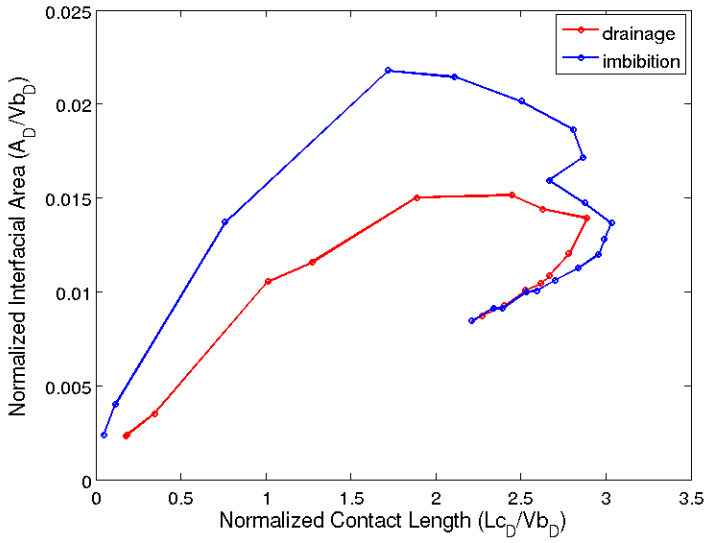

Figure 3.11: Normalized specific wetting-non-wetting interfacial area *vs*. normalized specific contact line length for a computer generated pack of 91 spheres of radius R using a resolution $dx = 0.04R$.

Observation of the behavior of contact line length and interfacial areas in large packs of spheres is not conclusive on what is the cause behind the shape of the contact line length curve during drainage and imbibition. In the next section we will take a closer look at how interfacial area between wetting and non-wetting phases and contact line length behave in a simple pore, in order to find an explanation to the shape of contact line length curve.

3.3.4. Analysis of Interfacial Area and Contact Line Length in a Single Pore

We can understand why the wetting-non-wetting interfacial area shows hysteresis (with respect to saturation) during simulations of drainage and imbibition in computer generated packs of spheres by analyzing the behavior of the wetting-non-wetting interface during drainage and imbibition in a simple pore.

In Figure 3.12a we see all drainage steps in a simple 2D pore. Between the first position of the interface (step 1) and the rest of the drainage steps there is an irreversible jump (Haines jump, Haines (1930)). The jump causes the initial single meniscus to split into two different ones (one in each adjacent throat). After that jump, the next 19 drainage steps are small and reversible. If drainage continues from step 20, then the throat in the upper right corner drains in another irreversible interface jump. If on the other hand the drainage simulation is halted at step 20 and imbibition is simulated from that step, Figure 3.12b, interfaces will reversibly trace the path followed during drainage for several steps. When the interface returns to position corresponding to the second drainage step, however, the next imbibition step does not reverse the Haines jump to the pore throat on the left side of the domain. Instead the interfaces continue advancing into the pore body until two menisci merge at the tip of the right hand side solid disk. This causes an instability (Melrose type of the imbibition event (Melrose, 1965)) and the interface will irreversibly jump to a new location (in this case, outside the pore/geometry shown - the pore imbibes). If we plot areas for these processes (as shown in Figure 3.12d and Figure 3.12e), we see the higher areas during imbibition beyond the Haines jump point. For imbibitions from step 21 the difference in areas is even more prominent because of two Haines jumps during drainage.

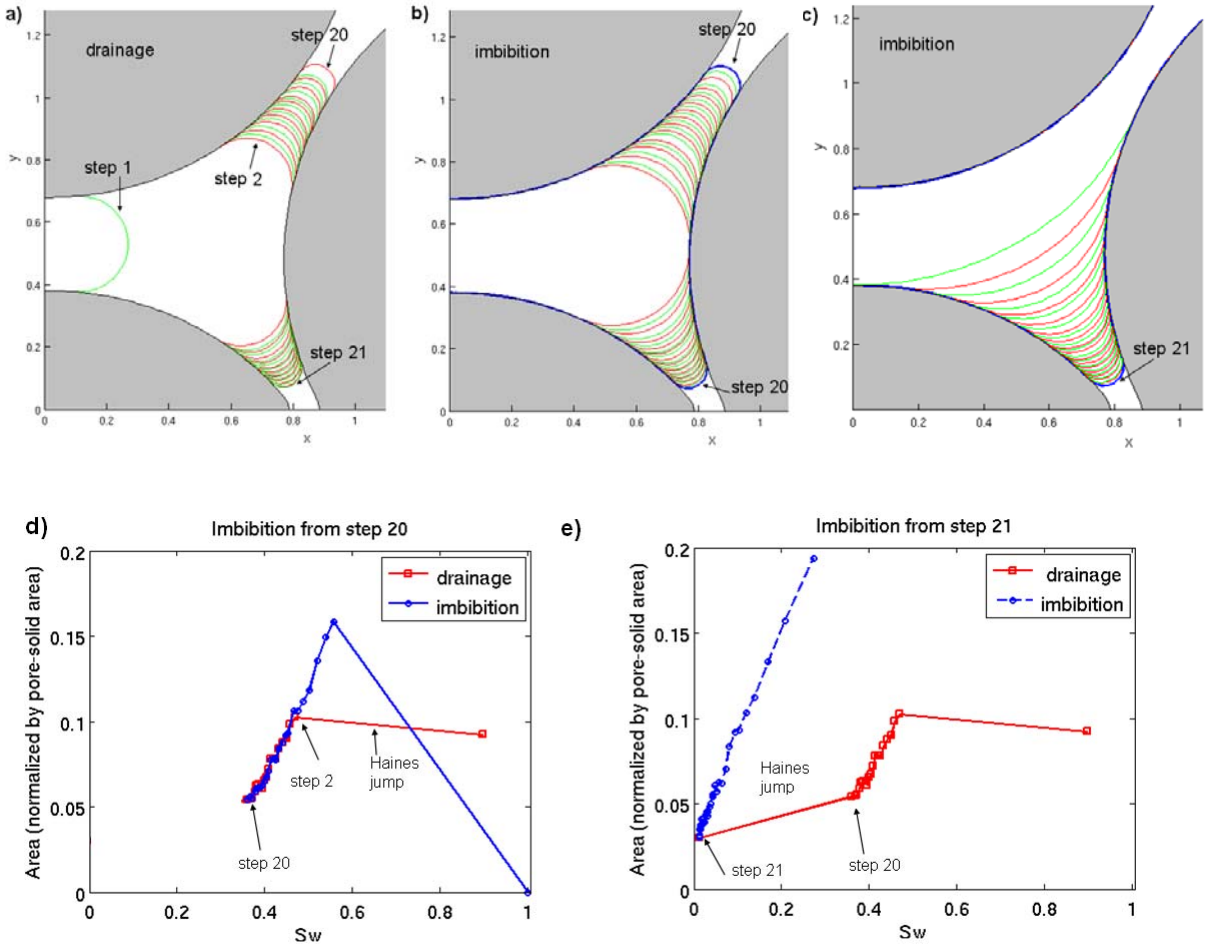

Figure 3.12: Drainage and imbibition steps in a 2D pore (in alternating red and green color). Locations of interfaces are shown for a) all the drainage steps; b) imbibition from step 20, with the starting location shown in blue; and c) imbibition from step 21. The corresponding trends of interfacial area *vs*. water saturation are shown for d) imbibition from step 20. e)-Imbibition starting from step 21.

We repeated the same exercise in a 3D pore body included between 4 spheres having 4 pore throats, shown in Figure 3.13. We did four drainage simulations with this pore, starting drainage through each of the four pore throats. Figure 3.14 shows the

interfacial area versus water saturation for drainage and imbibition through the pore throat indicated with an arrow in Figure 3.13. The drainage finished after 17 steps in this case and two Haines jumps occurred, between steps 9 and 10 and between steps 14 and 15. Imbibition was started from step 17. Interfacial areas for drainage and imbibition coincide until the point corresponding to the Haines jump at step 15 (the interfacial areas for imbibition follow the line of steps 17, 16 and 15 of drainage), as happened for the 2D case.

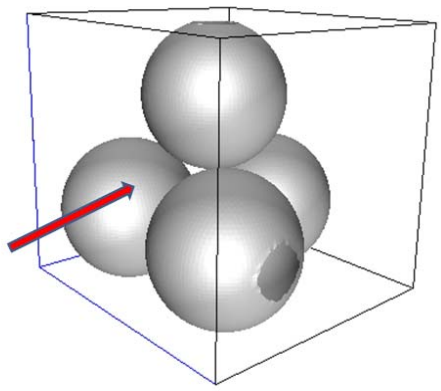

Figure 3.13: Geometry of a pore body between four spheres used to simulate drainage and imbibition. Simulations have been conducted starting drainage from all four possible pore throats.

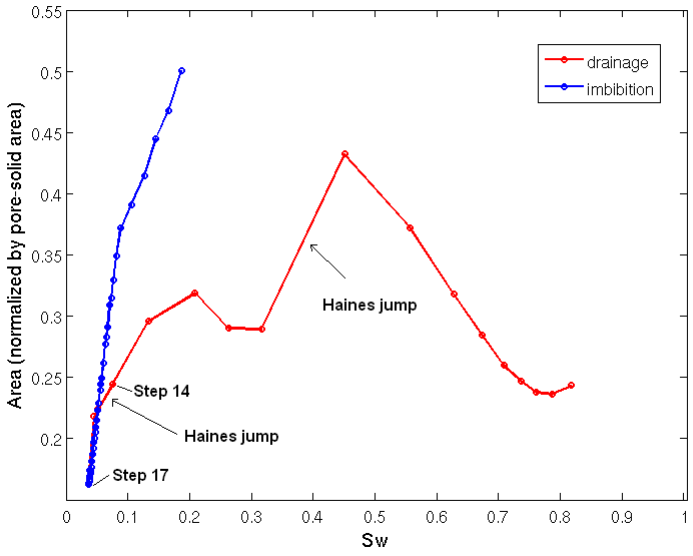

Figure 3.14: Interfacial area *vs.* water saturation for drainage and imbibition in a pore body between four identical spheres.

A multiplicity of such jumps integrated over multiple pores in a porous medium is what causes hysteresis of capillary-pressure-saturation curves in general porous media (Morrow, 1970) and as we saw in Figure 3.10 inverse hysteresis in area-saturation curves as well.

To study the behavior of the contact line length, we simulated drainage and imbibition in a simple 3D pore between three spheres in point contact, like the one shown earlier in Figure 3.7. The capillary pressure curve is shown in Figure 3.15.

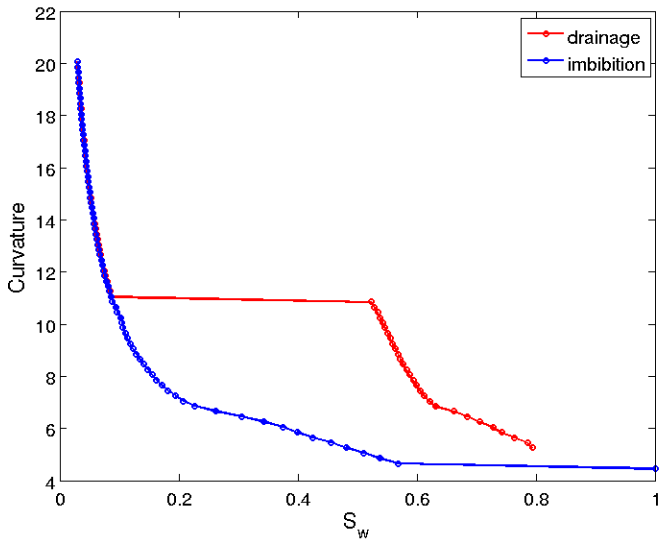

Figure 3.15: Curvature *vs.* wetting phase saturation for drainage and imbibition in a pore between three spheres of radius R in point contact ($dx = 0.04R$).

An irreversible Haines jump occurs at a curvature of 11, where the wetting phase saturation S_w is reduced from 0.53 to 0.09. From S_w= 0.09 the increase in curvature reduces the wetting phase saturation slowly in a reversible manner. Imbibition is started from the drainage endpoint and the initial decrease in curvature makes the wetting fluid to follow the reversible path of drainage until reaching the wetting phase saturation of 0.09. At this point, the next imbibition step does not reverse the Haines jump and the interface. The interface keeps advancing through the pore throat until reaching a wetting phase saturation equal to 0.57, after which point the pore is completely imbibed. The curves of normalized specific contact line length versus water saturation and curvature are shown in Figure 3.16 and Figure 3.17 respectively. Figure 3.18 shows the interfacial area-saturation curve.

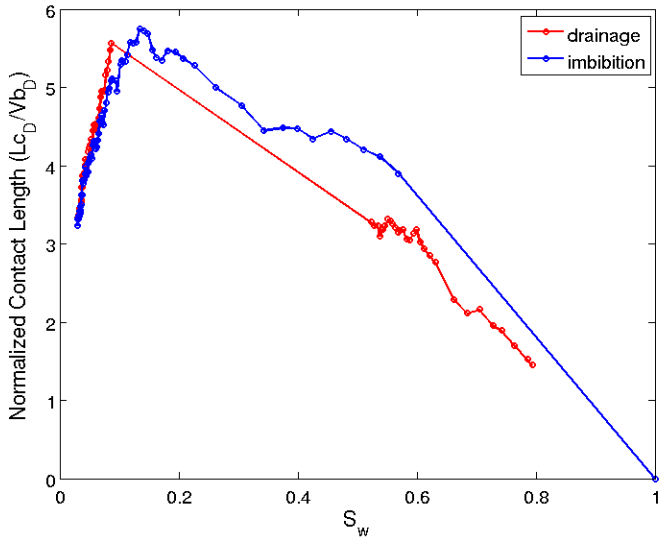

Figure 3.16: Normalized specific contact line length *vs.* wetting phase saturation for drainage and imbibition in a pore between three spheres of radius R in point contact ($dx = 0.04R$).

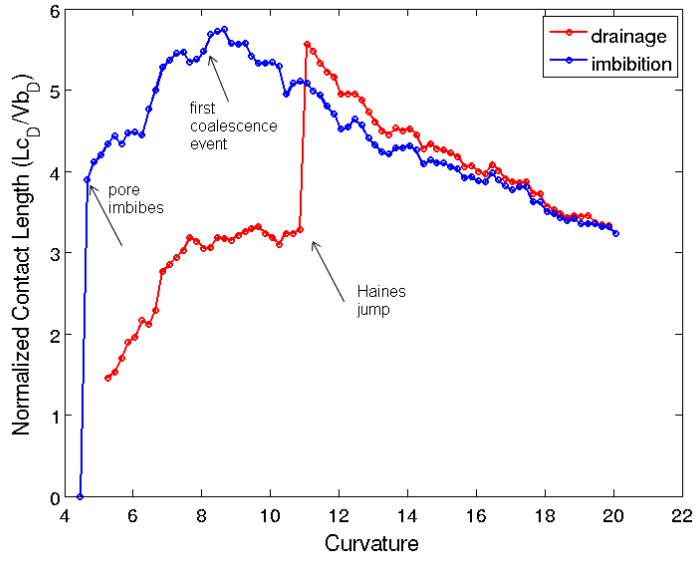

Figure 3.17: Normalized specific contact line length *vs*. curvature for drainage and imbibition in a pore between three spheres of radius R in point contact ($dx = 0.04R$).

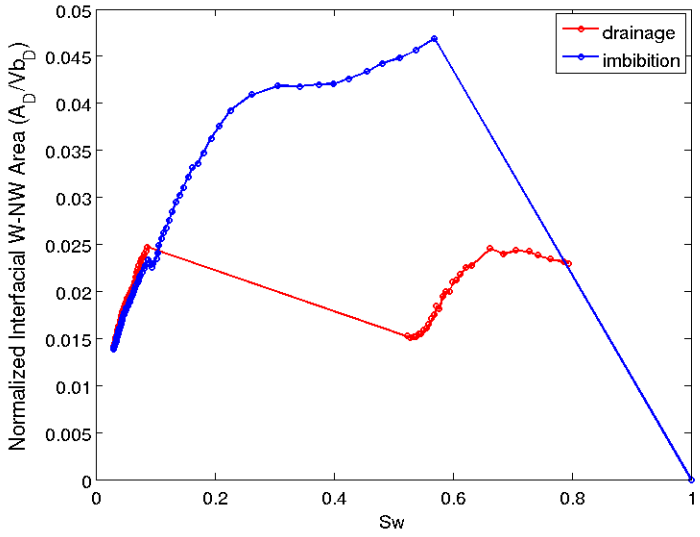

Figure 3.18: Normalized specific wetting-non-wetting interfacial area *vs*. curvature for drainage and imbibition in a pore between three spheres of radius R in point contact ($dx = 0.04R$).

The contact line length-saturation curve in Figure 3.16 exhibits some hysteresis after wetting phase saturation equal to 0.09, where the Haines jump occurred during drainage. However the hysteresis is more noticeable in the contact line length-curvature and interfacial area-saturation plots.

In the contact line length–curvature plot (Figure 3.17), contact line lengths for drainage and imbibition start to differ at a curvature of 11, where the Haines jump occurs in drainage. At the next curvature during imbibition, the pore does not imbibe, and it still supports the advance of the non-wetting phase, generating contact line. The first coalescence event during imbibition does not occur until a curvature equal to 8.25, and the pore eventually imbibes at a curvature of 4.65.

In the contact line length–saturation plot (Figure 3.16), at smaller saturations at the beginning of imbibition the fluid is following the reversible path of the last steps of

drainage. During imbibition, the pore is not suddenly imbibed at a wetting phase saturation of 0.09, rather the interface continues advancing until reaching a saturation of 0.57 where the pore imbibes. Therefore from saturation 0.09 to 0.57 in imbibition the advancing meniscus is generating interfacial area that was "skipped" during drainage because of the Haines jump. This causes the hysteresis in interfacial area shown in Figure 3.18.

We can look at the interface and contact line configurations at a wetting phase saturation of 0.57. For drainage, that is the point where the non-wetting fluid is about to drain the pore. For imbibition, at that point the non-wetting fluid has been steadily moving through the pore body since the beginning. The configuration of the interfacial phase is shown in Figure 3.19 where we see how different the status of drainage and imbibition is at the same water saturation. The normalized specific interfacial area ($A_{w\text{-}nw}/V_B$) is equal to 0.017 for drainage and 0.047 for imbibition.

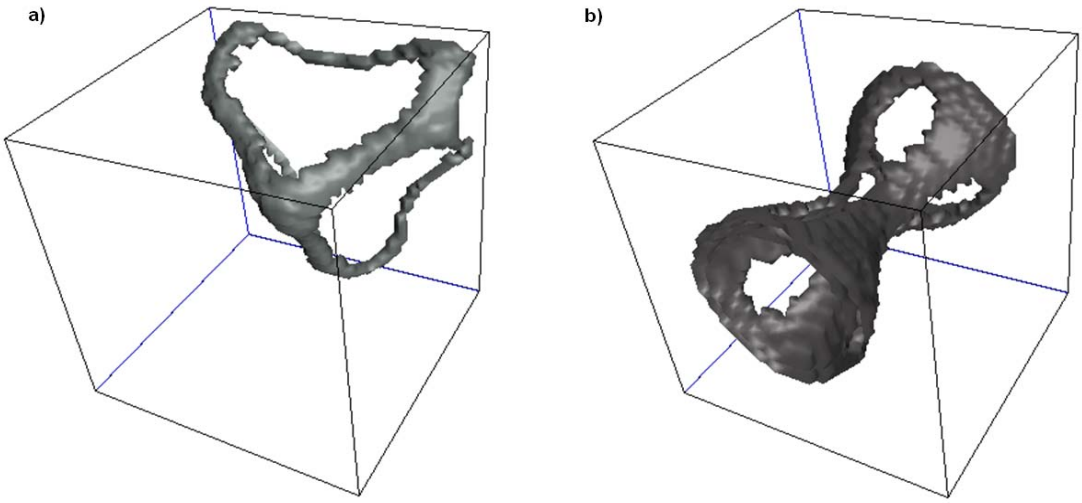

Figure 3.19: Wetting non-wetting interfacial area configuration at the same wetting phase saturation S_w during a) drainage and b) imbibition in a pore throat between three spheres in point contact. a) Drainage, $S_w = 0.57$, $C = 9$, $A_{w\text{-}nw}/V_B = 0.017$ b) Imbibition $S_w = 0.57$, $C = 4.7$, $A_{w\text{-}nw}/V_B = 0.047$.

The contact line configuration is shown in Figure 3.20. Even if the configuration is completely different for drainage and imbibition the value of (L_{cD}/V_{bD}) does not differ much, being equal to 3.3 for drainage and 3.9 for imbibition for $S_w = 0.57$. Therefore a larger interfacial area does not necessarily means a larger contact line length.

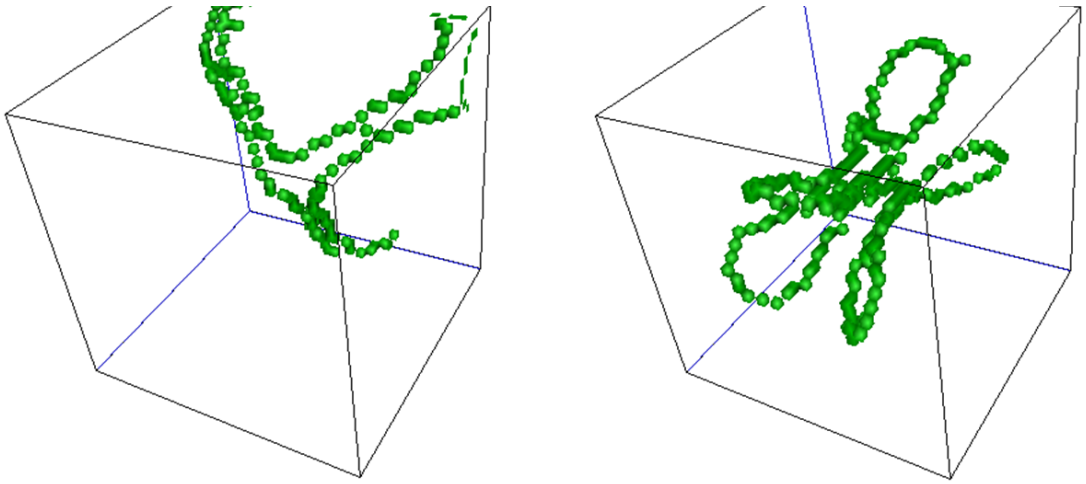

Figure 3.20: Wetting non-wetting contact line configuration at the same wetting phase saturation S_w during a) drainage and b) imbibition in a pore throat between three spheres in point contact. a) Drainage, $S_w = 0.57$, $C = 9$ $L_{cD}/V_{bD} = 3.3$ b) Imbibition $S_w = 0.57$ $C = 4.7$, $L_{cD}/V_{bD} = 3.9$.

This exercise suggests that the hysteresis in interfacial area does not necessarily leads to hysteresis in contact line length. At the same wetting phase saturation there is a 60% increase in area from drainage to imbibition (Figure 3.19) while there is a 15% increase on contact line length (Figure 3.20). Still, contact line length shows significant hysteresis versus curvature and wetting-non-wetting interfacial area in single pores and sphere packs.

In the next section, we are going estimate analytically a solution for contact line length in a pack of computer generated spheres.

3.3.5. Analytical Estimate of Contact Line Length in a Computer Generated Pack of Spheres

We are going to estimate an analytical solution for the contact line length in every step of drainage in a computer generated pack of spheres. We start by assuming that at a given saturation the contact line is associated to pendular rings and menisci. Depending on the stage of drainage there will be more pendular rings or more menisci present.

The drainage simulation for this estimate is independent of the LSMPQS approach, being based on a pore network model (Behseresht et al., 2009). From the network model we counted the number of complete pendular rings (i.e. rings surrounded by non-wetting phase) and assumed that all of them are between spheres in point contact. This is a reasonable approximation since the average of point contacts per sphere in packs of randomly distributed spheres of the same size has been estimated to be close to 6 (5.8 in Mellor (1989), 5.9 in Bryant and Johnson, (2003), 5.6 in Rodriguez, (2006)). Then the contact line was calculated analytically for the given curvature and assuming a toroidal shape for the pendular ring. We also counted the number of menisci at every drainage step in the computer generated pack of spheres. To estimate the amount of contact line associated with a meniscus, we used LSMPQS to compute the contact line length in three typical pore throat configurations, when the meniscus is at the point where is about to drain the pore. Table 3.2 shows the results.

Table 3.2: Contact line length associated with a meniscus for three typical configurations of spheres in a pore throat. The contact line is calculated at the step prior to the complete drain of the pore. (PC = point contact, G = gap, w = gap width)

Configuration	**Curvature**	**Contact line length (*R*)**
3PC	10	5.4
2PC, 1G w = 0.04*R*	5.4	4.9
1 PC , 1 G w= 0.01*R*, 1G w= 0.04*R*	5.7	4.5

Based on the results of Table 3.2 we assumed a constant contact line length equal to 5*R* for a meniscus all through drainage. It is important to notice that the presence of gaps between the spheres makes the length associated to the meniscus to decrease.

At the same curvatures (10, 5.4 and 5.7) that we calculated the contact line length for the meniscus between three spheres in point contact, the complete pendular ring between two spheres in point contact has an associated contact line length equal to 4.7, 5.8 and 5.7 respectively. Thus an individual pendular ring and a single meniscus in a pore throat make similar contributions to the contact line length.

Figure 3.21 shows the number of pendular rings and menisci during drainage. Every time a meniscus jumps through a pore throat, it leaves (partial) pendular rings behind at the grain contacts associated with that throat. As the throats around a grain contact are drained, a complete pendular ring forms, and once formed it will not disappear. Thus the number of pendular rings increases monotonically through drainage, and it is larger than the number of menisci by a factor of 2.5 at the end of drainage. The number of menisci increases through drainage reaching a maximum. In the last stages of drainage some menisci disappear as pores on the edges of the domain are drained.

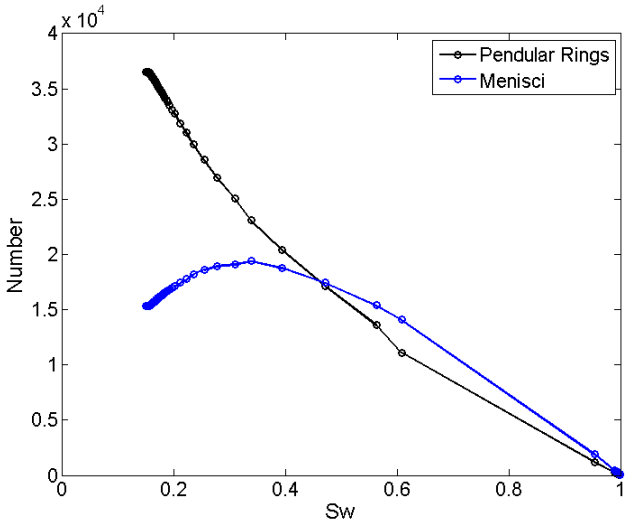

Figure 3.21: Number of pendular rings and meniscus during the simulation of drainage in a computer generated pack of 7000 spheres of the same size using network model (courtesy of Mr. Javad Behseresht).

For the pendular rings, we have calculated the length at each step assuming that all of the pendular rings are between spheres in point contact. This will be a higher bound for the contact length, because for the same curvature, if there is a gap between the grains, the length of the contact line will be smaller. At the beginning of drainage we have more menisci than pendular rings. As drainage progresses we increment both the number of menisci and pendular rings. At wetting phase saturation around 0.5 the number of pendular rings exceeds the number of menisci. At wetting phase saturation of 0.38 the number of menisci starts to decrease, indicating that the existent menisci are draining through pores and no new ones are created. The number of pendular rings keeps increasing until the end of drainage.

Figure 3.23 shows the contact line length associated to pendular rings and menisci, together with the total contact line (sum of menisci and pendular rings length.)

Here we have used the lengths described above, i.e. 5R for each meniscus and the corresponding value of length for the given curvature for pendular rings.

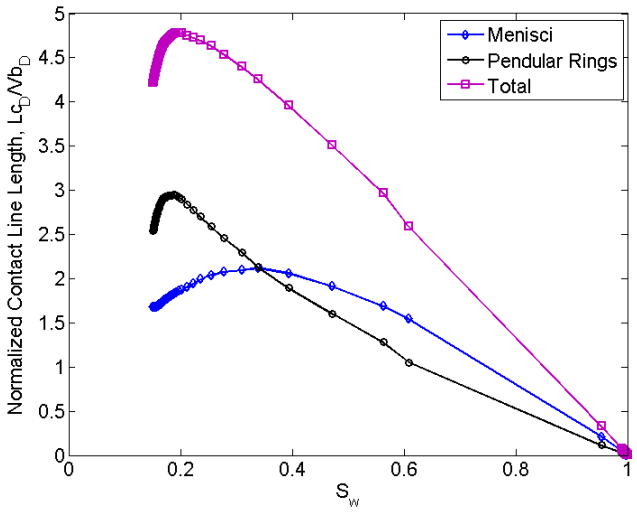

Figure 3.22: Normalized specific contact line length *vs.* wetting phase saturation for drainage in a computer generated pack of spheres of radius *R* showing the contribution of pendular rings and menisci at every step.

The contribution of the pendular rings to the total contact line length is larger than the contribution of the menisci at wetting phase saturations smaller than 0.38. At saturations smaller than 0.2 the contact line length associated to pendular rings starts to decrease because the effect of the increase in curvature (that reduces contact line length) that overcomes the number of new rings formed. Nevertheless their contribution to contact line length is still larger than the contribution of the menisci. This suggests that the contact line length is dominated by pendular rings at low water saturations while the contribution of menisci and pendular rings balances at higher wetting phase saturations.

Unfortunately, we do not have the count of pendular rings and menisci for imbibition. During imbibition, coalescence of two or three pendular rings as pressure decreases creates one meniscus. On the other hand, a Melrose event (two menisci that merge) destroys meniscus, because the merger yields one remaining meniscus and leaves no pendular ring. Our simulations of imbibition suggest that coalescence does not happen once imbibition starts (also showed by Gladkikh and Bryant (2003)) since first comes the growth of the pendular rings, reversing the shrinkage that happened during drainage. Therefore at the beginning of imbibition (small S_w) and until most of the pendular rings have merged, the contact line will be dominated by the contribution of the pendular rings. According to Figure 3.6 for a sphere pack and Figure 3.16 for a single pore, this is true until $S_w \cong 0.15$, where we see that the contact line length and interfacial areas for drainage and imbibition are almost identical (first 3 points at low S_w in Figure 3.6 and Figure 3.16). At $S_w > 0.15$ we have meniscus advancing through the pores generating interfacial area, as shown in Figure 3.18 for the single pore case, until they start to merge (Melrose event) and the interfacial area starts to decrease.

The interfacial area associated to a meniscus is larger than the area associated to a pendular ring, as we showed in Figure 3.19, and for that reason interfacial area at intermediate saturations reaches a maximum. However we also saw that a larger interfacial area does not necessarily means larger contact line (Figure 3.16 *vs* Figure 3.18; Figure 3.20) therefore the number of new menisci created during imbibition that greatly contribute to the increase in interfacial area before they coalesce, do not contribute in the same magnitude to a increase in contact line length as the interface moves through the throat. Also for contact line length, at the same saturation we have smaller curvature for imbibition. Smaller curvatures increase the length of pendular rings, but not as much the length associated to a meniscus as shown by the line for imbibition in Figure 3.17, before

coalescence. Thus to notice an increase in the contact line length during imbibition, new pendular rings would have to be created with the decrease in curvature, which clearly is not the case. Presumably it is the coalescence of pendular rings into menisci that creates the approximate balance (lack of hysteresis) during imbibition in sphere packs.

To conclude our analysis of computer generated packs of spheres, the effect of spatial configuration and grain size was also study in small packs of spheres. Please refer to Appendix H for this material. In the next sections we are going to analyze contact line length from high-resolution images of real porous media.

3.3.6. Results from Images of Drainage in Pack of Glass Beads of Different Hydrophobicity

We analyzed high resolution X-ray CT images of drainage endpoints in porous media made of glass beads of diameters ranging between 0.3 and 0.42 mm (courtesy of Dr. Willson from Louisiana State University). The images are of size 300^3 with a voxel size equal to 10.92 μm, or 0.05*R* to 0.07*R*. Three different types of packs were analyzed, one containing 100% hydrophilic beads, one containing 50% hydrophilic and 50% hydrophobic beads and a last one containing 25% hydrophilic and 75% hydrophobic beads. From these images we can extract the contact line between air water and solid phases and compare with the results in simulations of drainage in computer generated packs of spheres. The procedure to extract the contact line is detailed below.

For every image file we are going to generate LSMLIB type files analogous to the ones that LSMPQS method calculates for every simulation step. We start by creating three binary files for each image that will describe the geometry, wetting phase and non-wetting phase configuration of the image. In the original data files provided by Dr. Willson, solid, air and water were represented by voxels with values *0*, *1* and *2*

respectively. In the file that describes the geometry of the porous medium, we assign the values of *1* and *-1* to the voxels that originally represented solid and void space (air plus water) respectively. In the file that describes the non-wetting phase, we assigned the value of *-1* to the voxels that originally represented air and the value of *1* to the voxels that were originally solid or water phase. Finally, for the file representing the wetting phase, we assign the value of *-1* to the voxels originally representing water and the value of *1* for the rest of the voxels. We used Matlab to read the original files and generate the three new binary files.

Now we need to replace the level set function numerically defined in each of these binary files by a signed distance function that describes the same zero level set. This is necessary to avoid accumulation of numerical error in the calculations. This process is called "reinitialization" and is done periodically and automatically during LSMPQS simulations[1]. However, since we manually created the binary files we need to use the LSMPQS routines "`reinitialize_mask`" and "`reinitialize_data_step`" to generate the signed functions for the mask (function describing the pore space) and non-wetting phase, which will be analogous to what the output functions from a LSMPQS simulation step would be.

Once the non-wetting phase and mask files are reinitialized they are ready to be used as input for the C routine that we developed to identify contact lines. The resultant LSMPQS file that identifies the contact line voxels is then thinned down with 3DMA-Rock and the length of the contact line can be calculated.

Table 3.3 shows the results of the contact line length for the different bead packs extracted from their corresponding images, together with the porosity and the water

[1] LSMPQS Software Manual (v0.5), Maša Prodanović, 2009

saturation of the pack. These last two characteristics of the bead packs were calculated by voxel count.

Table 3.3: Porosity, water saturation and normalized specific contact line length for different packs of glass beads (I= 100% hydrophilic, E=50% hydrophilic 50% hydrophobic, O= 100% hydrophobic) obtained from CT images[2] by means of LSMPQS and 3DMA-Rock analysis as described in the text

Sample	Porosity (%)	S_w	L_{CD}/V_{bD}
I2	37.5	0.0775	1.04
I3	38.0	0.0805	1.34
E2	37.0	0.0553	0.60
E3	36.2	0.0566	0.64
O1	38.0	0.036	0.27
O2	37.9	0.0347	0.28

We observed that at these water saturations the majority of the contact line exists as isolated paths (Figure 3.23), which we believe belong to pendular rings. It is not possible to see complete pendular rings because of the error due to digitization (see Appendix G for more information).

[2] Courtesy of Dr. Willson of Louisiana State University

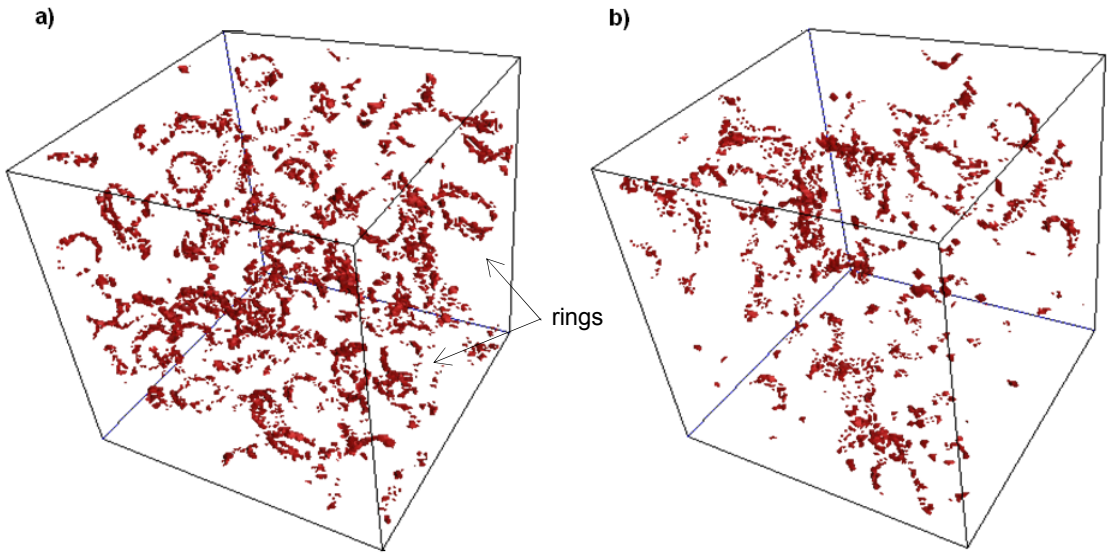

Figure 3.23: Contact line configuration in (a) a pack of 100% hydrophilic beads (sample I2 in Table 3.3) and (b) a pack of 50% hydrophilic beads (sample E3 in Table 3.3).

We can compare the contact line length extracted from these images with the contact line length calculated from LSMPQS simulations in sphere packs. Since in the sphere packs we assume a strongly water wet surface, the direct comparison is made with the results from the packs of 100% hydrophilic beads. We have also estimated contact line length analytically for the last steps of drainage in a computer generated pack as we showed in the previous section. The drainage simulation was based on a pore network model extracted from a dense disordered periodic packing of equal spheres (Behseresht *et al*., 2009) from where we estimated the number of complete pendular rings and assumed that all of them are between spheres in point contact. The contact line was calculated analytically for the given curvature and assuming a toroidal shape for the pendular ring. In this case we did not account for any menisci.

Figure 3.24 compares this analytical estimate with the results from the LSMPQS simulation and the estimated contact line length from the microtomography images. We can see how the contact line length extracted from the images is closer to the results of LSM simulation for a poor resolution (dx = 0.08). As we could see in Figure 3.23a) the double rings of contact line around pendular rings are not apparent because of digitization (see Appendix G). Thus it is likely that a higher resolution image would have yielded a contact line length up to two times larger, which would agree well with the sphere pack simulation. It is also worth noticing how the results from the pore network simulation of drainage are close to the results from the LSMPQS simulation. We can consider the pore network simulation results as an upper bound for contact line length since the network calculation assumed all the pendular rings have two rings of contact line and are between spheres in point contact. When the spheres are separated by a gap the length of the contact line will be smaller for the same curvature.

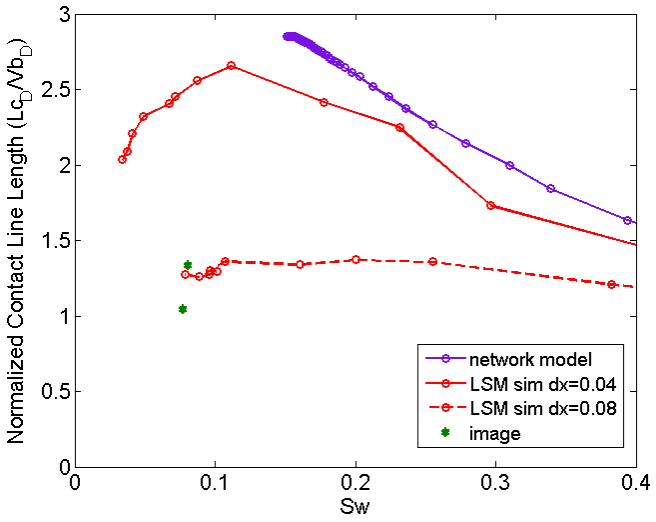

Figure 3.24: Normalized specific contact line length *vs.* water saturation from drainage and imbibition simulation in a sphere pack compared with contact line length from analytical calculation in a computer generated pack of spheres based on a pore network model simulation of drainage and with the contact line length extracted from microtomography images of glass bead packs (I2 and I3 in Table 3.3).

3.3.7. Contact Lines in High Resolution X-ray Images of Sedimentary Rocks

We have also computed contact line configurations in high resolution images of dry and wet Fontainebleau sandstone and sucrosic dolomite samples provided by Dr. Knackstedt of Australian National University. Figure 3.25 shows some sample slices from these images.

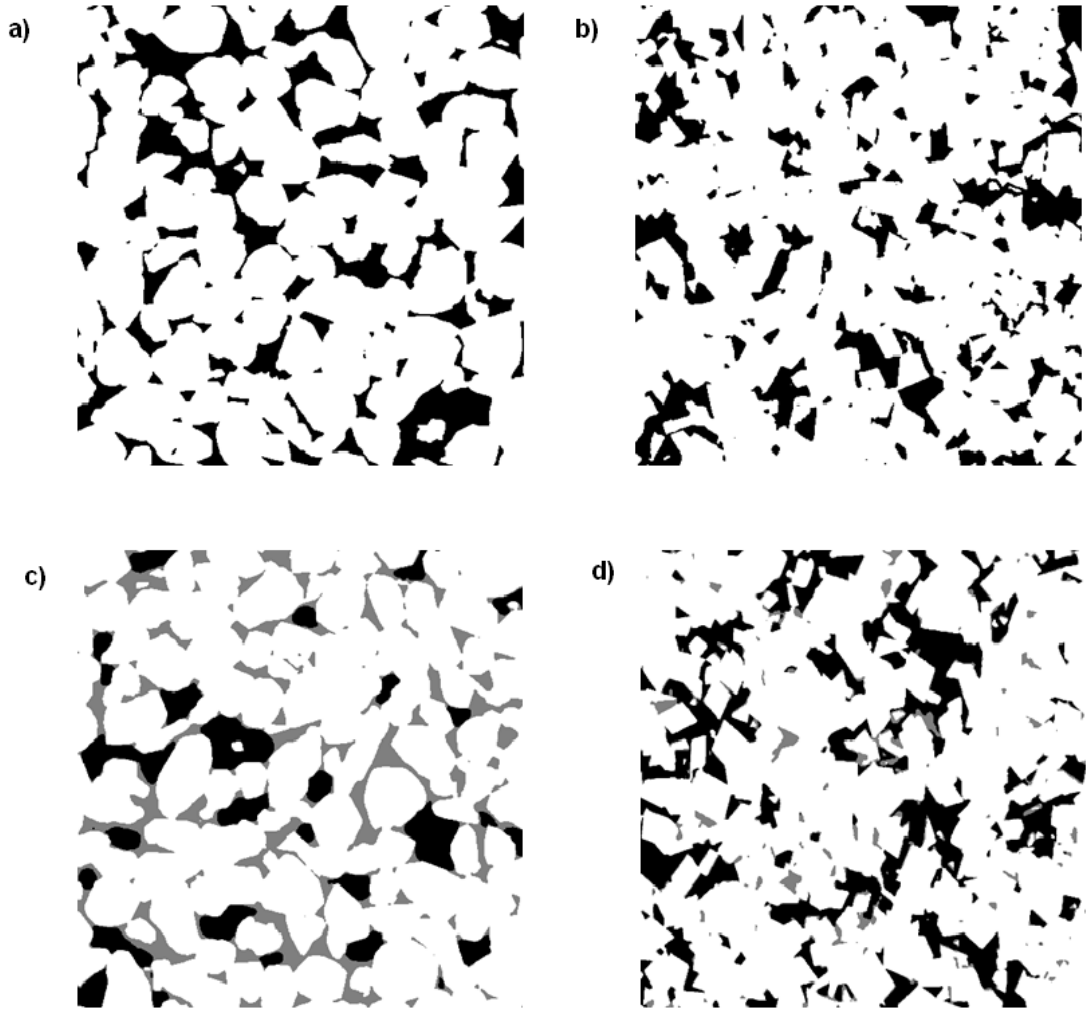

Figure 3.25 : a) 500×500 slice of dry Fontainebleau sandstone. b) 500×500 slice of dry sucrosic dolomite c) wet Fontainebleau sandstone at the last step of imbibition d) wet sucrosic dolomite at the last step of drainage. White: grains, black: air, grey: water (courtesy of Dr. Knackstedt of Australian National University).

The data of these images are contained in cubes of 500^3 voxels, each of size 3.5 μm. The original files were of the type unsigned binary character We converted the original data files (unsigned binary character type) for the dry images into 3DMA segmented files that defined the geometry of the porous media using “case2.22” in

3DMA-Rock (Lindquist 1994-2010). We are going to use these porous media geometries to simulate drainage and imbibition using LSMPQS. It is of primary interest whether the relative magnitudes of the contact lines in these sedimentary rocks are comparable to the trends observed for the model sediments. Because of computational time limits we simulated drainage and imbibition in 250^3 subsamples rather than in the full 500^3 sample. We run large cases (more than 100^3) in a compute node of the TACC (Texas Advanced Computing Center) "Stampede" cluster that has 8GB of memory. The LSMPQS code is written in serial mode and therefore is run by one processor. The simulation of drainage in one of these 250^3 samples took an average of 15 days (more or less depending on how difficult was the geometry), therefore it took about a month to run both drainage and imbibition, which discourage us to run simulations in 500^3 samples.

These 250^3 subsamples were created with "case2.2" in 3DMA-Rock which is used to resize segmented files. Figure 3.26 a) and b) show the images for two 250^3 subsamples of sandstone and dolomite respectively. The data files for the images were generated with the LSMPQS routine "initialize_geometry" using the resized 250^3 3DMA segmented file as geometry input data[3]. This routine creates the LSMLIB file "mask" which stores the level set function that defines the geometry configuration. The "mask" file was plotted using the routine "isosurface"

[3] LSMPQS Software Manual (v. 0.5), Maša Prodanović, 2009.

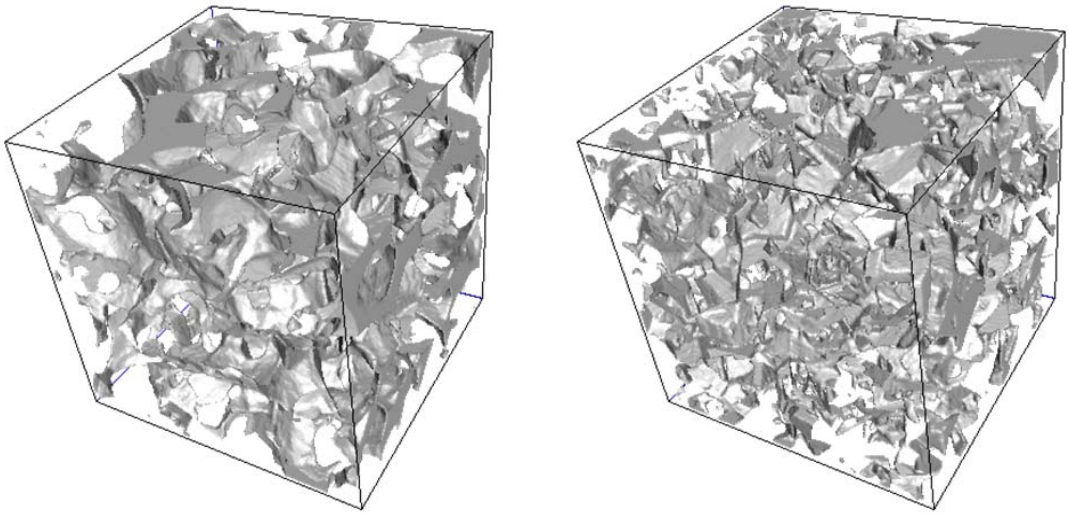

Figure 3.26: a) 250^3 subsample of Fontainebleau sandstone. b) 250^3 cube subsample of sucrosic dolomite.

We simulated drainage and imbibition displacements in these samples with LSMPQS and calculated the contact line length using the same approach as described above for the computer generated packs of spheres. Figure 3.27 shows simulated contact line versus water saturation for 250^3 subsamples of sucrosic Dolomite and Fontainebleau Sandstone. The normalized specific contact line length shows hysteresis, being larger for imbibition than for drainage especially at low water saturations. This behavior was not observed in the sphere packs (cf. Figure 3.5a; Figure 3.6).

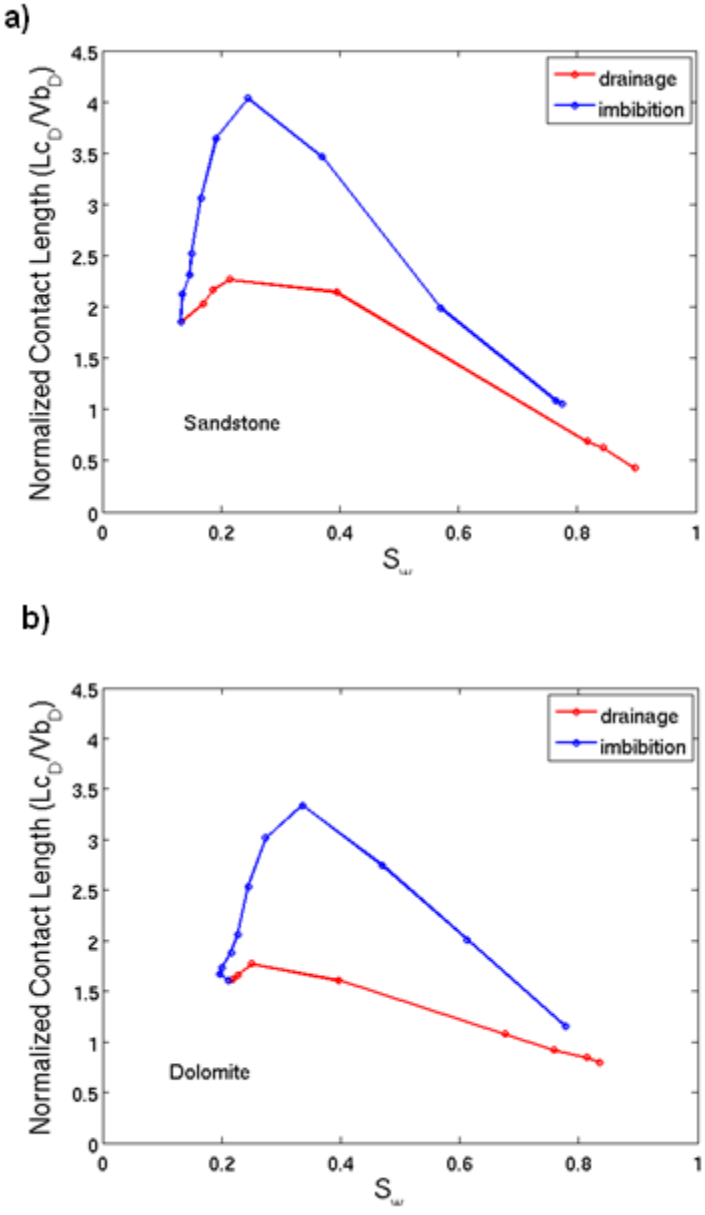

Figure 3.27: Normalized specific contact line length *vs.* water saturation for simulations of drainage and imbibition in a) 250^3 sample of Fontainebleau Sandstone b) 250^3 sample of sucrosic dolomite.

Figure 3.28 shows the configuration of the contact lines in a step of drainage in one of the Fontainebleau sandstone subsamples. Pairs of circles of contact line around pendular rings are not as easy to identify in these samples as for the model sediments because of the more complex geometry of the pore space. The resolution or voxel size for the simulation is given by the resolution of the image and cannot be changed. Taking an average grain size (diameter) of 250 μm for Fontainebleau sandstone (measured from the image) the resolution for the Fontainebleau sandstone images is $dx = 0.03R$, therefore the contact line is comparable with the simulations at resolution $dx = 0.04R$. Comparing with the results for contact line length in the periodic pack of spheres (recall Figure 3.6) we observe that the normalized specific contact line lengths for drainage are similar in the sandstone, dolomite and sphere pack simulations.

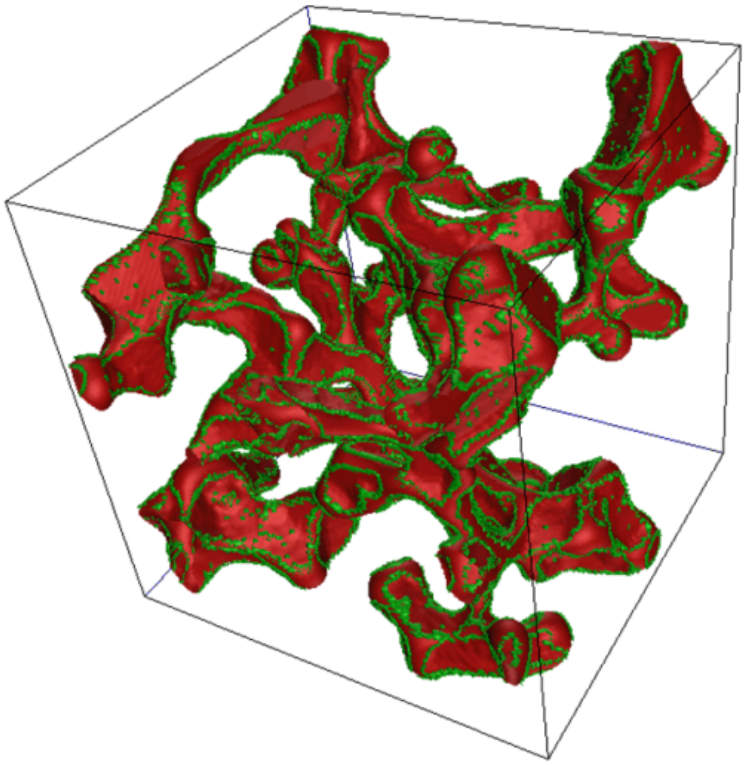

Figure 3.28: Contact line (green) and non-wetting phase (red) during drainage in a 250^3 subsample of Fontainebleau sandstone (S_w = 0.55, curvature = 3.66).

Figure 3.29 shows the curves of contact line length during drainage curves for these three cases and Figure 3.30 shows the corresponding curves for imbibition. A main difference between the three porous media is the saturation at which the maximum length occurs. This saturation is smaller in the sphere pack than in the sedimentary rocks, during both drainage and imbibition displacements.

The magnitude of the maximum length is larger in the sphere packs than in the rocks for drainage. For the sphere packs, since there is no hysteresis in contact line length, the maximum length during imbibition is reached at similar saturation, and it has similar value, than during drainage.

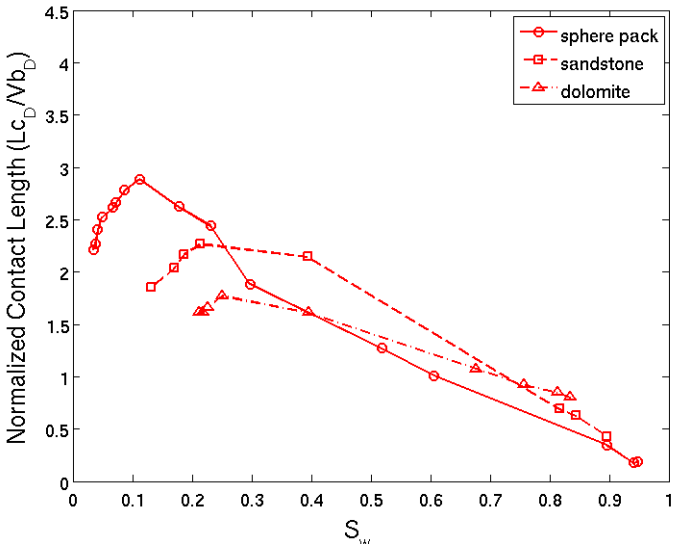

Figure 3.29: Comparison normalized specific contact line length *vs.* water saturation for simulations of drainage in a sphere pack (Figure 3.6, for $dx = 0.04R$), a 250^3 sample of Fontainebleau sandstone (Figure 3.27a), and a 250^3 sample of sucrosic dolomite (Figure 3.27b).

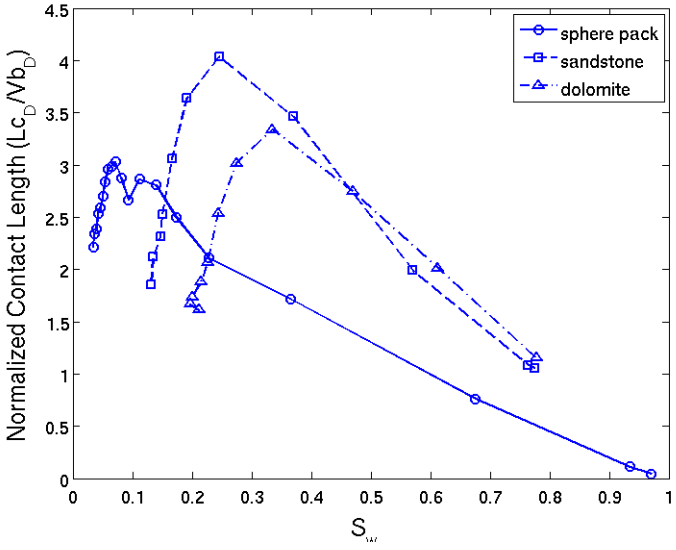

Figure 3.30: Comparison normalized specific contact line length *vs.* water saturation for simulations of imbibition in a sphere pack (Figure 3.6, for $dx = 0.04R$), a 250^3 sample of Fontainebleau sandstone (Figure 3.27a), and a 250^3 sample of sucrosic dolomite (Figure 3.27b).

However for the rocks we observe significant hysteresis, being the contact line length much larger during imbibition than during drainage. For sandstone and dolomite we do not have clearly defined pendular rings because of the complex geometry, we are not expecting the reversible first steps at the beginning of imbibition where contact line length and interfacial area took similar values as we observed in the sphere packs (Figure 3.6 and Figure 3.10). In this case drainage concludes after several pores are drained (Haines jumps) and no pendular rings are created (notice that the drainage endpoint occurs at larger wetting phase saturations for the rocks in Figure 3.29). Therefore we start imbibition after the Haines jumps and as shown in Figure 3.17 there is a large difference in contact line length for the same curvature.

For clarification, we also computed the interfacial area between wetting and non-wetting phases for drainage and imbibition in these samples and plot interfacial area versus wetting phase saturation (Figure 3.31) and contact line length versus interfacial area (Figure 3.32) for the same sandstone and dolomite samples as in Figure 3.27. Notice that here we are plotting the specific normalized area (A_D/V_{bD}) whereas we were plotting interfacial area normalized by solid area in Figure 3.31.

As was the case for computer generated packs of spheres, the interfacial area during imbibition is larger than the area during drainage for both sandstone and dolomite in Figure 3.31. Also, during imbibition, an increase in interfacial area is not associated with an increase in contact line length, as shown in Figure 3.32. The difference of this last result with respect to the sphere packs (cf. Figure 3.11) is noticeable, as we observe here how both contact line length and interfacial area keep increasing at the start of imbibition, while only area had a large increase during imbibition in the sphere packs.

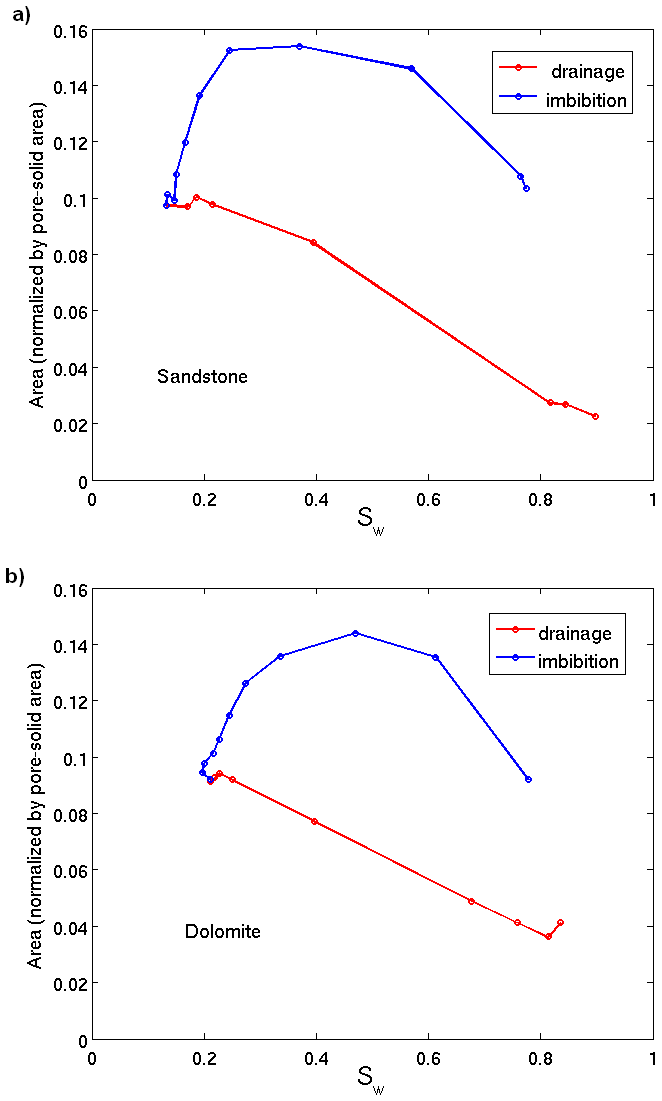

Figure 3.31: Interfacial area between wetting and non-wetting phases *vs.* saturation for simulations of drainage and imbibition in 250^3 samples of a) Fontainebleau sandstone and b) sucrosic dolomite

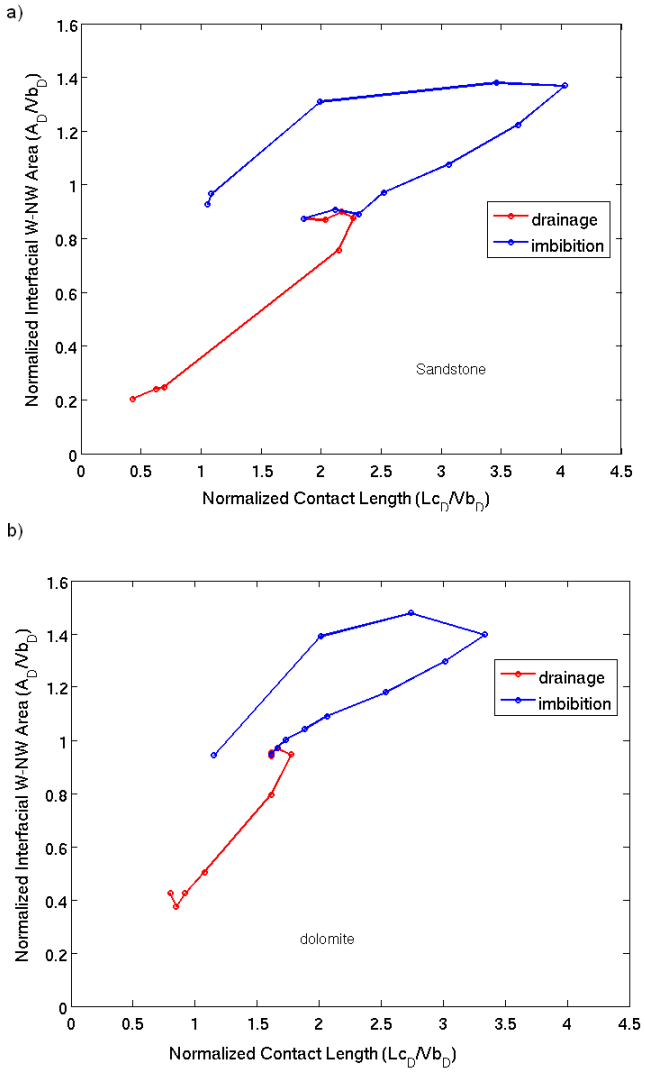

Figure 3.32: Normalized specific wetting-non-wetting interfacial area *vs* normalized specific contact line length for simulations of drainage and imbibition in 250^3 samples of a) Fontainebleau sandstone and b) sucrosic dolomite

Back to the behavior of the wetting-non-wetting interfacial area in Figure 3.31 we observe that it is quite similar to the trend for sphere packs (recall Figure 3.10): the interfacial area is larger for imbibition than for drainage and reaches a maximum value

around 0.15. However, a main difference is that the interfacial area at the imbibition endpoint is larger for sandstone and dolomite than for the sphere packs (compare a normalized interfacial area value of 0.03 at (1-S_{nwr}) = 0.96 for a sphere pack in Figure 3.10 with a value of about 0.10 for both rocks at (1 – S_{nwr}) = 0.8 in Figure 3.31).

The reason for this discrepancy is a larger amount of blobs of trapped non-wetting phase in the sandstone and dolomite packs than in the sphere packs, which create more interfacial area than the connected bulk phases, which can be seen in Figure 3.33 where the non-wetting phase configuration it is shown at a wetting phase saturation of S_w = 0.86 for a sphere pack (from imbibition in Figure 3.10) and S_w = 0.78 for Fontainebleau sandstone (last step of imbibition in Figure 3.31a). The normalized interfacial wetting-non-wetting areas for these cases are 0.05 and 0.10 respectively. While the non-wetting phase in the sphere pack (a) is present as a large connected blob and two small disconnected blobs, in the Fontainebleau sandstone the non-wetting phase is present as small trapped blobs that create more wetting-non-wetting interfacial area for similar water saturation. These trapped blobs also contribute to more contact line than the main bulk phase, therefore explaining the hysteresis at the end of imbibition.

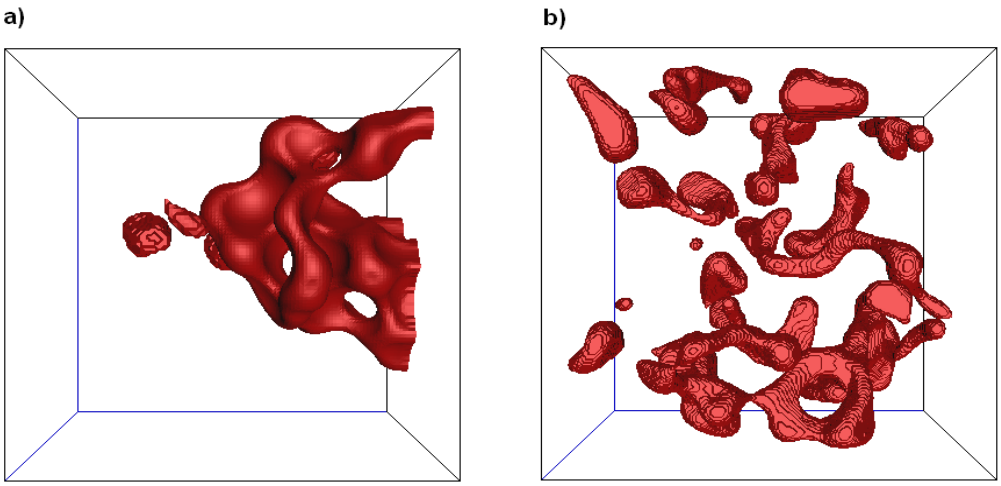

Figure 3.33: Non-wetting phase configuration at imbibition endpoint in a) Computer generated pack of spheres ($dx = 0.08R$) $S_w = 0.85$. b) Fontainebleau sandstone, $S_w = 0.78$.

Analysis of wet images of Fontainebleau Sandstone and Sucrosic Dolomite

Corresponding wet data files for the last step of drainage in the dolomite and the last step of spontaneous imbibition in Fontainebleau samples were also provided. We processed these images with 3DMA-rock to obtain segmented files for the solid and the non-wetting phases. The procedure to identify the contact lines was analogous to the one that we used to obtain the contact lines form the wet images of packs of glass beads (cf. section 3.3.5). The contact line length was calculated and compared with the results from the LSMPQS simulation in the same subset of the dry sample. Table 3.4 and Table 3.5 show the results.

Table 3.4: Normalized specific contact line length calculated from the wet images (full sample)

Sample	Porosity (%)	Sw	Lc_D/Vb_D
Dolomite	21.43	0.22	8.78
Fontainebleau	19.33	0.64	2.10

Table 3.5 : Normalized specific contact line length calculated from subsamples of the wet images and normalized contact line length from drainage and imbibition simulations.

Sample	Porosity (%)	Sw	Lc_D/Vb_D (LSM)	Lc_D/Vb_D (from image)
DM1 (sub 110)	22.13	0.21	1.70	8.90
DM2 (sub101)	21.02	0.21	1.95	8.88
DM3 (sub 111)	22.90	0.20	1.30	7.67
FB1 (sub 001)	18.73	0.63	1.50	2.11
FB2 (sub 011)	19.54	0.61	1.65	2.28
FB3 (sub 010)	19.78	0.66	1.60	1.92

The contact line extracted from the image is always larger than the one from LSMPQS simulation, but this difference is considerable in the case of the drainage endpoint in dolomite, where the contact line length from the image is around five times larger. The wet image for dolomite in Figure 3.25d corresponds to the last step of drainage (at a wetting phase saturation of 0.22). In Figure 3.34 we compare the configuration of the wetting phase from the image (a) with the configuration for our LSMPQS simulations of drainage in this rock (b), in a 100^3 subsample.

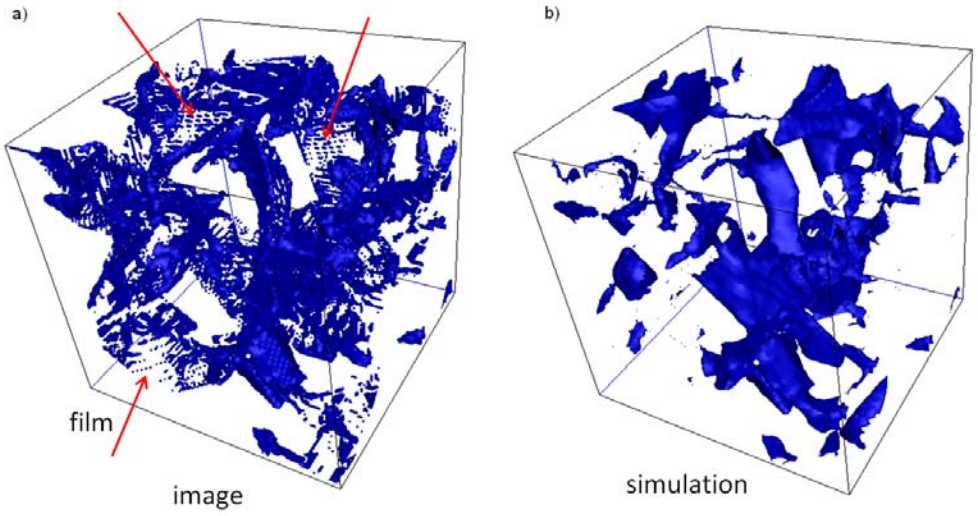

Figure 3.34: Wetting phase configuration in a 100^3 subsample of sucrosic dolomite a) from image and b) from simulation (S_w = 0.22).

After observation of the wetting phase configurations we conclude that the main cause of the difference between contact line length computed directly from the wet image and contact line length computed from the displacement simulation is the presence of wetting phase as thin films covering the grains. LSMPQS does not capture these films. Figure 3.35 a) and b) shows the configuration of the contact line and non-wetting phase in a subset of the wet sample of Fontainebleau and the configuration from secondary imbibition simulation in the same subsample at similar water saturation respectively. While the configuration of the non-wetting fluid is reasonably similar in both cases, we can see more "density" of contact lines in the result from the image. This accounts for the larger values of normalized specific contact line length in the images.

The water films are much more evident in the images of the dolomite than for sandstone, as shown in Figure 3.36. The more angular geometry of the dolomite makes the wetting fluid to remain in the roughness of the grain as thin films to a greater extent

than in the sandstone. Also, more water remains in form of films and pendular rings at low water saturations (20% in this dolomite sample) than at larger saturations (60% for the sandstone sample). Because the films are thin, about 1 or 2 voxels thick between the solid and the main non-wetting fluid phase, most of the film voxels are identified by the image processing algorithm as contact lines. Consequently the reported value of contact line length is much larger in the images than in the simulations in the same void space as the image.

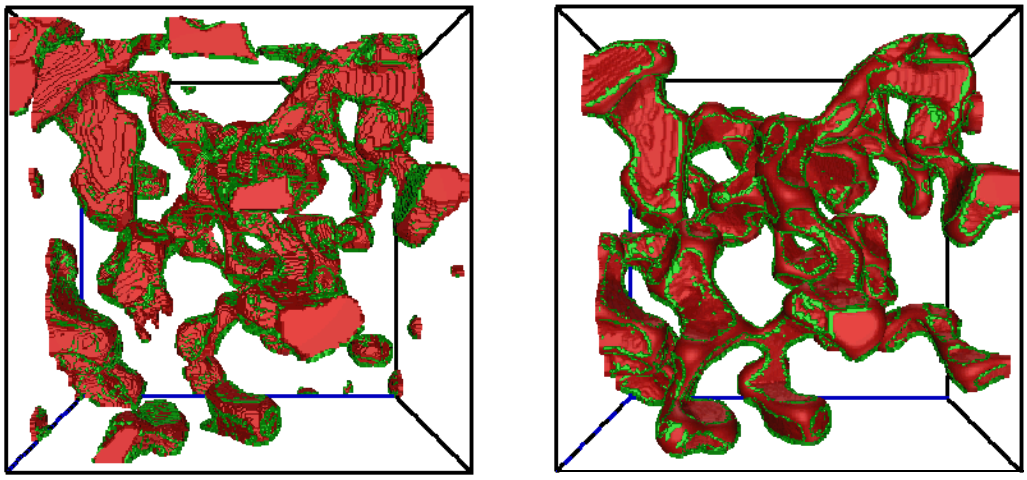

Figure 3.35: a) Contact line (green) and non-wetting phase (red) in a 250^3 subsample (sub 001; cf. Table 3.5) of Fontainebleau sandstone extracted from the wet image ($S_w = 0.63$). b) Contact line in the same 250^3 cube subsample from the simulation step at similar water saturation ($S_w = 0.60$).

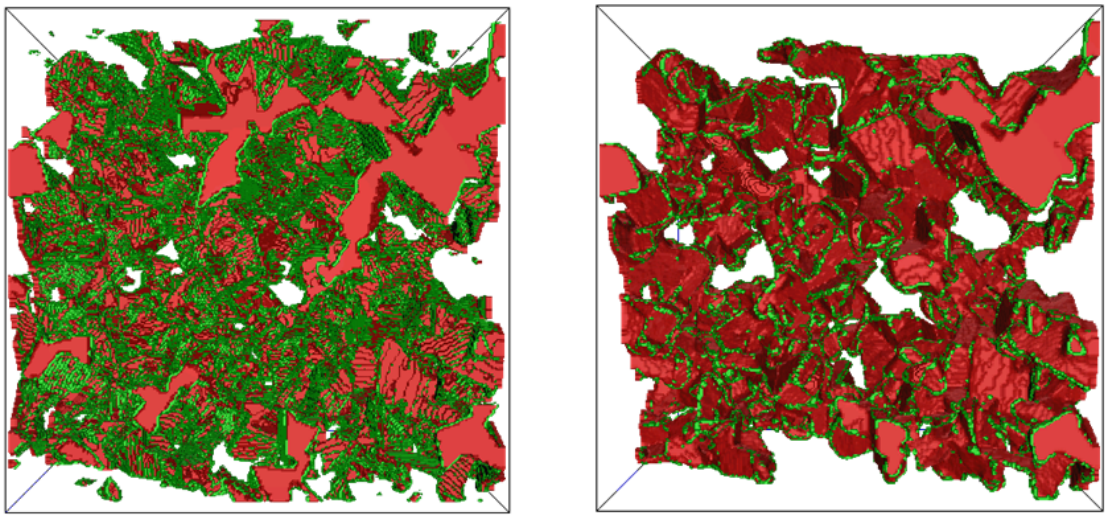

Figure 3.36: a) Contact line (green) and non-wetting phase (red) in a 250^3 subsample (sub. 110, cf. Table 3.5) of sucrosic dolomite extracted from the wet image ($S_w = 0.22$). b) Contact line length in the same 250^3 subsample from the LSMPQS simulation step at similar water saturation ($S_w = 0.21$).

Figure 3.37 shows the contact line in a close up view of sucrosic dolomite. Patches of contact line with a grid-like structure are evident. These presumably correspond to water films. The actual contact line will be only the perimeter of these patches. While the LSMPQS method is able to identify pendular rings, we are currently working in correctly identify water films. Notice that these water films did not exist for the case of the sphere pack because of the smoothness of the spheres.

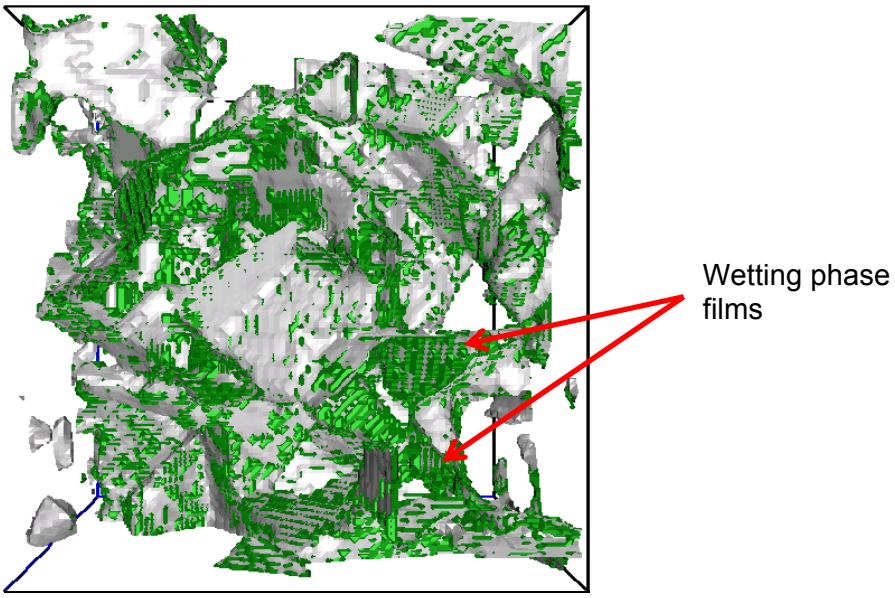

Figure 3.37: Contact line (green) extracted from image shown over grain surface in a 100^3 subset of sucrosic dolomite.

Figure 3.38 shows the contact line length computed from processing the wet images that correspond to the void space of the same 250^3 subsamples of sandstone and dolomite where we run the simulations of drainage and imbibition (shown in Figure 3.27)

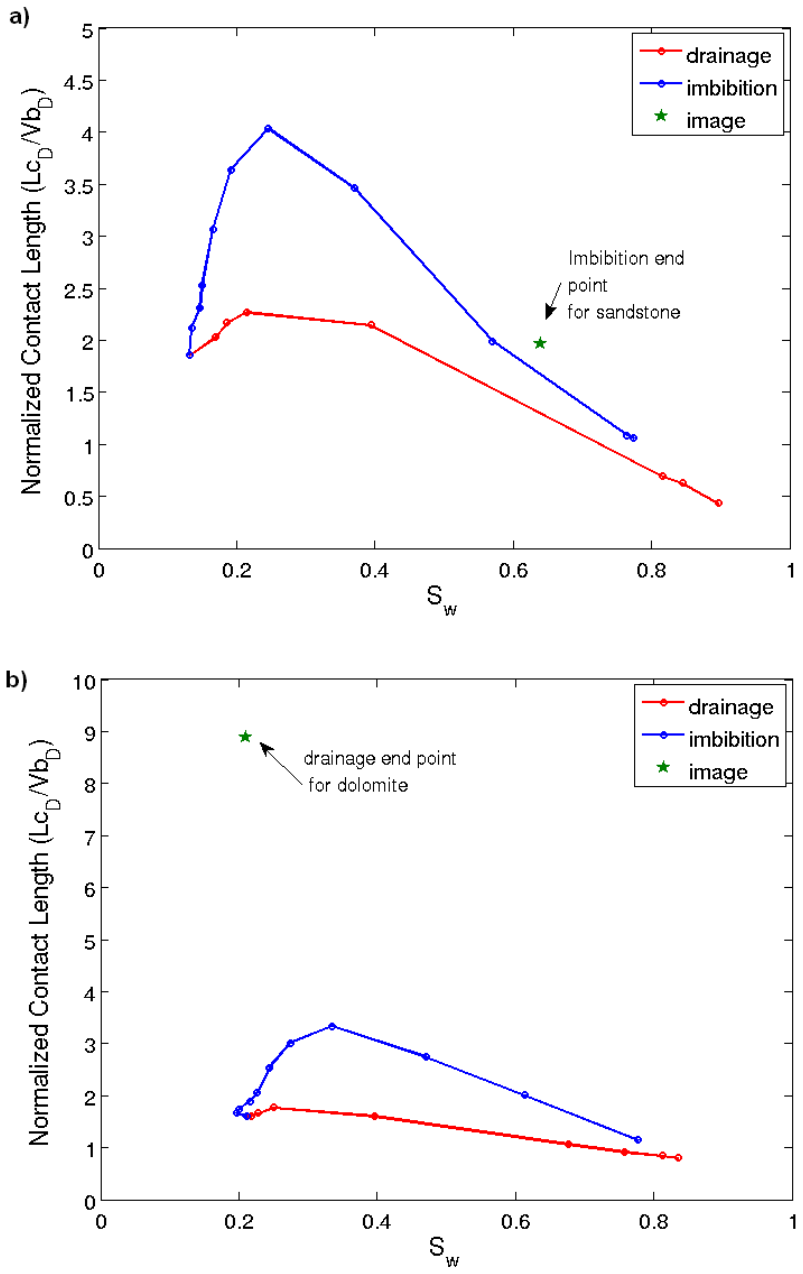

Figure 3.38: Same simulations as Figure 3.27 (solid curves) for the normalized specific contact line length *vs.* water saturation showing the contact line length estimated from the wet images as a green star in both plots. a) 250^3 sample of Fontainebleau sandstone. b) 250^3 sample of sucrosic dolomite.

We attempted to estimate the amount of contact line associated with water films in the wet images corresponding to the drainage endpoint in sucrosic dolomite. We "coarsened" the segmented wet dolomite images by replacing boxes of a given number of voxels by only one voxel whose value reflects the majority on the box. This local averaging tends to eliminate wetting films (the voxels tend to be reassigned as solid or as non-wetting phase) but preserve volumes of the wetting phase associated with the bulk phase. The coarsened image provides a better basis for comparison with our LSMPQS calculations since the latter only accounts for the contact line associated to the bulk phase and trapped phases. The difference between the contact line length associated to the main bulk phase and the total contact line from the image yields the contact line associated to wetting films. The percentage of contact line associated to wetting films calculated in this way ranged between 80 and 90%. This amount of films is enough to explain the difference between the contact line length from simulation and from images for dolomite in Figure 3.38b. The percentage of contact line associated to the wetting film is expected to be smaller for the Fontainebleau imbibition endpoint, since less amount of wetting films present at larger wetting phase saturations.

3.4. CONCLUSIONS

We have been able to identify and quantify the length of the contact line between wetting, non-wetting and solid phases during drainage and imbibition processes in different models for porous media using a level set based method (LSMPQS). In addition to computer generated models of sediments we also tested the contact line calculation in model geometries extracted from high resolution images of real sediments and sedimentary rocks.

The samples analyzed through high resolution images were columns of glass beads of different hydrophobicity, Fontainebleau sandstone and sucrosic dolomite samples. Besides simulating drainage and imbibition in these media to estimate contact lines, we also extracted the contact lines from high resolution images of wet porous media, at their drainage or imbibition endpoints. These are the first estimates of the contact line length in realistic porous systems to date.

The contact line length was normalized in order to provide an intrinsic quantity and facilitate comparison of systems of different size and geometry. The normalized specific contact line length is remarkably similar for drainage displacements in sphere packs and rocks. However, while no hysteresis was observed for imbibition in sphere packs, the contact line lengths for imbibition displacements in rocks were significantly large than the lengths for drainage.

The main factor affecting the computation accuracy of the contact line length is the image resolution or voxel size for the simulation. In unconsolidated systems (sphere packs), most of the contact line at small wetting phase saturations exists in pendular rings between spheres in point contact or having small gaps between them, and a fine resolution is necessary to distinguish the twin circles of contact lines associated with the pendular rings. Our analysis suggests that the contact line associated with pendular rings is the one that dominate drainage and imbibition process in sphere packs.

For the dolomite and sandstone cases, the high resolution of the sample images allowed the identification of water films, which were accounted as contact lines because of their thin voxel count. In this case, the comparison of the level set method simulation and result from the images give a corrected contact line estimate as well as an estimate of the amount of water films.

Our algorithm applied to LSMPQS simulations of drainage and imbibition passes several validation tests: it predicts lengths smaller than an upper bound obtained by independent calculation (for sphere packs), it is consistent with observations in glass bead packs, and it is consistent with observations in real rocks. Therefore we conclude that our calculated lengths are reasonably accurate.

Knowledge of the contact line lengths is useful for investigating trapping of colloids during transport in the unsaturated zone of sediments (shallow aquifers) or in hydrocarbon reservoirs (oil/water or gas/water). In Chapter 5 we used contact line length calculations in sphere packs to estimate trapping of colloids in unsaturated columns of glass beads. The energy associated to contact lines is also a factor to consider in the theories of thermodynamics of multiphase flow.

Chapter 4: Enhanced Migration of Surface-Treated Nanoparticles in Sedimentary Rocks

Engineered nanoparticles have properties potentially useful for certain oil recovery processes and formation evaluation. Nanoparticles are small enough to pass through pore throats in typical reservoirs and are not affected by straining, but they nevertheless can be retained by the rock. The ability to predict retention with distance traveled, and to predict the effect of different surface treatments on retention, is essential for developing field applications of such particles.

All the experimental work shown in this chapter was performed by Matthew Roberts and Haiyang Yu, graduate students at The University of Texas at Austin. Concentrated (up to ~20 wt%) aqueous suspensions of surface-treated silica nanoparticles (D = 5 nm and 20 nm) were injected into sedimentary rocks of different lithologies and permeabilities (10^{-14} to 10^{-12} m^2). The particles generally undergo little ultimate retention, nearly all being eluted by a lengthy postflush. Nevertheless the nanoparticles do not propagate as classical non-retained solutes or particles (e.g. conservative tracers). Effluent nanoparticle concentration histories show breakthroughs later than 1 PV injected plateau concentrations less than the injected value, and long tails. Longer elution times occur in samples with greater specific surface area. This set of observations is consistent with weak, reversible attachment of particles to pore walls. Such attachment is predicted by DLVO theory for very small particles when van der Waals attraction is the dominant force. This is the situation in our experiments, as the nanoparticles carry virtually no surface charge due to their surface coating.

Compared to viscosities measured on bulk suspensions, the apparent viscosities of suspensions flowing through sedimentary rocks are significantly smaller. Bulk phase

viscosities show little or no dependence on shear rate, and all experiments involved single-phase flow in water-wet samples. The simplest explanation for these observations is that a moderately thick layer (several hundred nm) of water depleted of particles exists at the pore walls. The mechanism for depletion of nanoparticles is presumably analogous to the mechanism for depletion of colloidal particles near rough confining surfaces.

4.1. INTRODUCTION

A recent surge of interest on possible use of nanotechnology to help locate bypassed oil and improve oil recovery raises a crucial question: Whatever ingenious nano-sensors or highly effective nano-EOR agents are developed is it possible to deliver them to where the oil exists deep in the reservoir? Nano-sized devices and agents will be solid aggregates, and the transport of colloidal dispersions (length scale between 100 nm and 10,000 nm) in reservoir rock is known to be very difficult. (We use the prefix "nano" to indicate length scale between 1 and 100 nm, and hereafter we refer to all such objects with the generic term "nanoparticles.") Clearly transportability is a prerequisite for any nanoparticles for reservoir applications.

Characterization of transport in reservoir rock has two major components: the nanoparticle retention and the mobility of the nanoparticle dispersion. The former quantifies the fraction of injected nanoparticles that survive and reach the target zone. The latter defines the operating conditions (*e.g.*, injection pressure and/or flow rate) to bring the injected nanoparticles through the desired pathway and time to the target location.

While the transport of engineered nanoparticles in reservoir rock for oil recovery applications has been little studied to date, extensive research has been and is being carried out by environmental engineers to investigate the impact of nanoparticles

unintentionally introduced into the subsurface alluvial zones and soils (see Brant *et al*., 2007; Bradford and Torkzaban, 2007 for review of recent literature). Direct application of those research findings to predict transport in the reservoir rock is, however, difficult for several reasons. First, the average permeability of reservoir rock is generally much smaller than that of the soil samples, and the surface charge states of the reservoir rock may also be quite different (Buffle 1990; Kaya and Yukselen 2005; Choi 2007). The nanoparticle retention mechanisms may therefore be quite different from those applicable for the above environmental studies. Second, in the above studies, only very dilute dispersions were employed, so that the mobility of the dispersion was not a concern. For the oil recovery applications, relatively large concentrations of the nanoparticle dispersions may be employed, and their mobility in the reservoir rock needs to be properly characterized for accurate prediction of their transport. Third, most of the nanoparticles studied for the environmental impacts tend to aggregate, generally forming particles with effective sizes in the range of colloids. In contrast, engineered nanoparticles for oilfield applications will have surface coatings to ensure that they stay individually dispersed in the injected fluid without aggregation, so that they can be transported through porous media easily.

4.1.1. Nanoparticle Retention in Porous Media.

In characterizing the retention of engineered nanoparticles for the environmental impact studies, researchers employed the mechanisms pertinent to colloidal particles, *i.e*., the clean-bed filtration theory (Elimelech *et al.*, 1995; Tufenkji and Elimelech, 2004; Bradford *et al.*, 2003; Wang *et al.*, 2008a; Wang *et al.*, 2008b; Li *et al.*, 2008) and its extensions, in which nanoparticle deposition is described as the particle transport to the vicinity of the soil grain surface followed by attachment. This is appropriate because, as

described above, the aggregates of nanoparticles rather than the individual nanoparticles have been studied. From such filtration theory, the attachment efficiency is calculated, and accordingly the retention. Interaction energies are calculated using DLVO theory for the case of a flat plate (surface of porous medium) and a sphere (nanoparticle) (Guzman *et al.*, 2006; Hoek and Agarwal 2006). In such model applications, the governing force is the van der Waals attractive force. As we discuss more in detail later with our own results, the attachment due to the van der Waals attraction appears to be also important for the surface-treated nanoparticles that do not aggregate.

To properly understand the retention of nanoparticles in reservoir rock whose surface generally carries ionic charges, the electrostatic forces need to be fully understood. The electrostatic forces between the nanoparticles, and between the nanoparticle and the rock surface, govern the conditions under which nanoparticles aggregate or attach to the reservoir rock surfaces. Electrostatic forces are highly dependent on ionic strength. High ionic strengths reduce or compress the size of the electrical double layer of particles. This decreases the repulsive forces between particles. Because the repulsive forces prevent aggregation of particles and particle attachment to surfaces, large ionic strengths therefore allow the attractive van der Waals forces to dominate (Saleh *et al*., 2008). In nanoparticle suspensions, particles tend to aggregate more quickly at higher ionic strengths (Kallay and Žalac 2002; Kobayashi *et al*., 2005). Therefore, in saline environments, like in many oil reservoirs, the deposition and attachment of nanoparticles is expected to increase. Interestingly, however, this expected dependence on ionic strength was not observed in retention experiments with large colloidal particles. For example, Lazouskaya *et al.* (2006) and Lazouskaya and Jin (2008) showed that non-DLVO forces dominate retention in unsaturated media.

pH values near the point of zero charge of the nanoparticles or the surfaces also yield a greater aggregation/attachment. Therefore, electrostatic interactions are also reduced at pH close to PZC. Because of the importance of DLVO interactions when interpreting laboratory retention measurements, it is essential to know the charge states of pore walls and nanoparticle surface at the experimental conditions. Also, the methods and conditions used to prepare the nanoparticles suspensions can strongly influence the aggregation and retention behavior, since characteristics of the nanoparticle such as surface charge or size can be affected (Espinasse *et al*., 2007).

Additional information about the mechanism of retention of small particles in porous media and the intervening forces can be found in Appendix A.

4.1.2. Nanoparticle Mobility in Porous Media.

For potential EOR applications, nanoparticle concentration in the injection fluids may be relatively high, and the mobility of the fluid must be considered. A number of researchers studied the rheology of concentrated nanoparticles (*e.g*., Kinloch *et al*., 2002; Tseng and Wu, 2002; Ding and Wen, 2005). Research is also being carried out to understand the unusual flow behaviors in nano-scale channels (see Quirke, 2006; Eijkel and van den Berg, 2005; Schoch *et al*., 2008 for review of recent literature).

Flow of colloidal particles and macromolecules in porous media can exhibit enhanced transport of the particles, for example, the early arrival (before one pore volume injected) of concentrations greater than injected. For polymer macromolecules, enhanced transport is mainly attributed to the inability of large polymer molecules to access small pores. This is commonly quantified in terms of the "inaccessible pore volume" (Sorbie, 1991). The polymer's inaccessible pore volume is also partially attributed to a depleted layer near the pore wall. Similarly, for flow of concentrated

colloidal particles in pipes and confined channels, the shear-induced migration of the particles and the formation of a thin depletion layer near the solid wall is well known (Russell *et al*., 1991; Phillips *et al*., 1992; Buyevich and Kapbsov, 1999).

The enhanced migration of concentrated nanoparticle dispersions has also been observed (*e.g*., Ding and Wen, 2005). Because the nanoparticles are solid and have some colloidal character, their enhanced migration may be at least partially attributed to the shear-induced migration. Due to the nanometer-scale diameter of the particles, however, the Brownian effect will be dominant with some slippage of the nanoparticle dispersion near the solid boundary, which will result in the enhanced transport of the nanoparticles. This leads to another manifestation of enhanced transport, namely a smaller pressure gradient is required for flow of the dispersion than for flow of an ordinary fluid with the same nominal viscosity. This phenomenon is variously described as "friction reduction", "permeability enhancement" or "apparent viscosity reduction", depending on context. The theoretical approach to this phenomenon usually involves relaxing the classical no-slip boundary condition. A reasonable slip boundary condition that has been employed for the nano-scale flow behavior is based on the Maxwell's theory of slip (Sokhan *et al*., 2001; Quirke, 2006). The model assumes that a particle, colliding with the wall, is thermalized by the wall with some probability α, or reflected with probability $(1- \alpha)$.

A slip velocity model has also been developed for adsorption of hydrophobic SiO_2 nanoparticles on porous walls (Gu and Di, 2007). The slip effect in the experiments described is caused by the formation of a hydrophobic layer in the walls, instead of a hydrated layer, which greatly enhances the flow velocity of an aqueous phase. An analytical model was developed by assuming that the slippage at the pore wall was responsible for the increase in effective permeability after the injection of the nanoparticle solution.

The slip length can be interpreted physically by the accumulation of low viscosity fluid at the interface between solid and liquid (Sanchez-Reyes and Archer, 2003). If the thickness of the depleted layer is very small when compared with the size of the flow channel, it will create the effect of the fluid slipping over the solid surface. We describe below an explicit model of the effect of the depletion layer and interpret the enhanced migration observed in our experiments with each model (slip length and depletion layer.)

Our experiments, described in the next section, complement the works discussed above in three main aspects. First, several experiments were performed in sedimentary rocks (Texas Cream limestone and Berea and Boise sandstone cores) instead of soil samples. Second, the nanoparticles were surface treated in order to prevent aggregation. Lastly, the concentration of nanoparticles in suspension was considerably larger than those used in previous experiments. Thus, these experiments provide new insight into the transportability of engineered nanoparticles in the oil reservoir environment. Unusual results have been obtained for nanoparticle retention and for the apparent viscosity during flow in porous media. The behavior has not been reported in the literature, and the possible reasons for the new observations are discussed in the "Discussions on the Mechanisms of Retention and Apparent Viscosity" section.

4.2. EXPERIMENTS ON TRANSPORT OF SILICA NANOPARTICLES

All the experimental work shown in this section was performed by Matthew Roberts and Haiyang Yu, graduate students at The University of Texas at Austin, in the summer of 2009.

4.2.1. Materials

Silica nanoparticles from 3M® (St. Paul, MN) with a nominal diameter of 5 nm or 20 nm and a polymer coating that gives them a total size of ~10 nm or ~25 nm, respectively, were used as received or were diluted to a target concentration as described below. The coating consists of polyethylene glycol (with about 7 EG units), which is covalently attached to the silica surface through silicon-oxygen-silicon bonds. The coating allows the individual nanoparticles to stay dispersed in water without aggregating. Since the non-ionic coating will essentially shield any ionic charges which were originally on the silica surface, the stability of the dispersion is believed to arise from the steric repulsion due to the configurational entropy between the PEG chains on the neighboring particle surfaces. The particles were received as a concentrated aqueous dispersion (18.64 wt% loading of 5 nm particles in 0.57M NaCl, 42 wt% loading of 20 nm particles.)

The viscosity of the nanoparticle dispersions was measured as a function of the nanoparticle concentration and the shear rate, as shown in Figures 4.1 and 4.2 respectively. The steady-state viscosity was measured using the TA Instruments' Advanced Rheometric Expansion System (ARES) LS-1 rheometer. Remarkably, even at large particle loadings, the viscosity was not more than 3 cp. Also, unlike typical concentrated colloidal dispersions, the viscosity showed little or no shear-rate dependence in the range of interest (shear rates greater than 10 sec^{-1}).

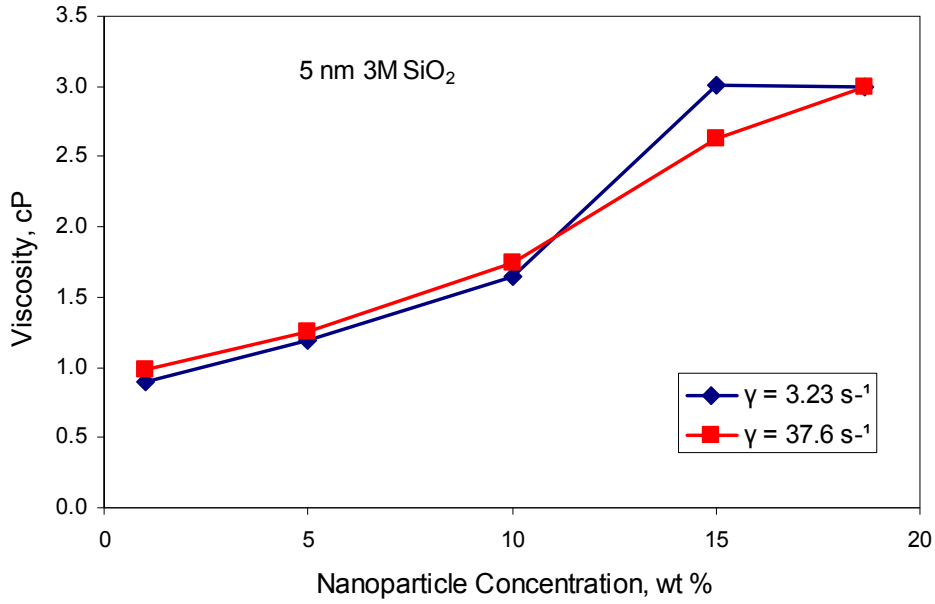

Figure 4.1: Viscosity of bulk phase dispersion of 5 nm silica nanoparticles treated with polyethylene glycol.

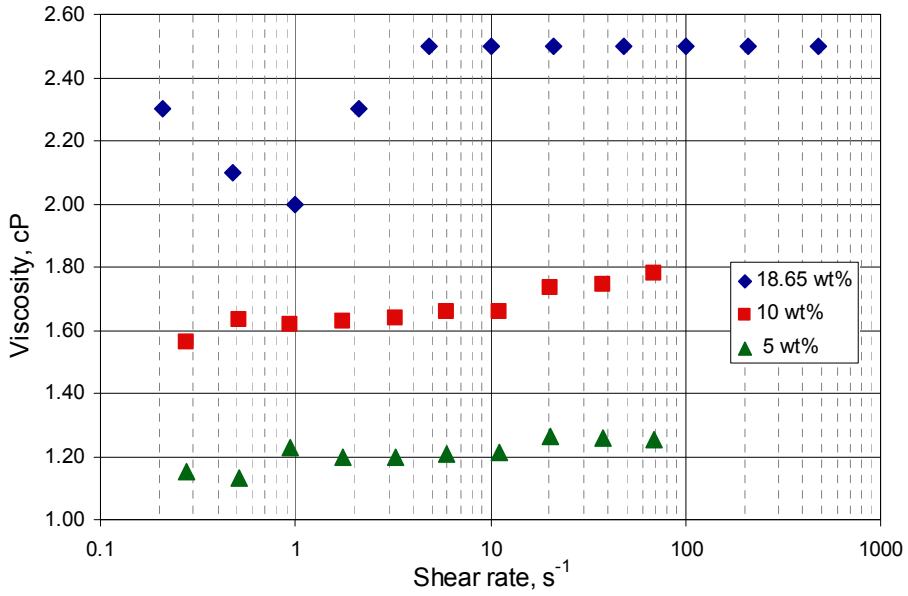

Figure 4.2: Dependence of viscosity with shear rate for aqueous dispersions of surface-treated 5 nm SiO_2 particles.

Core plugs 2.54 cm in diameter and 7.62 cm in length were cut from large blocks of Texas Cream limestone, Berea sandstone and Boise sandstone. Each core was vacuum saturated with deionized water (limestone) or 3 wt% NaCl brine (sandstone). The measured porosity and permeability of each plug are given in Table 4.1 at the end of this section. Typical pore throat sizes are also given in Table 4.1, taken from mercury porosimetry on a representative sample from each block. The specific surface areas of representative samples of limestone, Berea and Boise are 10, 6.2 and 3.0 m^2/g, respectively.

4.2.2. Experimental Method

The experimental set-up for the corefloods is schematically shown in Figure 4.3. A summary of the experimental conditions can be found in Table 4.1.

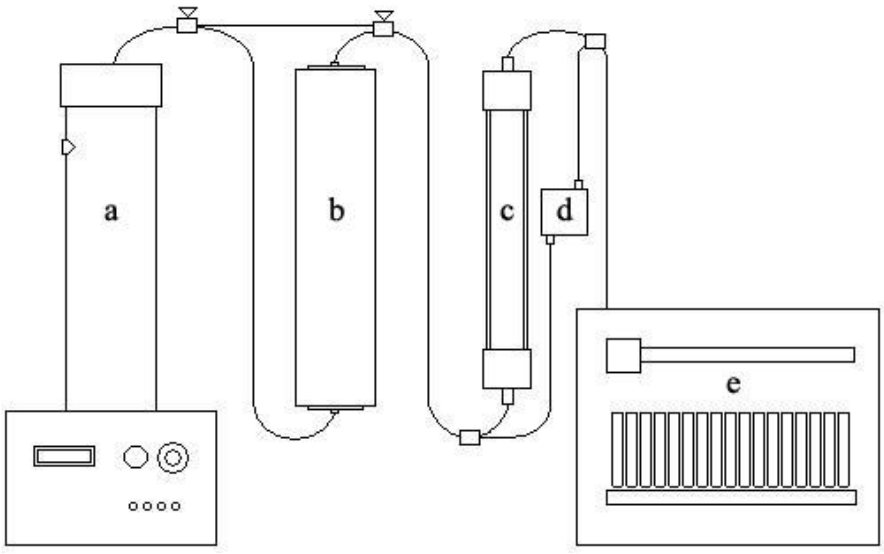

Figure 4.3: Schematic of coreflood set-up; (a) syringe pump, (b) accumulator (contains nanoparticle dispersion on downstream side of internal piston), (c) coreholder, (d) transducer, and (e) sample collector.

The coreflood setup consists of a Hassler core holder (which confines the core within a cylindrical sleeve, ensuring flow occurs only through the core), an injection pump, a pressure transducer (measuring difference between inlet and outlet pressure), and a fraction collector for effluent samples. The pump injects fluid into an accumulator containing a movable piston with the nanoparticle dispersion on the other side. In this manner the dispersion is displaced into the core without contacting the internal workings of the pump. Two corefloods in Texas Cream limestone cores (low permeabilities), one coreflood in Berea sandstone core (moderate permeability), and four corefloods in Boise sandstone cores (high permeabilities) were performed. A prescribed volume of suspension was injected into the core, then displaced using deionized water in the limestone cores and saline solution in the sandstone cores. A second volume of suspension was injected into the second limestone core.

Pressure drop across the core was monitored continuously with a data logger. The flow rate was checked by weighing effluent samples. The nanoparticles are too small to detect with the dynamic light scattering. Because the dispersions are optically almost clear, the refractive index measurement was mainly employed to determine the nanoparticle concentration in the coreflood effluent samples. Electrical conductivity also varies with nanoparticle concentration, and in early experiments conductivity of samples of the effluent was measured. Calibration curves of nanoparticle concentration *vs*. refractive index were prepared with known dilutions of the dispersion as received, using deionized water or 3 wt% NaCl brine. Figure 4.4 shows the calibration curves.

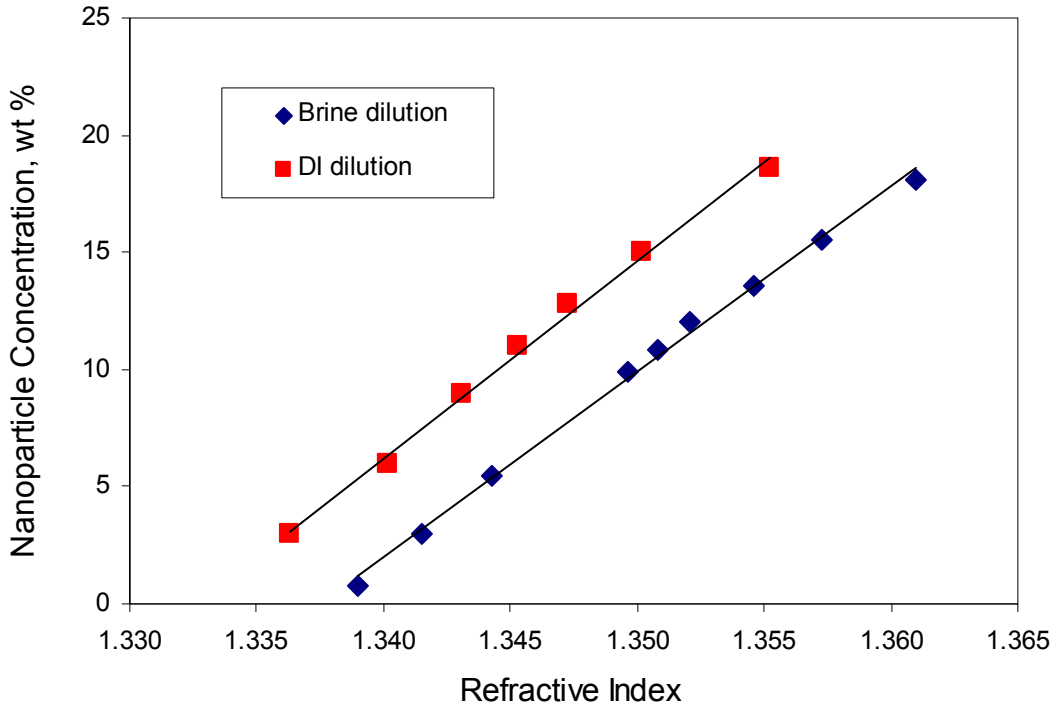

Figure 4.4: Calibration curves to obtain the effluent nanoparticle concentration from the refractive index. Salinity of brine is 3 wt%.

4.2.3. Experimental Results

Texas Cream Limestone Coreflood #1

The first core flood was perfumed in a limestone having a permeability of 15 mD. Three pore volumes (30 mL) of nanoparticle dispersion (18.65 wt%) were injected at a flow rate of 2mL/min. The nanoparticle concentration in the effluent samples increased for the first 3 pore volumes of injection, Figure 4.5, peaking at 70% of the injected concentration. A secondary peak in effluent concentration was observed after 6 pore volumes. The elution of this peak followed an 18 hour cessation of flow. Neither peak

would be expected if the nanoparticles had no interaction with the core. Yet the cumulative recovery of particles from the core during the postflush with deionized water is 96%. The eventual recovery of nearly all the injected particles during the postflush suggests the particle/rock interaction is reversible.

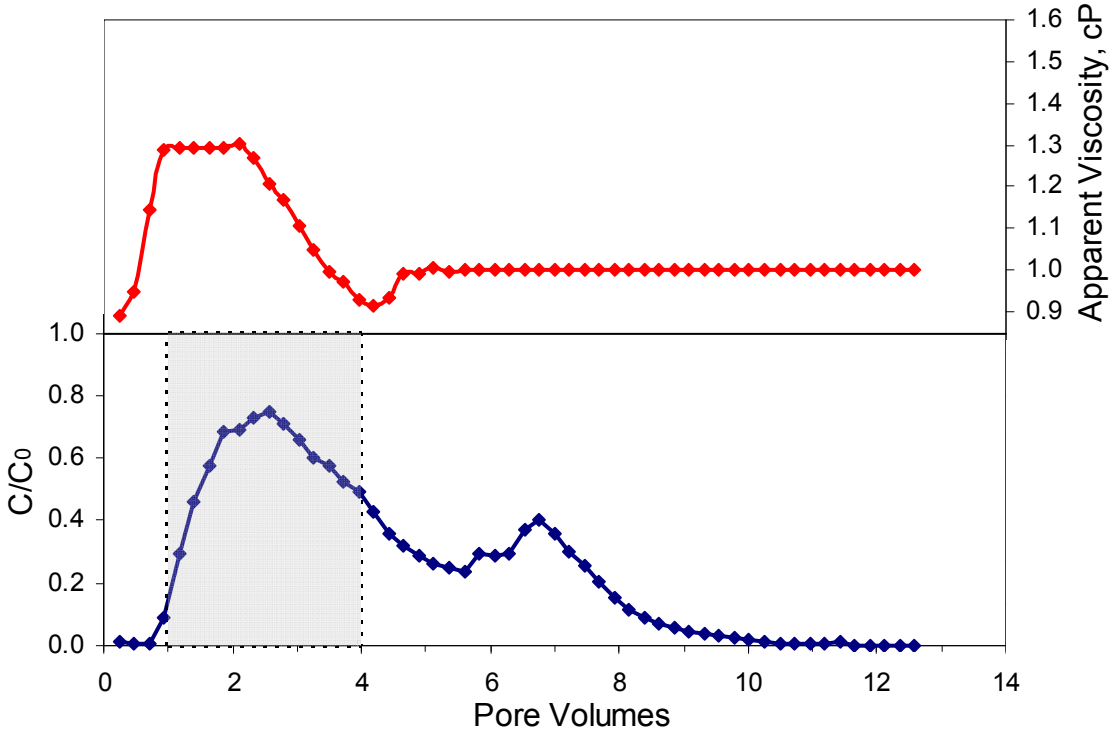

Figure 4.5: Histories of effluent concentration of nanoparticles normalized by injected concentration (lower panel) and of apparent viscosity (upper panel) for the limestone coreflood #1. Three pore volumes of an aqueous dispersion of nanoparticles (18.65 wt%) were injected, followed by deionized water. Flow was halted for 18 h after a total of six pore volumes were injected, then resumed at original rate. The shaded area indicates the concentration history for ideal piston-like transport.

We discuss possible explanations for this unusual effluent concentration history in the next section. The practical implication of this result is profound, however: a highly concentrated suspension of surface-treated nanoparticles particles was able to migrate through a low permeability sedimentary rock.

The pressure drop across the core increased as the nanoparticle dispersion was injected into the core. After the bulk of the nanoparticle dispersion had been displaced from the core, the pressure drop decreased to the value corresponding to water injection. There was no evidence of alteration of the core permeability and thus the variation in pressure drop is the consequence of variation of apparent viscosity of the fluids (injected suspension, deionized water) in the core. As shown in the upper panel of Figure 4.5, the apparent viscosity of the nanoparticle dispersion as it traveled through the core was 1.3 cp, about half the value measured using the rheometer. This is also a remarkable result: not only did the highly concentrated dispersion transport through the core, it did so with half the resistance to flow expected on the basis of its bulk properties. We discuss this observation in greater depth in the next section. Here we point out that the decrease cannot be attributed solely to the reduced particle concentrations in the effluent. The 1.3 cP apparent viscosity corresponds to the bulk dispersion viscosity at a particle concentration of 6 wt%, much smaller than the effluent concentrations between 1 and 4 PV. Table 4.1 and Figure 4.12 at the end of this section summarize the apparent viscosity for all the corefloods.

Texas Cream Limestone Coreflood #2

The second core flood was carried out in a new core, this one having permeability 10 mD, at the same experimental conditions as coreflood #1. Two slugs of nanoparticle

dispersion were injected. The first slug confirmed that the secondary peak in effluent concentration observed in coreflood #1 (cf Figure 4.5 between 6 and 8 PV) was due to the temporary cessation of flow. The effluent concentration declined steadily during the deionized water postflush after the first slug, Figure 4.6. Only 2% of the particles injected in the first slug were retained. The pressure measurements confirmed the reduction in apparent viscosity of the nanoparticle suspension as it flows through the rock, in this case yielding an apparent viscosity of 1.21 cP (cf. Table 4.1, Figure 4.12).

After the postflush, another two pore volumes of nanoparticle dispersion were injected. The effluent nanoparticle concentration versus the injected pore volume is also shown in Figure 4.6, after the post-flush of the first slug. The maximum effluent concentration after the second slug is less than half of the injected concentration. The peak value is less than the peak observed in the first slug or in coreflood #1. It is unclear whether the smaller injected volume of the second slug (2 PV) or the postflush contributed to this behavior. In other respects the effluent history from the second slug is qualitatively very similar to that of the first slug. But only 62% of the injected particles were recovered from the second slug, much less than from coreflood #1 or the first slug. From the pressure variation measured during this coreflood we estimated an apparent viscosity of 1.10 cP, Table 4.1. We observed a gradual decrease in pressure drop during the post-flush interval (similar to coreflood #1, the upper panel in Figure 4.5).

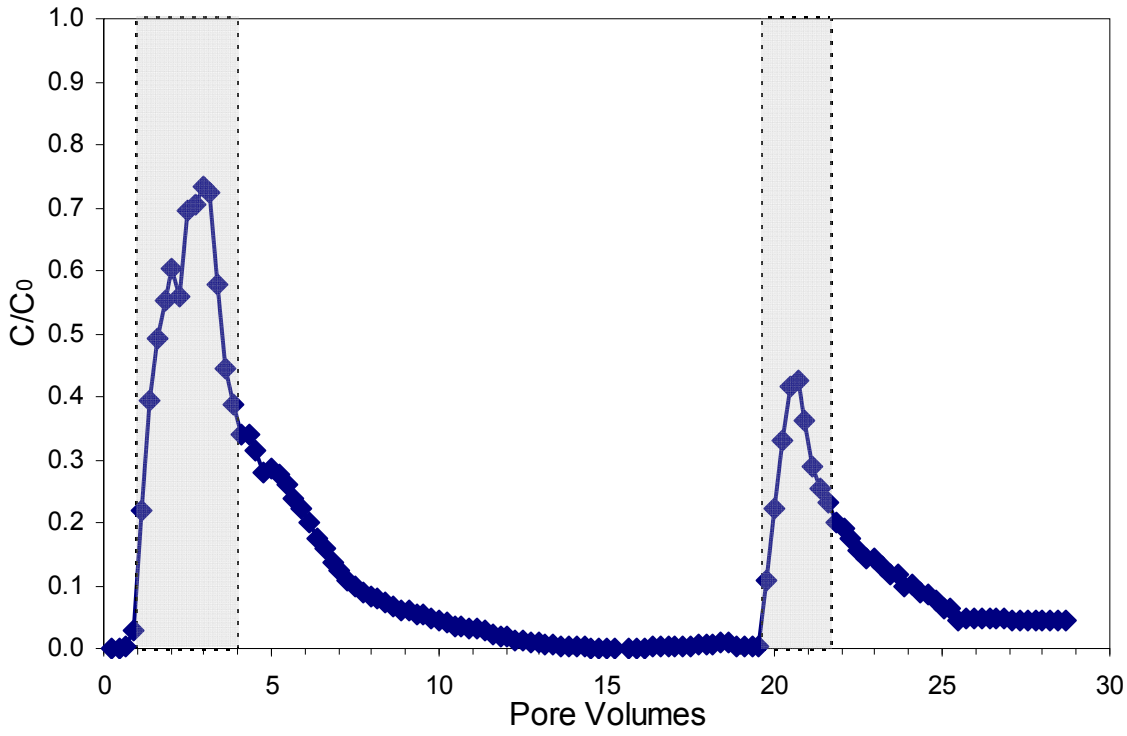

Figure 4.6: Normalized effluent concentration of nanoparticles for the limestone coreflood #2. Three pore volumes of an aqueous dispersion of nanoparticles (18.65 wt%) were injected first, followed by 15 pore volumes of deionized water. After that, two pore volumes of the same nanoparticle suspension were injected, followed by deionized water.

Berea Sandstone Coreflood

For the Berea sandstone coreflood, 3.46 pore volumes (29.76 mL) of nanoparticle dispersion (18.65 wt%) were injected at a flow rate of 1 mL/min. The effluent concentration history, Figure 4.7, shows a slight delay in breakthrough, with the 50% normalized concentration arriving at about 1.3 PV, similar to the Texas Cream limestone corefloods. In contrast to the limestone, however, the plateau effluent concentration is greater than 90% of the injected concentration, and the concentration tail during postflush

is relatively short. A mass balance shows that 7% of the injected nanoparticles were retained after a post-flush of 5 pore volumes. The pressure measurements again confirmed the reduction in apparent viscosity of the nanoparticle suspension as it flows through the rock: the injected dispersion exhibits a viscosity of 2.5 cP in the rheometer but only 1.6 cP in the core (cf. Table 4.1, Figure 4.12).

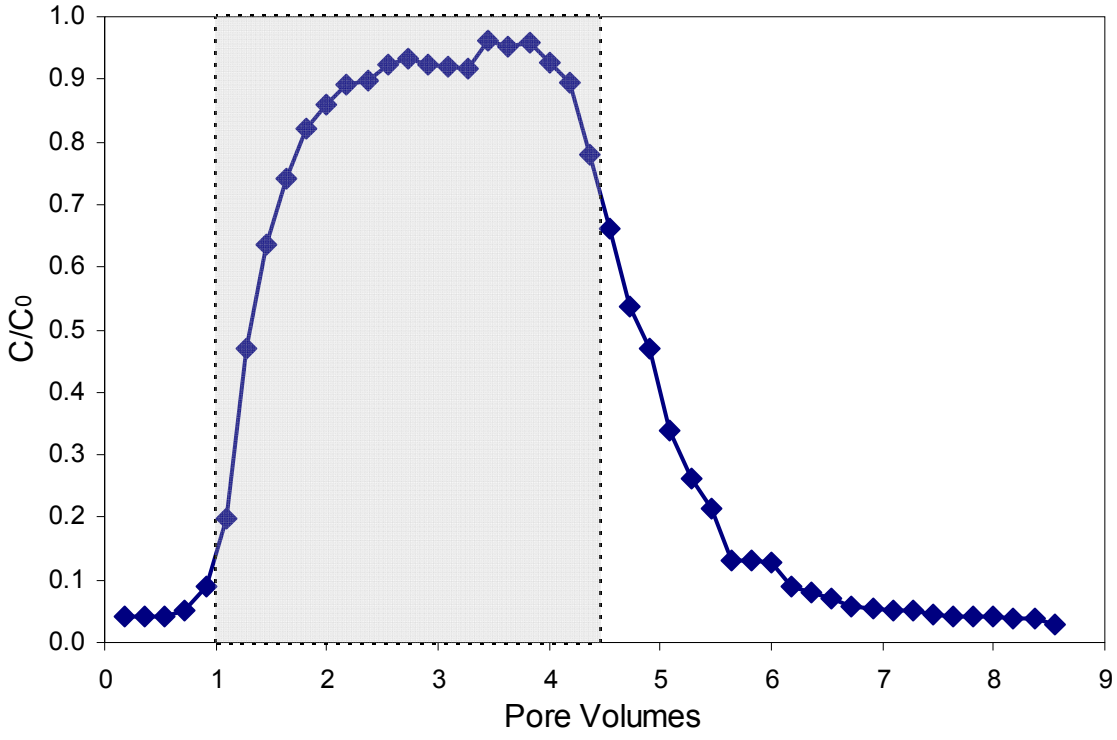

Figure 4.7: Effluent concentration of nanoparticles vs. pore volume for the Berea sandstone. 3.46 pore volumes of concentration nanoparticle suspension (18.65 wt%) in 3 wt% NaCl brine were injected, followed by the same brine.

Boise Sandstone Coreflood #1

For the first Boise sandstone coreflood (921 mD), 3.18 pore volumes (33.87 mL) of nanoparticle dispersion (18.65 wt%) were injected at a flow rate of 4 ml/min. The effluent concentration history, Figure 4.8, exhibits a longer delay than the Berea coreflood, but reaches a peak of 94% of the injected concentration. The retention of silica nanoparticles in this coreflood was 9% after postflush. We also observed an apparent viscosity (2.1 cP, Table 4.1 and Figure 4.12) smaller than the value for the bulk dispersion.

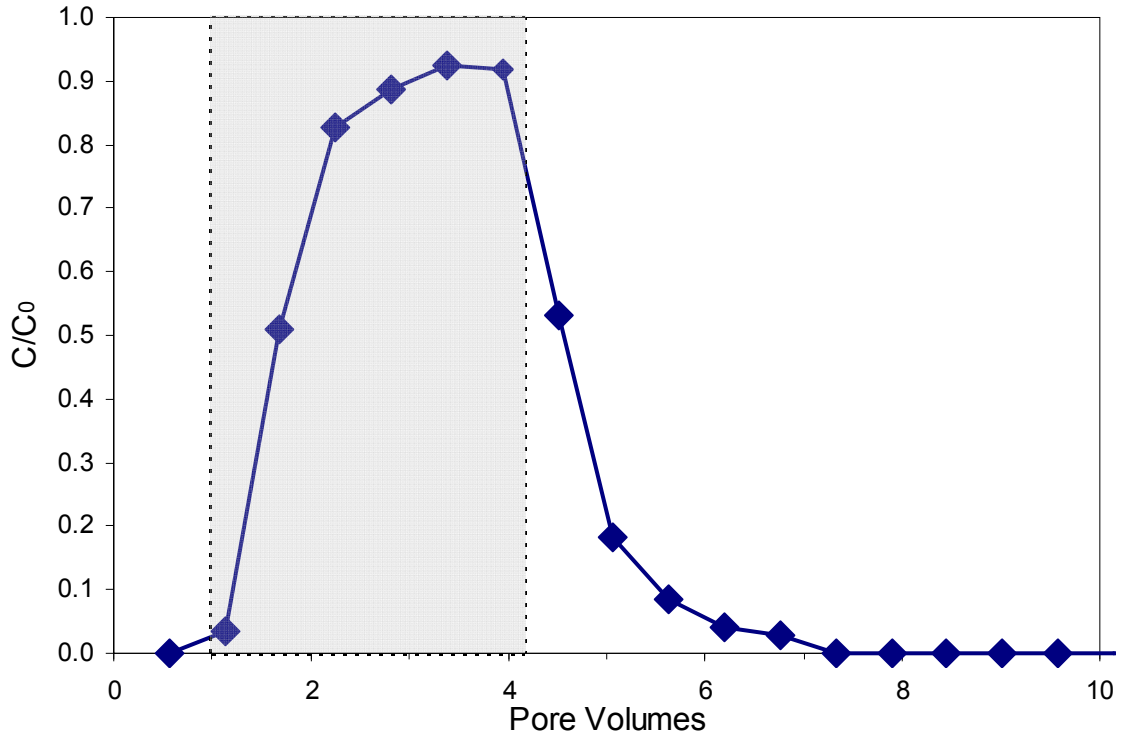

Figure 4.8: Effluent concentration of nanoparticles vs. pore volume for the Boise sandstone coreflood #1. 3.18 pore volumes of concentration nanoparticle suspension (18.65 wt%) in 3 wt% NaCl brine were injected, followed by the same brine.

Boise Sandstone Coreflood #2

The second Boise coreflood was intended to test the effect of flow rate. The permeability of the second Boise core plug (494 mD) is about half that of the first plug. We injected 2.66 pore volumes (27.93 mL) of 18.65 wt% nanoparticle suspension at 1.1 mL/min. The effluent concentration history, Figure 4.9, is essentially identical to that of Boise coreflood #1. Slightly more particles (9.4%) were retained in this experiment. As in the previous corefloods, the apparent viscosity of the nanoparticle dispersion during flow is smaller than that of the bulk dispersion. The value of 1.65 cP is smaller than observed in Boise coreflood #1. While this coreflood has a shear rate four times smaller than Boise coreflood #1, the shear-rate dependence of bulk suspension viscosity is weak. Thus the smaller apparent viscosity is likely to be a consequence of the smaller permeability of this core.

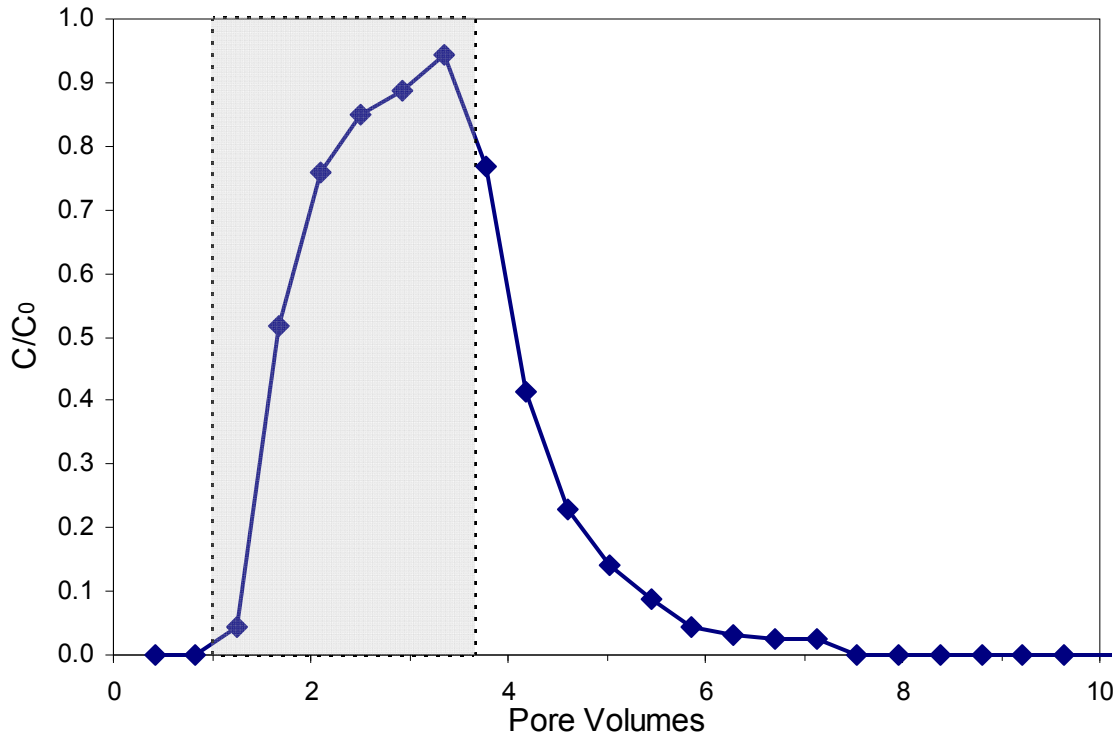

Figure 4.9: Effluent concentration of nanoparticles vs. pore volume for the Boise sandstone coreflood #2. 2.66 pore volumes of concentration nanoparticle suspension (18.65 wt%) in 3 wt% NaCl brine were injected at a low flow rate, followed by the same brine.

Boise Sandstone Coreflood #3

The third Boise coreflood was intended to test the effect of nanoparticle concentration. We injected 3.47 pore volumes (38.45 mL) of a 5 wt % nanoparticle suspension at a flow rate of 4 mL/min into a Boise core of permeability 867 mD. The effluent concentration history, Figure 4.10, is almost identical to the other Boise corefloods. The total recovery of injected particles after 7 pore volumes of post-flush is 91%, the same observed in Boise coreflood #2 using a more concentrated solution and a

smaller permeability core. The apparent viscosity from pressure measurements is 1.05 cP, while the bulk dispersion has a viscosity of 1.25 cP (Figures 4.1 and 4.2).

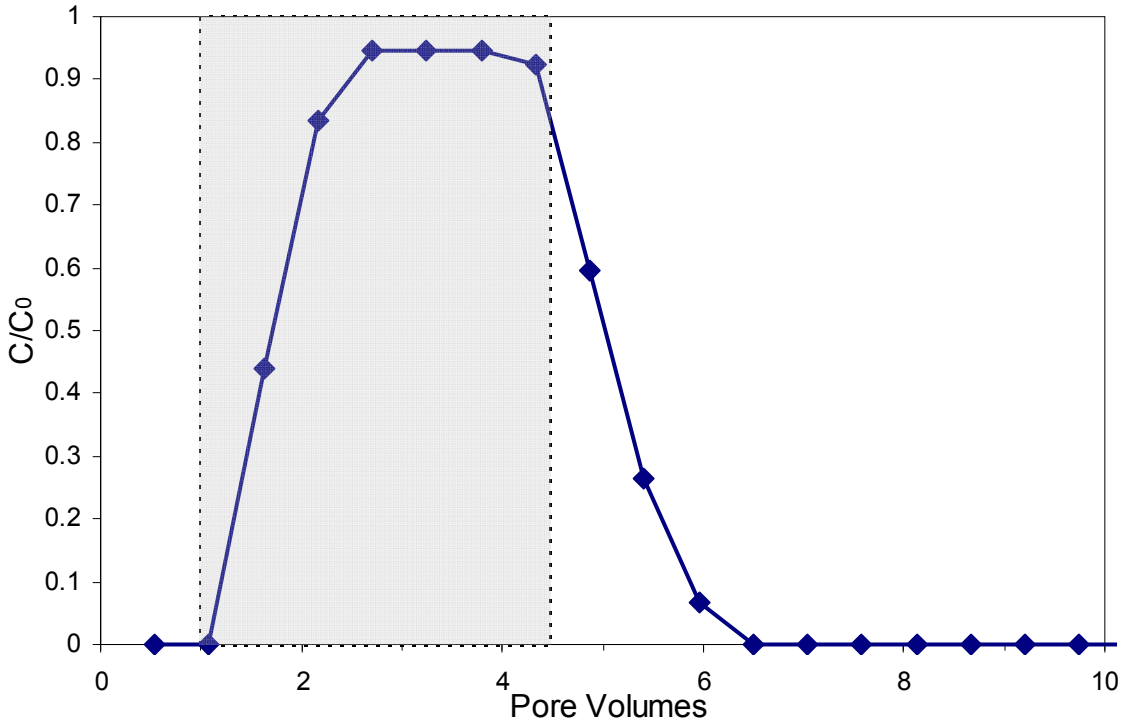

Figure 4.10: Effluent concentration of nanoparticles vs. pore volume for the Boise sandstone coreflood #3. 3.47 pore volumes of a lower concentration (5 wt%) nanoparticle dispersion in 3 wt% brine were injected followed by 7 pore volumes of the same brine.

Boise Sandstone Coreflood #4

The fourth Boise coreflood was intended to test the effect of nanoparticle size. We injected 2.89 pore volumes (31.65 mL) of 18.65 wt% suspension of 20 nm nanoparticles at a flow rate of 3.2 mL/min into a Boise core of permeability 421 mD. While the effluent concentration history, Figure 4.11, is very similar to the other Boise corefloods, 12% of

the injected particles were retained. From the pressure measurements we estimated an apparent viscosity is approximately 1.4 cP. The viscosity of the corresponding bulk solution is not available.

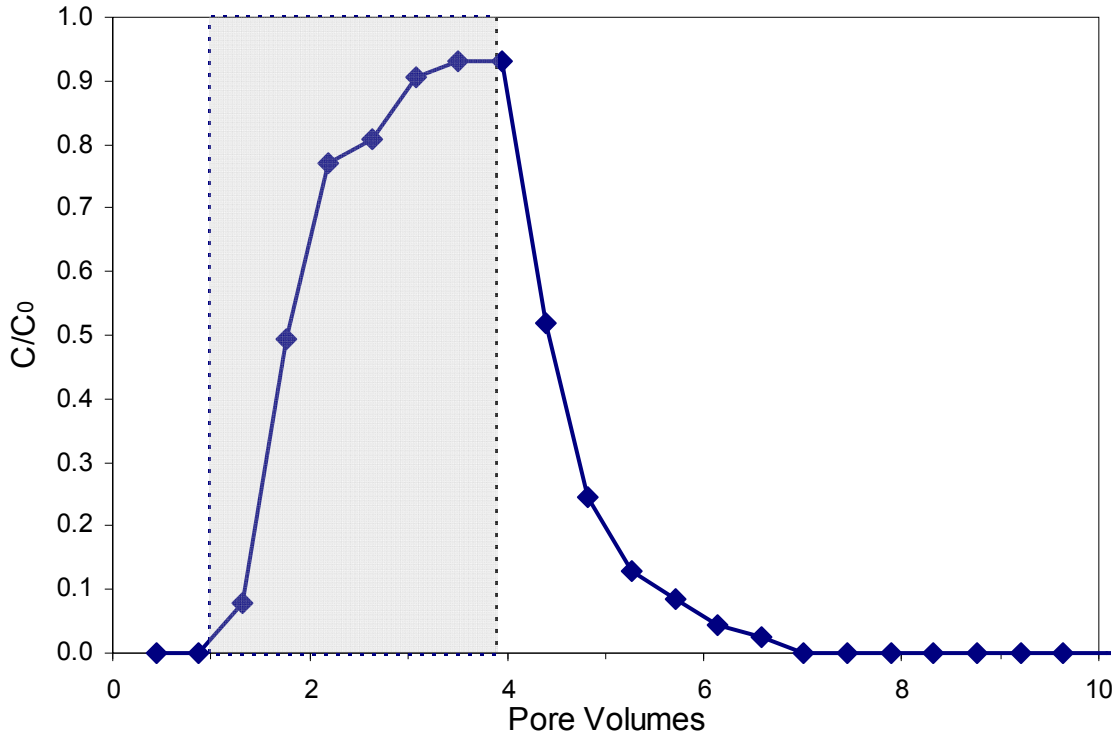

Figure 4.11: Effluent concentration of nanoparticles vs. pore volume for the Boise sandstone coreflood #4. 2.89 pore volumes of concentrated suspension (18.65 wt%) of larger nanoparticles (20 nm) in 3 wt% NaCl brine were injected, followed by 7 pore volumes of the same brine.

Table 4.1: Summary of corefloods conditions and results

Porous Medium	**Typical Throat Radius r_0 (μm)**	**k (mD)**	**ϕ**	**PV (mL)**	**Particle Size (nm)**	**C_0 (wt %)**	**q (mL/min)**	**PV injected**	**PV post-flush**	**Particle Recovery (%)**	**μ_n (cP)**	**γ (s^{-1})**
Texas Cream Limestone 1	2	15	0.29	11.2	5	18.65	2	3	9	96	1.30	526
Texas Cream Limestone 2a	2	10	0.22	8.6	5	18.65	2	3 (1st slug)	15	98	1.21	526
Texas Cream Limestone 2b	2	10	0.22	8.6	5	18.65	2	2 (2nd slug)	8	62	1.10	658
Berea Sandstone	6	136	0.22	8.6	5	18.64	1	3.46	5	93	1.60	100
Boise Sandstone 1	10	921	0.276	10.65	5	18.64	4	3.18	17	91.1	2.10	178
Boise Sandstone 2	10	494	0.272	10.5	5	18.64	1.1	2.66	11	90.6	1.65	53
Boise Sandstone 3	10	867	0.287	11.08	5	5	4	3.47	7	90.6	1.04	183
Boise Sandstone 4	10	421	0.284	10.95	20	18.64	3.2	2.89	7	88.1	1.40	148

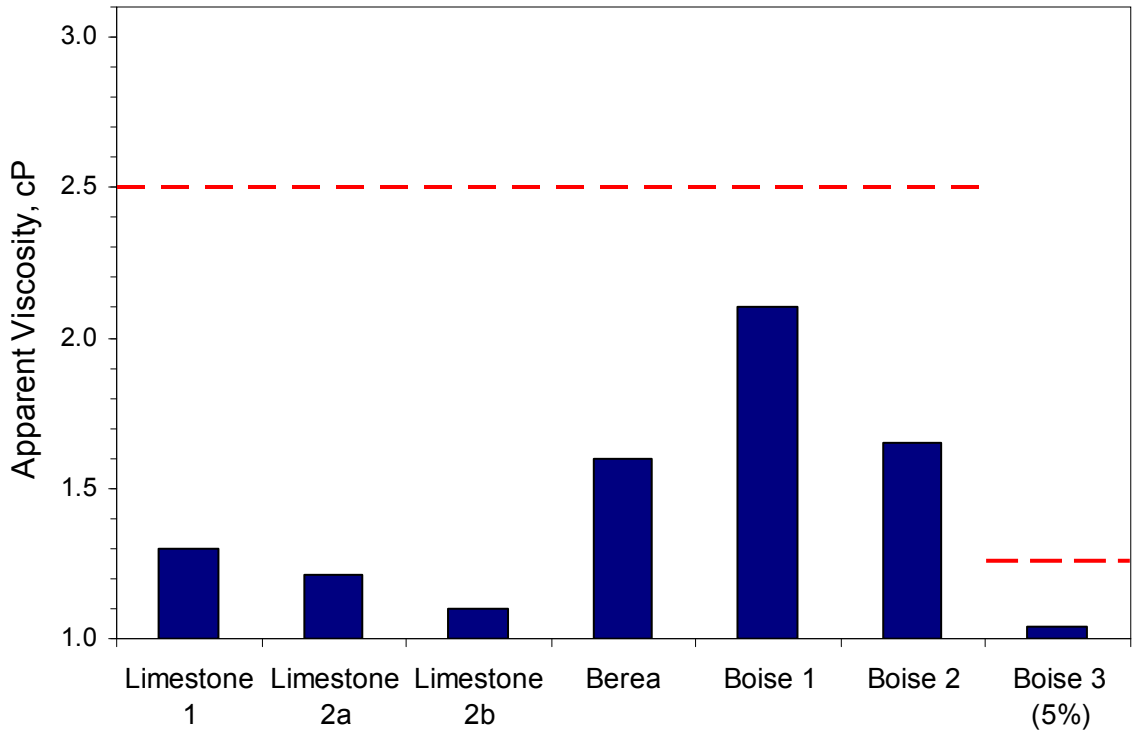

Figure 4.12: Apparent viscosities for the different core floods. The red line indicates the viscosity of the bulk solution injected into each core.

4.3. Discussions on the Mechanisms of Retention and Apparent Viscosity

4.3.1. Retention of the Surface-Modified Silica Nanoparticles.

The retention results obtained from the series of corefloods described above allow us to make some intriguing observations on the nanoparticle retention behavior. First, the overall retention (the fraction of injected particles remaining in the core after postflush) is usually small (between 1% and 10%) and does not depend on permeability. (The one example of large overall retention occurred when a second slug of nanoparticle dispersion was injected into a limestone core that retained a very small fraction of the particles in the

first slug.) The lack of dependence on permeability suggests that unlike colloidal particles, these particles do not undergo straining or filtration. This is not surprising considering the size (5 nm to 20 nm) of the particles is much smaller than the pore throats (> 1000 nm). On the other hand it is not obvious *a priori* that such large concentrations of rigid particles (approaching 20 wt %) would propagate through the cores.

Despite the small degree of overall retention, the effluent concentration histories differ substantially from the effluent history expected for a non-retained solute or particle. In the absence of interaction between the particle and the rock, and neglecting hydrodynamic dispersion, a slug of injected non-retained particles should elute as a square wave. This ideal behavior is depicted as the gray box in Figures 4.5 through 4.11: arrival of the injected concentration at 1 PV, a plateau concentration equal to the injected, and arrival of the postflush concentration at $1 + S$ PV, where S is the slug size in PV. Comparison of the observed and ideal effluent histories in Figures 4.5 through 4.11 shows three consistent characteristics for all corefloods: a small delay in arrival of the injected particles, a plateau smaller than the injected concentration, and a tail after $1 + S$ PV. The tail is asymmetric and thus not attributable only to hydrodynamic dispersion. These features suggest that significant attachment, or adsorption, of the nanoparticles occurs on the pore wall. The adsorption is however reversible (the postflush elutes almost all the injected particles) and in this regard is unlike the adsorption of polymer molecules, which is generally irreversible (Sorbie, 1991), and unlike the filtration of colloidal particles.

Another important observation is that the retentions in the sandstone and limestone cores are similar despite the fact that, at the near-neutral pH conditions, the surface charge of sandstone is negative and that of limestone is positive. Clearly electrostatic forces are not responsible for the retention. This is consistent with the fact

that the surface-modified silica nanoparticles essentially carry no surface charge. This suggests that the main mechanism for their reversible adsorption on the solid surface is the van der Waals attraction between the particle and the pore wall. This is similar to the retention mechanism for the colloidal particles that was adopted to explain the retention of the nanoparticle aggregates (Wang *et al.*, 2008a; Wang *et al.*, 2008b; Li *et al.*, 2008). One important difference between the retentions of colloidal particles and of the nanoparticles in our experiments appears to be that the nanoparticles have greater probability to detach from the solid surface due to their much smaller size and the relative importance of the Brownian motion.

We are thus led to consider the interaction of van der Waals attraction between very small particles and the pore walls, and the Brownian motion of the particles. The collision frequency between the flowing particles and the stationary pore wall is affected by Brownian motion, which becomes more important as the particle size decreases. The Brownian motion influences the efficiency of both the attachment of the particles to the pore wall and their transport through the porous media. For the particle size in our experiments, Brownian motion is more important for transport than for attachment. The Brownian motion of many particles is manifested as diffusion, which depends on the particle radius, r_p, according to the Stokes-Einstein equation, $\mathscr{D} = kT/6\pi\mu r_p$, where $\mathscr{D}$ is the Brownian diffusion coefficient, k is the Boltzmann constant, T is the absolute temperature in Kelvin, and μ is the viscosity of the surrounding fluid (van Oss, 2006). Thus, smaller particles have larger diffusion coefficients, which confers them larger mobility.

van der Waals interaction energy decays according to h^{-1}, where h is the separation distance between surfaces, as shown in the following equation for the interaction between a flat plate and a spherical particle: (Elimelech *et al.*, 1995):

$$U_{VDW} = - \frac{A_H d_p}{12h}\left[1 + \frac{h}{d_p + h} + \frac{2h}{d_p} \log\left(\frac{h}{d_p + h}\right)\right] \tag{4.1}$$

where U_{VDW} is the interaction energy in Joules, A_H is the effective Hamaker constant of the interacting media and d_p is the diameter of the particle. The absolute value of van der Waals energy decreases with particle size and also acts over a shorter range, as shown in Figure 4.13. For very small particles the van der Waals force is strong only at very short distances, less than 1 nm, and rapidly diminishes with distance. The electrostatic (repulsive) energy for the same conditions (not shown here) is generally orders of magnitude smaller than the van der Waals attractive force. Consequently, the total interaction energy, which is the sum of van der Waals and electrostatic energies, is almost always attractive, but it weakens as particle size decreases.

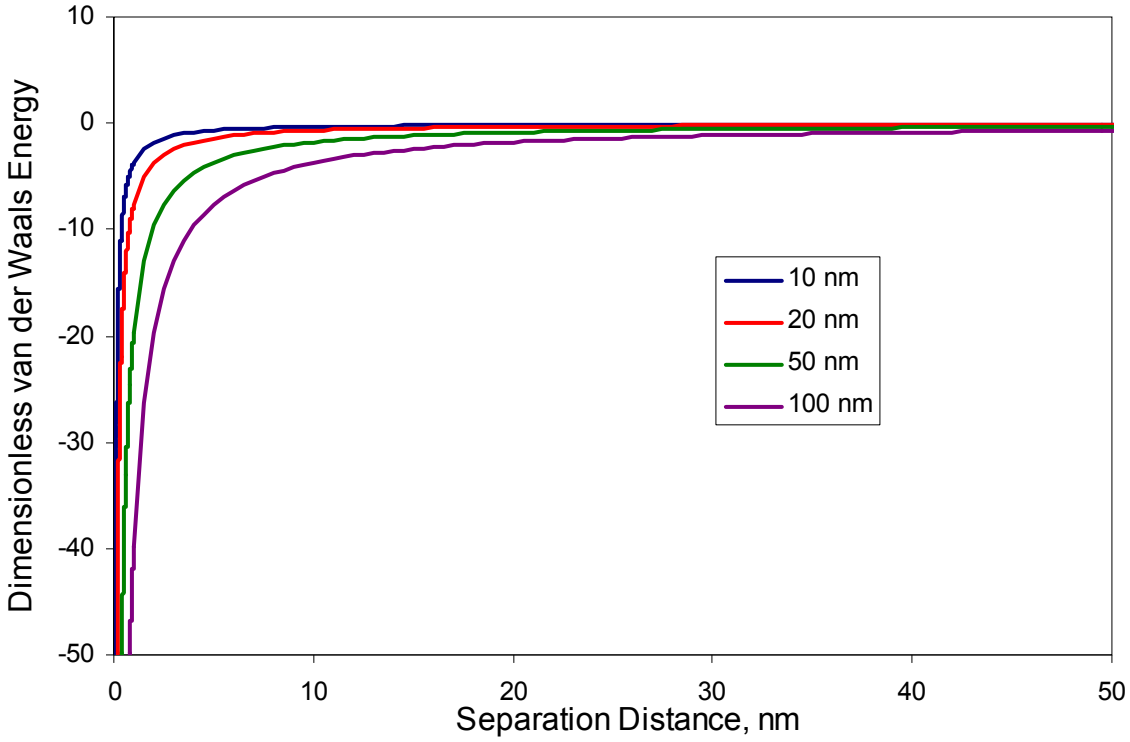

Figure 4.13: Variation of dimensionless (Energy/kT) van der Waals energy with separation distance for different particle sizes. (From equation 4 1, where $A_H = 10^{-20}$ J).

Since Brownian diffusion controls the transport of the nanoparticles and van der Waals forces controls their attachment to the pore walls, the reversible attachment of nanoparticles observed in our experiments can be attributed due to large hydrodynamic forces combined with high diffusion coefficients, or alternatively to weak adhesive forces. For the latter, the energy barrier that the particles have to overcome for detachment is not very large and the rate of detachment will be controlled by the ability of the nanoparticle to diffuse across the solution.

How do these competing phenomena give rise to the observed effluent concentration histories? Important insight comes from the mechanistic modeling of Jha *et*

al. (2008), who demonstrate the essential role of diffusion in enabling solutes to escape the boundary layer. Using a particle tracking algorithm and pore scale flow streamlines that eliminate mixing, they follow a large cloud of non-interacting particles from their random initial locations through hundreds of pores. (The particles of Jha *et al*. are mathematical points, unlike the nanoparticles of interest here.) In the absence of diffusion, particles initially located at or near a pore wall exhibit extremely long residence times, because the flow speed is very small near the pore wall. The resulting effluent concentration histories are severely non-Fickian. A small diffusion coefficient enables some of the particles to escape their slow streamlines, and the late-arriving non-Fickian effluent concentration anomaly is reduced.

The situation in our corefloods appears analogous to the zero-diffusion limit of Jha *et al*. (2008), the key physical difference being that the nanoparticles are held at or near the pore walls by weak van der Waals attraction. Eventually Brownian diffusion allows the nanoparticles to leave the slow streamlines near the pore walls. The modest delay in arrival of nanoparticles at the outlet would be the consequence of some nanoparticles being attracted to the rock surface. The long tails would be the consequence of those nanoparticles eventually diffusing beyond the range of attraction to the rock surface, joining faster streamlines and being eluted.

The peak in effluent concentration after an 18 h shut-in in Texas Cream coreflood #1 offers important support for this model. During flow the residence time in the cores ranges from 2 to 10 min. The much longer time available for Brownian diffusion during the shut-in should allow a much larger number of nanoparticles to escape the near-pore-wall region. Many of these would be eluted when flow resumed. Moreover, van der Waals attraction plays a role in nanoparticle transport, then the surface area of the pore walls should have a first order effect on the effluent concentration history. Our

experiments also support this prediction: the greatest deviation from ideal propagation occurs in Texas Cream limestone corefloods. The limestone has the largest specific surface area (10 m^2/g estimated from mercury porosimetry) of the three rocks (Berea has 6.2 m^2/g and Boise 3.0 m^2/g).

In summary the nanoparticles do not migrate through these sedimentary rocks like a tracer, nor like an adsorbed solute such as polymer, but rather like a colloid with very weak attachment properties. The unique feature for the nanoparticle transport and deposition in cores appears to be the presence of weak attractive forces that can be eventually overcome by diffusion. This slows the transport of some fraction of the injected particles but does not prevent their eventual migration through the rock.

4.3.2. Apparent Viscosity of the Nanoparticle Dispersion in Porous Media

The apparent viscosity results obtained from the series of the corefloods described above suggests that, despite their size, the nanoparticles still exhibit some colloidal character when dispersed in a flowing phase. That is, their flow behavior in micro-scale channels is closer to that for the concentrated colloidal dispersions than that for homogeneous fluids. One approximate way of representing the flow field for the concentrated nanoparticle dispersion is to introduce the slippage boundary condition at the pore wall, while assuming the dispersion is a continuum fluid with the same properties that it exhibits as a bulk phase. Another way is to postulate the existence of a layer of fluid near the pore walls that is depleted of nanoparticles. The depleted layer would have smaller viscosity. We examine each model in this section.

The slip length (λ) is defined as the extrapolated distance from the wall where the tangential component of the fluid velocity vanishes (Priezjev, 2007) and it is described by the Navier slip boundary condition:

$$u_{slip} = \lambda \left. \frac{\partial u}{\partial r} \right|_{wall} \tag{4.2}$$

where u_{slip} is the fluid velocity and $\partial u/\partial r$ is the velocity gradient at the wall. In capillary tube flows, the effect of slip on flow rate is equivalent to increasing the tube radius by λ (Berg *et al*., 2008). Below, we describe a model analogous to the slip model presented by Gu and Di (2007), but relate the slip length with the decrease in apparent viscosity, rather than with the increase in permeability.

The parabolic velocity profile for capillary tubes (Figure 4.14) is given by:

$$u = - \frac{\nabla P}{4\mu}\left(r_0^2 - r^2\right) \tag{4.3}$$

where u is the fluid velocity , μ is the viscosity of the fluid, ∇P is the pressure gradient, and r_0 is the radius of the capillary tube. For a constant pressure gradient, the flow velocity will increase if the radius of the capillary is increased. If we equate the slip length to an increase in tube radius, i.e. if we consider a tube of radius $r_0 + \lambda$, then the increment in average velocity, U, due to this slip length is given by:

$$\Delta U = - \frac{2 r_0 \lambda + \lambda^2}{6\mu} \nabla P \tag{4.4}$$

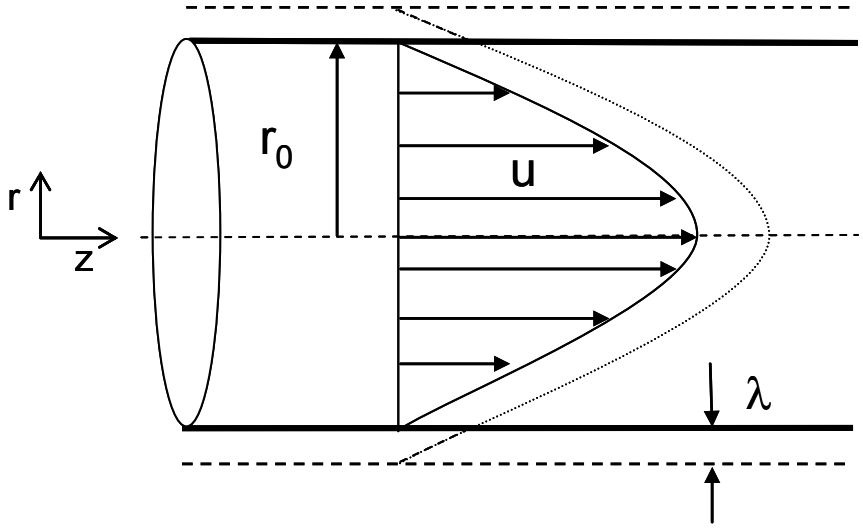

Figure 4.14: Sketch of the slip length (λ) in a parabolic velocity profile in a capillary tube.

The enhancement in the interstitial velocity, U, in a porous medium can be similarly calculated in terms of the reduction in the apparent viscosity that we observed, and employing the Darcy's law:

$$\Delta U = -\frac{k}{\phi}\left[\frac{1}{\mu_n} - \frac{1}{\mu}\right]\nabla P \tag{4.5}$$

where k is permeability, ϕ is porosity of the core, μ_n is the apparent viscosity measured from the pressure drop data, and μ is the viscometer-measured viscosity (the property of the bulk dispersion). Using the capillary-bundle model to relate permeability and throat radius r_0,

$$k = \frac{\phi r_0^2}{8} \tag{4.6}$$

we can determine the slip length corresponding to the measured apparent viscosity. Inserting equation (4.6) into equation (4.5) and equating the resulting equation with equation (4.4), we obtain:

$$\frac{\lambda}{r_0} = \sqrt{1+\frac{3}{4}\frac{\mu-\mu_n}{\mu_n}} - 1 \qquad (4.7)$$

The preceding equation suggests that, if there is a characteristic slip length for the nanoparticles of a given size and surface coating, the ratio of apparent viscosity to bulk dispersion viscosity would be smaller when they flow in the reservoir rock of lower permeability

We have estimated the ratio of the slip length to pore throat radius for our corefloods using equation (4.7) and the average pore radius obtained from mercury injection curves. The results are shown in Table 4.2 (at the end of this section) and Figures 4.15 and 4.16.

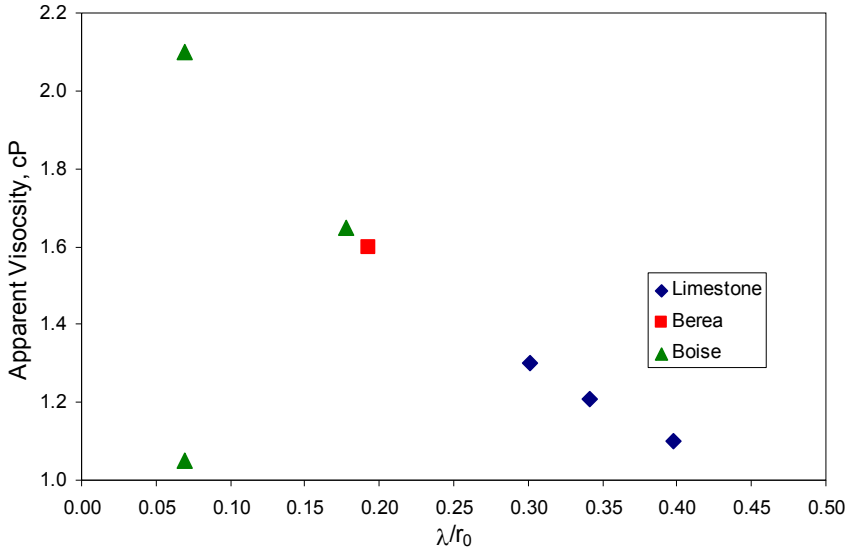

Figure 4.15: Ratio of calculated slip length to throat radius *vs.* apparent viscosity for the core floods.

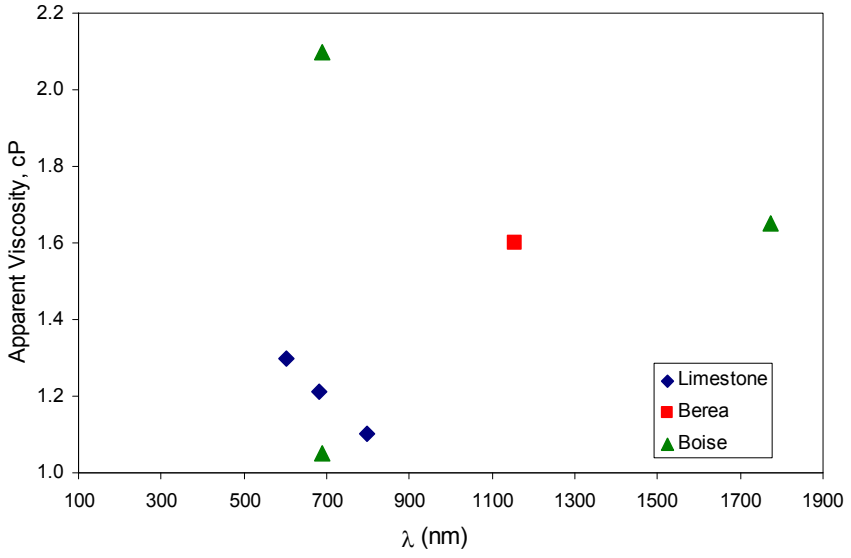

Figure 4.16: Slip length (λ) *vs.* apparent viscosity for the core floods.

We observed that the ratio of slip length to throat radius is larger for the low permeability limestone cores. The slip length for the Boise coreflood #3 deviates from the rest in Figure 4.15 because in this coreflood the injected 5 wt % nanoparticle dispersion had smaller viscosity than in the other experiments. The slip lengths are of order 1000 nm, Figure 4.16, and except for the low-rate injection into Boise sandstone are fairly tightly clustered. This suggests that a characteristic slip length exists for these nanoparticles, independent of the lithology or the permeability. The shear rates for our corefloods ranged from 50 to 700 s^{-1} (Figure 4.17), the larger rates being associated with the smaller permeability cores (limestones). Although the viscosity of bulk nanoparticle dispersions is only weakly dependent on shear rate, it may be that larger shear rates in a porous medium also enhance the establishment of low-viscosity regions near the pore walls.

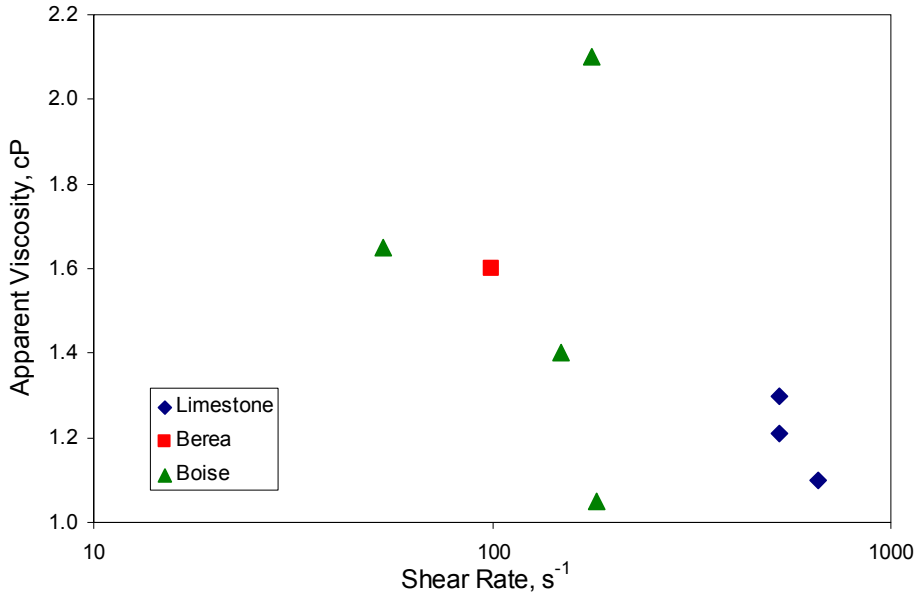

Figure 4.17: Apparent viscosity *vs.* shear rate for the coreflood experiments.

The concept of slip has been used to explain other observations of enhanced flow, but many of these involve a second fluid phase. For example, a thin film of wetting phase can enhance the flow of the nonwetting phase. An initially dry, suitably nanostructured surface offers much less resistance when water flows through it than an ordinary surface. In this case air trapped in the nanostructure reduces momentum transfer at the wall. A second fluid phase does not exist in our experiments, so the physical basis for a slip length of order 1000 nm remains to be determined.

Since the viscosity of these nanoparticle dispersions decreases as nanoparticle concentration decrease, the establishment of a depletion layer near pore walls could also account for small apparent viscosities. Figure 4.18 sketches the depletion layer in a tube of radius $r_{0.}$

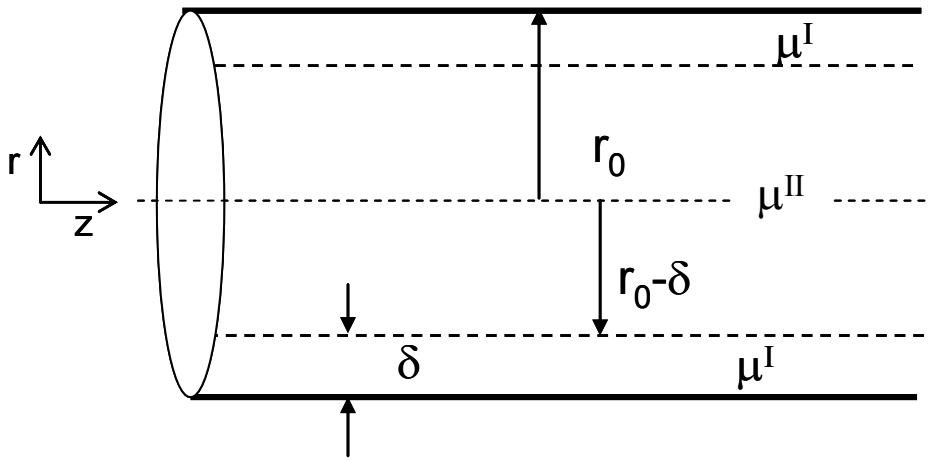

Figure 4.18: Sketch of the depleted layer (δ) in a parabolic velocity profile in a capillary tube.

The depletion layer thickness δ can be determined from momentum shell balances and the following boundary conditions: (*i*) no-slip at the tube wall and (*ii*) equal velocities at the interface between the depleted layer and the bulk dispersion and (*iii*) equal shear stresses at the same interface. We obtain two expressions for the velocities in the depleted and bulk zones, which we integrated over the area to obtain the two corresponding flow rates. We insert the total flow rate in the Hagen-Poiseuille equation, in which the viscosity is replaced by the apparent (observed) viscosity. This eliminates the pressure dependence, yielding an expression for the apparent viscosity (μ_n) as a function of the thickness of the depleted layer (δ):

$$\mu_n = \frac{\mu^I}{2}\left\{\begin{array}{l}\left[\frac{1}{2}-\left(1-\frac{\delta}{r_0}\right)^2+\frac{1}{2}\left(1-\frac{\delta}{r_0}\right)^4\right]- \\ -2\mu^I\left[\frac{1}{4\mu^{II}}\left(1-\frac{\delta}{r_0}\right)^4-\frac{1}{2}\left(1-\frac{\delta}{r_0}\right)^2\left[\frac{1}{\mu^I}+\left(\frac{1}{\mu^{II}}-\frac{1}{\mu^I}\right)\left(1-\frac{\delta}{r^0}\right)^2\right]\right]\end{array}\right\}^{-1} \qquad (4.8)$$

where μ^I is the viscosity of the depleted zone and μ^{II} is the bulk viscosity.

Let us consider the limiting case in which the viscosity of the depleted layer, μ^I, is equal to the viscosity of the brine solution without nanoparticles (approximately 1cP). We can then calculate the thickness of the depletion layer for the observed viscosity. The results are shown in Table 4.2 and Figures 4.19 and 4.20.

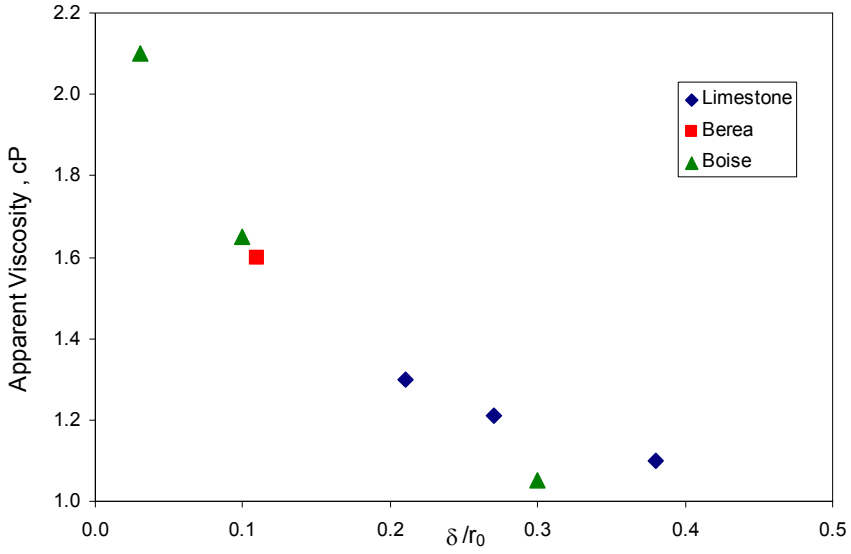

Figure 4.19: Apparent viscosity *vs.* relative thickness of depleted layer for the different core floods.

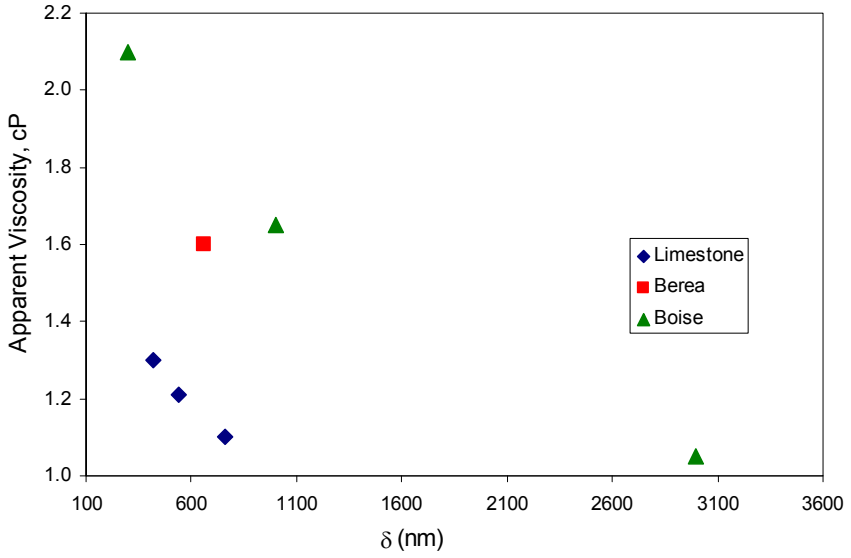

Figure 4.20: Apparent viscosity *vs.* thickness of depleted layer for the different core floods. From this data we can assume a characteristic value of depletion layer thickness of 700 nm.

The relative thickness of the depleted layer is larger for smaller permeability cores, therefore following the same trend as the thickness of the supposed slip length. In absolute terms, the depleted layers are around 500 nm thick, (Figure 4.20). For the limestone cores the depleted layer is a substantial fraction, 20% to 40%, of the throat radius. Such layers would be expected to yield earlier breakthrough and possibly concentrations exceeding injected. Neither expectation is met by our experiments. Moreover it is not clear how to reconcile a depleted layer with the weak attraction of nanoparticles to pore walls.

Though a satisfactory theoretical explanation for the small apparent viscosity of these nanoparticle dispersions is not yet available, the corefloods do enable an empirical estimate of enhanced migration. Considering the absolute slip lengths (Figure 4.16) and depleted zone thicknesses (Figure 4.20) we can suggest a single, characteristic value of each quantity. The values can be used to estimate apparent viscosity (and hence injectivity of a nanoparticle dispersion) knowing the viscosity of the bulk dispersion and the permeability or pore throat size of the rock. Figure 4.21 plots calculated *vs.* apparent viscosity for a slip length and depletion thickness of both 700 nm, which are about the average values for each model. The agreement is slightly better for the depleted layer model.

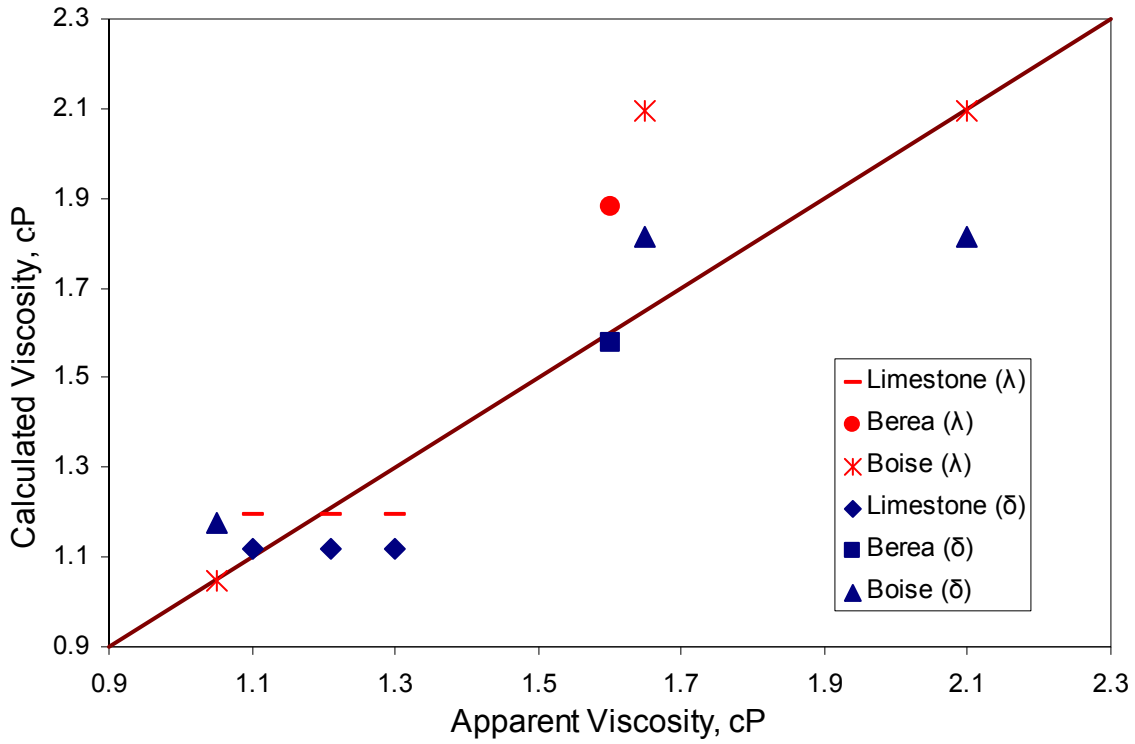

Figure 4.21: Apparent viscosity vs. calculated viscosity assuming a slip length of 700 nm (λ) or a thickness of 700 nm for the depleted layer (δ). The brown line indicates the 1:1 ratio.

Table 4.2: Slip length (λ) and thickness of depleted layer (δ) for different types of rocks, determined from the apparent viscosity of the nanoparticle dispersion during flow in that rock

Core Flood	**λ (nm)**	**λ/r_0**	**δ (nm)**	**δ/r_0**
Limestone 1	602	0.30	420	0.21
Limestone 2a	683	0.34	540	0.27
Limestone 2b	796	0.40	760	0.38
Berea	1155	0.19	660	0.11
Boise 1	690	0.07	300	0.03
Boise 2	1774	0.18	1000	0.1
Boise 3	690	0.07	3000	0.3

4.4. CONCLUSIONS

The following conclusions can be made from the series of the transport experiments employing the surface-treated silica nanoparticles:

The flow experiments demonstrate that concentrated dispersions of suitably surface treated nanoparticles can be transported through sedimentary rocks, even those of low permeability. This is a drastic departure from the transport of colloidal dispersions in porous media, which is known to be extremely difficult, especially when the dispersion concentration is high.

Two factors contribute to this exciting new development: (*i*) the small size of the nanoparticles allows their easy passage through typical rock pore throats; and more importantly, (*ii*) the surface coating of the nanoparticles ensures that the nanoparticles stay individually dispersed in water. The fact that the particle retention in the reservoir rock is very small indicated that the surface coating also eliminates electrostatic interaction between the nanoparticle and the pore walls, in both limestone and sandstone.

Comparison of effluent concentration histories from different corefloods indicates that the main retention mechanism for the surface-treated silica nanoparticles is not the straining and filtration as with the colloidal particles, but the reversible adsorption on the pore wall. Unlike the molecular adsorption, however, the nanoparticle attachment to solid appears to be according to the DLVO theory, the van der Waals attraction being the major contributor, because the nanoparticles carry virtually no surface charges with the surface treatment. The reversibility of adsorption means that Brownian diffusion can eventually liberate nanoparticles from the pore walls. Consequently very few particles are permanently retained, though some fraction is transported considerably more slowly than the rest.

The apparent viscosity measured as the nanoparticle dispersions flow through the cores is distinctly lower than the independently measured bulk viscosity. This indicates that despite their extreme small size the nanoparticles in concentrated dispersions still retain their colloidal character during flow in small pore channels. The enhanced migration may be explained by the apparent slippage at the wall caused by the existence of a viscosity depletion layer during the concentrated particulate flow.

Chapter 5: Application of Contact Line Length Calculation to the Retention of Colloidal Size Particles

5.1. INTRODUCTION

The calculation of contact line lengths and interfacial areas in computed generated packs of random spheres has been used to estimate the amount of colloidal size particles trapped per unit length and per unit area in actual packs of glass beads.

At given water saturation in a computer generated pack of spheres of radius *R*, the normalized specific contact line length per unit bulk volume (Lc_D/Vb_D) and the normalized specific interfacial area per unit bulk volume (A_D/Vb_D) can be extracted from LSMPQS simulations of drainage and imbibition as shown in Chapter 3. Assume that colloids adsorb with a characteristic separation distance between nearest neighbors (see Figure 5.1). This distance can be converted to a characteristic number density of colloids. Denote this density along a contact line as *C* per unit length of contact line. Then the number of colloids retained at the AWS contact line per dimensionless bulk volume of a grain pack would be:

$$\text{Amount of colloids per unit bulk volume at AWS} = \mathrm{C}\cdot\mathrm{R}\cdot\frac{\mathrm{L_{CD}}}{\mathrm{V_{bD}}} \qquad (5.1)$$

where V_{bD} is the dimensionless bulk volume and $Lc_D = \frac{Lc}{R}$, Lc being the length of the contact line in physical units. Similarly, assuming that colloids adsorb on the AWI in a square array, there will be C^2 colloids per unit area of AWI. In this case, the amount of colloids retained at the AWI per unit bulk volume would be:

$$\text{Amount of colloids per unit bulk volume at AWI} = C^2 \times 4\pi R^2 \times \frac{A_D}{V_{bD}} \qquad (5.2)$$

where $A_D = \frac{A_{w-nw}}{4\pi R^2}$, being $A_{w\text{-}nw}$ the interfacial area between wetting and non-wetting phases in physical units.

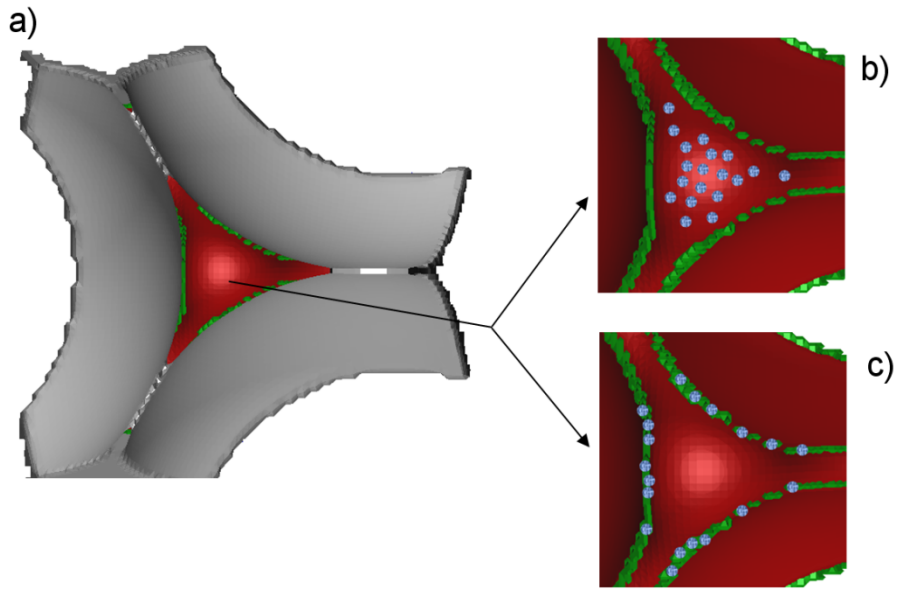

Figure 5.1: a) non-wetting phase (red) draining between three solid grains (in grey). The contact lines are shown in green. The flow is perpendicular to the plane of the paper with direction toward the reader. b) &c) close view of the meniscus minus the solid grains, showing colloids (in blue) trapped in the interface between wetting and non-wetting phases (b) and in the contact line between the three phases (c)

Let's see how retention in AWS contact line and AWI compare for different concentrations of colloids. Figure 5.2 and Figure 5.3 show plots of normalized specific contact line length and normalized specific interfacial area versus water saturation respectively.

At a water saturation of S_w = 0.2 near the drainage endpoint, a pack of spheres of radius R will have a normalized contact line length of 2.55 per dimensionless bulk volume according to Figure 5.2. Therefore, following equation 5.1, there will be $C \cdot R \cdot 2.55$ colloids retained per dimensionless bulk volume at AWS contact line. For a radius R=1 mm, the amount of colloids retained would be 2.55 C Alternatively, supposing colloids adsorb on AWI in a square array, there will be C^2 colloids per mm^2 of AWI. According to Figure 5.3, at Sw = 0.2 the same pack of spheres of radius 1 mm has a normalized AWI of 0.015 per dimensionless bulk volume during drainage. Thus, following equation 5.2, there will be $C^2 \cdot 4\pi R^2 \cdot 0.015 = 0.19 \cdot C^2$ colloids retained per dimensionless bulk volume at AWI.

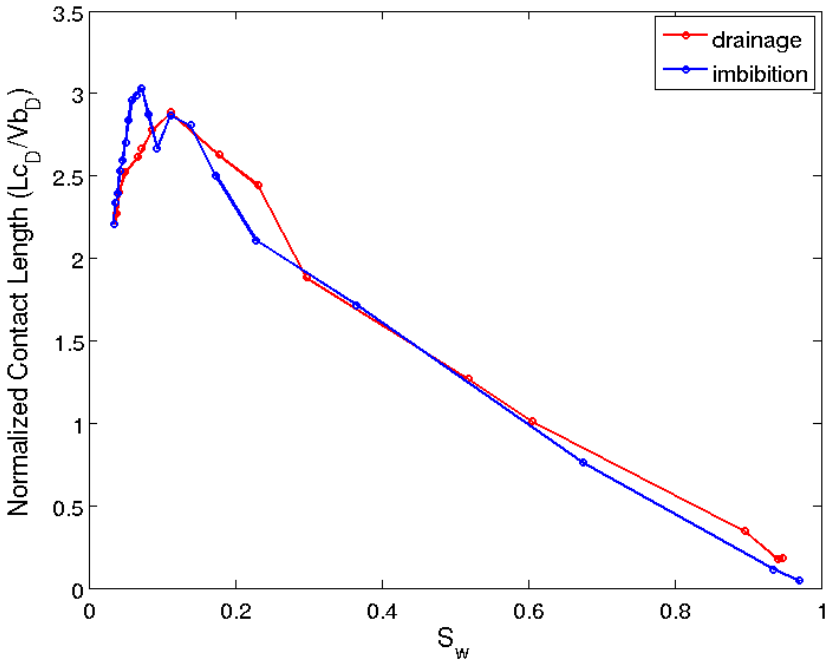

Figure 5.2: Normalized specific contact line length *vs.* water saturation from LSMPQS simulation of drainage and imbibition in a pack of randomly distributed spheres of the same radius R, with a resolution (voxel size dx = 0.04R).

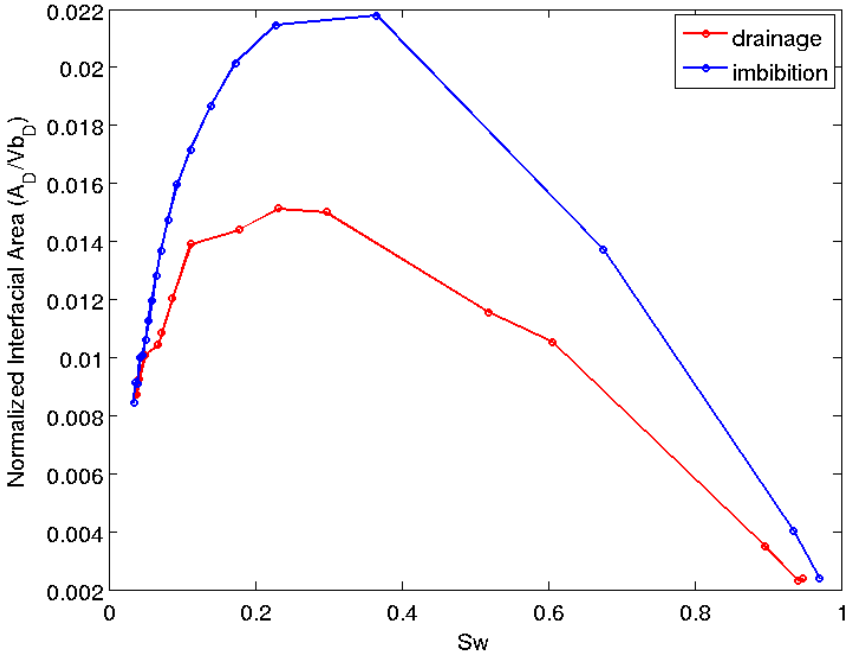

Figure 5.3: Normalized specific AWI area *vs.* water saturation from LSMPQS simulation of drainage and imbibition in a pack of randomly distributed spheres of radius R using a resolution $dx = 0.04R$

Based on this we can calculate and compare the amount of colloids per bulk volume retained at AWS contact lines and AWI for different concentrations C of adsorbed colloids. Table 5.1 shows the results.

Table 5.1: Retention of colloids at AWS contact line and AWI for different concentrations of retained colloids in a pack of random equal spheres of radius R = 1mm.

Concentration of colloids per mm (C)	**Retention at AWS (colloids/dimensionless bulk volume)**	**Retention at AWI (colloids/dimensionless bulk volume)**
1	2.55	0.19
10	25.5	19
100	255	1900

Adsorption at AWS contact line is dominant for dilute concentrations (C = 1 colloids/unit length) while adsorption at AWI is dominant for concentrated solutions (C = 100 colloids/unit length). For intermediate concentrations (C = 10 colloids/unit length) adsorption at AWI and AWS contact lines are comparable.

We can study the effect of grain size on the retention of colloidal size particles by repeating the previous exercise for the case of spheres of radius R = 0.1 mm. At Sw = 0.2 with a normalized contact line length of 2.55 per dimensionless bulk volume, a pack of R = 0.1 mm spheres will retain $0.255 \cdot C$ colloids per dimensionless bulk volume at AWS contact line and $0.0019 \cdot C^2$ colloids per dimensionless bulk volume at AWI. As in the previous case for spheres of radius of 1 mm, the retention of colloids per unit bulk volume for different concentrations of adsorbed colloid has been calculated and the results are shown in Table 5.2.

Table 5.2: Retention of colloids at AWS contact lines and AWI for different concentrations of retained colloids in a pack of random equal spheres of radius R = 0.1 mm.

Concentration of colloids per mm (C)	**Retention at AWS (colloids/dimensionless bulk volume)**	**Retention at AWI (colloids/dimensionless bulk volume)**
1	0.255	0.0019
10	2.55	0.19
100	25.5	19
1000	255	1900

As in the case for larger radius, adsorption at the AWS contact line is dominant for dilute concentrations while adsorption at the AWI dominates for larger concentrations. But in this case it takes a larger characteristic colloid concentration to

make the AWI be the dominant location for adsorption. Therefore, the smaller the grain size, the more likely the AWS contact line will make a significant contribution to colloid retention.

5.2. RETENTION OF COLLOIDS IN COLUMNS OF GLASS BEADS

Using the same approach that we showed in the previous section, we have estimated the amount of colloidal size particles trapped per unit of interfacial area and per unit of contact line length (C^2 and C above) in actual packs of glass beads. The experimental results were taken from the literature (Han *et al*., 2006). The experiments have been performed in columns packed with glass beads with diameters between 0.43 and 0.60 mm. The columns were 3.8 cm in diameter and 10 cm long and were packed with either 100% hydrophilic glass beads or a 1:1 mixture of hydrophilic and hydrophobic beads. Hydrophilic viruses bacteriophage MS-2 and ϕX174 with diameters between 24 and 27 nm were the selected particles for this study. Input solutions containing $5x10^5$ pfu/mL[4] of each virus and 0.05 g/L KBr tracer in a phosphate buffered saline solution were introduced into the columns as a step input. Both saturated and unsaturated experiments were conducted at different ionic strengths. For the unsaturated experiments, the columns were connected to a vacuum chamber whose pressure was changed to adjust the water saturation. After every experiment was completed the columns were flushed with an enzyme solution to detach the reversible adsorbed particles. Mass balance equations provided the amount of viruses irreversibly adsorbed in every experiment.

[4] pfu= plaque forming unit: a measure of the quantity of individual infectious particles (e.g. virus particles) based on the number of plaque formed per unit volume.

5.2.1. Experiments in Columns Filled with 100% Hydrophilic Glass Beads

A direct measurement of the contact line length and the interfacial area was not reported for the experiments. Thus for the unsaturated experiments in the 100% hydrophilic columns, the normalized specific contact line length and interfacial area at the drainage endpoint saturations were extracted from LSMPQS simulation of drainage in a pack of randomly distributed spheres of the same size. These values combined with the measurements of the amount of adsorbed particles from the experiments enable us to calculate the characteristic concentration of particles per unit length contact line, and per unit area of wetting-non-wetting interface, i.e. C and C^2 respectively.

The total solid area was also computed in the LSMPQS simulation. For the saturated experiments, this value will be used to estimate the characteristic amount of particles trapped per unit area of grain surface, that we call C_s^2. In order to evaluate the possible contribution of the contact line to particle retention, the values of C, C^2 and C_s^2 will be calculated assuming that all the retention has taken place at the AWS contact line, the AWI or the grain surface respectively.

From information provided in Han *et al.* (2006) regarding the total pore volumes (PV) of virus solution injected and the concentration of viruses in the input solution we calculated the total number of particles injected for each experiment as:

$$\begin{aligned}&\text{Total particles injected (pfu)} = \\ &\text{PV injected} \times \text{Column PV (mL)} \times \text{Input solution concentration (pfu/mL)}\end{aligned} \tag{5.3}$$

From information on percent of mass of viruses recovered, we estimated the total number of particles trapped as:

Particles trapped (pfu) =

$$\text{Total particles injected} \times \frac{100 - \%\ \text{mass recovered}}{100} \tag{5.4}$$

Table 5.3 shows the results for the experiments with bacteriophage MS-2. The experiments using bacteriophage ϕX174 showed almost no retention of the virus in the columns in both saturated and unsaturated cases and were not used for this part of the analysis.

Table 5.3: Experimental data for colloid retention in columns filled with 100% hydrophilic beads using bacteriophage MS-2. 20 pore volumes of virus solution of concentration equal to $5x10^5$ pfu/mL were injected in each experiment (Han *et al*., 2006).

	Exp 1	**Exp 2**	**Exp 3**	**Exp 4**
Sw (%)	100	100	16	20
Porosity	37	38	38	36
Ionic Strength (mM)	25	100	25	100
Mass Recovery (%)	79	67	69	13
Column Pore Volume (mL)	41.96	40.83	43.10	40.83
Total Particles Injected (pfu)	4.20×10^8	4.08×10^8	4.31×10^8	4.08×10^8
Particles Trapped (pfu)	8.81×10^7	1.42×10^8	1.34×10^8	3.55×10^8

The results in Table 5.3 show that the retention of viruses is larger at the larger ionic strength (compare "Particles trapped" row in column 2 to column 1 and column 4 to column 3). As we saw in Chapter 4, a larger ionic strength reduces the repulsive forces between surfaces, thus favoring attachment. Also there is more retention in the unsaturated experiments (3 and 4) than in the saturated ones. We will soon explain this observation based on our estimation of contact line length and interfacial area.

At this point, we need to convert the normalized specific length and area from LSMPQS simulations to their corresponding magnitudes in physical units in order to calculate meaningful values of C, C^2 and C_s^2. For the contact line length:

$$\text{Normalized } S\text{pecific AWS Contact Line Length} = \frac{\dfrac{\text{Contact Line Length}}{\text{Grain Radius}}}{\dfrac{\text{Bulk Volume}}{(\text{Grain Radius})^3}} \tag{5.5}$$

where bulk volume in this case is the total column volume, therefore:

$$\text{Contact Line Length} = \frac{\text{Normalized Specific AWS Contact Line Length} \times \text{Column Volume}}{(\text{Grain Radius})^2} \tag{5.6}$$

For the interfacial area:

$$\text{Normalized Specific AWI area} = \frac{\dfrac{\text{AWI area}}{\text{Grain Surface}}}{\dfrac{\text{Bulk Volume}}{(\text{Grain Radius})^3}} \tag{5.7}$$

and since bulk volume is the column volume, then:

$$\text{AWI Area} = \frac{\text{Normalized Specific AWI Area} \times \text{Column Volume} \times 4\pi}{(\text{Grain Radius})} \tag{5.8}$$

The area of the solid surface has been normalized in the LSMPQS simulations in the same way as the AWI area (see equation (5.7)); therefore we also use equation (5.8) to calculate the solid area in physical units. Since the solid area is as well equal to $Np4\pi R^2$, where Np is the number of grains, and the bulk volume is equal to $N_p[(4/3)\pi R^3]/(1-\phi)$, where ϕ is the porosity, we can also state for the solid area that:

$$\text{Normalized Specific Solid Area} = \frac{\dfrac{N_p 4\pi R^2}{(\text{Grain Surface})}}{\dfrac{N_p \dfrac{4}{3}\pi R^3 \dfrac{1}{(1-\phi)}}{R^3}} = \frac{3(1-\phi)}{R} \times \frac{R^3}{(\text{Grain Surface})} \tag{5.9}$$

We took an average grain (glass bead) diameter of 0.5 mm for these calculations. The estimated values for the number of particles retained per unit length (C), unit length square of wetting-non-wetting interface (C^2) and unit length square of solid surface (C_s^2) are shown in Table 5.4 for the experiments with virus MS-2 (relevant data from Table 5.3 is repeated here for easier reference).

Table 5.4: Calculated values for interfacial area, contact line length and solid area for a computer generated pack of spheres from LSM simulations and estimation of retention of colloids per unit area (C^2 and C_s^2) and length (C) (for columns filled with 100% hydrophilic beads).

		Exp 1	**Exp 2**	**Exp 3**	**Exp 4**
Particles Trapped (pfu) (cf. Table 5.3**)**		8.81×10^{7}	1.42×10^{8}	1.34×10^{8}	3.55×10^{8}
Sw (%) (cf. Table 5.3**)**		100	100	16	20
Ionic strength (mM) (cf. Table 5.3**)**		25	100	25	100
Normalized Contact Line Length at Sw from LSM (dimensionless)		-	-	2.70	2.55
AWS at Sw (mm) from LSM		-	-	4.90×10^{6}	4.63×10^{6}
Interfacial Area at Sw from LSM		-	-	0.01428	0.01470
AWI at Sw (mm^2) from LSM		-	-	8.14×10^{4}	8.38×10^{4}
Normalized Total Solid Area from LSM (dimensionless)		0.1462	0.1462	0.1462	0.1462
Grain area (mm^2)		8.33×10^{5}	8.33×10^{5}	8.33×10^{5}	8.33×10^{5}
MS-2 concentrations if all pfu are retained at:	**Contact line (pfu/mm) "C"**	-	-	27	77
	Air/water interface (pfu/mm^2) "C^2"	-	-	1641	4239
	Grain surface (pfu/mm^2) "C_S^2"	106	171	160	426

Notice that only in the unsaturated experiments (3 and 4) we have AWI and AWS contact lines besides the entire grain surface for the colloidal particles to be trapped. Also remember that the size of the viruses is between 24 and 27 nm. A first test of the calculated values of C, C^2 and Cs^2 reveals that the areas and length are large enough to accommodate 27 nm particles the particles without particle overlap.

The total grain surface calculated from LSMPQS is larger by one order of magnitude than the area of the AWI. If we assume that all the particles are trapped on grain surfaces, the amount of particles trapped per unit area C_s^2 is small. If we assume that all particles are trapped on air/water interfaces, the amount trapped per unit area C^2 is larger than C_s^2. It is important to notice that if all particles are assumed trapped only on the solid surface, the amount of colloids trapped per unit area of solid in experiment 4 is 2.5 times larger than the amount of colloids trapped per unit area of grain surface in experiment 2, which had the same ionic strength but was 100% saturated with water. There is no reason *a priori* to expect the characteristic concentration of adsorbed particles to change. Moreover the assumption of trapping only on the solid surface is valid for experiment 2, because they don't have any other place where to get trapped. Thus in experiment 4 the particles must be trapped at other locations in addition to the grain surface, in this case the AWI and the AWS contact lines. In fact we expect particles to be adsorbed at all three locations in any unsaturated experiment; the analysis confirms this expectation. The reason why there is more retention in the unsaturated experiments (3 and 4) than in the corresponding saturated ones (1 and 2) is the presence of AWI and AWS contact lines where particles can be trapped.

The estimates of C and C^2 in Table 5.4, obtained assuming all the retained particles are held at contact lines or at air/water interface, respectively, are reasonably

consistent with each other. That is, taking the square root of the values of C^2 yields a value of C that is within a factor of two of the values inferred for the contact lines, as shown in Table 5.5.

Table 5.5: Relationship between C and C^2 for retention of bacteriophage MS-2 in unsaturated columns of 100% hydrophilic glass beads.

	C (pfu/mm)	C^2 (pfu/mm^2)	C from C^2 (pfu/mm)	C^2 from C (pfu/ mm^2)
Exp. 3	27	1641	41	729
Exp. 4	77	4239	65	5929

The data of C, C^2 and Cs^2 in Table 5.4 are calculated assuming that all the retention has taken place in the AWS, AWI or the solid grains. In fact the particles are more likely to be trapped at all these places in different quantities. We can solve the following equation (5.10) to estimate the amount of colloids trapped per unit length in the system including all the places where they can be trapped:

$$\text{Total Colloids Trapped (pfu)} = (\text{AWI})\times C^2 + (\text{Contact Length})\times C + (\text{Area Solid})\times C_s^2 \qquad (5.10)$$

We have assumed that the three locations for trapping account in the same manner to the retention of particles. This equation can be solved for C in two ways. First, we assume that the entire solid surface is available for trapping in the unsaturated cases since the grains are hydrophilic and they will be covered by a thin film of water (remember the viruses are hydrophilic as well). Further, we assumed that the viruses will adsorb in the

same proportion in both fluid-fluid and solid-fluid interfaces, so C^2 is equal to C_s^2. Then equation (5.10) becomes a quadratic equation for C. The equation has two roots, one of which is negative and so is discarded. In the second method, we determine the value of C_s from the experiments in 100% saturated media (cf. Table 5.4). We then assume that C_s is a constant for an unsaturated experiment and that it has the same value as in the corresponding (same ionic strength) saturated experiment. Equation (5.10) then is quadratic in the unknown C. Table 5.6 shows the results of both solution approaches.

Table 5.6: Calculation of the retention of MS-2 particles in pfu per mm in columns of 100% hydrophilic glass beads assuming AWI, AWS contact line and grain surface all contribute to the retention.

	C (pfu/mm)	
Exp. 3	Assuming $C^2 = C_s^2$	10
(IS= 25 mM, S_w = 16%)	Taking C_s^2 = 106 (Exp. 1)	8
Exp. 4	Assuming $C^2 = C_s^2$	17
(IS= 100mM, S_w= 20%)	Taking C_s^2 = 171 (Exp. 2)	30

When taking the value for C_s^2 to be a constant equal to C_s^2 for the case of 100% saturated packing, the calculated value of C = 8 pfu/mm for experiment 3 indicates that both grain surface and interfaces plus contact lines are all equally attractive to attachment, since we would get a value for C^2 equal to 64 pfu/mm^2 which is within a factor of 1.5 from C_s^2. For experiment 4 (performed at a larger ionic strength) the value of C when taking C_s^2 to be a constant is more than 3 times larger (30 pfu/mm) than for exp. 3, which indicates that large ionic strength makes interfaces and contact lines more

attractive to attachment than grain surfaces. As expected, higher ionic strength turns into more particle retention.

The two approaches to estimating *C* yield similar values (of order 10 in exp. 3, of order 20 in exp. 4). We conclude that the assumption of a characteristic separation distance between adsorbed particles is reasonable.

5.2.2. Experiments in Columns Filled with a 1:1 Mixture of Hydrophilic and Hydrophobic Beads

We cannot perform a similar type of analysis for the case of columns filled with a 1:1 mixture of hydrophilic and hydrophobic beads because the LSMPQS simulations assume that the granular media is 100% water wet, but we can discuss the experimental observations based on what we have learned about interfaces and contact lines.

In these experiments less retention was observed in both saturated and unsaturated cases when compared with the 100% hydrophilic beads, except for an experiment performed at a larger ionic strength (163 mM, which was not tested in the homogeneous columns), where the retention was the largest. The particle retention was larger in the saturated experiments than in the unsaturated, contrary to what was observed in the hydrophilic columns. The key to explain this phenomenon may be in the wettability of grains and colloidal particles. Both viruses are hydrophilic and they will attach preferably to hydrophilic surfaces.

In the 100% saturated experiments, all the grains are covered with water so the colloids can attach to them. In the unsaturated experiments, the hydrophobic grains will not be covered by water, reducing the grain solid surface that is available for retention. The colloids in this case will attach only to the surface of the hydrophilic grains. The specific surface area in these columns will therefore be around 50% smaller than in the

hydrophilic columns. Another suggested reason for the smaller retention in unsaturated experiments is that even if we generate AWI and AWS contact lines, we do so in a smaller quantity per unit bulk volume than in the 100% hydrophilic columns. For example, only hydrophilic beads will support a contact line associated with a pendular ring, and only a throat formed by three hydrophilic beads will support an air/water meniscus.

In Chapter 3 we analyzed x-ray microtomography images of the drainage endpoints of experiments performed in 100% hydrophilic and 50 % hydrophilic - 50% hydrophobic glass beads columns in order to extract the contact line lengths. The images were cubes of 300 voxels per side with voxel sizes equal to 10.92 μm, being the glass bead diameters ranging between 0.3 and 0.42 mm. The procedure to extract the contact line from the images was explained in section (3.3.5). Those images were provided by Dr. Willson, coauthor of Han *et al.* (2006) from where we obtained the results of the experiments in columns of glass beads (the images are not of the actual columns used for the experiments but of analogous ones). In Table 3.3 we replicate the computed normalized specific contact line length for the different packs:

Table 5.7: Porosity, water saturation and normalized specific contact line length for different packs of glass beads obtained from CT images[5]. I= 100% hydrophilic, E=50% hydrophilic 50% hydrophobic

Sample	**Porosity (%)**	**Sw**	**Lc_D/Vb_D**
I2	37.5	0.0775	1.04
I3	38.0	0.0805	1.34
E2	37.0	0.0553	0.60
E3	36.2	0.0566	0.64

[5] Images courtesy of Dr. Clinton S. Willson from Louisiana State University

As expected, the contact line length for the 1:1 columns (E2 and E3) is around 50% of the value for the hydrophilic columns (I2 and I3). Figure 3.23 shows the configuration of contact lines that we extracted from two of the packs. At these water saturations the majority of the contact line consists of isolated paths, which we believe belong to pendular rings, as expected at small water saturations. What is noticeable here is that the number of contact lines is much smaller for the 1:1 pack than for the 100% hydrophilic pack.

Since contact line and interfacial area are closely related, the interfacial area will be also smaller. In his PhD dissertation, Motealleh (2009) showed that the trapped wetting phase at the endpoint of drainage in fractionally wet packs of grains (different proportion of hydrophilic and hydrophobic grains) was arranged into large blobs. The blobs are larger than in the case of single wettability grains, and consequently the interfacial area between wetting and non-wetting fluids is smaller. Therefore, in the 1:1 columns the colloids will encounter smaller amounts of AWI where they can be trapped. We recommend for future work to estimate the interfacial wetting-non-wetting area from these images.

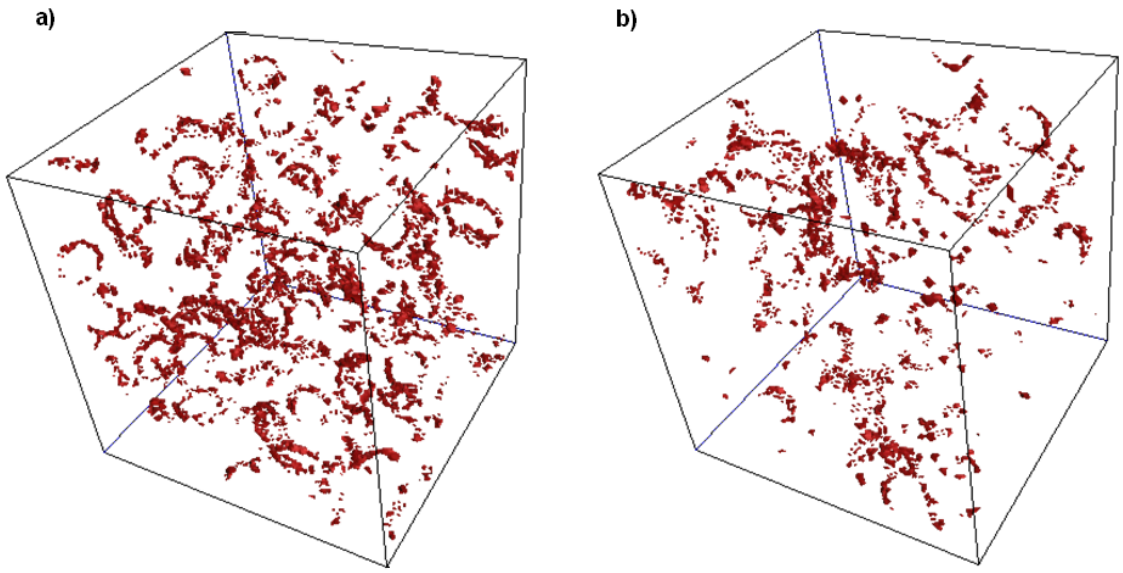

Figure 5.4: Contact line configuration in (a) a pack of 100% hydrophilic beads and (b) a pack of 50% hydrophilic and 50% hydrophobic beads

From the 100% saturated cases in this fractionally wet medium we can calculate the amount of colloids trapped in the grain surfaces and then assume that the solid surface available for retention in the fractionally wet columns is only 50% of the value in a hydrophilic column. We can also assume the values for A_D/V_{bD} and Lc_D/V_{bD} for the 1:1 fractionally wetted column are half of the corresponding values from the 100% hydrophilic column. We can then calculate the values of characteristic concentration C, C_s^2 and C^2 as we did for the 100% hydrophilic columns shown in Table 5.4. The experimental results from Han *et al*., (2006) and our estimation of number of particles trapped using equations (5.3) and (5.4) are shown in Table 5.8 and our calculation of C, C_s^2 and C^2 is shown in Table 5.9:

Table 5.8: Experimental data of colloid retention in columns filled with 50% hydrophilic and 50% hydrophobic beads using bacteriophages MS-2 and ϕX174 (Han *et al*., 2006).

		Exp 1	Exp 2	Exp 3	Exp 4	Exp 5	Exp 6
Sw (%)		100	100	100	17	19	16
Porosity		37	38	37	36	37	35
Ionic Strength (mM)		25	100	163	25	100	163
Mass Recovery (%)	**MS-2**	91	37	3.2	92	71	38
	ϕX174	78	76	74	92	86	83
Column Pore Volume (mL)		41.96	43.10	41.96	40.83	41.96	39.69
Total Particles Injected (pfu)		4.20×10^{8}	4.31×10^{8}	4.20×10^{8}	4.08×10^{8}	4.20×10^{8}	3.97×10^{8}
Particles Trapped (pfu)	**MS-2**	3.78×10^{7}	2.72×10^{8}	4.06×10^{8}	3.27×10^{7}	1.22×10^{8}	2.46×10^{8}
	ϕX174	9.23×10^{7}	1.03×10^{8}	1.09×10^{8}	3.27×10^{7}	5.87×10^{7}	6.75×10^{7}

Table 5.9: Calculated values for interfacial area, contact line length and solid area for a computer generated pack of spheres from LSM simulations and estimation of retention of colloids per unit area (C^2 and C_s^2) and length (C) (for columns filled with 50% hydrophilic and 50% hydrophobic beads).

		Exp 1	Exp 2	Exp 3	Exp 4	Exp 5	Exp 6
Contact Line Length at Sw from LSM, prorated by 50%		-	-	-	1.33	1.295	1.35
AWS at Sw (mm)		-	-	-	2.41×10^6	2.35×10^6	2.45×10^6
Interfacial Area at Sw from LSM prorated by 50%		-	-	-	0.00718	0.00729	0.007115
AWI at Sw (mm^2)		-	-	-	4.09×10^4	4.16×10^4	4.06×10^4
Total Solid Area in contact with aqueous phase from LSM		0.1462	0.1462	0.1462	0.0731	0.0731	0.0731
Grain Area in contact with aqueous phase (mm^2)		8.33×10^5	8.33×10^5	8.33×10^5	4.17×10^5	4.17×10^5	4.17×10^5
"C" (pfu/mm of AWS line)	**MS-2**	-	-	-	14	52	101
	ϕX174	-	-	-	14	25	28
"C^2" (pfu/mm^2 of AWI)	**MS-2**	-	-	-	798	2928	6068
	ϕX174	-	-	-	798	1414	1664
"C_S^2" (pfu/mm^2 of grain surface)	**MS-2**	45	326	487	78	292	591
	ϕX174	111	124	131	78	141	162

The estimated values of C, C^2 and C_s^2 increase in each experiment with the increase of ionic strength as expected. The values of C and C^2 for MS-2 estimated for experiments 4 and 5 are slightly smaller than the values estimated for the corresponding experiments with the same ionic strength in 100% hydrophilic columns (cf. Table 5.4, experiments 3 and 4). The difference, which is more noticeable in the case of C^2 than in the case of C, is still within a factor of two, and considering we are making an approximation by prorating interfacial areas and contact lines in these 1:1 columns we can conclude that the retention at AWS contact lines and AWI in terms of C and C^2 is consistent regardless the hydrophobicity of the porous media.

The number of MS-2 colloids trapped per mm^2 of grain surface (C_s^2) in unsaturated experiment 6 is larger by 100 pfu/mm^2 than in the corresponding saturated experiment 3. Since we expect the same trapping per unit area of solid in saturated and unsaturated experiments, the estimated C_s^2 for the unsaturated case will then not be plausible, suggesting that the colloids cannot be retained entirely at the grain surfaces in the unsaturated medium and that the excess of colloids retained in the grain surface should be actually retained in other locations (AWI or AWS contact line).

For the rest of the experiments the difference between C_s^2 in the saturated and corresponding unsaturated cases is not that evident. After the assumptions that we have made for this analysis we can conclude that in these cases the trapping of colloids per unit solid area is practically the same for the saturated and unsaturated cases.

As we did in the 100% hydrophilic columns, we applied equation (5.10) to this set of experiments to estimate a value for C when the colloids are assumed to be trapped in all three locations in the same proportion, and the results are shown in Table 5.10.

Table 5.10: Calculation of the retention of MS-2 and ϕX174 particles in pfu per unit length assuming equal contribution of AWI, AWS contact line and grain surface to the retention.

C (pfu/mm)		MS-2	ϕX174
Experiment 4 (IS= 25 mM, Sw= 17%)	Assuming $C^2 = C_s^2$	6	6
	Taking $C_s^2 = 45$ for MS-2 and C_s^2=111 for ϕX174 (from Exp. 1)	5	-6
Experiment 5 (IS= 100 mM, Sw= 19%)	Assuming $C^2 = C_s^2$	14	9
	Taking $C_s^2 = 326$ for MS-2 and C_s^2=124 for ϕX174 (from Exp. 2)	-7	3
Experiment 6 (IS= 163 mM, Sw= 16%)	Assuming $C^2 = C_s^2$	21	10
	Taking $C_s^2 = 487$ for MS-2 and C_s^2=131 for ϕX174 (from Exp. 3)	14	5

Comparing the calculated C for MS-2 with the results for the 100% hydrophilic columns (Table 5.6), the value of C for experiments 4 and 5 is slightly smaller that the value of C for their corresponding experiments 3 and 4 in Table 5.6, when assuming C^2 to be equal to C_s^2, yet again the difference is not remarkable (10 and 17 pfu/mm for 100% hydrophilic columns versus 6 and 14 pfu/mm for these 1:1 columns.)

When we assumed constant C_s equal to C_s for the corresponding saturated experiment, the calculated C for MS-2 in experiment 4 is similar than the estimated for

the 100% hydrophilic column for corresponding experiments in Table 5.6 (5 pfu/mm *vs.* 8 pfu/mm).

The analysis in Table 5.10 reveals a new case, when using the value of C_s^2 as a constant from the experiment with the 100% hydrophilic beads, in which we get a negative value for *C*. The negative value is the result of the term (*Area Solid)*$\times C_s^2$ in equation (5.10) being larger than the total number of colloids trapped. We can think of two causes that explain this negative value. First, it may be that the assumed value of C_s^2 for the available area is too large. This will be an indication that, in unsaturated media, the colloids prefer to attach to other locations even if plenty of grain surface is available for attachment. On the other hand, it may be that we are overestimating the available area for retention of C_s^2 colloids when we assume that it is 50% of the total solid area. A smaller value of *Area Solid* in equation (5.10) will make the value of *C* to be positive. We can decrease this number until we get a positive value for *C* and see what percentage of the total solid area represents. We obtained plausible results assuming 30% of the area is available for retention. The results are shown in Table 5.11.

Table 5.11: Re-calculation of the retention of MS-2 and ϕX174 particles in pfu per mm assuming AWI, AWS contact line and grain surface all contribute to the retention, and that the available percentage of grain surface for colloid retention is 30% of the total solid surface when assuming C_s^2 is constant.

C (pfu/mm)		**MS-2**	**ϕX174**
Experiment 4 (IS= 25 mM, Sw= 17%)	Assuming $C^2 = C_s^2$	6	6
	Taking C_s^2 = 45 for MS-2 and C_s^2 =111 for ϕX174 (from Exp. 1)	8	2
Experiment 5 (IS= 100 mM, Sw= 19%)	Assuming $C^2 = C_s^2$	14	9
	Taking C_s^2 = 326 for MS-2 and C_s^2=12 for ϕX174 (from Exp. 2)	14	10
Experiment 6 (IS= 163 mM, Sw= 16%)	Assuming $C^2 = C_s^2$	21	10
	Taking C_s^2 = 487 for MS-2 and C_s^2=131 for ϕX174 (from Exp. 3)	33	12

When C_s^2 is considered to be constant and equal to C_s^2 from the saturated case, the calculated C is comparable in magnitude to the square root of the assumed constant C_s^2. This is an indication that attachment of particles at AWS is plausible and consistent with attachment at AWI and grain surface.

5.3. SUMMARY

We have shown how we can apply the calculation of the contact line length and interfacial areas to estimate the amount of trapped particles in interfaces from experimental data. The same procedure can be repeated if more experimental data becomes available, to check if the values of C, or amount of trapped colloids per unit length, are representative of granular porous media. With the current state of the art, several assumptions must be made in order to estimate colloid retention per unit length or length square in porous media. In this chapter we presented a few of them, and show that they provide plausible consistency.

Since our level set method simulations do not handle fractionally wet porous media, we made several assumptions for the values of contact line lengths and interfacial areas in the columns filled with beads of different wettability. The assumptions are based on observations from a mechanistic calculation of drainage and imbibition in fractionally wet media using idealized interface geometry (Motealleh, 2009).

Our premise is that the viruses in the study of Han *et al*., (2006) adhere to retention sites with a characteristic separation between viruses. This leads to a simple formula to calculate the amount of viruses trapped per unit length. This concentration is applied to all the possible trapping locations, in order to understand how trapped colloids distribute in the porous media.

With the available data we cannot find an accurate value for retention of colloids, but we can show that retention is likely to occur simultaneously at grain surfaces, air-water interfaces and air-water-solid contact lines. The retention at the latter two becomes preferred as ionic strength of the aqueous phase increases. The exercises shown in this chapter illustrate an approach that can be applied as more measurements and more

detailed simulations become available to provide a better understanding of colloid retention.

Chapter 6: Estimation of the Contribution of Interfacial Areas and Helmholtz Free Energy to Capillary Pressure Using Level Set Method

In previous chapters the role of fluid/fluid interfaces in colloid retention has been examined. The Level Set Method was used to provide quantitative prediction of interfacial area, which has a first-order influence on retention. This chapter seeks independent confirmation of the predicted trends in interfacial area. For this purpose, we will test the thermodynamic theories for multiphase flow in porous media of Morrow (1970) and Hassanizadeh and Gray (1991; 1993) with independent quantitative assessments of interfacial area, from LSMPQ simulations and column experiments.

6.1. INTRODUCTION

Morrow (1970) studied the thermodynamics of immiscible displacement in porous media. He defined the motion of the interface as a series of reversible events (changes in interface curvature), where there is a continuous variation of pressure with saturation, and irreversible, spontaneous events, where the interface is unable to change location smoothly with the variation in pressure. The irreversible events are known as "Haines jumps" in drainage and "Melrose events" in imbibition (Haines, 1930; Melrose, 1965). The change in surface free energy, ΔF, during the smooth reversible displacement is defined by Morrow as:

$$\Delta F = \int \sigma_{w\text{-}nw} \, d\left\{A_{w\text{-}nw} + A_{s\text{-}nw}\cos\theta\right\} \tag{6.1}$$

where $\sigma_{w\text{-}nw}$ is the surface tension between wetting and non-wetting phases, $A_{w\text{-}nw}$ is the interfacial area between wetting and non-wetting phases, $A_{s\text{-}nw}$ is the interfacial area

between solid and non-wetting phases, and θ is the contact angle between the solid and wetting phase. During drainage, work is done on the system and therefore the surface free energy increases from one saturation step to the next, making ΔF positive. During imbibition, the system does work on the surroundings, therefore the surface free energy decreases and ΔF is negative.

Morrow's analysis of the displacement mechanism in porous media concludes that the difference in surface free energy ΔF of the states corresponding to wetting phase volumes V_1 and V_2, where $V_1 > V_2$, lies between the work done on the system for drainage and the work recovered from the system for imbibition. Therefore:

$$\int_{V_1}^{V_2} P_c \, dV > \Delta F > \int_{V_2}^{V_1} P_c dV \qquad (6.2)$$

where the first integral from V_1 to V_2 corresponds to drainage and the second integral from V_2 to V_1 corresponds to imbibition. The first inequality means that the difference between the PV work done on the system during the process of drainage and the surface free energy corresponds to the Helmholtz free energy, ΔA, that will go into the bulk phases, dissipated during irreversible events. Similarly, the second inequality means that the difference between the PV work done by the system during the process of imbibition and the released surface free energy corresponds to the Helmholtz free energy that is dissipated into the bulk phases.

By analyzing equation (6.2) we can find the nature of this dissipation term. The left hand side of the equation corresponds to work done on the system during drainage, where the system moves from a volume of wetting phase V_1 to a smaller volume V_2. Part of this work will be used to displace the interface, and is represented by the surface free

energy ΔF, which is also positive. The rest will be dissipated into the bulk phases. Therefore we can express the side of equation (6.2) corresponding to drainage as:

$$\int_{V_2}^{V_1} P_c \, dV = \Delta F + \Delta A \tag{6.3}$$

The right hand side integral of equation (6.2) corresponds to imbibition and indicates that the release of surface free energy is larger than the work done by the system. This work is negative since it is done by the system to the surroundings. The increment on surface free energy, ΔF, for imbibition is negative according to Morrow's analysis. However, in equation (6.2) we are comparing the magnitudes of work and energy. Analogous to the case of drainage, the integral evaluates the work done by the system as the area under the capillary pressure curve between volumes V_1 and V_2. The value of the integral as written is positive. Since the released surface free energy is larger than the work done by the system during imbibition, the energy dissipated into the bulk phases, ΔA, in this case appears on the right hand side of an equality corresponding to the right side inequality in equation (6.2), yielding:

$$\Delta F = \int_{V_2}^{V_1} P_c \, dV + \Delta A \tag{6.4}$$

Regarding contact lines, Morrow (1970) states that since the region occupied by the three phases contact line contains few molecules when compared with the other surface regions, the contribution to the free energy of the system due to variation in the length as result from variation in surface areas can be neglected. The results of Chapter 3

of this dissertation could be used to test this assumption, if a value of specific energy associated with a contact line were available.

Theoretical studies of multiphase systems based on thermodynamics by Hassanizadeh and Gray (1993) claim that macroscopic capillary pressure must be independent of external forces and rely on intrinsic properties of the system, such as the free energy of the interfaces. These studies suggested that capillary pressure, P_c, is related to the change in free energy of the phases and interfaces as a result of the changes in saturation. A change in the saturation of the wetting phase, for instance during drainage or imbibition, modifies the distribution of phases, causing a change in the free energy of the interfaces. Therefore capillary pressure is a function of not only the saturation but also the interfacial area between the fluid phases and between each fluid phase and the solid. Hassanizadeh and Gray (1993) proposed a relationship between capillary pressure, saturation, interfacial areas and Helmholtz free energy for two phase fluid flow in porous media:

$$P_C = -S_w \rho_w \frac{\partial \hat{A}_w}{\partial S_w} - S_{nw} \rho_{nw} \frac{\partial \hat{A}_{nw}}{\partial S_w} - \sum_{\alpha\beta} \frac{\sigma_{\alpha\text{-}\beta}}{\varphi} \left(\frac{\partial a_{\alpha\text{-}\beta}}{\partial S_W} \right) \Bigg|_{T,\phi,\Gamma_{\alpha\beta},\hat{A}_{\alpha\beta}} \tag{6.5}$$

where $\sigma_{\alpha-\beta}$ is the interfacial tension between phases α and β, $a_{\alpha-\beta}$ is the interfacial area per bulk volume of porous medium between phases α and β, $\hat{A}_\alpha$ is the Helmholtz free energy of phase α per unit mass of phase α, ρ_α is the mass of phase α per unit volume of phase, ϕ is the medium porosity, and S_w is the saturation of the wetting phase. The change in interfacial areas with respect to S_w is evaluated at conditions of constant temperature T, medium porosity ϕ, interfacial mass density $\Gamma_{\alpha\beta}$, and Helmholtz free energy of interface αβ per unit mass of interface, $\hat{A}_\alpha$. This equation states that macroscopic capillary

pressure determines the change in the free energy of phases and interfaces as a result of change in the saturation. The third term on the right hand side of equation (6.5) can be expanded to yield:

$$\sum_{\alpha\beta}\frac{\sigma_{\alpha\beta}}{\phi}\left(\frac{\partial a_{\alpha\beta}}{\partial S_W}\right)\Bigg|_{T,\phi,\Gamma_{\alpha\beta},\hat{A}_{\alpha\beta}} = \frac{1}{\phi}\left[\sigma_{w-nw}\frac{\partial a_{w-nw}}{\partial S_w}+\sigma_{nw-s}\frac{\partial a_{nw-s}}{\partial S_w}+\sigma_{w-s}\frac{\partial a_{w-s}}{\partial S_w}\right] \tag{6.6}$$

This term includes the derivatives of the interfacial areas with respect to the saturation of the wetting phase and can be interpreted as the rate of change of surface free energy, ΔF in Morrow's notation, per unit pore volume with respect to wetting phase saturation.

The first and second terms on the right hand side of equation (6.5) correspond to the rate of change of Helmholtz free energy, ΔA, per unit pore volume with respect to wetting phase saturation. The change ΔA can be viewed as energy dissipated by irreversible pore-level events (jumps by menisci). We can relate equation (6.5) with equations (6.3) and (6.4) to estimate the contribution of the rate of change (with respect to S_w) of surface free energy and dissipated energy per unit pore volume to the capillary pressure. We can denote by D the rate of change of dissipated energy per unit pore volume with respect to wetting phase saturation, which groups the terms related to the Helmholtz free energy in equation (6.5), such that:

$$D = -S_w\rho_w\frac{\partial\hat{A}_w}{\partial S_w}-S_{nw}\rho_{nw}\frac{\partial\hat{A}_{nw}}{\partial S_w} \tag{6.7}$$

and by *S* the rate of change of surface free energy per unit pore volume with respect to wetting phase saturation, which is the term related to the interfacial areas in the same (6.5) equation:

$$S = -\sum_{\alpha\beta} \frac{\sigma_{\alpha\beta}}{\phi} \left(\frac{\partial a_{\alpha-\beta}}{\partial S_W} \right) \Bigg|_{T,\phi,\Gamma_{\alpha\beta},\hat{A}_{\alpha\beta}} \tag{6.8}$$

The relationship between capillary pressure and the rates of change of surface free energy and dissipated free energy per unit volume during drainage or imbibition can be obtained by comparing equations (6.3) and (6.4) from Morrow's analysis with equation (6.5) from Hassanizadeh and Gray and using the terms *D* and *S* just defined.

For drainage, equation (6.3) indicates that part of the PV work done on the system goes to the interface and the rest is dissipated to the bulk phases. Thus, for drainage, equation (6.5) can be re-written as:

$$P_c = D + S \qquad \text{(drainage)} \tag{6.9}$$

For imbibition, Morrow's analysis indicated that part of the released surface free energy goes to PV work done by the system and the rest is dissipated to the bulk phases. In this case, equation (6.5) can be re-written as:

$$S = P_c + D \qquad \text{(imbibition)} \tag{6.10}$$

This relationship between capillary pressure, saturation and free energy has been tested by Pyrak-Nolte *et al*. (2008) who used the results from drainage experiments

performed on transparent two dimensional micromodels to investigate the ability to calculate the rate of change of free energy of the bulk fluid phases from measurements of saturation and interfacial area. Image analysis software was used to extract phase saturations, interfacial areas and curvature of the interface from high resolution images of the micromodel at different drainage steps. Pressures were calculated from curvature measurements. After estimating every derivative of interfacial area in equation (6.6) from sequences of images, the rate of change of surface free energy per unit pore volume was found to be essentially the same for all drainage steps, suggesting that contributions to capillary pressure from the free energy associated with the saturation gradient of each phase (first and second terms in equation (6.5), or the D term in equation (6.9)) are not negligible. Their estimation of this contribution yielded negative values at low pressures (beginning of drainage) and decreased in absolute value as pressure increased, to eventually become zero at pressures approaching breakthrough of the non-wetting fluid.

This behavior is not in agreement with Morrow's study, from which we concluded that the system's rate of change of dissipated energy per unit volume, D in equation (6.9), should be positive. The authors credit this behavior to the presence of saturation gradients at all pressures in the experimental device and that can contribute to additional terms related with the free energy of the system. They also conclude that experiments in three dimensional devices are needed to confirm if these results are typical for the drainage and imbibition processes.

Pyrak-Nolte's work is the only one that we found in the literature that tested the validity of the thermodynamic analysis of Morrow (1970) and Hassanizadeh and Gray (1990; 1993) with experimental data. In the next section we will test if our LSMPQS simulations of drainage and imbibition follow the expectations of this thermodynamic analysis. For this purpose we are going to estimate the rates of change of surface free

energy and dissipated energy per unit pore volume in equation (6.5) using our quantitative estimation of interfacial areas from LSMPQS simulations of drainage and imbibition in model sediments. Later we will also test the thermodynamic consistency of the interfacial areas experimentally measured in columns packed with glass beads and volcanic tuff.

6.2. Estimation of Surface and Dissipated Free Energy Contributions to Capillary Pressure from LSM Simulations and Experimental Data

Interfacial area measurement is a complex problem. There are two main methods for the measurement of fluid-fluid interfacial areas. One is based on interfacial partitioning tracer tests and the other is based on analysis of high resolution microtomography images of drainage/imbibition experiments. Several studies have shown that the interfacial areas estimated with tracer tests are larger than the ones estimated by microtomography, the reason being image analysis is unable to measure interfacial area associated with surface roughness because of resolution issues (Narter and Brusseau, 2010).

LSMPQS simulation offers an independent estimate of both solid-fluid and fluid-fluid areas. We can use our computed values of interfacial areas from LSMPQS simulations to calculate the rate of change of surface free energy per unit pore volume (S) during drainage or imbibition following equation (6.8). Since the capillary pressure applied during the LSMPQS simulation is known, we can then estimate the rate of change of dissipated energy per unit pore volume (D) from equation (6.9) or (6.10) for drainage or imbibition respectively. After examination of literature we could not find a method to individually evaluate the rate of change of free energy dissipated to each phase individually (first and second terms in equation (6.5)).

Besides the interfacial areas derived from LSMPQS simulation of drainage and imbibition in our computer generated packs of spheres, we are going analyze the interfacial areas from simulation of drainage in geometries extracted from microtomography images of real porous media, namely glass beads and volcanic tuff[1]. We also have available the interfacial area measurement from drainage experiments in those porous media, obtained by image analysis[6]. We will test whether simulations and experiments are in agreement with the thermodynamic analysis of Morrow (1970) and Hassanizadeh and Gray (1990; 1993).

6.2.1. Method

To calculate the partial derivatives of area with respect to water saturation in equation (6.6) we fit the values of specific interfacial area versus water saturation, in both the simulated and the experimental cases, to polynomials of the type $a_{\alpha\beta} = f(S_w)$. Third order polynomials were found to be the better fit for the characteristic shape of the wetting-non-wetting interfacial area versus saturation curves. During drainage, typically the area increases as saturation decreases until it reaches a maximum (usually at around 25% saturation) and then starts decreasing at lower saturations. Polynomials of third order were also proven to give a good fit for the interfacial areas between solid and non-wetting and solid and wetting phase. Plots of interfacial area versus wetting phase saturation with their corresponding polynomial fitting will be shown for each case studied in this analysis.

From the fitted polynomials we calculate the analytical derivatives ($\partial a_{\alpha\text{-}\beta}/\partial S_w$) at each wetting phase saturation (S_w) where we have a simulated or experimental

[6] Courtesy of Dr. Dorthe Wildenschild from Oregon State University

measurement of interfacial area. The values of the derivatives are introduced in equation (6.8) to estimate the rate of change of surface free energy per unit pore volume, *S*. Afterward we use the value of *S* in equation (6.9) for a drainage process or (6.10) for imbibition to estimate the rate of change of dissipated free energy per unit pore volume, *D*, with respect to wetting phase saturation. Remember that the capillary pressure used is the result directly from either LSMPQS simulations or experimental measurements.

The values of the interfacial tension $\sigma_{\alpha-\beta}$ for the simulated cases were selected assuming that wetting and non-wetting phases are water and air respectively, since those were the fluids used in the experiments of Dr. Wildenschild. $\sigma_{w\text{-}nw}$ for water-air systems at ambient conditions is equal to 0.072 N/m. From this value, using Young's equation (6.11) for a contact angle θ of 0° we force the values for $\sigma_{w\text{-}s}$ and $\sigma_{nw\text{-}s}$ to be consistent:

$$\sigma_{nw\text{-}s} - \sigma_{w\text{-}s} = \sigma_{w\text{-}nw}\cos\theta \qquad (6.11)$$

Because of the lack of experimental values of interfacial tensions between solid and fluids, we used arbitrary values for $\sigma_{nw\text{-}s}$ and $\sigma_{w\text{-}s}$ but require their difference to satisfy equation (6.11) and be of similar magnitude to $\sigma_{w\text{-}nw}$. Because $a_{w\text{-}s} + a_{nw\text{-}s} = a_s = constant$, the derivatives $(\partial a_{nw\text{-}s}/\partial S_w)$ and $(\partial a_{w\text{-}s}/\partial S_w)$ in equation (6.6) necessarily have the same absolute value but opposite sign. In the next section we will show the polynomials for the area-saturation curves and check that this claim is true. Finally, we used $\sigma_{nw\text{-}s} = 0.1228$ N/m and $\sigma_{w\text{-}s} = 0.0508$ N/m.

The calculated rates of change of surface and dissipated free energies per unit pore volume (*S* and *D*, respectively) and their relationships with capillary pressure are shown in the next sections. We estimated their values for three situations: simulations of drainage and imbibition in computer generated packs of spheres, simulations of drainage

and imbibition in geometries extracted from microtomographic images of real porous media, and experimental data collected from experiments in glass beads and volcanic tuff.

6.2.2. Simulation of Drainage in Computer Generated Packs of Spheres

Having the configuration of phases at each drainage step from LSMPQS simulation in a computer generated dense disorder pack of 91 spheres of radius R = 100 μm and voxel size dx = 0.04 R, we start by calculating the interfacial areas at every drainage step, using the LSMPQS routine "compute_area_simulation". The simulation gives us the total solid area a_s, total wetting phase area a_w, total non-wetting phase area a_{nw}, and the wetting-non-wetting interfacial area $a_{w\text{-}nw}$ but we still need to calculate the wetting-solid $a_{w\text{-}s}$ and non-wetting-solid $a_{nw\text{-}s}$ interfacial areas. We do so by using the following relationship between interfacial areas (Dalla *et al.*, 2002):

$$a_{nw\text{-}s} = \frac{1}{2}\,(a_{nw} + a_s - a_w) \tag{6.12}$$

$$a_{w\text{-}s} = \frac{1}{2}\,(a_w + a_s - a_{nw}) \tag{6.13}$$

These areas are subsequently normalized by the bulk volume as equation (6.6) requires specific interfacial areas. Afterward, we found the third order polynomial that fit the curves of interfacial area ($a_{w\text{-}nw}$, $a_{w\text{-}s}$ and $a_{nw\text{-}s}$) to wetting phase saturation. The wetting-non-wetting interfacial area curve is expected to increase as wetting phase saturation decreases, reaching a maximum at saturations between 20 and 30% and then decreasing for smaller saturations, according to experiments reported in the literature

(Kim *et al.*, 1997; Anwar *et al.*, 2000; Rao *et al.*, 2000; Schaefer *et al.*, 2000). The wetting-solid area is expected to decrease monotonically from a value equal to the total solid area at 100% wetting phase saturation whereas the non-wetting-solid interfacial area is expected to increase monotonically from a value of 0 at 100% wetting phase saturation at the same rate that the wetting-solid interfacial area decreases.

Plots of the specific interfacial area versus water saturation are shown in Figure 6.1, Figure 6.2 and Figure 6.3, together with the fitted 3rd order polynomial. Indicated by a dashed line in the plots for $a_{w\text{-}s}$ and $a_{nw\text{-}s}$ is the value of the specific solid area calculated from simulation. The shape of the curves agrees with the expectations from experiments mentioned above as well as from simulations obtained with a different algorithm (Gladkikh and Bryant, 2003).

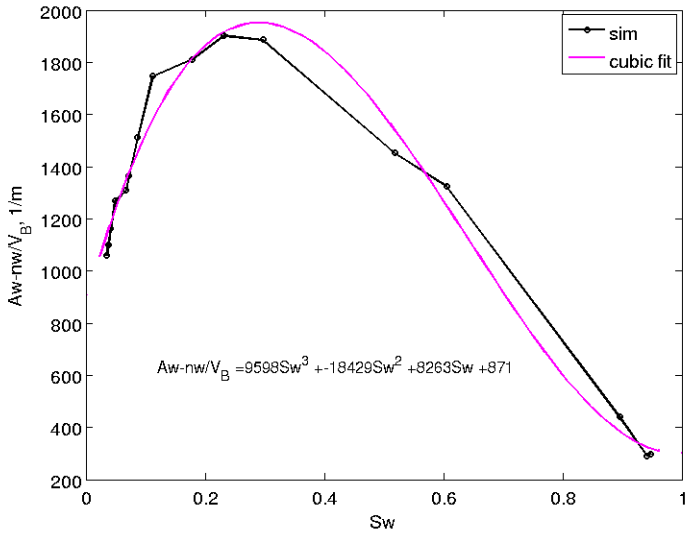

Figure 6.1: Wetting-non-wetting interfacial area per bulk volume *vs*. water saturation for simulated drainage of a computer generated pack of 91 spheres of radius R = 100 μm with a voxel size $dx = 0.04R$.

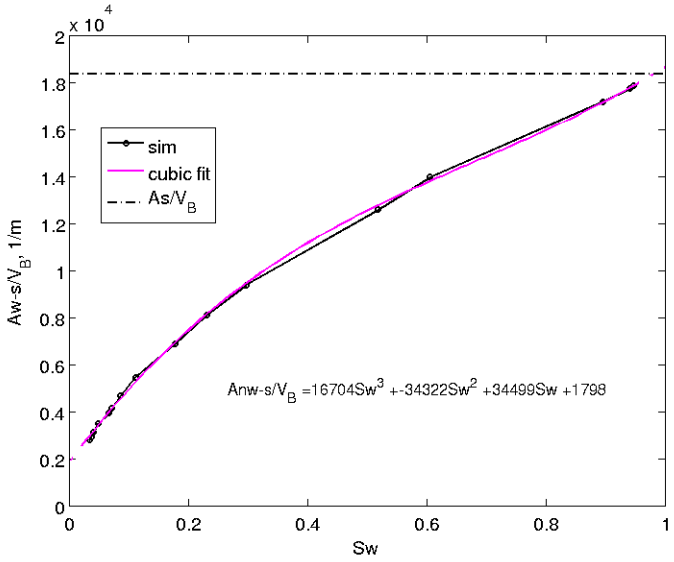

Figure 6.2: Wetting-solid interfacial area per bulk volume *vs*. water saturation for simulated drainage of a computer generated pack of 91 spheres of radius R = 100 μm with a voxel size $dx = 0.04R$.

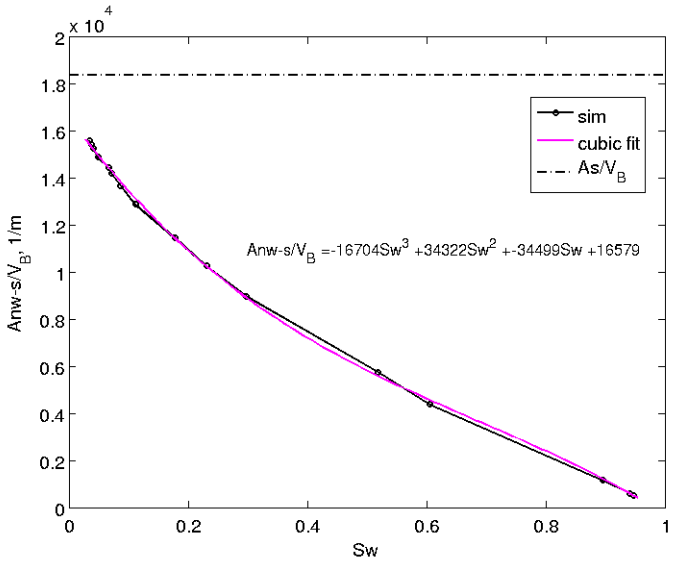

Figure 6.3: Non-wetting-solid interfacial area per bulk volume *vs*. water saturation for simulated drainage of a computer generated pack of 91 spheres of radius R = 100 μm with a voxel size $dx = 0.04R$.

Notice that the fitted 3rd order polynomials for the wetting-solid and non-wetting solid interfacial area curves have the same value but opposite sign for every coefficient except for the constant. The derivatives of these two polynomials with respect to wetting phase saturation ($\partial a_{w\text{-}s}/\partial S_w$) and ($\partial a_{nw\text{-}s}/\partial S_w$) will have the same value but opposite sign at every drainage step. As we said earlier (section 6.2.1) we can take this value as common factor that multiplies the difference in the interfacial tension between $\sigma_{nw\text{-}s}$ and $\sigma_{w\text{-}s}$ in equation (6.6). Since $a_{w\text{-}s} + a_{nw\text{-}s} = a_s$, the sum of the two polynomials should be a constant of value close the total solid area per unit bulk volume. In this specific case the sum of the polynomials yields a value of 18,377 m^{-1}. The value of the specific solid area from LSMPQS simulation is 18,378 m^{-1}. We are going to check these values with the value of specific solid area from the analytical expression:

$$\frac{A_s}{V_B} = \frac{3}{R}(1-\phi) \qquad (6.14)$$

This pack of spheres of radius R = 100 μm has a porosity ϕ equal to 34.5%, yielding a specific area from equation (6.14) equal to 19,650 m^{-1}. The values of specific solid area from the polynomial fitting and the LSMPQS simulation are within 7% of the analytical value from equation (6.14), indicating that the polynomial fitting and LSMPQS method estimations are fairly accurate.

From the polynomials, we calculated the derivative of the specific interfacial area with respect to wetting phase saturation S_w for every drainage step, and applied equation (6.8) to estimate the rate of change of surface free energy per unit pore volume (S) and then (6.9) to estimate the rate of change of dissipated energy to bulk phases per unit pore volume (D) during drainage.

Figure 6.4 shows a plot of the individual terms in equation (6.6), i.e. the derivatives with respect to wetting phase saturation of $a_{w\text{-}nw}$, $a_{w\text{-}s}$ and $a_{nw\text{-}s}$ multiplied by their corresponding interfacial tension σ and $(-1/\phi)$, with respect to S_w, in order to see how they individually compare. Shown in the same figure is the computed rate of change of the surface free energy per unit pore volume with respect to wetting phase saturation, S, which is the sum of the individual contributions of the interfaces. Notice that the derivative of the specific wetting-non-wetting interfacial area changes sign during drainage being equal to zero at the maximum value of $a_{w\text{-}nw}$ (cf. Figure 6.1)

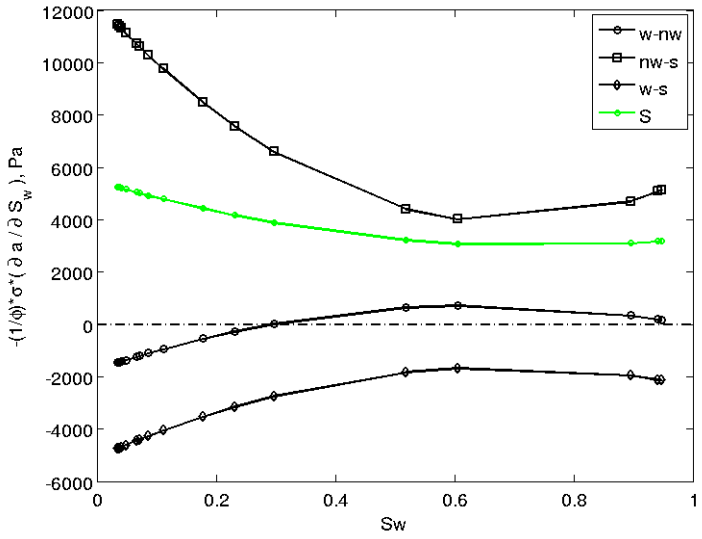

Figure 6.4: Partial derivatives of specific interfacial areas and rate of change of surface free energy per unit pore volume with respect to S_w for simulated drainage of a computer generated pack of 91 spheres of radius R = 100 μm with a voxel size $dx = 0.04R$.

Figure 6.5 shows the capillary pressure curve for the LSMPQS simulation of drainage in the computer generated pack. Shown in the same figure is the computed rate

of change of the surface free energy per unit pore volume with respect to wetting phase saturation, S, which has a positive value that increases in all through drainage. The value of S is smaller than the capillary pressure as expected from the thermodynamic analysis previously discussed in this chapter. Following equation (6.9) we subtract the value of S from the capillary pressure P_c at every saturation point to estimate the rate of change of dissipated energy per unit volume with respect to wetting phase saturation, D. The result is shown in Figure 6.6.

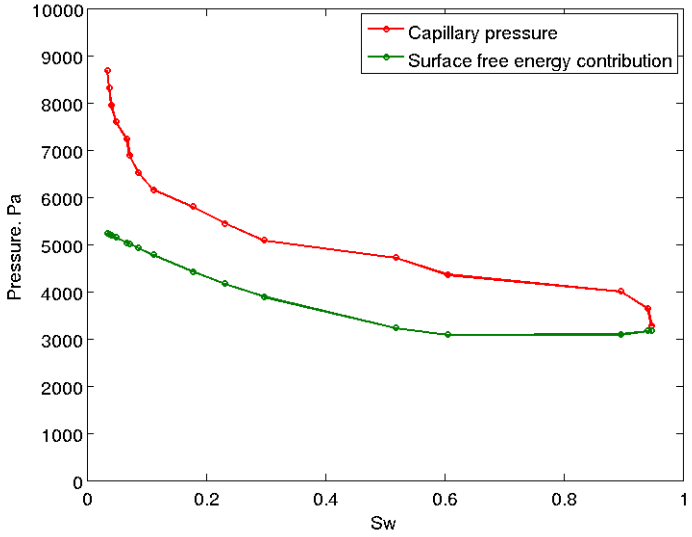

Figure 6.5: Capillary pressure and rate of change of surface free energy per unit pore volume with respect to S_w for simulated drainage of a computer generated pack of 91 spheres of radius R = 100 μm with a voxel size $dx = 0.04R$.

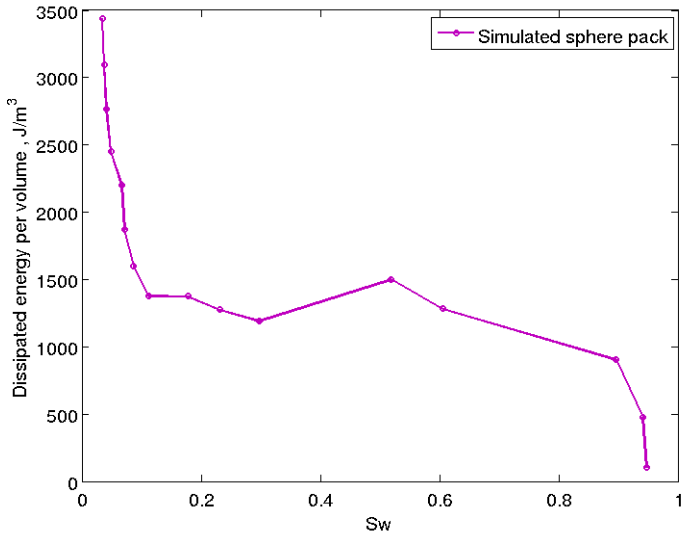

Figure 6.6: Rate of change of dissipated free energy per unit pore volume with respect to S_w for simulated drainage of a computer generated pack of 91 spheres of radius R = 100 μm with a voxel size $dx = 0.04R$.

The rate of change (with respect to wetting phase saturation) of energy dissipated to the bulk phases per unit pore volume for drainage, D, is positive throughout drainage as shown in Figure 6.6 as expected from Morrow's work. The dissipation term D is small during the first part of the drainage displacement ($S_w > 0.9$), is roughly constant ($10 < D < 15$ J/m^3) during percolation, then increases in the late stage of drainage ($S_w < 0.1$).

The fact that D is larger near the drainage endpoint (i.e. for $S_w < 0.1$) may be caused by a large number of irreversible events (menisci pushing through pore throats) per increment in S_w compared to during percolation, when a single Haines jump can fill many pores and the irreversibility per increment in S_w is smaller.

Effect of Grid Resolution

To assess the effect of the computational grid we repeated the calculation in the same pack of 100 spheres of radius R = 100 μm but with a larger voxel of size, dx = 0.08R. Figure 6.7, Figure 6.8 and Figure 6.9 show the curves of specific interfacial areas versus water saturation with their corresponding polynomial fitting. The specific solid area from simulation in this case is 16,220 m^{-1} and is shown as a dotted line in the plots for $a_{w\text{-}s}$ and $a_{nw\text{-}s}$. The result of adding the two fitted polynomials in Figure 6.8 and Figure 6.9 is 16,221 m^{-1}. The porosity of the pack with a voxel size dx = 0.08R is 35.5% and the analytical value of the specific area from equation (6.14) is equal to 19,347 m^{-1}, therefore we are underestimating this interfacial area by 16%. Most possibly we will be underestimating the interfacial areas as well.

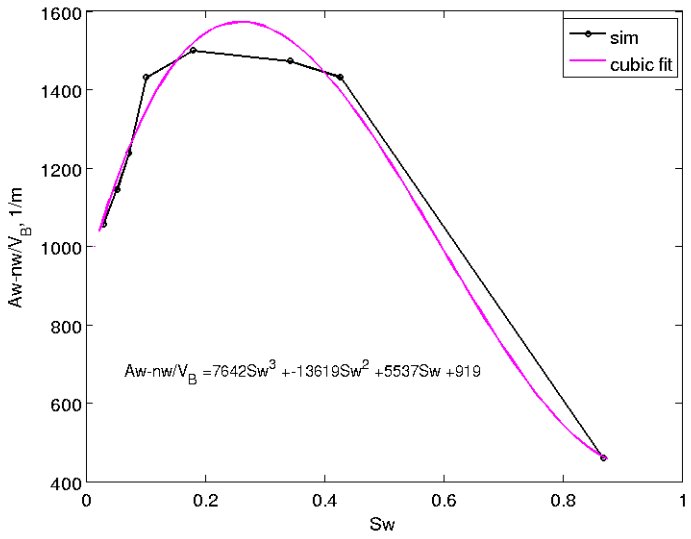

Figure 6.7: Wetting-non-wetting interfacial area per bulk volume *vs*. water saturation for simulated drainage of a computer generated pack of 91 spheres of radius R = 100 μm with a voxel size dx = 0.08R.

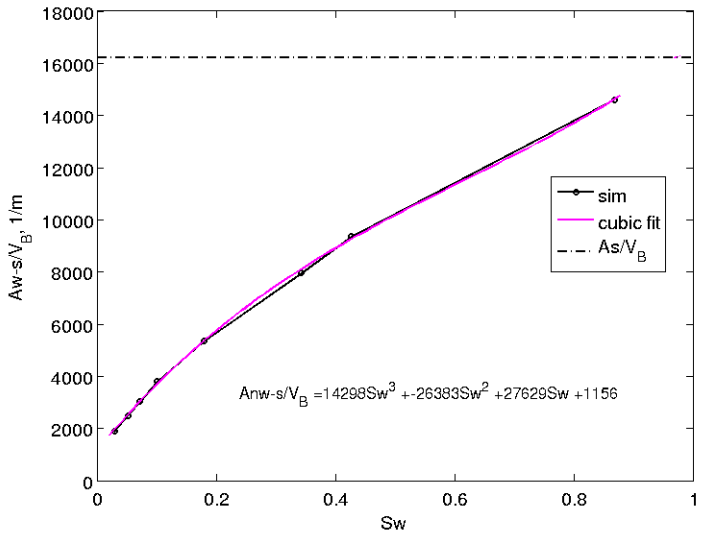

Figure 6.8: Wetting-solid interfacial area per bulk volume *vs*. water saturation for simulated drainage of a computer generated pack of 91 spheres of radius R = 100 μm with a voxel size $dx = 0.08R$.

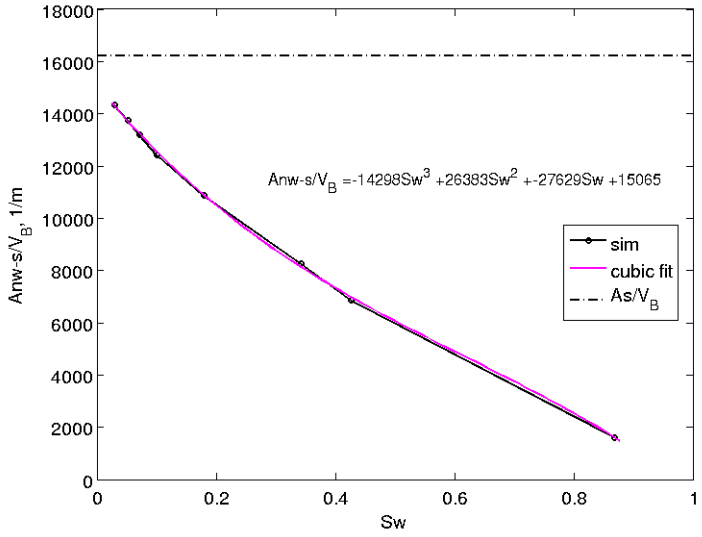

Figure 6.9: Non-wetting-solid interfacial area per bulk volume *vs*. water saturation for simulated drainage of a computer generated pack of 91 spheres of radius R = 100 μm with a voxel size $dx = 0.08R$.

Figure 6.10 shows the partial derivatives of the specific interfacial areas with respect to wetting phase saturation and the rate of change of surface free energy per unit pore volume with respect to S_w, S, that results from adding the 3 partial derivative terms (cf. equation (6.8)). We observe smaller values in general for each interfacial area contribution and the value of S than in the case of finer grid resolution (cf. Figure 6.10).

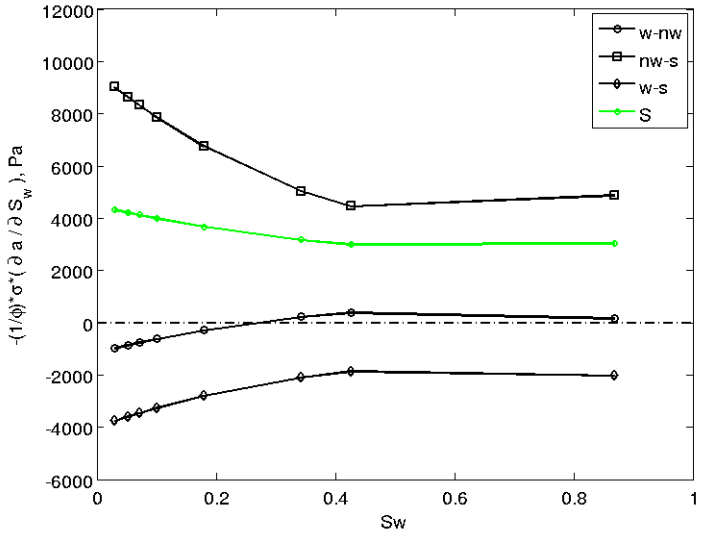

Figure 6.10: Partial derivatives of specific interfacial areas and rate of change of surface free energy per unit pore volume with respect to S_w for simulated drainage of a computer generated pack of 91 spheres of radius R = 100 μm with a voxel size $dx = 0.08R$.

In Figure 6.11 we show the capillary pressure curve for drainage together with the rate of change of surface free energy per unit pore volume with respect to wetting phase saturation. The trend is the same as found with finer resolution simulation (Figure 6.5),

with the rate of change of surface free energy per unit pore volume being positive and smaller than the capillary pressure.

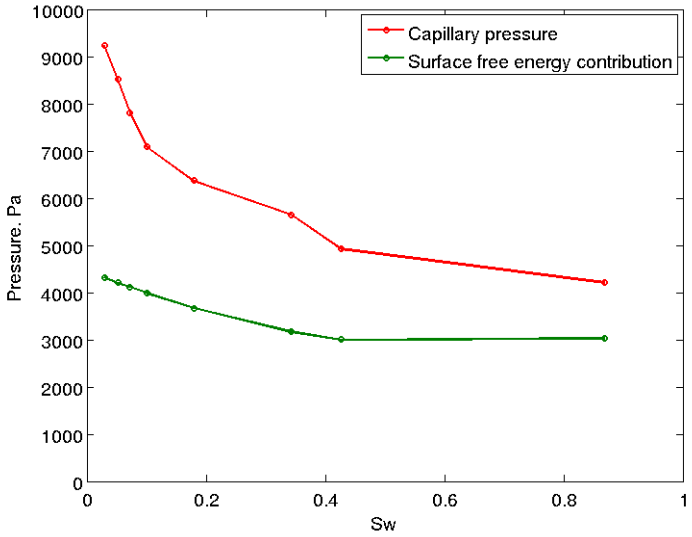

Figure 6.11: Capillary pressure and rate of change of surface free energy per unit pore volume with respect to S_w for simulated drainage of a computer generated pack of 91 spheres of radius R = 100 μm with a voxel size $dx = 0.08R$.

The rate of change of dissipated energy per unit pore volume D computed for this case is shown in Figure 6.12 together with the value from the finer resolution case. D takes larger values for the larger voxel size, but the general increasing trend during drainage process is observed for both cases. The capillary pressure P_c had larger values for the simulation in the coarser grid (dx =0.08R) than in the finer grid (dx =0.08R). On the other hand, the value of S was smaller for the coarser resolution, as a result of underestimating the interfacial areas. We have slightly larger values for the fitting of $a_{w\text{-}nw}$ versus S_w for the finer resolution (Figure 6.1) than for the coarser (Figure 6.7) and as we mention before, the terms of the interfacial area derivatives take on larger values for the finer resolution (Figure 6.4 *vs.* Figure 6.10), making S larger in the finer resolution

case. Since D is calculated as the difference between P_c and S per equation (6.9), its value is larger for the coarser resolution. Figure 6.13 shows P_c and S for the two studied resolutions.

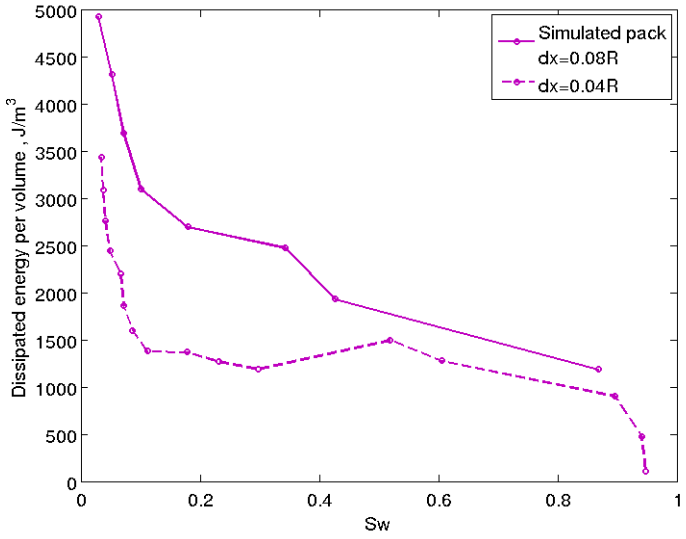

Figure 6.12: Comparison of the rate of change of dissipated free energy per unit pore volume with respect to S_w for simulated drainage of a computer generated pack of 91 spheres of radius R=100 μm using two different voxel sizes dx = 0.04R and dx = 0.08R.

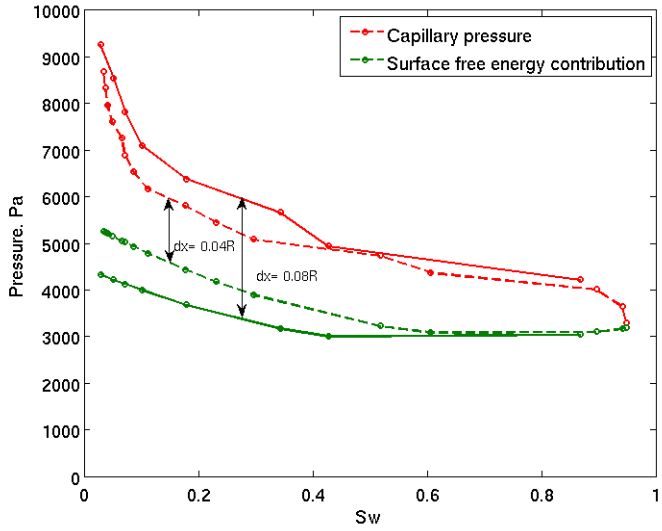

Figure 6.13: Comparison of the capillary pressure and rate of change of surface free energy per unit pore volume with respect to S_w for simulated drainage of a computer generated pack of 91 spheres of radius R = 100 μm for two voxel sizes $dx = 0.08R$ (continuous line) and $dx = 0.04R$ (dashed line).

The quantity D is a measure of how fast bulk phase free energies change with saturation. The results in Figure 6.12 suggest that this rate is larger near drainage endpoint, where presumably we are just seeing the last few pore throats undergoing Haines jumps one at a time. An interesting observation in these results (Figure 6.12) is that even if the general trend of the rate of change of dissipated free energy per unit pore volume is to increase in magnitude as drainage progresses, there are a couple of places for the case finer resolution case ($dx = 0.04R$) in which the rate of change from one saturation to the succeeding saturation decreases (e.g. between $S_w = 0.5$ and $S_w = 0.3$) in Figure 6.6). A possible explanation for this may be that there are a larger number of reversible events (that do not contribute to the dissipation of energy) occurring in those steps. However, the same effect was not observed in the case of $dx = 0.08R$, probably

because the coarser resolution is not as effective as the finer estimating the small variations in interfacial area that take place during reversible events.

In the next section we will analyze the results from the simulations of imbibition in the same pack of spheres shown here, also for two different grid resolutions.

6.2.3. Simulation of Imbibition in Computer Generated Packs of Spheres

Here we repeat the analysis of the previous section to the capillary pressure and interfacial areas that result from the simulation of imbibition in the same dense disordered pack of 91 spheres of 100 μm radius where we analyzed drainage. Imbibition was started from the endpoint of the drainage simulation. Figure 6.26, Figure 6.27 and Figure 6.28 show the curves of specific interfacial area versus wetting phase saturation for the simulation having a resolution of $dx = 0.04R$. The specific solid area from simulation in this case is 18,378 m^{-1} and is shown as a dotted line in the plots for $a_{w\text{-}s}$ and $a_{nw\text{-}s}$. The result of adding the two fitted polynomials in Figure 6.15 and Figure 6.16 is 18,388 m^{-1}. The porosity of the pack with a voxel size $dx = 0.04R$ is 34.5% and the analytical value of the specific area from equation (6.14) is equal to 19,650 m^{-1}, thus our simulation value is within 7% of the analytical as was the case for drainage.

The wetting-non-wetting specific interfacial area for imbibition in Figure 6.14 is larger than specific area for drainage in Figure 6.1 because of the hysteresis in interfacial areas that we discussed in Chapter 3. On the other hand, the results from simulation of imbibition using a network model reported by Gladkikh and Bryant (2003) show larger values for the wetting-non-wetting interfacial area at large wetting phase saturations than our results from LSMPQS. This is caused by trapped blobs of non-wetting phase in the network model that we did not observe in the LSMPQS simulation.

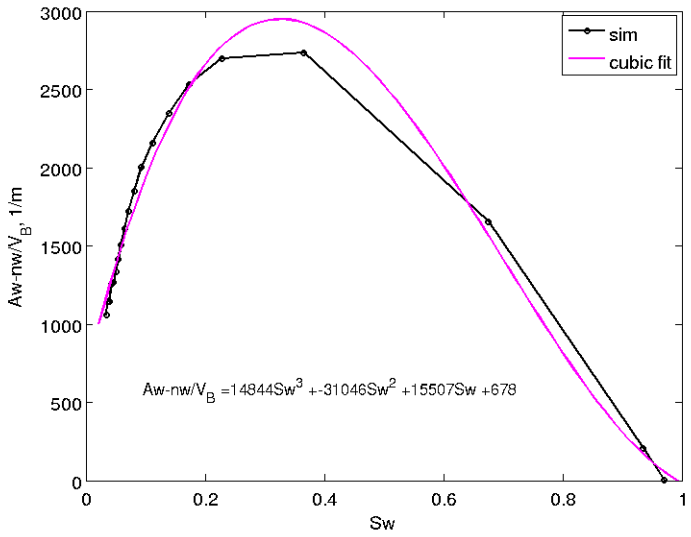

Figure 6.14: Wetting-non-wetting interfacial area per bulk volume *vs*. water saturation for simulated imbibition of a computer generated pack of 91 spheres of radius R = 100 μm with a voxel size $dx = 0.04R$.

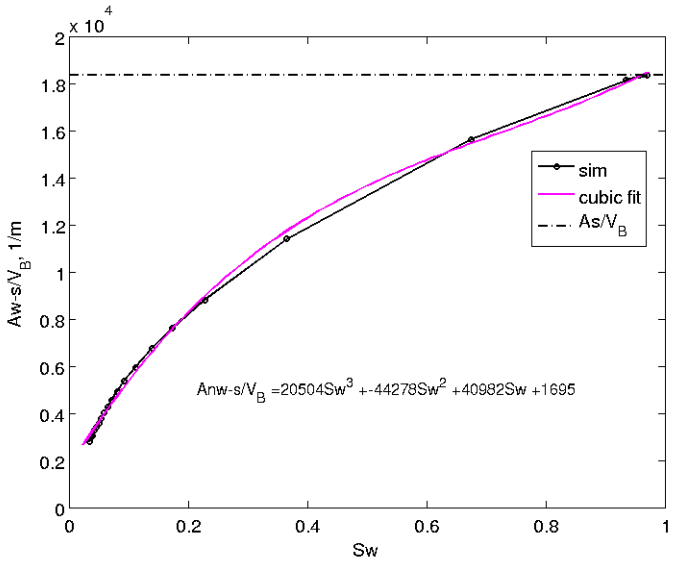

Figure 6.15: Wetting-solid interfacial area per bulk volume *vs*. water saturation for simulated imbibition of a computer generated pack of 91 spheres of radius R = 100 μm with a voxel size $dx = 0.04R$.

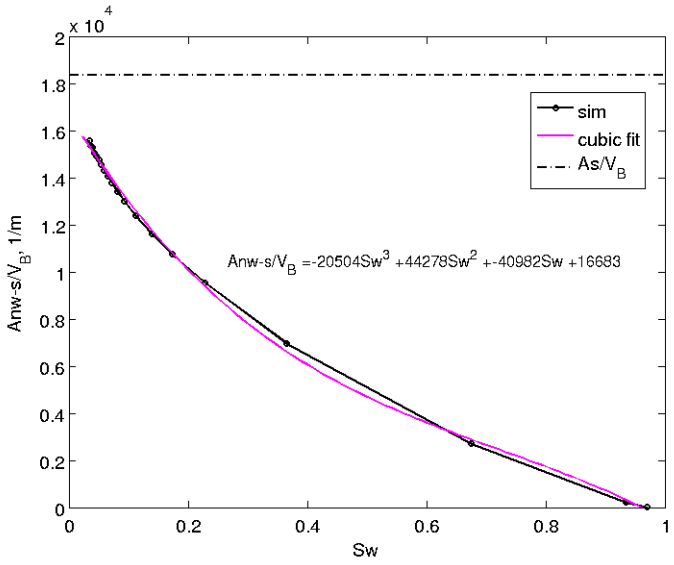

Figure 6.16: Non-wetting-solid interfacial area per bulk volume *vs*. water saturation for simulated imbibition of a computer generated pack of 91 spheres of radius R = 100 μm with a voxel size $dx = 0.04R$.

Figure 6.17 shows the individual terms partial derivatives of the specific interfacial areas with respect to wetting phase saturation (cf. equation (6.6)) together with the value of the rate of change of surface free energy per unit pore volume with respect to wetting phase saturation (S) that results from adding the partial derivative terms.

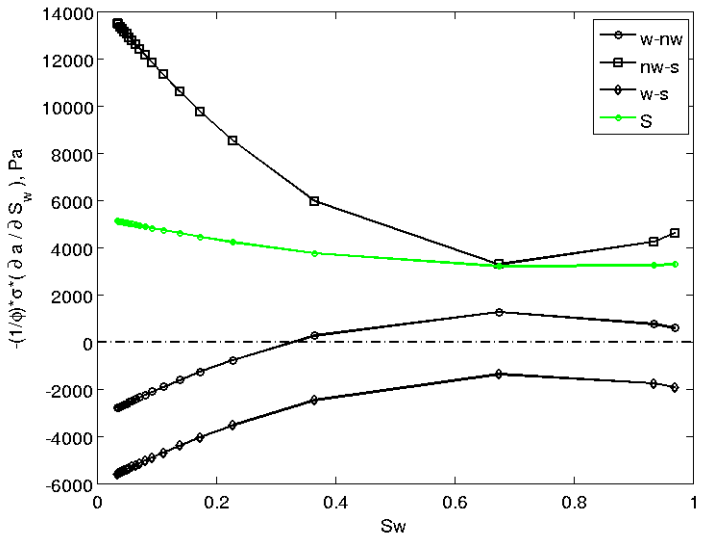

Figure 6.17: Partial derivatives of specific interfacial areas and rate of change of surface free energy per unit pore volume with respect to S_w for simulated imbibition of a computer generated pack of 91 spheres of radius R=100 μm with a voxel size $dx = 0.04R$.

The specific interfacial area curves follow the expected trend with wetting phase saturation. The rate of change of surface free energy per unit pore volume with respect to wetting phase saturation (S) for imbibition in the sphere pack is calculated with equation (6.8) and shown in Figure 6.18 together with the capillary pressure curve for imbibition.

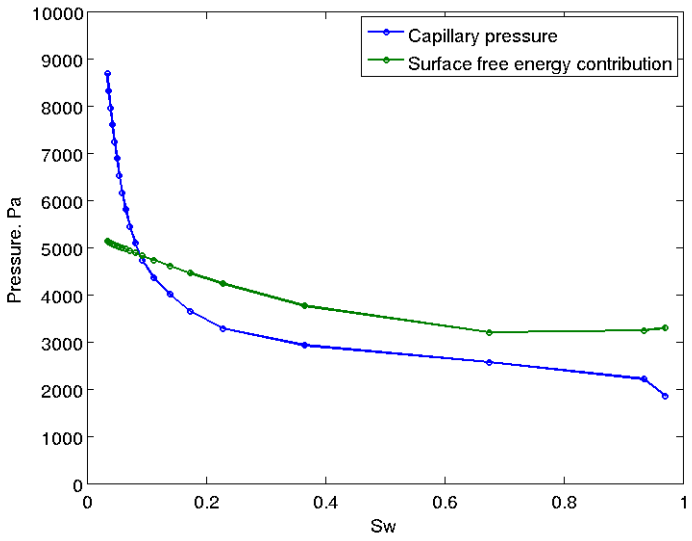

Figure 6.18: Capillary pressure and rate of change of surface free energy per unit pore volume with respect to S_w for simulated imbibition of a computer generated pack of 91 spheres of radius R = 100 μm with a voxel size $dx = 0.04R$.

The value of S is positive all through imbibition and shows a decreasing trend as imbibition progresses. The value of S is larger than the capillary pressure starting at wetting phase saturation of 9% and until the end of imbibition. This is the expected behavior from Morrow's analysis. However, S is smaller than the capillary pressure at the beginning of imbibition, where wetting phase saturation changes only slightly with the change in capillary pressure. The imbibition simulation started from the endpoint of drainage, where all of the wetting phase is in form of pendular rings, as we saw earlier in Chapter 3. The decrease in pressure at the beginning of imbibition causes the expansion of the pendular rings. Pendular ring expansion is a reversible series of events until snapoff of the non-wetting phase occurs and menisci are formed. Comparing the P_c-S_w curves for drainage and imbibition, as shown in Figure 6.19, we can conclude that only the last 3 drainage steps are all pendular rings, because the first steps of imbibition curve overlie these drainage steps.

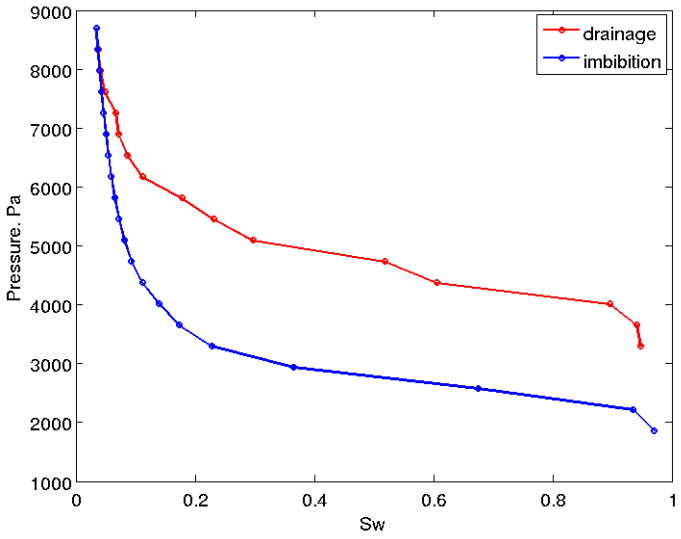

Figure 6.19: Capillary pressure *vs.* wetting phase saturation for simulated drainage and imbibition of a computer generated pack of 91 spheres of radius R = 100 μm with a voxel size $dx = 0.04R$.

Alternatively, we compared the value of S for drainage (Figure 6.5) with the value for imbibition (Figure 6.18) and we observed that both terms are almost indistinguishable, as shown in Figure 6.20. The contributions of the derivatives of the interfacial area terms that make up the value of S, shown separately for drainage and imbibition in Figure 6.10 and Figure 6.17 respectively, are compared in Figure 6.21 where we see that the absolute values of the derivatives are consistently larger for imbibition than for drainage at small S_w (before the maximum on $a_{w\text{-}nw}$, which corresponds to zero derivative) then take similar values in the range of S_w between 0.3 and 0.6 before they start to differ at larger Sw. The summation of these terms result on the value of S per equation (6.6).

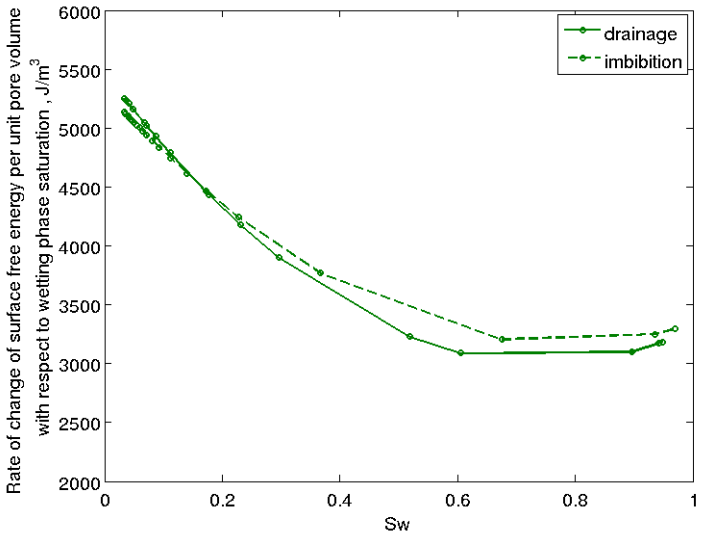

Figure 6.20: Comparison of the rate of change of surface free energy per unit pore volume with respect to S_w for simulated drainage and imbibition of a computer generated pack of 91 spheres of radius R = 100 μm with a voxel size $dx = 0.04R$.

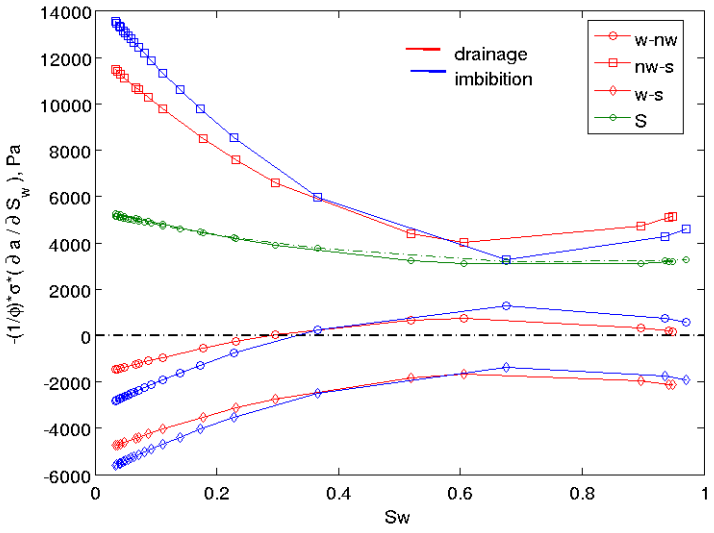

Figure 6.21: Comparison of the partial derivatives of specific interfacial areas and rates of change of surface free energy per unit pore volume with respect to S_w for simulated drainage and imbibition of a computer generated pack of 91 spheres of radius R = 100 μm with a voxel size $dx = 0.04R$.

This absence of hysteresis in the S term suggests that irreversible events during drainage dissipate more energy for a given increment in S_w than during imbibition, since D results from the difference between P_c and S, and P_c is larger during drainage than during imbibition.

Besides the observation of the lack of hysteresis in S, what is important to notice here is that the behavior of S at the early stages of imbibition is not in agreement with Morrow's theory, which predicts that the released surface free energy has to be larger than the PV work done by the system during imbibition (cf. equations (6.4) and (6.10)). The fitting of polynomials to the interfacial area-saturation curves at low wetting phase saturations in Figure 6.14 to Figure 6.16 is good and does not appear to be the cause of this violation of Morrow's principle.

At the beginning of imbibition, if all the wetting phase is in form of pendular rings, the decrease in pressure will start expanding the rings without a perceptible change in the configuration of the bulk phases until menisci are formed. In this case the PV work done by the system should be equal to the reduction in energy associated with the interfaces, and the energy dissipated to the bulk phases should be minimal. We are going to check if P_c is equal to S in the simple case of a pendular ring between two spheres of radius R in point contact in a box of dimensions $4R \times 2R \times 2R$. Figure 6.22 shows a schematic of the toroidal liquid bridge between the two grains.

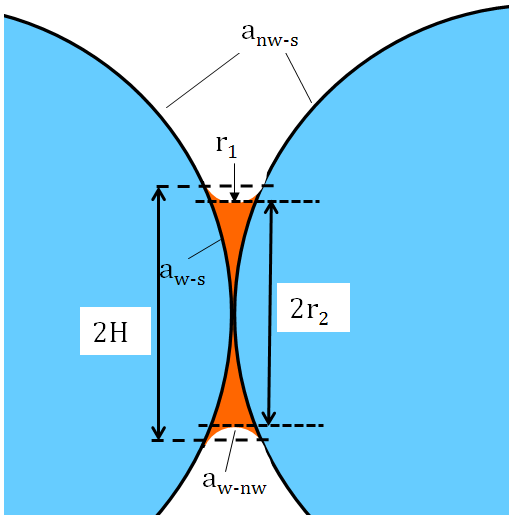

Figure 6.22: Schematic of toroidal bridge between two spheres in point contact.

The formula for the w-nw interfacial area for a pendular ring, assuming a toroidal shape, is calculated in Anna Johnson's MS thesis (2001) and reproduced here in Appendix E. We calculated the w-s interfacial area as the surface of a spherical cap (Appendix E), and the nw-s interfacial area as the surface of the sphere minus the surface of the spherical cup. We calculated the three interfacial areas for different curvatures of the w-nw interface, and then calculated *S* with equation (6.8), using the same interfacial tensions that we used for the simulations in the sphere packs. P_c was calculated as curvature times the w-nw interfacial tension. 1 full pendular ring exists between the two spheres in the box and 10 "half" pendular rings exist in the contacts of the spheres with the sides of the box, making a total of 6 full pendular rings. The results are shown in Figure 6.23, where we see that P_c and *S* steadily increase at the same rate with the decrease in S_w (increase in curvature). There is a consistent difference of 0.036 $Nm^{-1}R^{-1}$ for this case presumably due to the fact that a nodoid, rather than a toroid is the correct

shape for a pendular ring, thus equations for a nodoid would have to be used to find S equal to P_c.

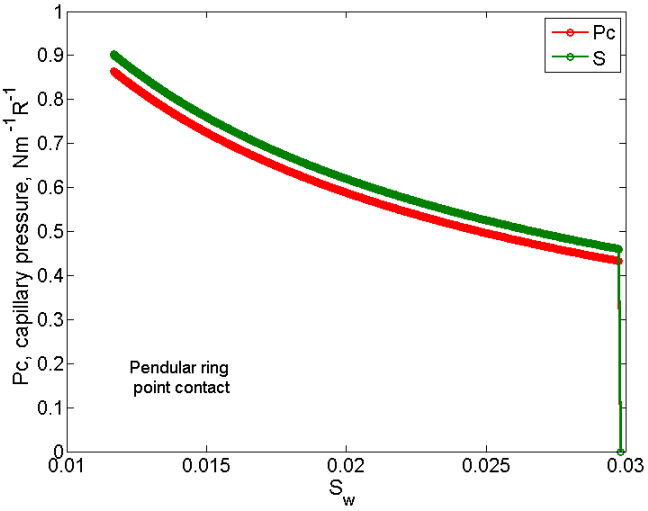

Figure 6.23: Capillary pressure and rate of change of surface free energy per unit pore volume with respect to S_w for the pendular rings between two spheres of radius R, contained in a box of dimensions equal to $4R \times 2R \times 2R$.

The same exercise was repeated in 2D. In this case we calculated the variation of the length of the line that separates w-nw, w-s and nw-s phases with respect to the wetting phase saturation, measured as the ratio of the area of the wetting phase over the area of the void space. The system in this case consists of two circles of radius R inside a rectangle of dimensions $4R \times 2R$. Relevant formulas are shown in Appendix E. The result is shown in Figure 6.24, where we can see that P_c and S (named $P_c(A)$ and $S(A)$ in Figure 6.24 to indicate 2D) coincide during the reversible displacement, thus only one line is shown.

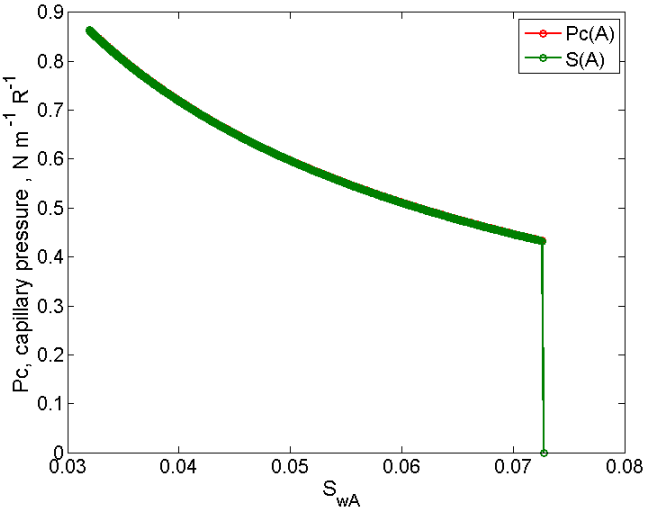

Figure 6.24: Capillary pressure and rate of change of surface free energy per unit pore area with respect to S_w for the pendular rings between two circles of radius R, contained in a rectangle of dimensions equal to $4R \times 2R$.

This simple scenario proves that, in a reversible displacement, the rate of change of the surface free energy per unit pore volume with respect to wetting phase saturation is nearly equal to the capillary pressure, being the dissipated energy minimal.

Additionally the Meyer-Stowe-Princen (MSP) method to estimate critical curvatures in 2D (Meyer and Stowe, 1965; Princen, 1969a; 1969b; 1970) is based on equating the pressure difference across the meniscus between two phases α and β to a piston-like displacement, yielding:

$$P_c dV = \sum_{\alpha\beta} \sigma_{\alpha\beta} a_{\alpha\beta} \tag{6.15}$$

This method has been widely used to compute capillary pressures in piston like displacements in porous media that contain circular and angular cross sections (Mason and Morrow, 1991; Ma *et al.*, 1996).

The rate of change of dissipated energy per unit pore volume with respect to wetting saturation (D) is calculated with equation (6.10) and shown in Figure 6.25. Because of the anomalous behavior of the rate of change of surface free energy, D takes negative values at the beginning of imbibition. Dissipation cannot be negative, so this part of the curve is contrary to what we expect from Morrow's work. At wetting phase saturation of 9% the rate of change of dissipated energy is equal to zero and then starts taking positive values until the end of imbibition as expected. Per our previous discussion, we would expect the rate of change of dissipated energy per unit pore volume to be equal to zero during the first steps of imbibition while the displacement is most likely reversible.

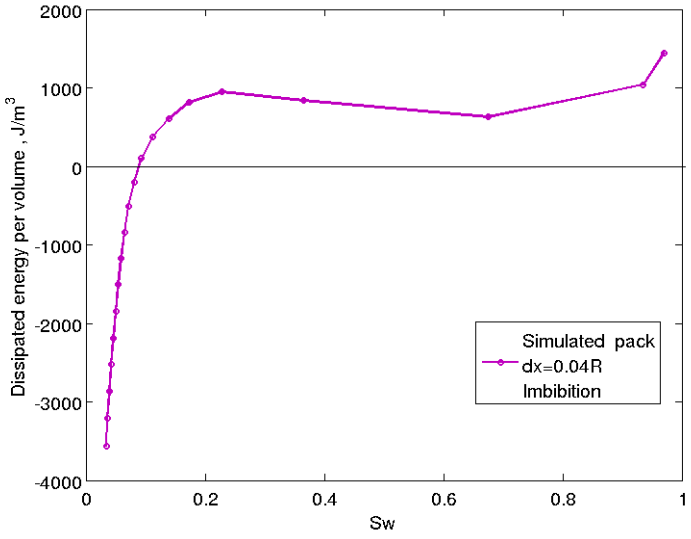

Figure 6.25: Rate of change of dissipated free energy per unit pore volume with respect to S_w for simulated imbibition of a computer generated pack of 91 spheres of radius R=100 μm with a voxel size dx = 0.04R.

Drainage and Imbibition Efficiencies

We have calculated the efficiency of the drainage and imbibition displacements in sphere packs a similar way as shown by Morrow (1970). For drainage, we calculated the fraction of dissipated energy as the ratio of the area under the dissipation curve (Figure 6.6, area equal to 1173 Pa) over the area under the capillary pressure curve (Figure 6.5, area equal to 4492 Pa). Recall that the area under the capillary pressure curve represents the work done in the system during drainage. For drainage we calculated that 26% of the work was dissipated. Morrow (1970) predicted the efficiency for drainage to be equal to 79%, which indicated that the remaining 21% would be dissipated.

For imbibition (recall equation (6.10)) we calculated the fraction of dissipated energy as the ratio of the area under the dissipation curve (Figure 6.25, area equal to 631Pa) over the area under the rate of change of surface free energy per unit volume (Figure 6.18, area equal to 3491 Pa). For imbibition we calculated an 18% of dissipation. Morrow (1970) predicted an efficiency of 92.5% for imbibition which indicates that 7.5% of the work is dissipated. However in Morrow's work, an extra amount of energy corresponding to the trapped non-wetting phase at the end of imbibition was added to the recovered work during imbibition, which increased imbibition efficiency. The amount of trapped non-wetting phase at the end of imbibition in the sphere pack simulations (S_w = 0.97) is not as significant as in Morrow's experiments (S_w = 0.8) and therefore we cannot compare the efficiencies for imbibition directly. Some interesting observation here is that since we observe no hystereis in the rate of change of surface free energy per unit volume (Figure 6.2) the area under the S curves is very similar for drainage (3319 Pa) and imbibition (3491 Pa). This is indicates that the surface free energy during drainage and imbibition is very similar which is possible because of the small residual saturation.

Effect of Grid Resolution

The same anomalous behavior of the rate of change of surface free energy and dissipated energy per unit pore volume has been observed when we repeated the analysis for a coarser resolution (dx = 0.08R). The curves of interfacial specific area versus wetting phase saturation with the 3rd order polynomial fitting line are shown in Figure 6.26, Figure 6.27 and Figure 6.28. The specific solid area from simulation in this case is 16,220 m^{-1} and is shown as a dotted line in the plots for $a_{w\text{-}s}$ and $a_{nw\text{-}s}$. The result of adding the two fitted polynomials in Figure 6.27 and Figure 6.28 is 16,221 m^{-1}. The porosity of the pack with a voxel size dx = 0.08R is 35.5% and the analytical value of the specific area from equation (6.14) is equal to 19,350 m^{-1}, therefore we are underestimating this interfacial area by 16% as was the case for the simulation of drainage in a grid of resolution dx = 0.08R.

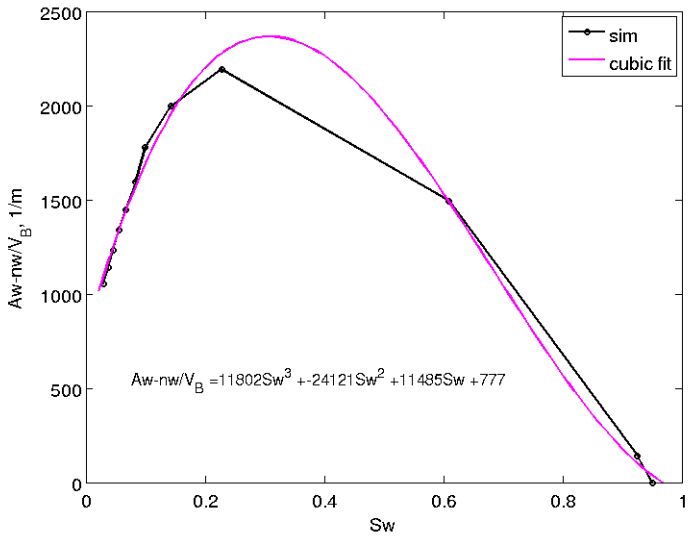

Figure 6.26: Wetting-non-wetting interfacial area per bulk volume *vs*. water saturation for simulated imbibition of a computer generated pack of 91 spheres of radius R=100 μm with a voxel size dx = 0.08R.

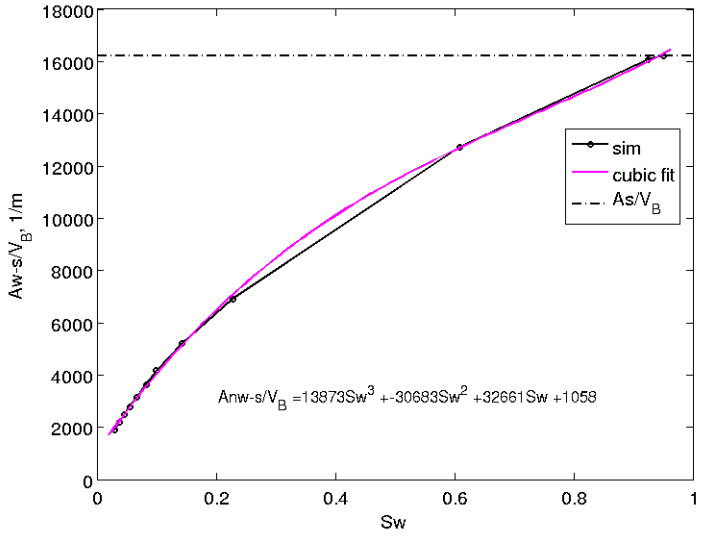

Figure 6.27: Wetting-solid interfacial area per bulk volume *vs*. water saturation for simulated imbibition of a computer generated pack of 91 spheres of radius R=100 μm with a voxel size $dx = 0.08R$.

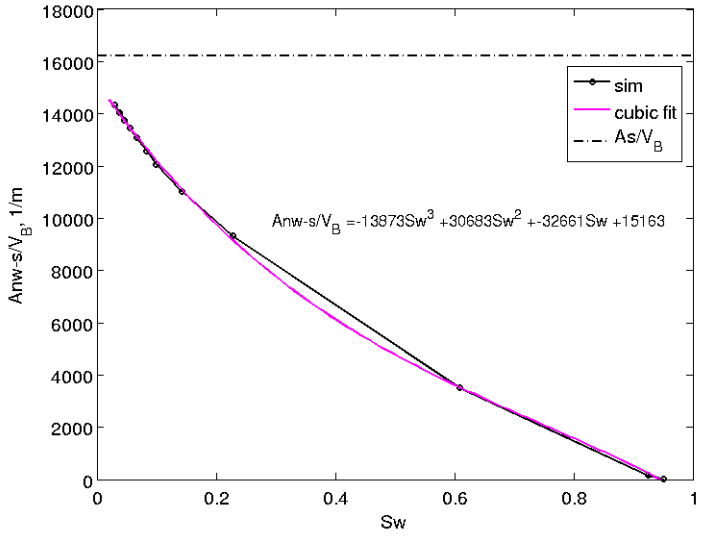

Figure 6.28: Non-wetting-solid interfacial area per bulk volume *vs*. water saturation for simulated imbibition of a computer generated pack of 91 spheres of radius R=100 μm with a voxel size $dx = 0.08R$.

Figure 6.29 shows the partial derivatives of the specific interfacial areas with respect to wetting phase saturation together with the total value of the rate of change of surface free energy per unit volume, *S*.

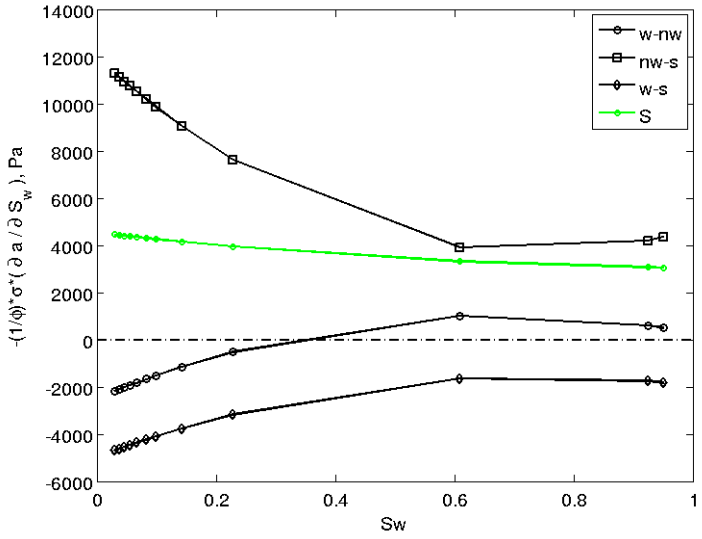

Figure 6.29: Partial derivatives of specific interfacial areas and rate of change of surface free energy per unit pore volume with respect to S_w for simulated imbibition of a computer generated pack of 91 spheres of radius R = 100 μm with a voxel size $dx = 0.08R$.

The capillary pressure and the rate of change of surface free energy per unit pore volume (*S*) are shown in Figure 6.30. The rate of change of dissipated energy per unit pore volume (*D*) is shown in Figure 6.31 together with the result for simulation of imbibition in a grid of voxel size $dx = 0.04R$. In this case *S* is smaller than the capillary pressure and *D* takes negative values from the beginning of imbibition until a wetting phase saturation of 15%, thus the region of anomalous behavior of *S* is larger than the case for $dx = 0.04R$. This suggests another possibility for the anomalous behavior of *S*

near the drainage endpoint: the simulation grid size $dx = 0.04R$, and therefore $dx = 0.08R$, are not good enough to accurately gauge changes in surface area and therefore surface energy. It may be possible that a voxel of size $0.04R$ is larger than the displacement of the interface from one saturation step to the next during the reversible movement of the interface at low S_w, and for that reason we see the rate of change of surface free energy per unit volume to move with remain almost constant at small wetting phase saturations while P_c is increasing. We suggest to run the simulation with an even smaller resolution (e.g. $dx = 0.02R$) to prove this claim.

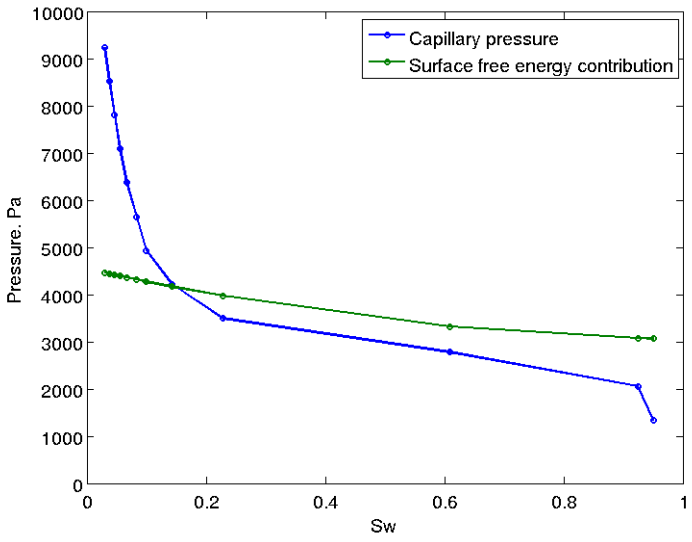

Figure 6.30: Capillary pressure and rate of change of surface free energy per unit pore volume with respect to S_w for simulated imbibition of a computer generated pack of 91 spheres of radius R=100 μm with a voxel size $dx = 0.08R$.

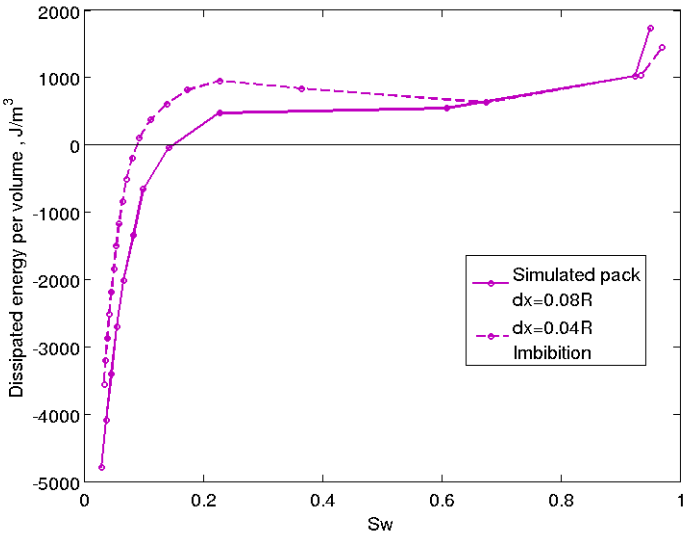

Figure 6.31: Comparison of the rate of change of dissipated free energy per unit pore volume with respect to S_w for simulated imbibition of a computer generated pack of 91 spheres of radius R = 100 μm using two different voxel sizes $dx = 0.04R$ and $dx = 0.08R$.

6.2.4. Simulation of Drainage in a Porous Medium Extracted from X-Ray Images of a Column Packed with Glass Beads

We have seen how surface free energy and dissipated energy contribute to capillary pressure in simulations of drainage and imbibition in computer generated packs of spheres. Now we extend the analysis to geometries of porous media extracted from high-resolution x-ray images of actual packs of glass beads[7].

The procedure to translate the image to a 3D porous media suitable for LSMPQS simulation was explained in Chapter 3. We ran LSMPQS simulations of drainage in these geometries and computed the interfacial areas as we did for the sphere packs. Figure 6.32 is the corresponding 3D model extracted from an image for a section of a column filled

[7] Images courtesy of Dr. Dorthe Wildenschild from Oregon State University

with glass beads whose radii range between 300 and 700 μm. The porosity of the column is 34%. The voxel size is 17 μm. The LSMPQS simulation is run in a smoother version of the digitized image after reinitialization (see Appendix G).

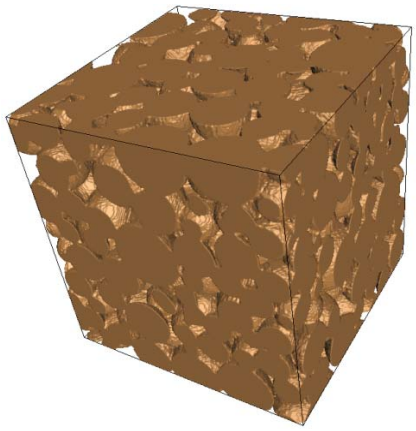

Figure 6.32: Grains identified in high resolution x-ray images of columns packed with glass beads (average grain radius 600 μm).

The specific interfacial area versus water saturation plots that result from LSMPQS simulation of drainage are shown in Figure 6.34, Figure 6.35 and Figure 6.37. The shape of the interfacial area curves is similar to the shape for the computer generated packs of spheres but the specific areas take smaller values since the size of the glass beads here is about 5 times larger than the size of the spheres in the computer generated packs. The total specific solid area from simulation is 3,626 m^{-1}. The result of adding the polynomials that fit the w-s and nw-s curves is 3,626 m^{-1} and the result of applying equation (6.14) for the average radius of 600 μm and a porosity of 34% is 3,300 m^{-1}. Our simulated value for the specific solid area is within 10% of the analytical value.

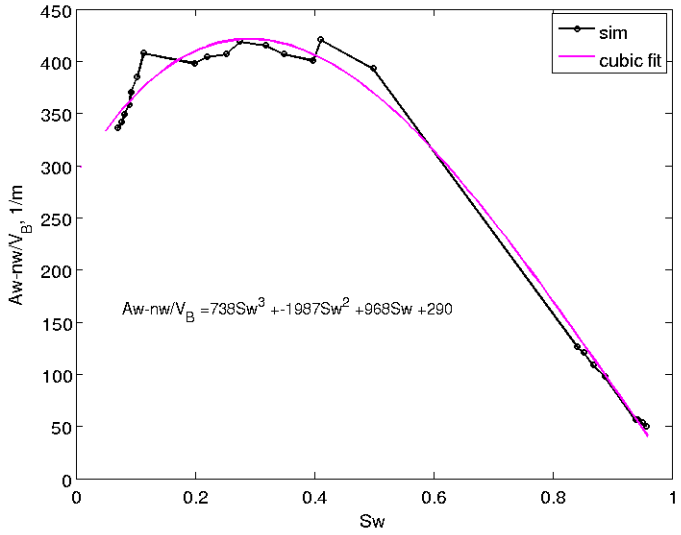

Figure 6.33: Wetting-non-wetting interfacial area per bulk volume *vs*. water saturation for simulated drainage of a porous medium geometry extracted from high resolution x-ray images of a column of glass beads. The voxel size is 17 μm and the average radius of the beads is 600 μm.

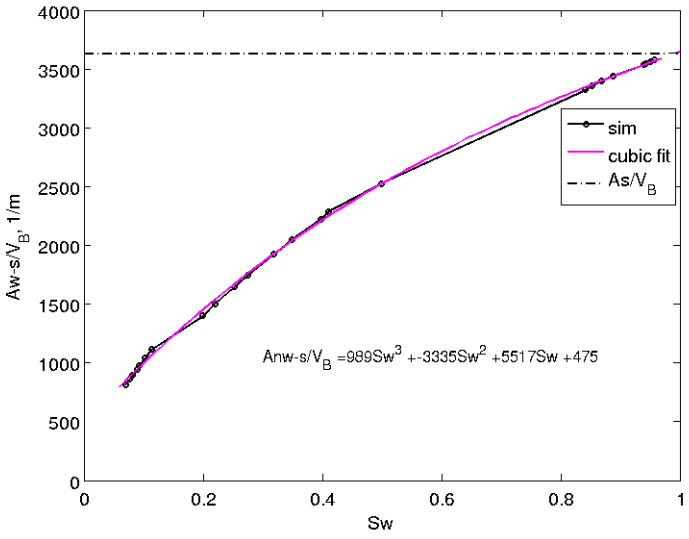

Figure 6.34: Wetting-solid interfacial area per bulk volume *vs*. water saturation for simulated drainage of a porous medium geometry extracted from high resolution x-ray images of a column of glass beads. The voxel size is 17 μm and the average radius of the beads is 600 μm.

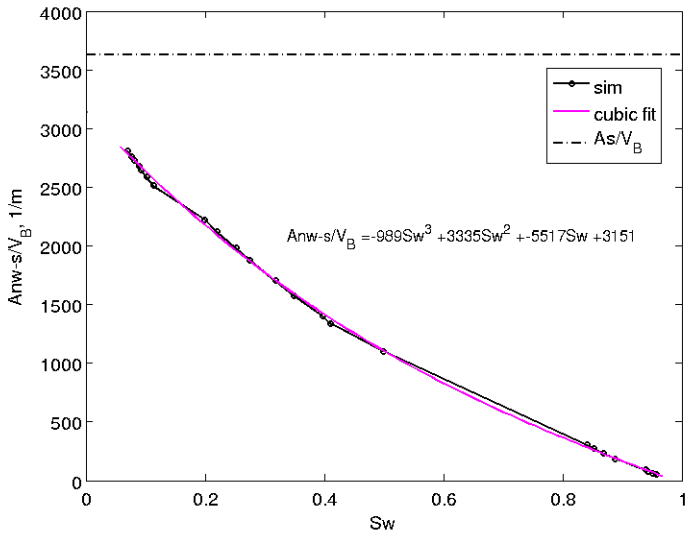

Figure 6.35: Non-wetting-solid interfacial area per bulk volume *vs*. water saturation for simulated drainage of a porous medium geometry extracted from high resolution x-ray images of a column of glass beads. The voxel size is 17 μm and the average radius of the beads is 600 μm.

Figure 6.36 shows the partial derivatives of the specific interfacial areas with respect to wetting phase saturation.

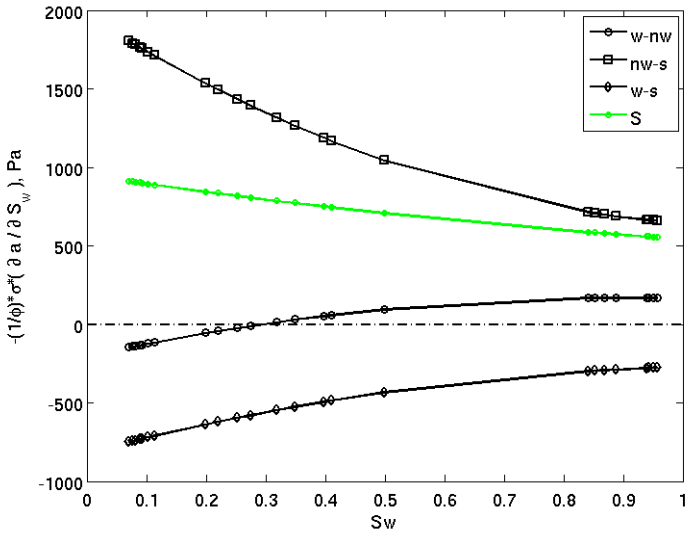

Figure 6.36: Partial derivatives of the interfacial areas *vs*. water saturation for simulated drainage of a porous medium geometry extracted from high resolution x-ray images of a column of glass beads. The voxel size is 17 μm and the average radius of the beads is 600 μm.

We computed the derivatives of the specific interfacial areas using the fitted 3rd order polynomials and calculated the rate of change of surface free energy per volume, S, with equation (6.8). The rate of change of surface free energy per unit pore volume with respect to wetting phase saturation, shown in Figure 6.37, is positive during drainage and smaller than the system's capillary pressure, as was the case in the computer generated packs of spheres, except for the very first step of drainage. The fitting of the polynomials does not seem to be a problem here. In this case we can be facing the same phenomena as in the last steps of imbibition, where a reversible movement of the interface is taking place and the expected behavior would be for S to be equal to P_c. The grid resolution for the LSMPQS simulation may not be fine enough to track the movement of the interface, since it may move less than one voxel size during these reversible steps.

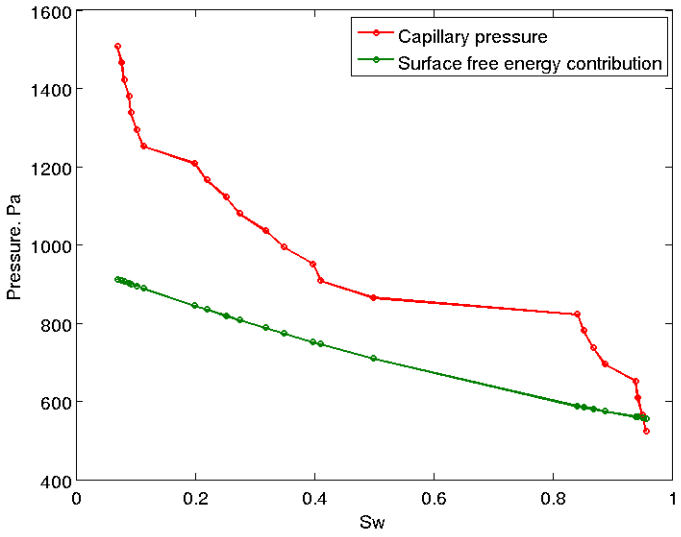

Figure 6.37: Capillary pressure and rate of change of surface free energy per unit pore volume with respect to S_w for simulated drainage of a porous medium geometry extracted from high resolution x-ray images of a column of glass beads. The voxel size is 17 μm and the average radius of the beads is 600 μm.

The rate of change of dissipated energy per unit pore volume with respect to wetting phase saturation, D, is shown in Figure 6.38. Except for the first step, the value of D is positive and shows an increasing trend as drainage advances, as expected from the thermodynamic analysis of Morrow (1970) and Hassanizadeh and Gray (1993).

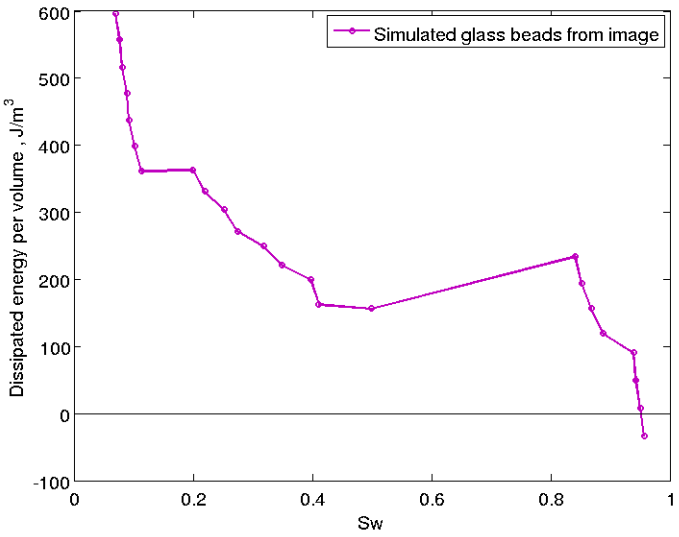

Figure 6.38: Rate of change of dissipated free energy per unit pore volume with respect to S_w for simulated drainage of a porous medium geometry extracted from high resolution x-ray images of a column of glass beads. The voxel size is 17 μm and the average radius of the beads is 600 μm.

No imbibition simulations were run for this porous medium.

As we observed for the simulation of drainage in computer generated packs (Figure 6.6) there are several instances in which the rate of change of surface free energy decreases from one saturation step to the next, for example between $S_w = 0.8$ and $S_w = 0.5$. We discussed for the computer generated packs that this behavior may indicate a smaller number of spontaneous events and consequently less energy is dissipated.

6.2.5. Simulation of Drainage in a Porous Medium Extracted from X-Ray Images of a Column Packed with Volcanic Tuff

As we did with the glass beads, we constructed a 3D porous media from high resolution x-ray images of columns packed with volcanic tuff, having an average radius of 0.8 mm, to be able to run LSMPQS simulations of drainage and compute interfacial

areas. The porosity of the columns is 36%. An example of the imaged volcanic tuff is shown in Figure 6.39.

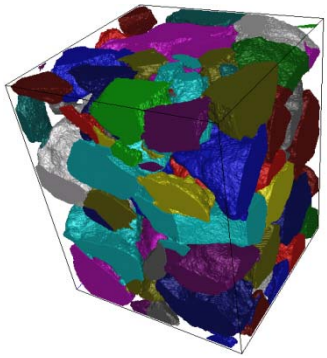

Figure 6.39: Grains identified in high resolution x-ray images of columns packed with volcanic tuff (average grain radius 800 μm.)

After running drainage simulation we calculated the interfacial areas, plotted curves of interfacial specific area versus wetting phase saturation and fit them to 3rd order polynomials, as shown in Figure 6.40, Figure 6.41 and Figure 6.42. The shape of the curves follows the trend seen in packs of beads. The specific solid area calculated analytically for an average grain radius of 800 μm and 36% porosity with equation (6.14) is 2,400 m^{-1}. The result of adding the polynomials fitting the w-s and nw-s curves is 2,635 m^{-1} and the result from LSMPQS simulation shown as a dotted line in Figure 6.41 and Figure 6.42 is 2,532 m^{-1}. There is a 4% difference between the simulated value of specific solid area and the value from the polynomial fitting. The simulated value of the interfacial solid area is within 10% of the analytical value in this case.

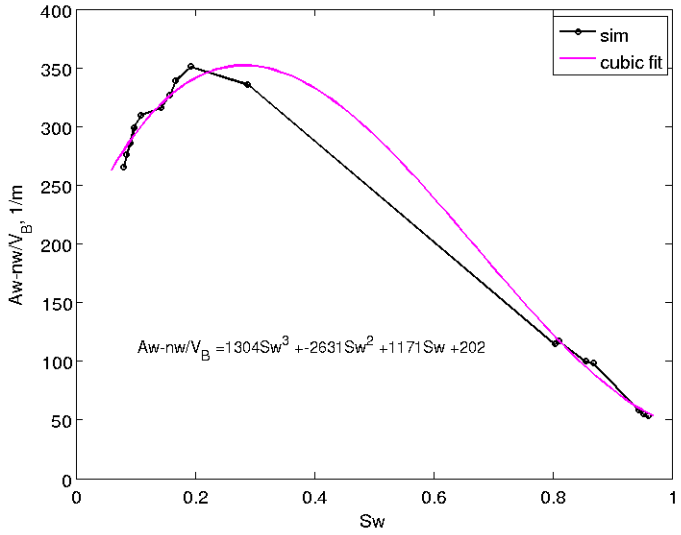

Figure 6.40: Wetting-non-wetting interfacial area per bulk volume *vs*. water saturation for simulated drainage of a porous medium geometry extracted from high resolution x-ray images of a column of volcanic tuff. The voxel size is 17 μm and the average radius of the grains is 800 μm.

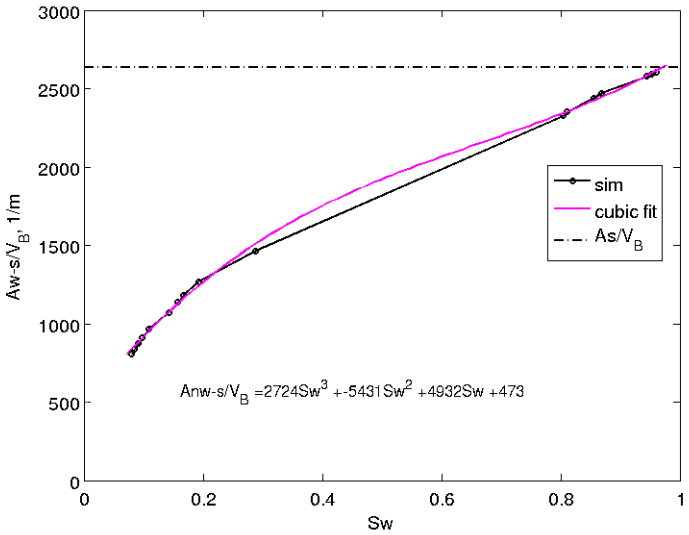

Figure 6.41: Wetting-solid interfacial area per bulk volume *vs*. water saturation for simulated drainage of a porous medium geometry extracted from high resolution x-ray images of a column of volcanic tuff. The voxel size is 17 μm and the average radius of the grains is 800 μm.

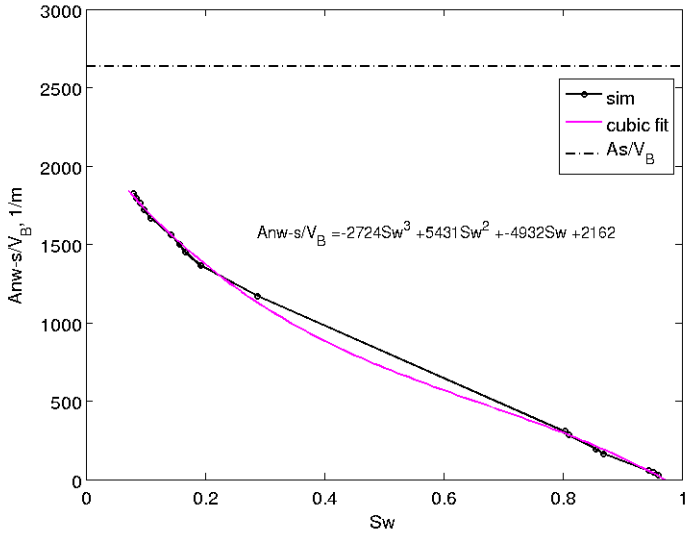

Figure 6.42: Non-wetting-solid interfacial area per bulk volume *vs*. water saturation for simulated drainage of a porous medium geometry extracted from high resolution x-ray images of a column of volcanic tuff. The voxel size is 17 μm and the average radius of the grains is 800 μm.

Figure 6.43 shows the partial derivatives of the specific interfacial areas with respect to wetting phase saturation

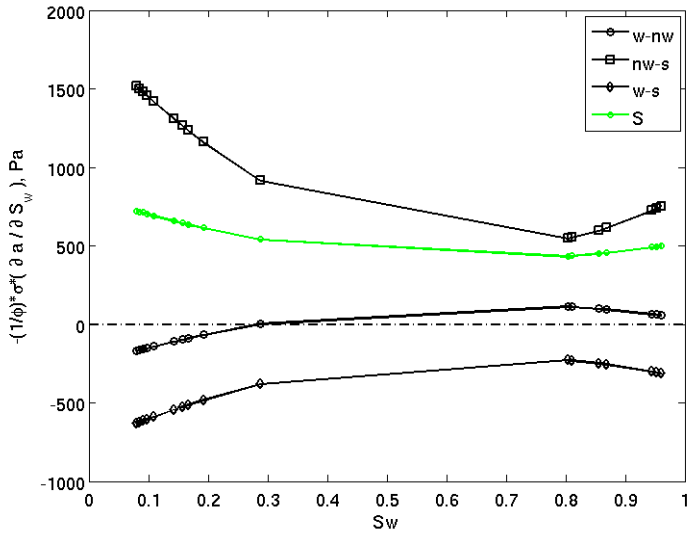

Figure 6.43: Partial derivatives of the interfacial areas with respect to wetting phase saturation for simulated drainage of a porous medium geometry extracted from high resolution x-ray images of a column of volcanic tuff. The voxel size is 17 μm and the average radius of the grains is 800 μm.

The capillary pressure curve and the rate of change of surface free energy per unit pore volume with respect to S_w, S, are shown in Figure 6.44. As in the previous simulation of drainage in the extracted porous media of glass beads, the rate of change of surface free energy per volume is positive and smaller than the capillary pressure except for a few points at the beginning of the simulation. Again we can attribute this behavior to the finite grid resolution. At the beginning of drainage the value of S decreases until S_w = 0.8. This is reflected as an increase in the rate of change of dissipated energy per unit pore volume with respect to wetting phase saturation, D, as shown in Figure 6.45. S increases after the large jump in water saturation at from S_w = 0.8 to 0.3 at a rate larger than P_c, which translates in a decrease in D, as shown in Figure 6.45.

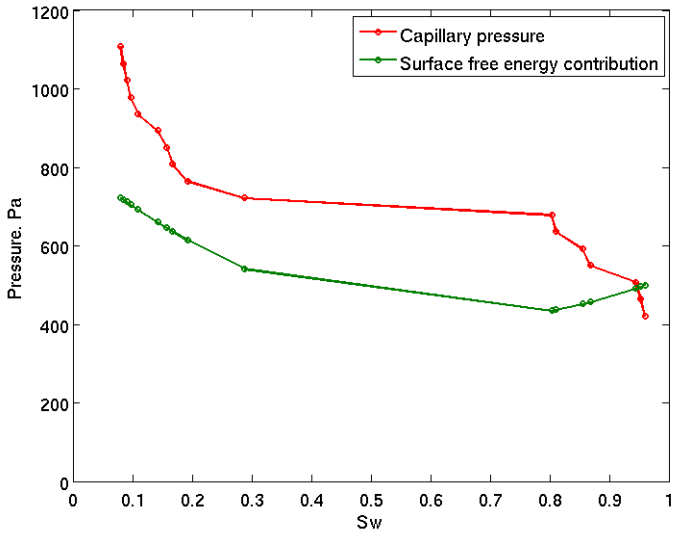

Figure 6.44: Capillary pressure and rate of change of surface free energy per unit pore volume with respect to S_w for simulated drainage of a porous medium geometry extracted from high resolution x-ray images of a column of volcanic Tuff. The voxel size is 17 μm and the average radius of the grains is 800 μm.

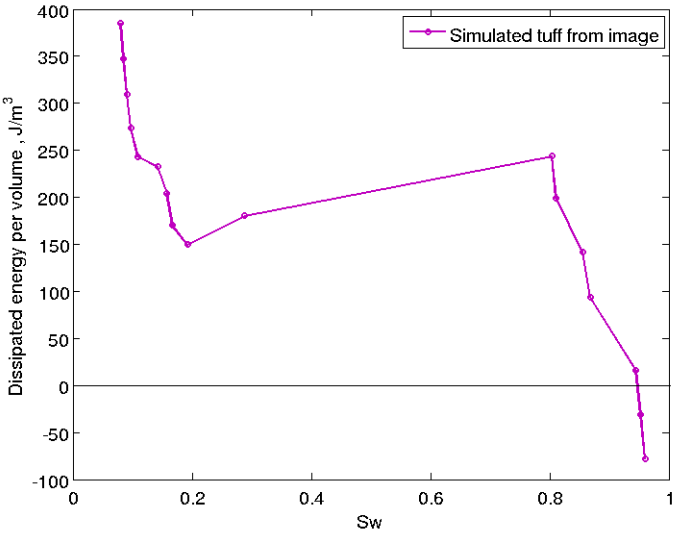

Figure 6.45: Rate of change of dissipated free energy per unit pore volume with respect to S_w for simulated drainage of a porous medium geometry extracted from high resolution x-ray images of a column of volcanic Tuff. The voxel size is 17 μm and the average radius of the grains is 800 μm.

6.2.6. Results from Experimental Data in Columns of Glass Beads

Dr. Wildenschild provided us with experimental measurements of specific interfacial areas (normalized by bulk volume) during secondary drainage (started from residual non-wetting saturation) in a column of glass beads with a range of radii between 0.3 and 0.7 mm having a porosity of 34%. Analysis of the microtomographic images was used to estimate the interfacial areas. We treated these data in the same way as the computed data from simulations and fitted the interfacial areas to a third degree polynomial in order to calculate the derivatives in equation (6.8).

The plots of interfacial area versus wetting phase saturation are shown in Figure 6.46, Figure 6.47 and Figure 6.48. The curves follow the expected trend with water saturation. The value of the specific solid area from the experiments is 3,323 m^{-1} and is shown as a dotted line in Figure 6.47 and Figure 6.48. This value is within 9% of the value that we calculated from LSMPQS simulations (cf. Figure 6.34, Figure 6.35), which was 3,637 m^{-1}. The result from adding the two polynomials fitting the w-s and nw-s solid area curves is 3,324 m^{-1}. On the other hand, the specific solid area calculated with equation (6.14) for a grain radius of 600 μm and a porosity of 34% is 3,300 m^{-1}. The experimental value is within 0.7% of the analytical.

In this case we observe that fitted polynomial for the w-nw specific interfacial area in Figure 6.46 is clearly wrong for $S_w > 0.7$. We will later see the effect of this on the value of S. The partial derivatives of the specific interfacial areas with respect to wetting phase saturation are shown Figure 6.49 together with the value of the rate of change of surface free energy per unit pore volume.

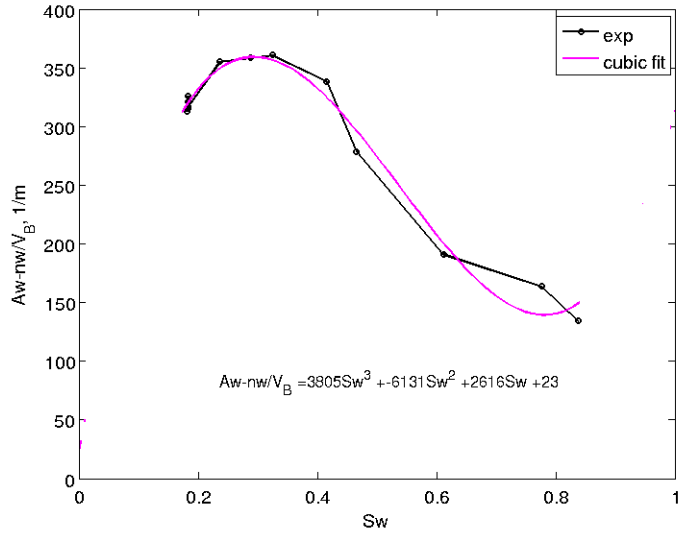

Figure 6.46: Wetting-non-wetting interfacial area per bulk volume *vs*. water saturation from experimental data of drainage in a column of glass beads of average radius 600 μm.

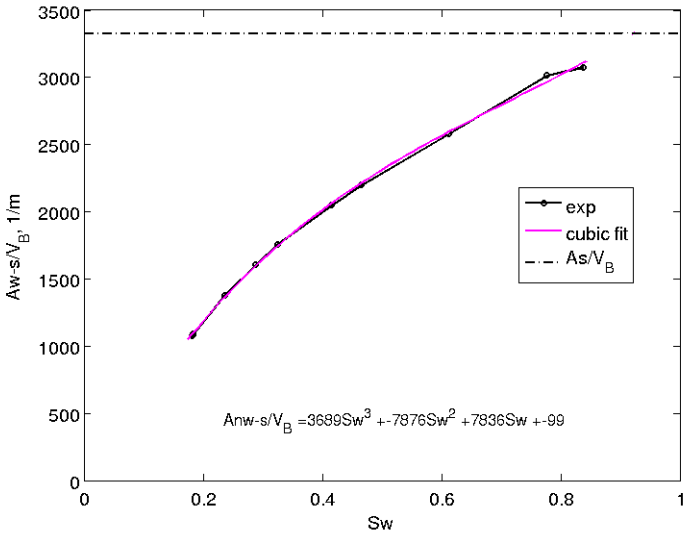

Figure 6.47: Wetting-solid interfacial area per bulk volume *vs*. water saturation from experimental data of drainage in a column of glass beads of average radius 600 μm.

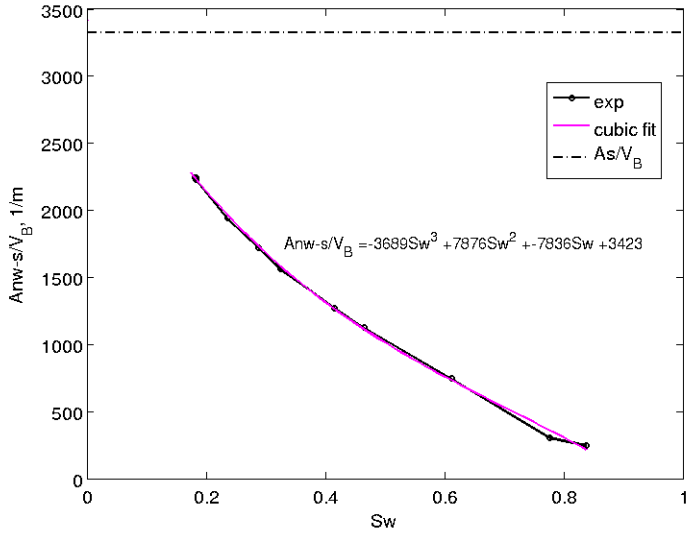

Figure 6.48: Non-wetting-solid interfacial area per bulk volume *vs*. water saturation from experimental data of drainage in a column of glass beads of average radius 600 μm.

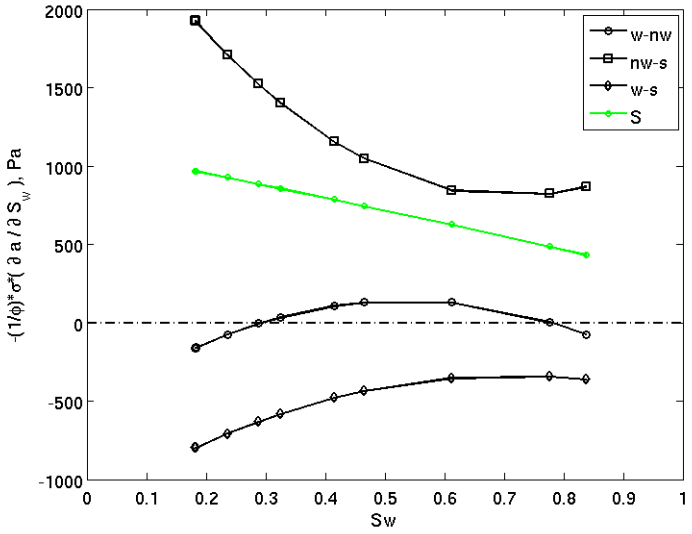

Figure 6.49: Partial derivatives of the specific interfacial areas with respect to wetting phase saturation from experimental data of drainage in a column of glass beads of average radius 600 μm.

Since the fitted polynomial for $a_{nw\text{-}w}$ is wrong for $S_w > 0.7$ (Figure 6.46) we have two instances where the derivative of $a_{nw\text{-}w}$ with respect to S_w is equal to zero in Figure 6.49, while we would expect only one, the one at S_w close to 0.3. The value of the derivative of $a_{nw\text{-}w}$ for the first two points of drainage should be larger than zero, and therefore the value of S would be larger at those two points. The value of the rate of change of surface free energy per unit pore volume with respect to S_w is shown again in Figure 6.50 together with the capillary pressure curve.

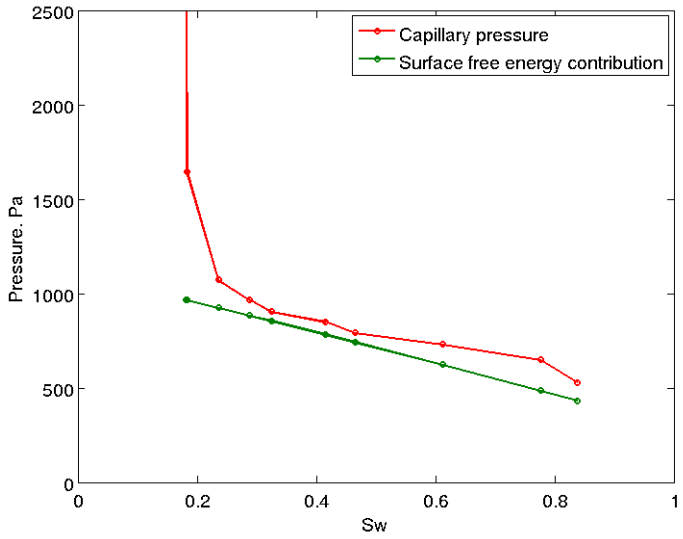

Figure 6.50: Capillary pressure and rate of change of surface free energy per unit pore volume with respect to S_w from experimental data of drainage in a column of glass beads of average radius 600 μm.

The estimated value of S is always positive during drainage and smaller than the capillary pressure, as we expect from Morrow's analysis. We would expect the first two values of S to be closer to P_c had the polynomial fitting of $a_{w\text{-}nw}$ been better. In that case, it could be that we observe the same behavior as in the simulation (Figure 6.37) where P_c and S where equal at the first step of drainage indicating reversibility of the interface

movement. The values of S and P_c from simulation and experiments are compared in Figure 6.51 , where we see that S changes faster in the experiments and its value is also closer to P_c than in the simulations.

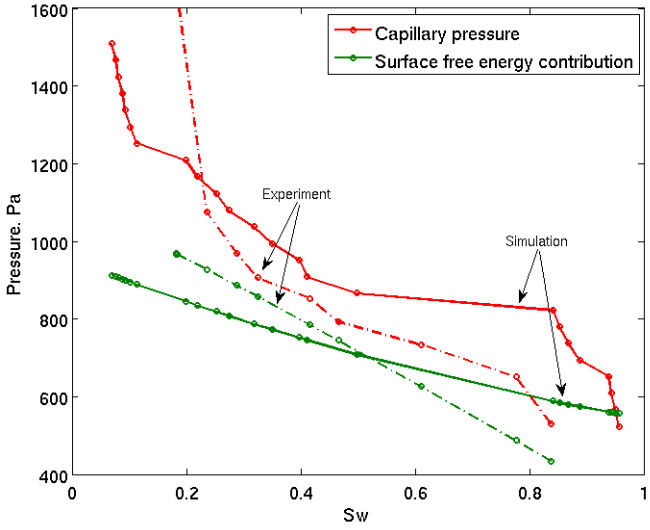

Figure 6.51: Comparison of capillary pressure and rate of change of surface free energy per unit pore volume with respect to S_w from simulation of drainage (continuous line) and experiments (dashed line) in a column of glass beads of average radius 600 μm.

Applying equation (6.9) we estimated of the rate of change of the dissipated energy per unit pore volume that goes to the bulk phases, D. The result is shown in Figure 6.52, where we see that it takes smaller values than in its simulation counterpart since the values of P_c and S are closer. These experimental results suggest that most of the PV work during drainage went to reversibly move the interface and only a small amount was dissipated to the bulk phases.

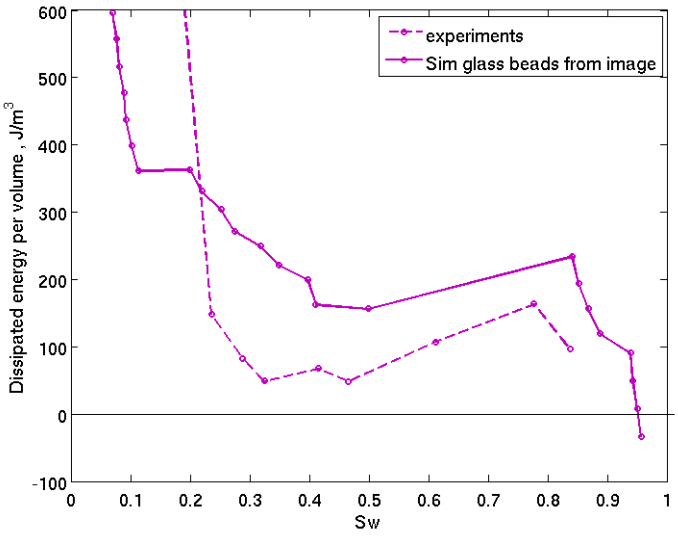

Figure 6.52: Comparison of the rate of change of dissipated free energy per unit pore volume with respect to S_w for simulation of drainage and experimental data of drainage in a column of glass beads of average radius 600 μm.

On the other hand, when we reach the drainage endpoint in the experiments, an increase in pressure does not reduce water saturation anymore. This behavior was not observed in either simulation in the computer generated sphere packs or in extracted geometries form images of glass beads and is due to the existence of trapped wetting phase and during the drainage experiments.

For this case we have calculated efficiency of the drainage process in the style of Morrow's work (1970). We integrated the area under the P_c-S_w curves and the S-S_w curves. The difference divided by the P_c-S_w integrated area is the fraction of work that gets dissipated during drainage. In this case the fraction dissipated from experimental results is 14% while the fraction dissipated from simulation is 24%.

6.2.6. Results from Experimental Data of Drainage in Columns of Volcanic Tuff

We repeated the same exercise for the experimental data from columns filled with volcanic tuff. The specific interfacial areas versus wetting phase saturation curves together with the 3rd order polynomials are shown in Figure 6.53, Figure 6.54, and Figure 6.55. The specific solid area calculated experimentally is equal to 2,587 m^{-1}, which is within 2% of the 2,635 m^{-1} calculated from LSMPQS simulation. The analytical value using equation (6.14) for an average radius of 800 μm and a porosity of 36% is 2,400 m^{-1}, therefore the experimental specific solid area is within 10% of the analytical value. The result of adding the polynomials fitting the $a_{w\text{-}s}$ and $a_{nw\text{-}s}$ curves is 2,531 m^{-1} which is within 3% of the experimental value of 2,587 m^{-1}. Notice that since tuff grains are bigger than the glass beads were the specific solid area is smaller for tuff than for beads.

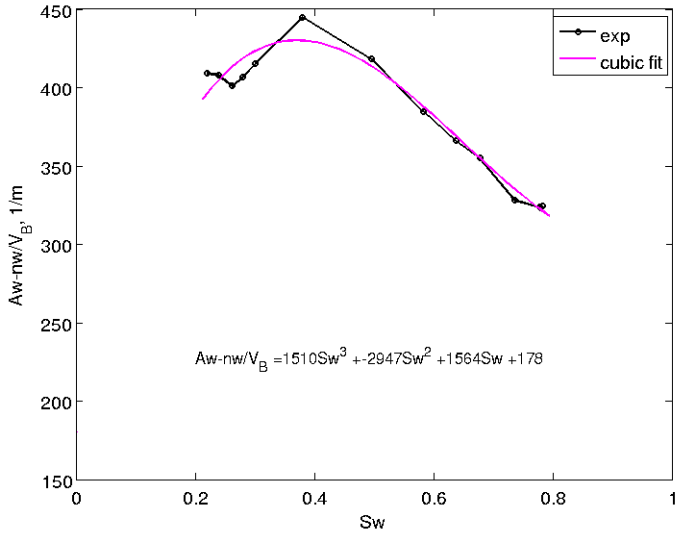

Figure 6.53: Wetting-non-wetting interfacial area per bulk volume *vs*. water saturation from experimental data of drainage in a column of volcanic tuff of average radius 800 μm.

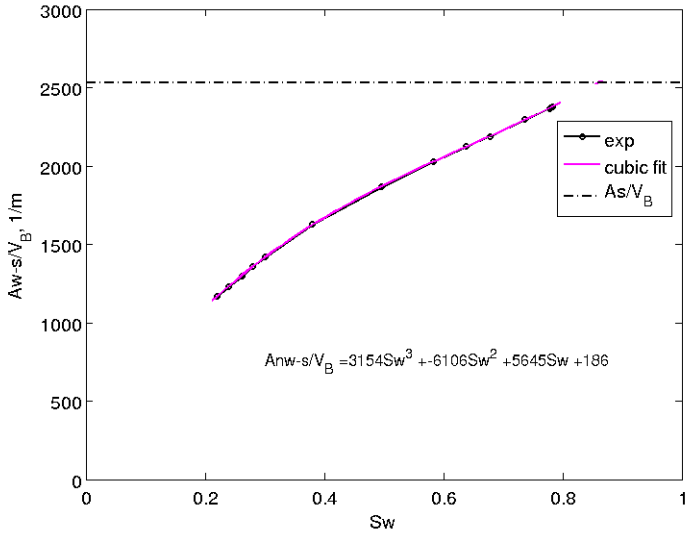

Figure 6.54: Wetting-solid interfacial area per bulk volume *vs*. water saturation from experimental data of drainage in a column of volcanic tuff of average radius 800 μm

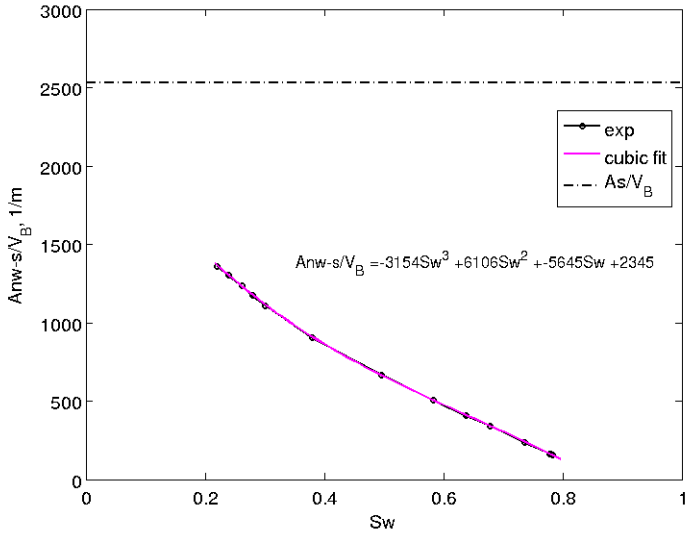

Figure 6.55: Non-wetting-solid interfacial area per bulk volume *vs*. water saturation from experimental data of drainage in a column of volcanic tuff of average radius 800 μm.

Figure 6.56 shows the partial derivatives of specific interfacial areas together with the value of the rate of change of the surface free energy per unit pore volume, S, calculated as the sum the interfacial area derivatives terms per equation (6.8).

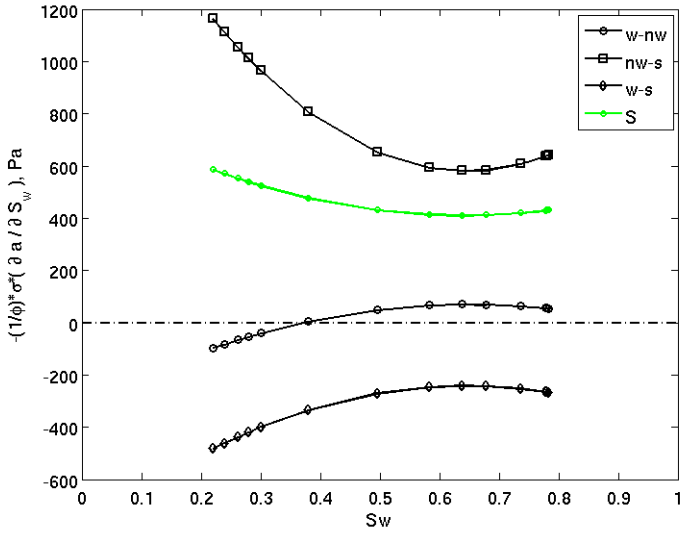

Figure 6.56: Partial derivatives of specific interfacial areas with respect to S_w from experimental data of drainage in a column of volcanic tuff of average radius 800 μm.

Figure 6.57 shows the capillary pressure P_c and the rate of change of surface free energy per unit pore volume with respect to water saturation for the drainage measurements. Similar to the experiment with glass beads, the value of S is positive during the drainage process and smaller than the capillary pressure (as expected from Morrow's work) except for a few points at the beginning of drainage. We expect the value of S to be equal or larger than P_c during drainage. In this case there may be an error in the experimental measurement of the areas or the capillary pressure that causes this behavior. We will disregard these entry point measurements since we are interested in the behavior of the the main displacement region.

S also takes values closer to the capillary pressure than in its simulation counterpart (Figure 6.44). This makes the rate of change (with respect to water saturation) of dissipated energy per unit pore volume to be smaller than in the case of simulation, as shown in Figure 6.58. Still, except for the first drainage point, the rate of change of dissipated energy per volume is positive as expected from Morrow's analysis. Also here, similarly to what happen with the experimental data for glass beads, the dissipated energy takes a very large value when reaching the drainage endpoint, while this behavior was not observed in simulations, because of the existence of trapped wetting phase in the experiments.

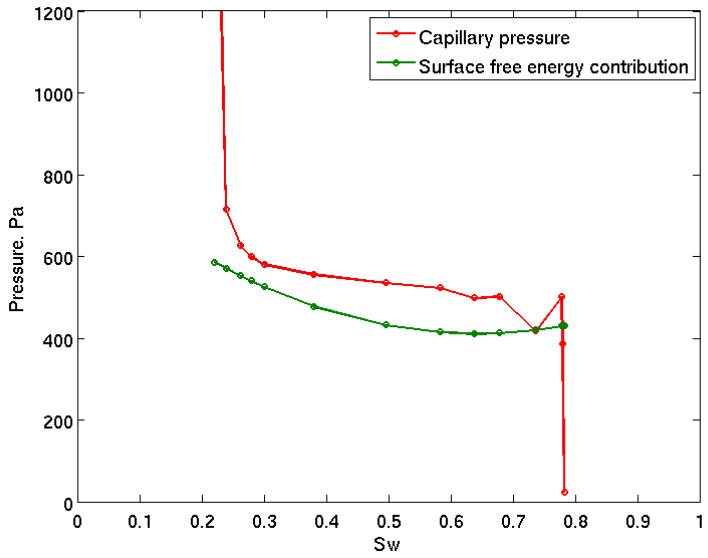

Figure 6.57: Capillary pressure and rate of change of surface free energy per unit pore volume with respect to S_w from experimental data of drainage in a column of volcanic Tuff of average radius 800 μm.

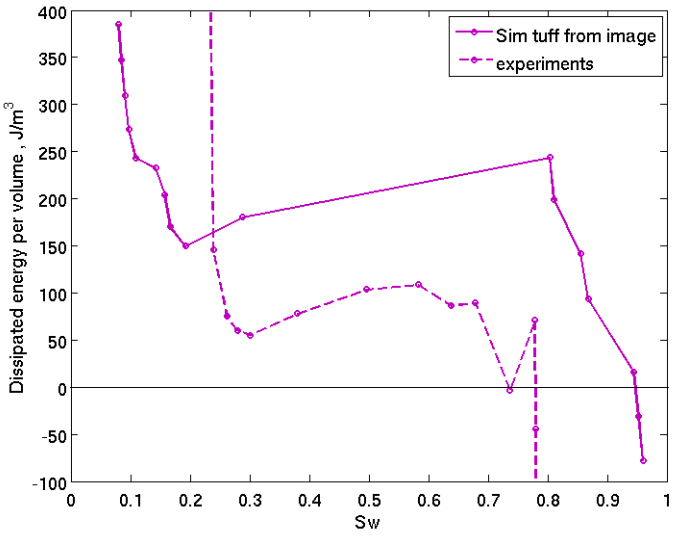

Figure 6.58: Comparison of the rate of change of dissipated free energy per unit pore volume with respect to S_w for simulation of drainage and experimental data of drainage in a column of volcanic tuff of average radius 800 μm.

We observe a decrease in the rate of change of dissipated energy per volume from one step to the next as we did when simulating drainage in the model tuff (Figure 6.45), in this case for water saturations between 0.78 and 0.7 and between 0.55 and 0.25. As we explained before this may indicate that the PV work is used on reversibly movement of the interface and less number of irreversible events is occurring. Similar to what we did with the experiments in glass beads we calculated the fraction of dissipated work in experiments and simulations in the style of the efficiencies calculated by Morrow (1970) for drainage and imbibition. In this case the percentage dissipated from simulation results is 27% while it is 18% from experiments.

6.2.7. Results from Experimental Data of Imbibition in Columns of Volcanic Tuff

We also received experimental measurements of interfacial areas during imbibition in volcanic tuff from Dr. Wildenschild. The curves of specific interfacial area versus wetting phase saturation are shown in Figure 6.59, Figure 6.60 and Figure 6.61 with their corresponding fitted polynomials of 3rd order.

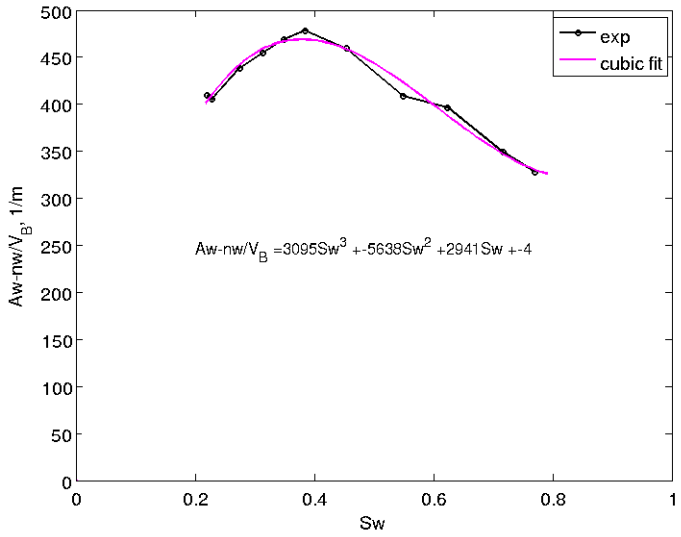

Figure 6.59: Wetting-non-wetting interfacial area per bulk volume *vs*. water saturation from experimental data of imbibition in a column of volcanic tuff of average radius 800 μm.

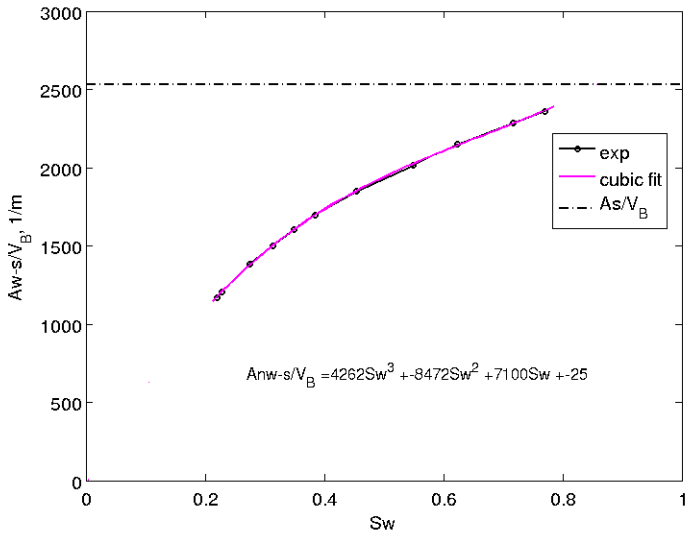

Figure 6.60: Wetting-solid interfacial area per bulk volume *vs*. water saturation from experimental data of imbibition in a column of volcanic tuff of average radius 800 μm.

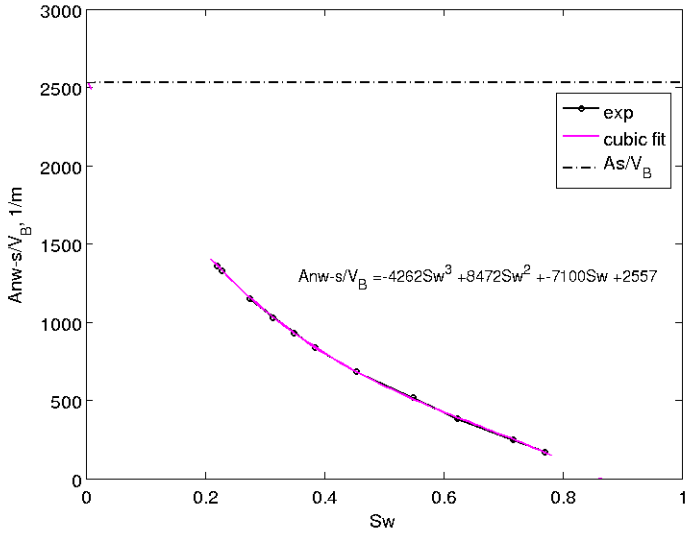

Figure 6.61: Non-wetting-solid interfacial area per bulk volume *vs*. water saturation from experimental data of imbibition in a column of volcanic tuff of average radius 800 μm.

To compare with the results from drainage we have plot the wetting-non-wetting specific interfacial area curves in the same plot, Figure 6.62, where we can see hysteresis between drainage and imbibition curves. This behavior was observed also in the results from simulation in sphere packs, as we shown in Chapter 3.

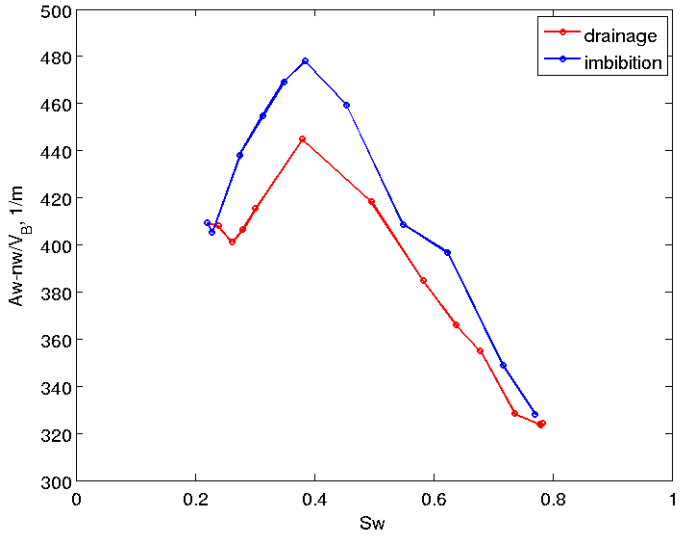

Figure 6.62: Wetting-non-wetting interfacial area per bulk volume *vs*. water saturation from experimental data of drainage and imbibition in a column of volcanic tuff of average radius 800 μm.

Figure 6.63 shows the partial derivatives of the specific interfacial areas with respect to S_w together with the rate of change of surface free energy per unit pore volume, S, that results from adding the individual interfacial area contributions, per equation (6.8). S is shown again together with the capillary pressure curve in Figure 6.64.

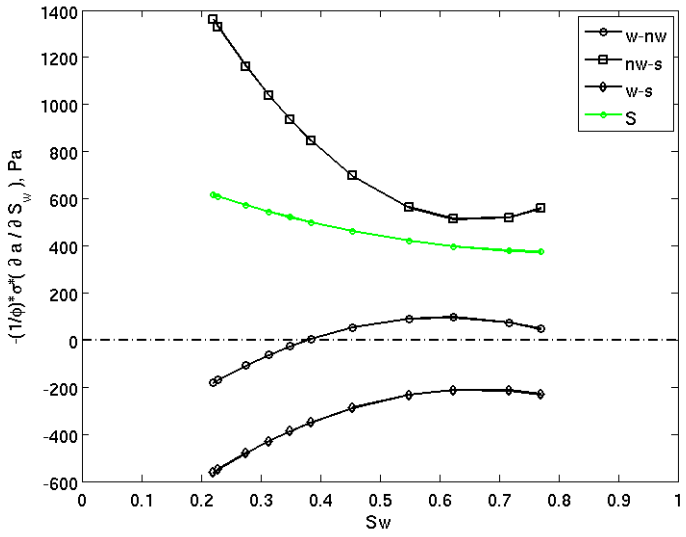

Figure 6.63: Partial derivatives of specific interfacial areas with respect to S_w from experimental data of imbibition in a column of volcanic tuff of average radius 800 μm.

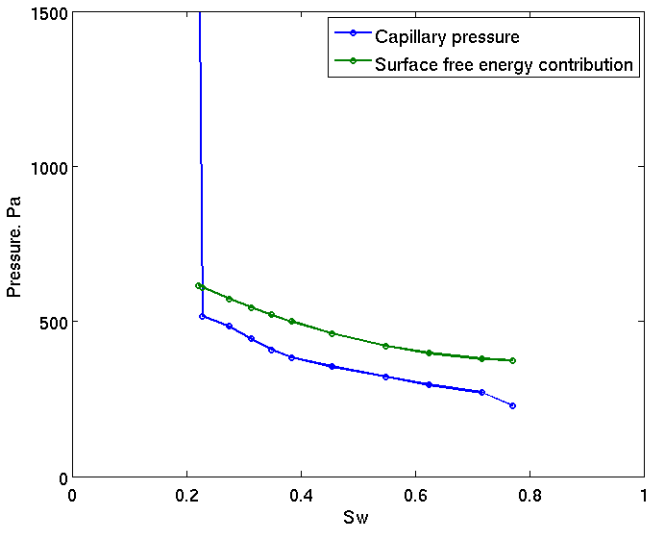

Figure 6.64: Capillary pressure and rate of change of surface free energy per unit pore volume with respect to S_w from experimental data of imbibition in a column of volcanic tuff of average radius 800 μm.

Unlike in the simulation of imbibition in a computer generated pack of spheres (cf. Figure 6.18 and Figure 6.30), in this case the rate of change of surface free energy per unit pore volume with respect to S_w is always larger than the capillary pressure, as expected from Morrow's analysis (except for the first point of imbibition that is subject to experimental error). The values of S for drainage and imbibition show little hysteresis, as Figure 6.65 shows.

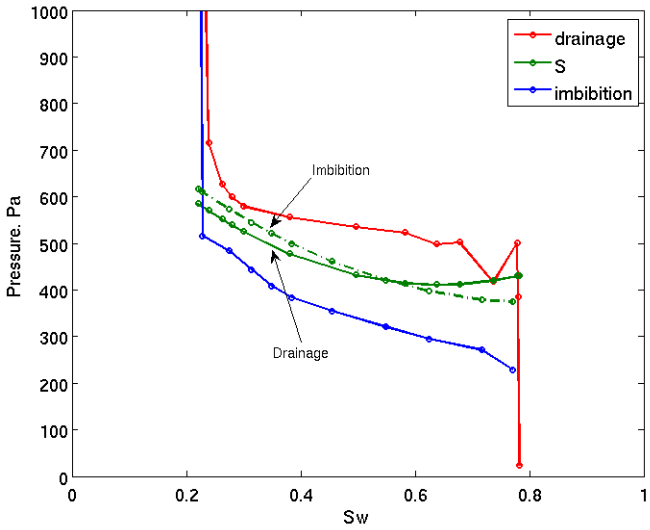

Figure 6.65: Comparison of the rate of change of surface free energy per unit pore volume with respect to S_w from experimental data of drainage and imbibition in a column of volcanic tuff of average radius 800 μm. The capillary pressure curve for drainage and imbibition is shown in the same plot.

This behavior was also observed in the sphere pack simulations (cf. Figure 6.20) suggesting that the dissipation of energy will be large during drainage than during imbibition. The estimated rate of change of dissipated free energy per unit pore volume with respect to S_w is calculated with equation (6.10) and the result is shown in Figure

6.66, with the value of D estimated from drainage and shown by a dashed line in Figure 6.58.

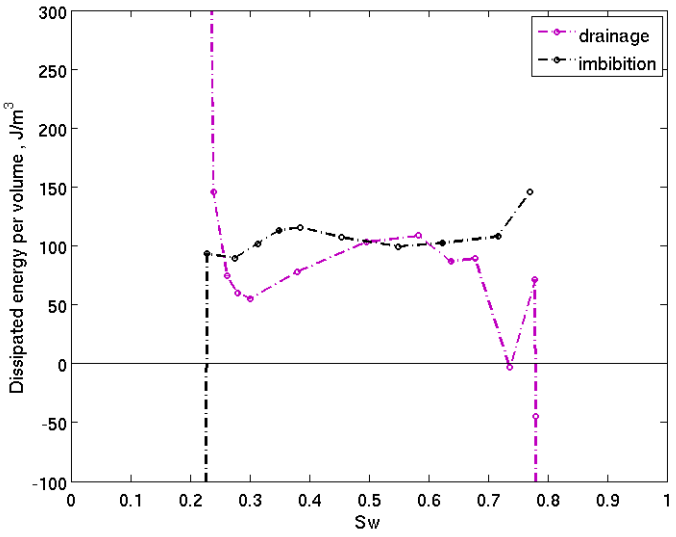

Figure 6.66: Comparison of the rate of change of dissipated free energy per unit pore volume with respect to S_w from experimental data of drainage and imbibition in a column of volcanic tuff of average radius 800 μm.

Drainage and Imbibition Efficiencies

We calculated the fraction of dissipated work during drainage and imbibition, as shown in section 6.2.3, by integration and comparison of the area under the P_c-S_w and P_c-S curves. For drainage, the area under the P_c-S_w curve in Figure 6.57 is equal to 314 Pa and the area under the dissipation curve in Figure 6.58 is 57 Pa. Therefore 18% of the work is dissipated. Recall that Morrow (1970) predicted the efficiency for drainage to be equal to 79%, being the remaining 21% dissipated into the bulk phases.

For imbibition, the area under the S-S_w curve in Figure 6.64 is equal to 253 Pa and the area under the dissipation curve in Figure 6.66 is equal to 52 Pa. Therefore, there is a 20% of energy dissipated during imbibition. Morrow (1970) predicted that 7.5% of the work is dissipated during imbibition, when the amount of energy corresponding to the trapped non-wetting phase was added to the work recovered during imbibition. However, before we are ready to make any analogy, an inconsistency in the data (or in our interpretation of the data) arises here. As shown in Figure 6.65 the surface energy released is very similar during drainage and imbibition. The integral over the S-S_w curves in Figure 6.65 is equal to 257 Pa for drainage and 253 Pa for imbibition. Since there is about 20% of trapped non-wetting phase at the end of imbibition we would expect a smaller value for the surface energy released during imbibition. The drainage and imbibition calculations are internally consistent, but they are not logical when compared. More investigation is needed regarding this subject.

6.3. CONCLUSIONS

We have applied the thermodynamic theories developed by Morrow (19070) and Hassanizadeh and Gray (1990; 1993) to evaluate the rate of change of surface free energy per unit pore volume with respect to wetting phase saturation, and the rate of change of dissipated free energy to bulk phases per unit pore volume with respect to wetting phase saturation during drainage and imbibition processes. These two terms contribute to the capillary pressure of the system according to the thermodynamic analysis of multiphase flow in porous media.

We have used our interfacial area data from LSMPQS simulations of drainage and imbibition in computer generated models of porous media, as well as in geometries

extracted from high resolution images of real porous media, to test if our results follow the theories of Morrow and Hassanizadeh and Gray. We find that our results from drainage simulations agree with the thermodynamic expectations however, for imbibition, the simulations did not appear to follow Morrow's prediction at very small saturations. We conjecture this is an effect of grid resolution, when the size of one voxel in the grid is larger than the displacement of the interface from one step to the next when the change in wetting phase saturation is small, as was the case in the first steps of imbibition in our simulations. In this case the computation of the area will not be accurate and will affect the value of the rate of change of the surface free energy per unit volume. From observation of these results seems to be clear evidence that the nonphysical behavior of the S term at small S_w is just an artifact of grid resolution.

We also tested the thermodynamic consistency of experimental data of interfacial areas, obtained from image analysis of drainage and imbibition in packs of glass beads and volcanic tuff. These experimental results support Morrow's predictions.

Regarding contact lines, Morrow's work stated that their contribution to the free energy of the system can be neglected since the region occupied by the contact line contains few molecules when compared with the other surface regions. Our results of contact line lengths in Chapter 3 could be used to test this assumption, if a value of specific energy associated with a contact line were available or a relationship between contact line length and energy in the same fashion as equation (6.5) were available. We recommend reviewing the work by Gray (1998) who presents equations for energy conservation on contact lines.

Chapter 7: Concluding Remarks and Future Work Recommendations

7.1. CONCLUDING REMARKS

The objective of the work presented in this dissertation was to investigate several incidences of the retention of small particles in granular sediments.

We investigated a long-standing observation of anomalous straining behavior of colloidal size particles in saturated porous media, namely that particles smaller than the smallest pore throats in the media undergo straining. We tested the hypothesis that the particles are trapped in gaps between pairs of spheres. Unlike pore throats, these gaps do not have a minimum size. The hypothesis was tested by finding a relationship between the straining rate constant in the gaps and the ratio of particle to grain size and comparing it with similar correlations found in the literature (Hall, 1957; Bradford *et. al*, 2003). To obtain the relationship we extended an existent theory for straining in throats (Sharma and Yortsos, 1987c) to account for the gaps in model sediments (packs of spheres). Different straining rate constants were obtained from several alternative models of the nature of straining: flow rate weighted, geometry weighted, range of capture weighted, momentum weighted and kinetic energy weighted. We found that the common assumption that straining depends only on the rate of flow through the constriction greatly overestimate the scaling exponent between straining rate constant and particle size. However, introducing the possibility of particle rebound and escape from the gap after a collision we found scaling exponents closer to the experimental. A more rigorous treatment of particle/fluid dynamics and particle/grain collision, involving the calculation of a detailed flow field in the vicinity of the gap, confirmed the overestimation of the scaling exponent when the straining rate is assumed to be dependent on flow rate alone,

and revealed that straining also depends on the angle of incidence of the particle when approaches the gap. This observation accounts for the possibility of rebound and escape of particles that otherwise could be strained.

In unsaturated sediments, we quantified the interfacial areas between wetting, non-wetting and solid phases in model sediments and sedimentary rocks as well as the length of the contact line between three phases, in order to estimate their relative contribution to the retention of particles. For this purpose we developed an algorithm based on a previously developed Level Set Method approach for simulating drainage and imbibition displacements in porous media (Prodanovic and Bryant, 2006). We obtain an unprecedented description of contact line lengths as functions of saturation, curvature and interfacial area. The algorithm applies equally well to fluid configurations from the level-set method based fluid displacement simulation and to configurations captured from imaged experiments. Our method for contact line identification is applicable to any type of porous system, as long as the detailed pore scale information is available.

The interfacial area calculated from the results of Level Set based method simulations make thermodynamic sense for quasi-static process that follow Young-Laplace equation. That is, they are consistent with the thermodynamic theory of Morrow (1970) for capillarity in porous media. The theory predicts that irreversible events (Haines jumps during drainage, Melrose events during imbibition) cause dissipation of free energy, so that the work done on the system during drainage exceeds the increase in surface energy, and the energy released during spontaneous imbibition exceeds the work done on the surroundings. Minor discrepancies between theory and simulation are caused by grid resolution. Because contact lines exist where interfaces meet, the thermodynamic consistency of the area measurements gives additional confidence of the accuracy of our contact line length estimations.

The normalized contact line length that we predicted with the level set method based algorithm is consistent with an independent calculation of contact line length in sphere packs and with observations of contact lines from high resolution images of fluid displacement in glass bead packs and real rocks. A main difference between the contact line from simulations on spheres packs and rocks was the presence of hysteresis with respect to wetting phase saturation during imbibition in the latter, which is mainly due to the different balance between pendular rings and menisci in the more complicated geometry of the rock when compared with smooth sphere packs.

We used our knowledge of the contact line lengths and interfacial areas to investigate trapping of colloids during transport in the unsaturated zone of sediments, in terms of retention per unit length or per unit area in porous media. Results of colloid retention in packs of glass beads of different wettability obtained from the literature (Han *et al.*, 2006) were used to determine the relative amount of retention in interfaces or contact lines. We made assumptions for the values of contact line lengths and interfacial areas in columns filled with beads of different wettability based on calculations of drainage and imbibition in fractionally wet media using idealized interface geometry (Motealleh, 2009), since our level set method simulations only handle homogeneously wet porous media. Our results indicate that retention in contact lines and interfacial areas may be comparable and larger than in grain surfaces for some instances, such as the case of larger ionic strength in the porous media. Consequently more colloid trapping can occur in unsaturated media.

We also investigated the mechanisms of interaction between nanoparticles and reservoir rocks in the light of a new set of applications that use dispersions of surface treated nanoparticles for oil recovery purposes. After a series of transport experiments with surface-treated silica nanoparticles in cores of sedimentary rocks, we found that the

nanoparticles were transported through low permeability sedimentary rocks with a small amount of retention. This is remarkably different from the large retention observed during transport of dispersions of colloidal size particles. While nanoparticles are about 100 times smaller than colloids, the main reason for the lack of retention is the surface coating of the nanoparticles, which prevents them from aggregating into colloidal size clusters. Because of this, the retention mechanism for the surface-treated silica nanoparticles is neither straining nor filtration. Retention in this case is dominated by van der Waals attractions between nanoparticles and rock surfaces. However the magnitude of Brownian diffusion for these small particles is large enough to eventually detach the nanoparticles from the pore walls, leading to a small amount of particles being permanently retained. The low retention in the experiments is derived from the fact that the surface coating eliminates electrostatic interaction between the nanoparticle and the pore walls, weakening the attractive van der Waals forces.

7.2. FUTURE WORK RECOMMENDATIONS

When investigating the straining of particles in Chapter 2 we made the assumption for our straining model that a diluted suspension of particles is flowing through the porous medium, based on the experimental work of Bradford *et al*. (2002). We thus considered the retention of only one particle at a time in a given gap. The next step would be to investigate how the injection of a concentrated solution of particles would affect the relationship between the constant for straining rate and the ratio of trapped particle to grain size. A trapped particle in a gap changes the geometry of the gap and therefore the flow through it. Thus subsequently arriving particles would encounter a

different physical situation. Most likely the straining rate will not follow the same expressions as the ones shown in Chapter 2.

We have introduced a new element in the theory of straining, namely the probability of a particle of being trapped once it has arrived to the constriction. In the theory developed in Chapter 2, this probability is related to the angle of incidence of the particle with the center of the gap and to the approaching velocity of the particle. Straining is then the combination of this probability of trapping and the probability of arriving at a constriction, which depends on the flow rate through the constriction. A mathematical analogy between filtration and straining models has emerged here, even though the physics of the two processes remains distinct. The filtration theory of Tufenkji and Elimelech (2004) considers the removal (trapping) efficiency of particles to be the product of a contact efficiency, which depends on the approaching velocity of the fluid, and an attachment efficiency, which depends on the repulsive/attractive interactions between suspended particles and collector. It would be good for validation purposes to perform experiments at the single pore scale (under conditions where no physicochemical forces are involved) in which particles of different sizes are directed through the gap between two spheres at different angles and with different velocities. The probability of trapping could be then estimated as a function of angle of incidence and approaching velocity.

In Chapter 4 we investigated the reasons for the decrease in the apparent viscosity of concentrated suspensions of nanoparticle when travelling through cores of sedimentary rocks. While two possible causes have been presented in the chapter (slip at the rock walls or presence of a layer depleted of nanoparticles at the pore walls), none of them provides a satisfactory explanation for the decrease in viscosity. An adequate theoretical explanation is still pending.

In Chapter 3 we showed an analytical estimate of the contact line length in a computer generated pack of spheres based on the number of pendular rings and menisci at every step during simulation of drainage. We recommend obtaining the number of pendular rings and menisci during imbibition in a pack of spheres to estimate the contact line length in a similar manner and compare its value with the length during drainage. This exercise will provide insight into the subject of contact line length hysteresis in model sediments and rocks.

We also suggest finding a method to discriminate wetting films from contact lines when processing wet images of rocks. Several methods have been tried without success in this research that with more dedication could lead to meaningful results. One possibility is an algorithm that will identify 2D objects (wetting film) that are sandwiched between two other phases (solid, non-wetting phase). The contact line would be the perimeter of such an object. The difficulty is that the imaged film usually has many "holes" where one of the sandwiching phases appears, so identifying the film as a single object is a challenge. The non-wetting phase or the solid phase (extracted from the image) could be "grown" a few voxels in each direction using the LSMPQS routine "`constant_curvature_model`" (refer to LSMPQS manual). The contact line could be recalculated for the new configuration of phases. On the other hand, an algorithm could be found to fill the empty voxels in the patches of contact line that belong to wetting films. An edge detection tool will be useful in this case to accurately determine the perimeter of the film that will correspond to the contact line.

An application of the contact line length to the retention of colloids was presented in Chapter 5. The values of retention per unit length or unit length squared shown correspond to a static moment in the displacement of the interface. We recommend investigating how the retention of the colloids varies as the contact line moves with the

displacement of the fluids. Experiments performed by Dr. Jin and Dr. Zevi at the University of Delaware (personal communication) showed that during displacement the interface acts as transport medium for the colloids, while the contact line fixes the colloids to the porous media.

It will also be instructive to obtain experimental data of retention of colloids in columns of glass beads of smaller size than the ones used in the experimental work of Han *et al.* (2006) in order to evaluate the predicted effect of grain size in the relative contribution of contact line length and interfacial areas to colloid retention.

On the other hand our results regarding the number of particles retained per unit length in Chapter 5 is based on limited data and, while they show no inconsistency, it would be beneficial to find an experimental method to measure directly the retention of colloids at the interfaces and contact lines to assess if the values shown in this chapter are plausible. Existing methods for column experiments provide only the mass of particles retained, not the amount per unit area of interface or length of contact line.

In Chapter 6, LSMPQS results of interfacial areas were proven to satisfy the thermodynamic theories for multiphase flow in porous media of Morrow (1970) and Hassanizadeh and Gray (1990; 1993). It would be valuable to test the thermodynamic consistency of our computed values of contact line length in a similar way. A work by Gray and Hassanizadeh (1998) provides energy balance equations for the "common lines" between phases. With the adequate manipulations of these equations, the contact line length values could be used on them to investigate if they satisfy the thermodynamic theory.

More investigation needs to be done regarding the behavior of the rate of change of surface free energy per unit volume (S) during imbibition. An inconsistency was found when trying to calculate drainage and imbibition efficiencies (based on the integration of

S-S_w curves) using experimental data for imbibition displacements where there is residual non-wetting phase. A good starting point would be to perform the calculations with different sets of experimental data or with data form simulations in porous media where trapped non-wetting phase is present at the imbibition endpoint.

Appendix A: Review of Mechanisms of Retention of Small Particles in Porous Media and Intervening Forces

A.1. Review of Mechanism of Retention of Small Particles

This appendix reviews the mechanisms of retention of polymer molecules and colloids. Nanoparticles are ten to one hundred times smaller than colloids, and the solution chemistry of surface-modified nanoparticles is clearly different from that of ionic solutes or polymers. Nevertheless important analogies exist between nanoparticles and colloids, and between surface-modified nanoparticles and polymers. Insight into nanoparticle retention in porous media can therefore be obtained from the very extensive literature on the retention of polymers that are used for an enhanced oil recovery process known as polymer flooding.

Typical polymers used for polymer flooding are xanthan gum and partiallyk hydrolyzed polyacrylamide (HPAM). For a typical xanthan gum with molecular weight of ~3 x 10^6 Da, the length of a molecule is between 2 and 10 μm, and its diameter is 2 to 4 nm. For a typical HPAM with molecular weight of ~4 x 10^6, the length of a molecule is of the order of 10 μm with a diameter between 0.7 and 2.5 nm. The retention of polymer molecules in reservoir rock is known to occur by the following three mechanisms: (1) adsorption, (2) mechanical entrapment, and (3) hydrodynamic retention. These mechanisms will be discussed below.

Extensive literature is also available on the retention of colloidal particles, not only in petroleum engineering discipline but also in environmental engineering discipline. The retention of colloidal dispersions in reservoir rock is known to occur by the following three mechanisms: (1) filtration, (2) straining, and (3) adsorption. These

mechanisms will also be discussed below. Obviously, the adsorption mechanisms for polymer molecules and for small-size colloidal particles are similar. The mechanical entrapment for polymer molecules and straining for colloids are also similar in that they arise from the physical trapping due to the large size of the dispersion and the small pore opening.

A.1.1. Filtration

In the recent publications on the nanoparticle retention in porous media, the filtration mechanism has been almost exclusively employed to interpret the laboratory results. We therefore discuss it first. A leading retention mechanism for colloidal particles, filtration involves the attachment of particles to the surfaces of the grains comprising the porous medium. For colloidal dispersions in single-phase flow, the filtration equation describes the variation of particle concentration with time and space as (Tufenkji and Elimelech, 2004):

$$\frac{\partial C}{\partial t} + \mathbf{v}\cdot\nabla C = \mathscr{D}\,\nabla^2 C - \nabla\cdot\left(\frac{\mathscr{D}\,\mathbf{F}}{kT}C\right) \qquad (A.1)$$

where C is the particle concentration in flowing phase, $\mathscr{D}$ is the particle diffusion coefficient, $\boldsymbol{v}$ is the particle velocity vector induced by fluid flow, k is the Boltzmann constant, T is the absolute temperature, $\boldsymbol{F}$ is the external force vector that causes particle retention in solid matrix. As shown below, the external force of interest is the attractive van der Waals force between the particles, and between a particle and the solid surface.

Elimelech (1994) solved equation (A.1) analytically using boundary conditions in agreement with the classical filtration model of Happel (1958) that assumes the medium

to be made of spherical collectors of radius d_p surrounded by a spherical cell of fluid of radius d_c. Once the concentration of particles C is determined, the perpendicular flux of particles at the collector surface and the overall rate of particle collisions with the collector (I) can be calculated. The latter parameter can be used to estimate the theoretical single collector contact efficiency (η_0):

$$\eta_0 = \frac{I}{\pi a_c^2 U C_0} \tag{A.2}$$

where a_c is the radius of the spherical collector, U is the approaching velocity of the fluid, C_0 is the bulk fluid concentration. The denominator of equation (A.2) represents the convective transport of upstream particles towards the projected area of the collector.

Contact efficiencies can be regarded as a summarized way to express the solution of equation (A.1), i.e., the variation of the concentration of solute with time and space. Tufenkji and Elimelech (2004) developed a correlation equation for the single collector contact efficiency:

$$\eta_0 = \eta_D + \eta_I + \eta_G \tag{A.3}$$

where η_D is the contact efficiency for transport by diffusion; η_I is the efficiency for transport by interception, and η_G is the efficiency for transport by gravity. While interception and gravitational settling mechanisms are important for micron size particles, nanoparticle transport to a collector will be dominated by diffusion. The single collector contact efficiency due to diffusion is calculated as:

$$\eta_D = 2.4\left(\frac{2(1-\gamma^5)}{2-3\gamma+3\gamma^5-2\gamma^6}\right)^{\frac{1}{3}}\left(\frac{d_p}{d_c}\right)^{-0.081}\left(\frac{v_t d_c}{\mathscr{D}_\infty}\right)^{-0.715}\left(\frac{A}{kT}\right)^{0.052} \quad (A.4)$$

where $\gamma=(1-\phi)^{1/3}$, d_p is the diameter of the particle, d_c is the diameter of the spherical collector, $\mathscr{D}_\infty$ is the diffusion coefficient in the bulk fluid. A is the Hamaker constant, k is the Boltzmann constant, v_t is the superficial velocity of the fluid. The fourth term in the above equation is the Peclet dimensionless number and the fifth term is the van der Waals number. For nanoparticles smaller than 300 nm the contact efficiency will be mainly controlled by diffusion (Brant *et al.*, 2007). For low flow rates (small Peclet numbers) such as the ones typically present in groundwater aquifers, the mobility of nanoparticles may be especially low. Mobility is usually defined in the literature as the distance that the solute has to travel through the porous media to reduce its initial particle concentration by 99%. Mobility is calculated from models fitted to laboratory experiments since experiments rarely result in a 99% reduction of the initial concentration.

The collector contact efficiency η_0 is lower than the actual collector removal efficiency (η) because of repulsive interactions between particles and collector. An empirical attachment efficiency (α) is introduced to account for the fact that because a particle does not necessarily attach to the collector surface when it reaches the collector (Elimelech *et al.*, 1995). Thus:

$$\eta = \eta_0\alpha \quad (A.5)$$

where α represents the fraction of the collisions of the suspended particles that result in attachment. The attachment efficiency is estimated by measuring effluent

concentrations in columns packed with spherical grains of the same size as (Yao *et al.*, 1971):

$$\alpha = \frac{2d_c}{3(1-\varepsilon)\eta_0 L}\ln\left(\frac{C_L}{C_0}\right) \tag{A.6}$$

where L is the length of the porous medium in the column, d_c is the diameter of the spherical grains, ε is the porosity, and C_L and C_0 are respectively the particle number concentrations in the effluent and influent to the column.

Because of their small size, nanoparticles have a large diffusion coefficient that gives them a large mobility in liquids and gases but also large contact efficiencies with collector surfaces. Thus even though attachment efficiencies can be less than 1%, nanoparticles can nevertheless be strongly retained, becoming relatively immobile even for attachment efficiencies smaller than 1% (Brant *et al.*, 2007). After the particle attaches to the collector surface, it can be remobilized through changes in the solution chemistry and/or hydrodynamic conditions.

A.1.2. Adsorption

Adsorption traditionally refers to the process of interaction between molecules and the solid surface as mediated by the solvent in which the molecules are suspended (Sorbie, 1991). This process can be seen as a competition between the solute and the solvent for a place at the interface surface. Adsorption causes polymer or colloidal molecules to be bound to the surface of the solid mainly by physical forces (van der Waals and hydrogen bonding) rather than by chemisorption in which full chemical bonds

are formed between the molecule and the surface. High levels of adsorption are observed in solids with large surface areas.

Adsorption is the main fundamental mechanism of polymer retention. An important parameter to describe adsorption is the surface excess, Γ_s which is the mass polymer per unit area of substrate, and it can be calculated as:

$$\Gamma_s = \frac{V\Delta C}{A} \tag{A.7}$$

where A is the total surface area of adsorbent substrate, V is the volume of polymer solution of initial concentration C_1, C_2 is the bulk solution concentration when adsorption has reached equilibrium and $\Delta C \equiv (C_1\text{-}C_2)$. The number of polymer molecules adsorbed per unit area is not enough to describe adsorption. Because of the geometry of the polymer molecules, it is necessary to know the number of polymer segments as a function of distance from the adsorbent surface. It is also important to know the thickness of the adsorbed layer, δ_s, the fraction of adsorbed polymer molecular segments in the interfacial plane, p, and the polymer segment density distribution normal to the solid interface (mass/volume) $\rho(z)$.

Polymer adsorption can be measured in laboratory scale in dynamic or static conditions. In the static method, the core is crushed and mixed in the polymer solution and the polymer concentration in solution is measured before (C_1) and after (C_2) the mixing. In the dynamic method, a solution of polymer is injected in the core and a mass balance in the effluent will determine the amount of adsorption. Generally, polymer adsorption depends on the polymer type and specific properties of the molecule, the

solvent conditions (pH, salinity, hardness, and temperature) as well as on the surface chemistry of the adsorbing substrate (silica, clay, sandstone, and carbonate) (Choi, 2007).

The time to attain equilibrium in an adsorption process is delayed by the time of access to the surface, which is often controlled by diffusion, thus favoring faster access of low molecular weight fractions. Even after the molecules reach the surface further changes are expected (Sorbie, 1991). For example, the molecular conformation can change from its bulk state to a new state characteristic of being adsorbed. The polymer can also change its conformation because of the competition with newly arriving macromolecules. There may be exchanges between surface and solution due to preferential adsorption of high molecular weight fractions.

It has been observed (Sorbie, 1991) that adsorbed amounts of polymer are much higher on carbonates and clay minerals than on sandstone and silica. In the case of carbonates, this has been attributed to the stronger bonding between Ca^{2+} on the surface and the polymer carboxylate groups. In clays there is both a chemical and a structural aspect of polymer adsorption which is mediated by the interaction between the polymer molecule and the silanol and aluminol groups. In sandstones or silica the adsorption is mediated by the polymer interaction with the silanol group.

To describe the equilibrium adsorption of polymer molecules (or small size colloidal particles) to solid surfaces, Langmuir and Freundlich isotherms are typically used. The isotherms describe the variation of Γ_s with the concentration of solute. Langmuir isotherm relates solute concentration C and surface adsorption in the following way:

$$\Gamma_s = \frac{\Gamma_{max} K_L C}{1 + K_L C} \tag{A.8}$$

where K_L is the equilibrium constant and Γ_{max} is the concentration of adsorption sites on the surface (Frimmel *et al.* 2007)

A.1.3. Straining (Mechanical Trapping)

Straining is a geometric mechanism of retention or removal of particles from a solution in which large particles are trapped in small pores that do not allow their passage. Retention by straining does not involve physico-chemical forces but is dependent on the size and shape of the strained particles and the formation grains. Over time, this process leads to pore blocking. Smaller particles are predicted to be removed more efficiently by diffusive transport at the interface between pores and the flowing water.

For a given particle size a sediment will have a certain number density of throats that will strain that particle. Thus continued injection of particles of that size will eventually fully block those throats. In a coreflood experiment full blocking will cause the concentration of particles in the effluent to reach the injected concentration, since once the trapping sites have been blocked the flow will be through the larger pores.

In the case of polymer solutions, it is often observed that the polymer is trapped close to the core inlet, and the concentration of trapped polymer decreases exponentially along the core. This behavior is characteristic of trapping rates that are proportional to the particle concentration. This concentration dependency arises for the straining mechanism when multiple particles or molecules arrive simultaneously at a pore throat large enough to admit one but not several. For porous media in which a large fraction of the throats are trapping sites, the polymer may completely block the core reducing the permeability to almost zero.

The retention of colloids by straining follows the same trend as the polymer retention. Because of the different shape of colloids the entrapment sites will be different than the sites for entrapment of polymers. Colloids will be trapped in the small crevices or gaps between grains as well as near point contacts, rather that in the main flow paths of the pore throats.

There are only few models that account for straining (Sharma and Yortsos, 1987c; Bradford *et al.*, 2003; Rodriguez and Bryant, 2007). Bradford *et al.* (2003) added a sink term to the classical filtration theory to represent mass transfer due to straining. The mass balance equation in the liquid phase was written as:

$$\frac{\partial \mathrm{C}}{\partial \mathrm{t}} = -\nabla \mathrm{J} - \mathrm{E}_{\mathrm{att}} - \mathrm{E}_{\mathrm{str}} \tag{A.9}$$

where C is the concentration of particles (polymers or colloids) in the solution in number per unit volume, J is the flux of particles in number per unit area per unit time and E_{att} and E_{str} are the mass transfer terms between liquid and solid phases due to attachment and straining respectively, in number per unit volume per unit time.

Bradford *et al.* (2003) propose a simple functional form for the straining term:

$$\mathrm{E}_{\mathrm{str}} = \mathrm{k}_{\mathrm{str}} \Psi_{\mathrm{str}} \mathrm{C} \tag{A.10}$$

where Ψ_{str} is a dimensionless straining function that depends on the spatial distribution of the colloids along the column and k_{str} is the straining coefficient which has units of reciprocal time. This straining coefficient is essentially a rate constant, but it depends on the size of particles being strained and the number density of trapping sites in

the porous medium. Experiments suggest that k_{str} has a power-law dependence with the ratio of the particle size and the sediment grain, where the exponent is between 1.2 and 1.5 (Bradford *et al.*, 2003). The theory of Sharma and Yortsos (1987c) relates the straining coefficient to the structure of the porous medium (specifically, the frequency distribution of pore throat sizes, the average number of throats per pore, and the average pore length). The underlying assumption is that trapping rate for a given particle size is proportional to the probability of encountering a trapping site, which in turn is proportional to the volumetric flow rate through that site.

Retention by straining more likely occurs in low permeability materials where the pore sizes are small and appears to increase at residual oil saturation compared with the fully water saturated situation (Sorbie, 1991). It is also important to consider the roughness of the surfaces. Small asperities (<1 nm) can considerably increase the contact area between nanoparticles and collector and therefore the extension of the attachment. The size of the nanoparticles allows them to fit in between tightly spaced surface asperities (Shellenberger *et al.*, 2002). This is in contrast with the case of larger particles where the adhesion is reduced because asperities reduce the contact area between particle and surface (Bowen and Doneva, 2000). Roughness features may also physically trap nanoparticles on the surface once contact has been made

In polymer solutions, the high molecular weight fraction can be trapped by straining in narrow flow channels. For polymers with an effective size of 1 μm, approximately 14% of the pore volume would be inaccessible in Berea sandstone (Willhite and Dominguez, 1977). When the polymers get trapped in the pore throats, the portion of the throat remaining open is narrower, thus leading to the retention of more particles. This situation is similar to the well-known deep-bed filtration case.

A.1.4. Hydrodynamic Retention

Hydrodynamic retention is a flow-rate-dependent effect. In general, more retention is observed at larger flow rates (Sorbie, 1991). Recently, Li *et al.* (2005) observed that the deposition rate coefficients of colloidal particles increased with increasing flow rate in the absence of electrostatic repulsive forces between colloids and grain surface. When electrostatic repulsive forces exist, the deposition rate coefficients decreased with increasing flow rate. Hydrodynamic drag also caused re-entrainment of colloids when repulsive forces are present.

On the other hand, hydrodynamic drag forces may temporarily trap some of the particles in stagnant flow regions, where the local concentration of particles can exceed that of the injected fluid (Sorbie, 1991). When the flow stops these particles may diffuse out into the main flow channels and, when the flow resumes, they are produced as a peak in concentration

Hydrodynamic retention gives a small contribution to the total retention of polymers and colloids (Sorbie, 1991; Bradford and Torkzaban, 2008).

A.2. INTERACTION FORCES RELEVANT TO PARTICLE RETENTION

This section reviews the forces involved in the interaction between the porous media, the carrier fluid and the particles in solution.

A.2.1. Brownian motion

Brownian motion is the rapid and erratic movement of particles originated from the energy acquired after their collision with solvent molecules. Brownian motion affects the collision frequency between particles and with stationary surface and it becomes more

important as particle size decreases (diameter smaller than 1 μm). Therefore Brownian motion has to be taken in account when determining nanoparticle stability and mobility in aqueous systems. Lecoanet and Wiesner (2004) predicted that particles smaller than 100 nm have very high efficiencies of transport to collector surfaces due to Brownian diffusion. Brownian motion affects transport rather than attachment.

A.2.2. DLVO theory

Derjaguin-Landau-Verwey-Overbeek (DLVO) theory describes the total energy of interaction between two surfaces as the sum of van der Waals and electrostatic interactions. An extended DLVO theory (XDLVO) considers also acid–base interactions and Born repulsion energy. The total interaction energy or potential between particles or surfaces is usually plotted as a function of their separation distance. Negative potential indicates an attractive force, whereas positive potential indicates repulsion. Figure A.1 shows an example of a DLVO interaction energy curve. A shallow minimum occurs at $\kappa D = 8$. Thus if the particle approaches a surface and comes within a distance $D = 8/\kappa$ it is likely to become attached to the surface. Figure A.2 shows a situation in which the total interaction energy is positive for all separations greater than about $1/\kappa$. In this case, the particle is less likely to become attached, because considerable energy must be added to the particle as it approaches the surface. Otherwise it cannot overcome the the surface repulsion to reach the energy minimum at very small separation. The factors that control the competition between attractive and repulsive forces, and hence the occurrence of minima in the total interaction energy, are discussed below.

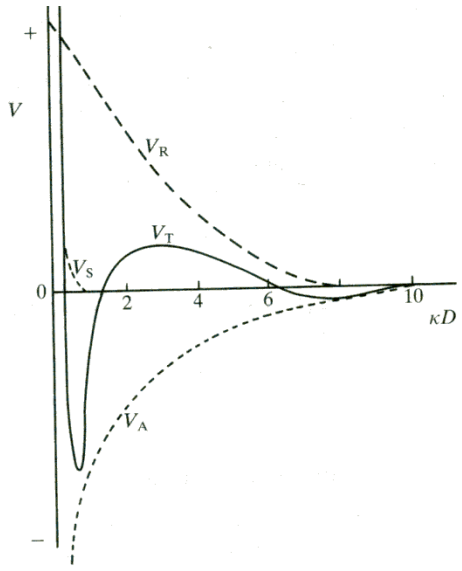

Figure A.1: Typical interaction energy vs. separation distance. V=Interaction energy, V_R=repulsive energy, V_A=attractive energy, V_S=potential energy of repulsion due to the solvent layers (negligible until D<10nm), V_T=total interaction energy, κD=dimensionless separation distance, where $1/\kappa$ is the Debye length. A primary (small κD) and secondary minimum in total interaction energy are shown. (From Hunter, 2001).

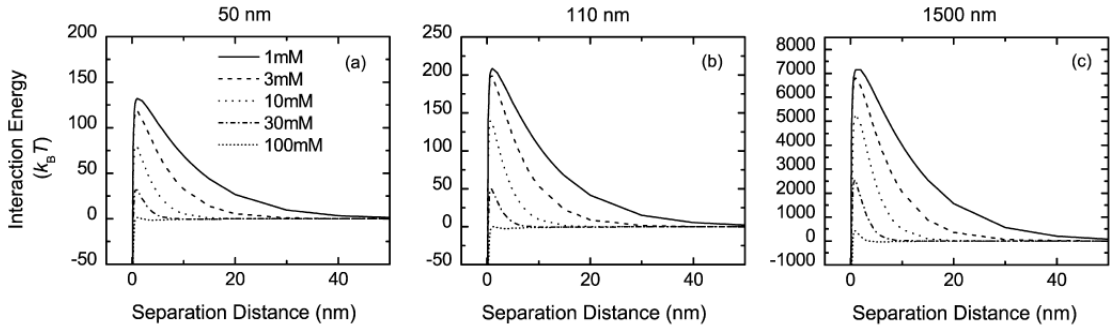

Figure A.2: Calculated DLVO interaction energy plotted as a function of separation distance between the grain surface and the latex particle for a range of solution ionic strengths (pH 5.7 ±0.2): (a) for the 50 nm colloid; (b) for the 110 nm colloid; (c) for the 1500 nm colloid (Pelley and Tufenkji, 2008).

A.2.2.1. van der Waals forces

van der Waals interactions are mostly attractive, and incorporate three types of electrodynamic forces: dispersion, induction and orientation (Israelachvili, 1991). For the case of the interaction between a flat plate and a spherical particle, van der Waals interaction energies decay according to h^{-1}, where h is the separation distance between surfaces, as shown in the following equation (Elimelech *et al.*, 1995):

$$U_{VDW} = -\frac{A_H d_p}{12h} \qquad (A.11)$$

where U_{VDW} is the interaction energy in Joules, A_H is the effective Hamaker constant of the interacting media and d_p is the diameter of the particle. The Hamaker constant for inorganic colloids is of the order of 10^{-20} J (Israelachvili, 1991). The previous equation shows that when the particle size decreases, the magnitude of the van der Waals attraction decreases and it acts over shorter separation distance.

A.2.2.2. Electrostatic interactions

Electrostatic interactions are mostly repulsive as they result form the interaction of the particle's electrical double layers. The first layer of charge is located at the surface and the other one in a diffuse region that spreads into the solution (Adamson and Gast, 1997). Figure A.3 illustrates this concept.

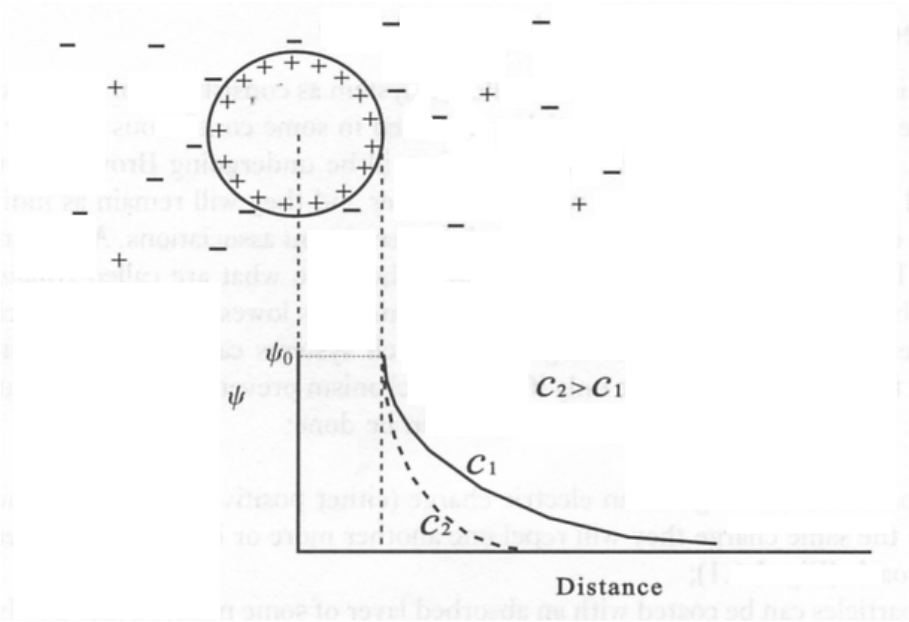

Figure A.3: Variation of potential (Ψ) vs. distance for a positively charged particle in a symmetrical electrolyte, showing the location of the electrical double layer. Positive charges are repelled from the surface and negative ones are attracted creating an excess of negative charges in the particle surface with respect to the bulk solution. Increasing ionic strength (*C*) causes the potential to decrease more rapidly with distance. (From Hunter, 2001).

The electrostatic interaction energy (U_E) between a spherical particle of radius r_p and a flat surface decays with separation distance h according to (Hoek and Agarwal, 2006):

$$U_E = \pi\varepsilon\varepsilon_0 r_p \left[2\zeta_p\zeta_c \ln\left(\frac{1+\exp(-\kappa h)}{1-\exp(-\kappa h)}\right) + \left(\zeta_p^2 + \zeta_c^2\right)\ln(1-\exp(-2\kappa h)) \right] \quad (A.12)$$

where ε_0 is the electric permittivity of vacuum, ε is the dielectric constant of water, and ζ_p and ζ_c are the surface potentials of the particle and the collector surface respectively. This equation shows that the electrostatic interaction energy decays with

separation distance and decrease with decreasing particle size (d_p) favoring particle aggregation or deposition. The effect of particle size can be observed in Figure A.2 at the beginning of this appendix. Also, repulsive interaction forces are a function of Debye length ($1/\kappa$). Debye length measures the thickness of the ionic double layer around each charged surface and its inverse κ provides the length scale for the screening when multiplied by the separation distance (Adamson and Gast, 1997). κ is calculated as:

$$\kappa = \left(\frac{2n_{\infty} z^2 e^2}{\varepsilon_r \varepsilon_0 kT} \right)^{1/2} \tag{A.13}$$

where e is the electron charge, n_∞ is the number concentration of ions in the bulk solution, z is the valence of the ion, T is the temperature and k is the Boltzmann constant.

Equation (A.12) above shows that Debye length is dependent on the ionic strength of the solution and the valence of the ionic species present. Debye length increases when the ionic strength decreases. For example, the Debye length in a 100 mM NaCl solution is 1.0 nm, whereas in a 0.01 mM NaCl solution it is 100 nm (Brant *et al.*, 2007). Reservoir brines tend to have relatively large ionic strength, in the range of 1 mM NaCl to a few tens of mM NaCl, for which the Debye length is 1 to 10 nm. These lengths indicate that repulsive interactions occur over a distance from charged surfaces similar to the size of nanoparticles. Therefore, models assuming that the distance κh is much less than the diameter of the particle are not valid for the case of nanoparticle solutions (Brant *et al.*, 2007).

The decrease in Debye length with ionic strength may lead to a decrease in the repulsive electrostatic forces according to equation (A.11). Therefore, the ionic strength

(salt concentration) and types of ions in the solution strongly affect the region of influence of electrostatic forces.

A.2.2.3. Born Repulsion

Born repulsive forces are the strong repulsive forces between atoms that arise when their electron shells begin to overlap. These repulsive forces act over a distance of up to several nanometers and may not affect nanoparticle interactions (Elimelech *et al.* 1995). It affects the depth of the primary minimum in the total interaction energy profile and may affect the reversibility of nanoparticle attachment (Brant *et al.*, 2007).

A.2.2.4 Acid-Base Interactions (Hydrogen Bonding)

Acid-Base interactions describe how a surface interacts with water by means of hydrogen bonds. These forces act over a shorter range (decay length 0.2-1.1nm) than attractive hydrophobic and decay exponentially with separation distance.

Nanoparticles are usually hydrophobic but can also be hydrophilic if they are functionalized, i.e., they contain surface groups that may coordinate water molecules through hydration (van Oss, 2006). When water is adsorbed in the functional sites of hydrophilic nanoparticles a proton is released, making the particles act as an acid or a base. A layer of water on the surfaces of nanoparticles holds them back from aggregating, and dehydration must occur before the underlying surfaces come into contact. This hydration energy becomes another repulsive barrier. In contrast, hydrophobic nanoparticles are pushed together in water, favoring aggregation in what is called hydrophobic effect (van Oss, 2006).

According to Brant *et al.* (2007) hydrophobic interactions will be significant for all but the smallest nanoparticles (1 nm to 2 nm) and will tend to favor particle

aggregation. Acid-base interaction energy between a sphere and a flat plate decay exponentially with the separation distance and decrease with decreasing particle size. These forces can be comparable to electrostatic interactions even when particles size is below several tens of nanometers (Brant *et al.*, 2007).

Discussion on DLVO Theory

The problem in the DLVO theory when describing interaction of nanoparticles is that it treats the intervening fluid (water for example) as an uniform structureless medium that is well described as a function of its bulk properties (Israelachvili, 1991).

When particles are larger than several tens of nanometers, classical models for colloidal systems may be effective for describing the behavior of nanoparticles in aqueous systems. However, particle behavior is comparable to that of a molecular solute when particles are smaller than approximately 20 nm (Brant *et al.*, 2007), making the role of intermolecular forces more significant for the processes of retention and aggregation. Therefore, a satisfactory description of the phenomena that affect nanoparticle aggregation and deposition will be reached through a molecular view of the interactions involved. As said above, the value of the Debye length is similar to the size of the nanoparticles, limiting the effectiveness of this theory when surfaces approach 5 nm or less. Also, molecular interactions such as steric repulsion become significant when considering particles with dimensions similar to that of ions (Brant *et al*., 2007).

DLVO theory predicts a reduction in the height of the energy barrier as particle size decreases, suggesting that smaller particles are likely to have larger attachment efficiency (Pelley and Tufenkji, 2008). DLVO theory also predicts a reduction in the energy barrier for attachment for larger ionic strength, i.e. larger salinity of the solution containing nanoparticles, due to compression of the electrical double layer. According to

the last two points, nanoparticle remobilization will be more sensitive to changes in solution chemistry for the smaller particles.

A.2.3. Dipole-Dipole Interactions

Dipole-dipole forces are attractive forces between a positively charged zone of one polar molecule and a negatively charged zone of another polar molecule. Electronic structure and magnetic properties are strongly dependent on particle size for particles smaller than 10 nm (Murray *et al.*, 2000). For some types of nanoparticles, such as semiconductor (CdSe) and magnetic ($CoPt_3$) nanoparticles, the dipole interactions are an inherent part of different low-dimensional self-organizing systems. For example the existence of a dipole moment sometimes leads to self-organization of nanoparticles into nanowires. Rabani *et al.* (1999) found that for CdSe nanocrystals, the dipole-dipole electrostatic interaction is the dominant interaction term and it is larger than the van der Waals interactions, for interparticle separations approximately 5 times the size of the particle.

Dipole interactions can be particularly important during the initial phases of the formation of aggregates. Computer simulations performed by Sinyagin *et al.* (2006) to model the self assembly of nanoparticles into nanowires showed that other short-range interparticle forces such as van der Waals also play a role in the self organization of nanoparticles.

A.2.4. Aggregation

Nanoparticles can aggregate when they are in a thermodynamically unstable dispersion, if the reduction in interfacial area that occurs through aggregation lowers the total free energy of the system (Brant *et al.*, 2007). Changes in solution chemistry or

modification of the particle surface can stabilize suspensions of nanoparticle and prevent their aggregation, though functional changes in the nanoparticles surface may transform them into nanoparticles inappropriate for their original purpose. Nanoparticles can aggregate into a micron size structures similar to colloids and experience gravitational settling. Recall that retention of aggregates by straining in a sedimentary rock will be much greater than retention of individual particles, so aggregation is to be avoided for oil reservoir applications.

Bellona *et al.* (2004) observed that nanoparticles in suspensions tend to aggregate more quickly at higher ionic strengths, as predicted by the DLVO theory and at pH values near the zero point of charge (ZPC), since these two changes in solution chemistry reduce repulsive electrostatic interactions.

The surface charge of nanoparticles is an important property that can be estimated through electrophoretic mobility measurements. Hunter (2001) observed that the surface potential becomes more negative as solution pH becomes more basic, affecting the aggregation and attachment of nanoparticle. For example, Kobayasi *et al.* (2005) observed more aggregation at low pH values. On the other hand, surface charge approaches zero with increasing ionic strength, facilitating aggregation. As stated before, DLVO calculations predict a reduction in the energy barrier between nanoparticles as ionic strength increases by making the van der Waals attractive interactions dominant. The aggregation behavior also depends on the size of the nanoparticles and the presence of hydration forces as experimentally observed by Kobayasi *et al.* (2005).

The following Figure A.4 shows aggregates of four fullerene based nanoparticles.

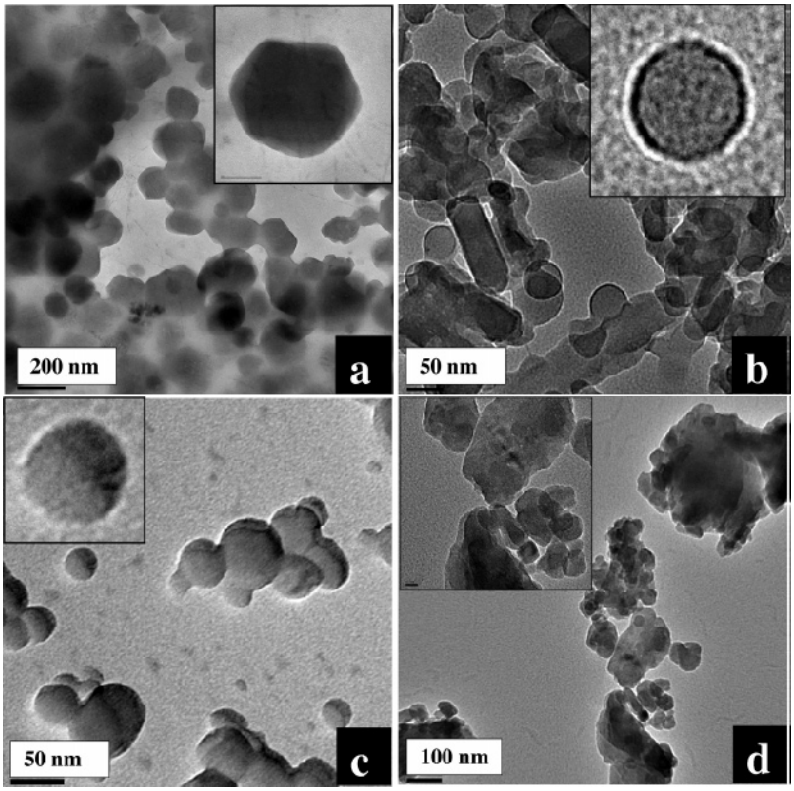

Figure A.4: TEM images of suspensions of clusters of a)TTA/nC_{60}, b)THF/nC_{60}, c)SON/nC_{60}, and d) aqu/nC_{60} (Brant *et al.*, 2006).

Appendix B: Matlab Code for the Calculation of the Weighted Flow Rate in the Annulus of Capture

B.1. Function to Calculate the Weighted Flow in a Pair Gap- Trapped Particle

```
function [Q]=compflow(w,dD,x, y, z, u)
% "w" is the gap size, in units of R
% "dD" is the ratio of particle size to grain size
% "x", "y", and "z", are the x, y, z coordinates of each point the
% mesh extracted from COMSOL
% the direction of the flow is along the "x" axis
% "u" is the velocity at every point extracted from COMSOL

D=2;
R=D/2;

%% Identify annulus of capture
s=0; %counter

a=0.5*D*sqrt(dD^2-(w/D)^2+2*(dD-w/D)); %Edge of the range of capture

p=a-dD; % this is the inner radius of the annulus

for i=1:max(size(y))
    %"annulus of capture" the widht of the annulus is the radius of the
    % particle being trapped. Only the points that are in the annulus
    % are kept, and they are renamed ufi, xfi, yfi and zfi
    if ((x(i)^2+ y(i)^2)<=a^2 && (x(i)^2+ y(i)^2)>=p^2)
        s=s+1;
        ufi(s)=u(i);
        xfi(s)=x(i);
        yfi(s)=y(i);
        zfi(s)=z(i);
    end
end

%% Plot annulus of capture
figure('Position', [1 0 800 600]);
     plot3(xfi,yfi, zfi, 'bx');
     set(gca, 'FontSize', 16);
     xlabel('X', 'FontSize', 14)
     ylabel('Y', 'FontSize', 14);
     zlabel('Z', 'FontSize', 14);

%% Remove points with velocities equal to zero that correspond to the
```

```
% surface of the sphere and were giving wrong results

 F=find (ufi>0);
 UF=mean(ufi(F)); % this is the average velocity of all the velocities
                  % in the annulus and it will be used at the end, to
                  % divide the final cosine weigthed velocity.
 uff=ufi(F);
 xf=xfi(F);yf=yfi(F);zf=zfi(F);

%% Multiply velocities by the cosine of the angle of incidence
     for i=1:max(size(uff))
     cosa(i)=(xf(i)/sqrt((xf(i)^2+ yf(i)^2)));
     uf(i)=uff(i)*abs(cosa(i));
     end

     % plots to see how velocities have changed
     figure('Position', [1 0 800 600]);
     plot(yf, acos(cosa)*180/pi, 'bx');
     set(gca, 'FontSize', 16);
     xlabel('point', 'FontSize', 14);
     ylabel('cosine of angle', 'FontSize', 14);

     figure('Position', [1 0 800 600]);
     plot(yf, uf, 'bx'); hold on ; plot(yf, uff, 'rx');
     set(gca, 'FontSize', 16);
     xlabel('y, distance from the center of the gap', 'FontSize', 14)
     ylabel('velocity', 'FontSize', 14);

% This far I have an annulus of velocities

%% Integration

% Select an incrment for the integral in the y and z directions:
dy=0.01;
dz=0.005;

% This loop is to include the exact value of "a" in the last interval
Dy=[];
DY=repmat(dy,100,1);
A=repmat(a,100,1);
O=repmat(0,100,1);
for i=1:100
    Dy(i)=O(i)+(i-1)*DY(i);
    if Dy(i)>A(i)
        Dy(i)=A(i);
        break;
    end
end
%%%
Z=sparse(650,32);
U=sparse(650,32);
```

```
Y=sparse(650,32);
X=sparse(650,32);

% Group velocities in their intervals and calculate the average
m=0;
for j=2:max(size(Dy))  %for every interval of "y"
    m=m+1;n=0;
    for i=1:max(size(yf))  %check every point
        %group velocities in slices along "y" axis
        if (yf(i)>Dy(j-1) && yf(i)<=Dy(j))
            n=n+1;
            Z(m,n)=zf(i);
            U(m,n)=uf(i);
            Y(m,n)=yf(i);
            X(m,n)=xf(i);
        end
        Xx(m)=mean(X(m,:));  %mean "x" in every "y" interval
    end
    %     figure(1)
    %     plot(Z,U,'o')
    %     xlabel('Z'); ylabel('U'); title('every set corresponds to a
slice in "y"');
    %     xlim([0.95, 1.04]);ylim([0,0.011]);
    Yy(m)=0.5*(Dy(j-1)+Dy(j)); %average "y" in the interval
end

el=0;
for k=1:m %m is the number of "y" intervals
    if (Z(k,:)==zeros(size(Z(k,:))))
       break
    else
        el=el+1;
    %calculate min and max z in every slice of z
    zm(el)=min(nonzeros(Z(k,:))); %%it doesn't decrease with the
increase in "y"...
    zM(el)=max(nonzeros(Z(k,:)));

    %%%% I do this to include the last interval of Dz
    Dz=[];
    ZMm=repmat(zm,1000,1);
    DZ=repmat(dz,1000,1);
    ZM=repmat(zM,1000,1);
    for l=1:1000
        Dz(l)=ZMm(l)+(l-1)*DZ(l);
        if Dz(l)>ZM(l)
            Dz(l)=ZM(l);
            break;
        end
    end
    %%%%%%%%%%%%%%%%%%%%%%%%%%%%%%%%%%%%%%%%%%%%%%%%%%%%%%%%%%%%%%%%%%%%
    m2=0;
    for j=2:max(size(Dz))
```

```
        m2=m2+1; n2=0;
        for i=1:max(size(Z(k,:)))
            %group velocities in slices of "z" in each slice of "y"
            if (Z(k,i)>=Dz(j-1) && Z(k,i)<=Dz(j))
                n2=n2+1;
                UU(el,m2,n2)=U(k,i);
                ZZ(el,m2,n2)=Z(k,i);
            else
                n2=n2+1;
                UU(el,m2,n2)=0;
                ZZ(el,m2,n2)=0;
            end
        end
        %             figure(2)
        %             plot(ZZ(:,:,k), UU(:,:,k), 'o');
        %             hold on
        %             xlim([0.95, 1.04]);
        %             ylim([0,0.011]);

        Uu(el,m2)=mean(nonzeros(UU(el, m2,:)));
        if isnan(Uu(el,m2))
            Uu(el,m2)=0;
        end
        Zz(el,m2)=0.5*(Dz(j-1)+Dz(j));
    end
% figure(3)
% plot(Zz(:,k), Uu(:,k), 'o') %this is avg Z vs. avg U for every %
interval in y
% xlabel('<Z>'); ylabel('<u>'); title('every curve corresponds to a "y"
slice')
% hold on
UZ(el)=trapz(Zz(el,:),Uu(el,:));
end
end

YY(1)=0;
ZU(1)=UZ(1);
for i=2:el+1
    YY(i)=Yy(i-1);
    XX(i)=Yy(i-1);
    ZU(i)=UZ(i-1);
end
YY(el+2)=a;
XX(el+2)=0;
ZU(el+2)=UZ(el);
% figure(4)
% plot(YY, ZU, 'o')
% xlabel('<Y>'); ylabel('UZ, u integrated along z');
% hold on

%% 2nd integral, equals the flow in the domain
```

```
UZY=trapz(YY, ZU);

% the final flow for the combination gap size (w) particle size (dD) is
% divided by the average velocity in the gap, for that particle size
% (UF) calculated
Q=UZY/UF;
```

B.2. Code to Calculate Dimensionless Constants for Straining Rate

```
%% This code calculates the dimensionless constant for straining rate
% for different particle sizes in the same gap.
% The result is just an array of values of dimensionless k_str for
% different d/D in the same gap of width w.
% A table needs to be filled with all the combinations of gap size -
% trapped particle size before calculating the dimensionless constant
% for straining rate for the pack (using gap frequencies).

% This code It needs the function "compflow"

load uqh5.txt; % This is how I called the  file extracted from COMSOL
               % that has the flow field for a gap of size w=0.05R

x=uqh5(:,1); %  x coordinate
y=uqh5(:,2); %  y coordinate
z=uqh5(:,3); %  z coordinate
u=uqh5(:,4); %  velocity

%% Change gap size here!!, according to the file that is loaded
% this is gap size relative to R (radius of the grain)
w=0.05;

%%  Particle sizes
% can be only one size or a range. Pay attention to the gap size
% considered
% (w)
dD=((w/2)+0.005):0.005:0.1;
%dD=[0.03, 0.035, 0.04, 0.045, 0.05, 0.055,  0.065,...
%0.07, 0.075, 0.08, 0.085, 0.09, 0.095, 0.1];

for i=1:max(size(dD))
[Q]=compflow(w,dD(i),x,y,z,u); % compflow is a function
so(i)=[Q];
end
```

Appendix C: Calculation of the Prefactor for the Constant for Straining Rate from Sharma and Yortsos Theory (1987)

The following equation is the population balance from Sharma and Yortsos (1987a) theory:

$$q\frac{\partial \rho_x f_s}{\partial x} + \phi\frac{\partial \rho_s f_s}{\partial t} = \text{Rate of mechanical trapping at pore throats} \qquad \text{(C.1)}$$

where q is the fluid superficial velocity (LT^{-1}), ρ_x and ρ_s are particle concentrations per unit volume (number/L^3), f_s is the size distribution of suspended particles (dimensionless) and ϕ is the porosity.

The rate of plugging of pores in the size interval (r_p, r_p+dr_p) by particles in the size interval (r_s, r_s+dr_s) is given, in Sharma and Yortsos (1987a), by:

$$\frac{\rho_s f_s q P(r_s) dr_s}{\phi l_p} \times \frac{N_p f_p r_p^2 u_R dr_p}{\int_0^{r_s} N_p f_p r_p^2 u_R dr_s} = \frac{\rho_s f_s q P(r_s) dr_s}{\phi l_p} \times \frac{I'(r_p)}{I(r_s)} dr_p \qquad \text{(C.2)}$$

where $P(r_s)$ is the fraction of particles of size (r_s, r_s+dr_s) that are trapped at each step and is given by:

$$P(r_s) = \frac{I(r_s)}{I(\infty)} \qquad \text{(C.3)}$$

N_p is the number of pores per total volume (number/L^3), and I is a cumulative flow given by:

$$I(r) = \int_0^r f_p \, r_p^2 \, u_R \, dr \tag{C.4}$$

In the case that straining (size exclusion) is the only mechanism responsible for particle trapping (Sharma and Yortsos, 1987c), the rate of trapping in equation (C.2) is equal to $k_{str}\rho_s$, therefore, using the left hand side of equation (C.2):

$$\frac{\rho_s \, f_s \, q \, dr_s \, N_p \, f_p \, r_p^2 \, u_R \, dr_p}{\phi \, l_p \int_0^\infty N_p \, f_p \, r_p^2 \, u_R \, dr_p} = k_{str} \; \rho_s \tag{C.5}$$

On the other hand, using the left hand side of equation (B.2), the rate of trapping is also equal to:

$$k_{str}\rho_s = \frac{\rho_s \, q}{\phi \, l_p} \int_{r_p}^\infty f_s \, dr_s \, \frac{I'(r_p)}{I(\infty)} dr_p \tag{C.6}$$

or:

$$k_{str}\rho_s = \frac{\rho_s \, q}{\phi \, l_p} \int_{r_p}^\infty \frac{f_s \, dr_s \, N_p \, f_p \, r_p^2 \, u_R \, dr_p}{\int_0^\infty N_p \, f_p \, r_p^2 \, u_R \, dr_p} \tag{C.7}$$

therefore:

$$k_{str} = \frac{q}{\phi \, l_p} \int_{r_p}^\infty \frac{f_s \, dr_s \, N_p \, f_p \, r_p^2 \, u_R \, dr_p}{\int_0^\infty N_p \, f_p \, r_p^2 \, u_R \, dr_p} \tag{C.8}$$

The integral from r_p to infinity in equation (C.8) is the dimensionless constant for straining rate (k'_{str}), and therefore the prefactor is given by:

$$\text{Prefactor} = \frac{q}{\phi l_p} \tag{C.9}$$

Appendix D: Identification and Measure of Contact Line Lengths during Drainage and Imbibition Displacements

The C routines, perl scripts and Matlab codes referred in this section are part of the LSMPQS package that is available for download in:

http://users.ices.utexas.edu/~masha/lsmpqs/index.html

D.1. Procedure to Identify and Calculate the Contact Line Length for Every Step of Drainage or Imbibition

D.1.1. Contact Line Identification

In the same directory containing the drainage or imbibtion steps from LSMPQS simulation (data_stepID.gz), the simulation input file (in_file), the grid file (grid.gz), and the mask file (mask.gz), run the routine:

- compute_tripleContact_simulation d (for drainage)
- compute_tripleContact_simulation i (for imbibition)

For every drainage or imbibition step the binary file "triple_stepID.gz" is written in the same directory where is run. This file contains the configuration of the contact line between the 3 phases. To visualize the contact line, do:

- isocolor triple_stepID.gz g

where *g* is the color (green in this case) for the voxels of the contact line.

To identify the contact line associated to trapped phases, run the perl script:

- contact_line_trapped_d (for drainage)
- contact_line_trapped_i (for imbibition)

This script must be copied in the same directory where the simulation steps are. Before running the script, open the perl file and modify *start_step* and *end_step* numbers according to the first and last steps in the simulation where wetting phase (for drainage)

or non-wetting phase (for imbibtion) are trapped. Binary files of the type "triple_stepID_trap_w.gz" or "triple_stepID_trap_nw.gz" are created in the same directory after the script runs.

D.1.2. Contact Line Length Calculation

The contact line length is calculated by means of obtaining the Medial Axis of the voxel configuration obtained after running "compute_tripleContact_simulation". After all the "triple_stepID.gz" files are generated, create a folder under the same directory where the simulation steps are called "tripleContact" and move all the triple contact files there.

Copy the perl script "create_MA_files_simulation.pl" into the "tripleContact" folder. Open the perl script to modify, *start_step* and *end_step*, which are the first and last steps for which the contact line length will be calculated) as well as *NX*, *NY* and *NZ*, which are the number of voxels of the geometry in the x, y and z directions.

Run the perl script. This will create a folder named "ma" containing the subfolder "geomview" and as many "stepID" folders as indicated by *start_step* and *end_step*. Every "stepID" folder has the subfolders "ma", "burn", "cases", "ma_t" and "seg", which contain medial axis files that are needed to compute the length.

Once the script is done, run the Matlab function "maLengthSimulation" in the same directory where the "triple_stepID.gz" files are. This Matlab function has the following arguments: *step_init* (first step for which length is calculated), *step_fin* (last step for wich length is calculated), *R* (radius of the grains), *dx* (size of the voxel on units of *R*), and *NXYZ* (bulk volume in units of R^3). This Matlab code creates the binary array "MALength_simulation.gz", that contains the total contact line length for every step in the simulation, besides the arrays "MALength_simulation_trap_w.gz" and

"MALength_simulation_trap_nw.gz" that contain the contact line length associated to the trapped wetting and non-wetting phases respectively. This arrays can be read in Matlab using the function "readDataArray1D (file_name)" and can be plotted versus curvature or wetting phase saturation.

D.2. Procedure to Identify and Calculate the Contact Line Length for a Single Step of Drainage or Imbibition

D.2.1. Contact Line Identification

In this case, run the routine "compute_tripleContact_step" with the arguments input_file, data_file, grid_file, and mask_file, where data_file is the LSMPQS file "data_stepID.gz" for the step whose length will be calculated. This routine generates a binary file called "triple.gz" in the same directory where the simulation step is.

D.2.2. Contact Line Length Calculation

Copy the perl script "create_MA_files_simulation.pl" in the same directory where the file "triple.gz" is. Open the script and modify *step_start*, *step_end*. Because this is a single step, *step_start* and *step_end* are the same numer. Modify *NX*, *NY*, and *NZ* which are the number of voxels of the geometry in the x, y and z directions. Run the perl script. As in the case of the full simulation, a folder called "ma" will be created, containing the subfolders "geomview", and "stepID" (only one folder in thie case). The "stepID" folder contains the subfolders "ma", "burn", "cases", "ma_t" and "seg".

Once the script is done, run the Matlab function "maLengthStep" in the same directory where the "triple.gz" file is. The arguments for this function are: *step* (the number of the step whose length is going to be calculated), *R* (the radius of the grain), *dx*

(the voxel size in units of R), and $NXYZ$ (the bulk volume in units of R^3). This function creates a text file named "length_stepID.txt" that contains the normalized length.

D.3. PROCEDURE TO IDENTIFY AND CALCULATE THE CONTACT LINE LENGTH FROM A HIGH RESOLUTION IMAGE OF AN UNSATURATED POROUS MEDIA

For this procedure, the segemented file of the image is needed, where voxels of solid, wetting and non-wetting phases are identified by different numbers (0, 1 and 2 for example).

Use the Matlab function "xrayimage" whose argument "file_name" is the name of the segmented file. Open the file to make sure that the phases are assigned their correct number (by default, solid is 0, non-wetting is 1 and wetting is 2). Run the matlab function. The binary files "step.gz", step_w.gz" and "mask.gz" are created in the same directory where the original segemented file for the image is. These files correspond to the non-wetting phase, wetting phase and solid phase respectively

LSMLIB files need to be created to be able to later use the "compute_tripleContact_step" routine. The method to do this this is detailed next:

1) Create a folder named "create_grid" and copy there the three files previously generated with Matlab.
2) Make an input file (in_file) containing the following information:

```
geom_type       LSMLIB_REAL_data_pad
geom_fname      mask.gz
ic                   i
ic_type          LSMLIB_REAL_data_pad
ic_fname         step.gz
```

3) Run "initialize_geometry in_file"

This creates the file “grid.gz” which is the final grid, and the files “data_init.gz” and “mask.gz” that still need reinitialization to be used.

4) Create a new folder under the folder “create_grid” called “reinitialize_mask”

   In this folder, create an input file (in_file) with the following information:

```
geom_type      LSMLIB_REAL_data
geom_fname     ../mask.gz
```

   mask.gz is the file created in the previous step

5) Run “reinitialize in_file”

This creates the file “data_final.gz” which is the mask reinitialized as LSMLIB file, besides the files “data_init.gz” and “grid.gz” which will not be used.

6) Create a new folder under the folder “create_grid” called “reinitialize_data_step”. In this folder, create an input file (in_file) with the following information:

```
tmax_r    0.1
```

7) Run

   “reinitialize in_file ../data_init.gz ../grid.gz ../reinitialize_mask/data_final.gz”

   This generates the file “data_final.gz” which is the LSMLIB file for the non-wetting phase of the image, equivalent to the “data_stepID.gz” files created by a LSMPQS simulation.

8) Use the routine “compute_tripleContact_step” as shown in section D.2 to identify the contact line and calculate its length.

Appendix E: Geometric Analysis of Pendular Rings

In several instances in this dissertation we have used pendular rings. In this appendix we show the geometry of the pendular rings

E.1. Analytical Calculation of the Contact Line Length in a Pendular Ring

In this section we show the analytical calculation of the contact line length associated to a pendular ring between two spheres of the same size, assuming a toroidal shape for the pendular ring. This analysis is based on the calculation of areas of pendular rings show by Motealleh (2009).

Figure E.1 shows a schematic of the liquid bridge between two spherical grains of radius *R*.

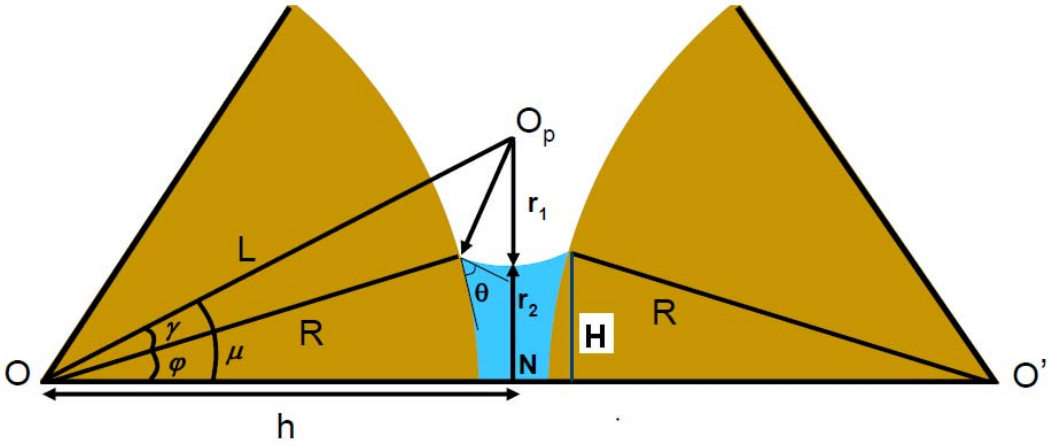

Figure E.1: Schematic of a toroidal liquid bridge of the wetting phase between two grains with radius *R*. The contact angle between the pendular ring and grains is θ. the vertices O and O' correspond to the sphere centers. Line OO' that joins the sphere centers is the axis of symmetry for the liquid bridge. For the toroid approximation the surface of the liquid bridge has radii of curvature r_1 and r_2. The grain centers are separated by distance 2*h*. Point N is the equidistance from grain centers. (From Motealleh, 2009)

From the definition of the mean curvature:

$$C = \frac{1}{r_1} - \frac{1}{r_2} \tag{E.1}$$

Applying the cosine rule to the triangle OO_pN:

$$\begin{aligned} L^2 &= R^2 + r_1^2 - 2 \cdot R \cdot r_1 \cdot \cos(\pi - \theta) \\ &= R^2 + r_1^2 + 2 \cdot R \cdot r_1 \cdot \cos(\theta) \end{aligned} \tag{E.2}$$

which can also be expressed as:

$$L = \sqrt{R^2 + r_1^2 + 2 \cdot R \cdot r_1 \cdot \cos(\theta)} \tag{E.3}$$

For the triangle OO_pN we can also write:

$$L^2 = h^2 + (r_1 + r_2)^2 \tag{E.4}$$

Substituting E.1 and E.3 in E.4 we get the following cubic equation:

$$r_2^3 + p \cdot r_2 + q = 0 \tag{E.5}$$

which has three real roots if:

$$\left(\frac{p}{3}\right) + \left(\frac{q}{2}\right) < 0 \tag{E.6}$$

where:

$$p = \frac{3n - m^2}{3} \tag{E.7}$$

$$q = t + \frac{2m^3}{27} - \frac{m \cdot n}{3} \tag{E.8}$$

$$n = \frac{C\,(h^2 - R^2) - 2R\cos(\theta)}{C} \tag{E.9}$$

$$m = \frac{3}{C} \tag{E.10}$$

$$t = \frac{h^2 - R^2}{C} \tag{E.11}$$

For point contacts the value of the half length between grain centers (h) is equal to the grain radius R. Therefore r_2 in equation (E.5) has only one positive root that exists for all values of curvature. If there is a gap between the two spheres r_2 has two positive roots. For each gap size there is a maximum of curvature at which r_2 has at least one positive root. For larger curvatures the liquid bridge is not stable and will rupture. When r_2 has two roots, the larger value is chosen since it yields to smaller specific area, which is thermodynamically stable.

Therefore r_2 is calculated from (E.5), r_1 from (E.1) and L from (E.3). The filing angle of the rings/bridges φ is the angle between the line connecting the two grains

centers (line OO') and the line connecting a center of a grain and the point that the pendular ring touches the grain. From the trigonometry of the triangle OO_pN:

$$\varphi = \mu - \gamma \tag{E.12}$$

where:

$$\mu = \sin^{-1}\left(\frac{r_1 + r_2}{L}\right) \tag{E.13}$$

$$\gamma = \cos^{-1}\left(\frac{R^2 + L^2 - r_1^2}{2RL}\right) \tag{E.14}$$

The radius of the contact line associated to a pendular ring in one sphere is given by *H* where:

$$H = R\sin(\varphi) \tag{E.15}$$

Therefore the contact line length associated to the pendular ring is:

$$\text{Contact line length} = 2\times(2\pi H) \tag{E.16}$$

where *2* accounts for the two circles of contact line, one per sphere holding the pendular ring.

E.2. Analytical Calculation of the Interfacial Areas for a Pendular Ring between two Spheres of the Same Size

We used the interfacial areas in the simple case of a pendular ring between two spheres to estimate its rate of change of surface free energy per unit pore volume with respect to wetting phase saturation in Chapter 6. Pertinent formulas for the calculation are shown in this section.

The area of the pendular ring having a toroidal shape that can be regarded as the interfacial wetting-non-wetting area is given by (Anna Johnson MS thesis, 2001):

$$A_{ring} = a_{w\text{-}nw} = 4\pi r_1 \left[\left(r_1 + r_2 \right) \cdot \sin^{-1}\left(\frac{h}{r_1 + R} \right) - \frac{h r_1}{r_1 + R} \right] \tag{E.17}$$

where h, r_1 and r_2 are the same magnitudes as shown in Figure E.1. For a point contact, $h = R$.

The area of the wetting-solid interface is calculated as the surface of the spherical cap defined by $2H$ and x in Figure E.2:

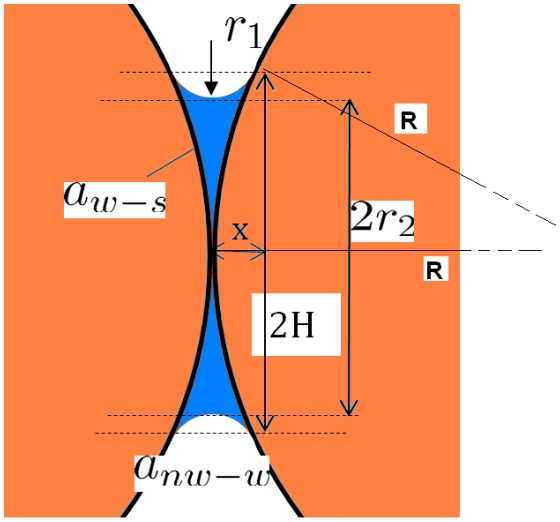

Figure E.2: Schematic of the pendular ring between two grains of radius *R*

The surface of the cap is:

$$a_{s\text{-}w} = 2\pi (H^2 + x^2) \tag{E.18}$$

where the *2* accounts for the two spheres, and being x equal to:

$$x = R - \sqrt{R^2 - H^2} \tag{E.19}$$

Finally the non-wetting-solid interfacial area is given by the total solid surface of the two grains minus the surface of the non-wetting-solid area (equation E.18). Therefore:

$$a_{s\text{-}nw} = 2(4\pi R^2) - 2\pi (H^2 + x^2) \tag{E.20}$$

The volume of the pendular ring, and therefore the volume of the wetting phase, is given by (Anna Johnson MS thesis, 2001):

$$V_{ring} = 2\pi\left(r_1^2\left(h - \sqrt{(R+r)^2-h^2}\ \sin^{-1}\left(\frac{h}{r+R}\right)\right)-\frac{h}{3}+ hR^2 - \frac{2R^3}{3}\right) \quad \text{(E.21)}$$

E.3. Analitical Calculation of the Length of the Interfaces in a Pendular Ring (2D)

For a given curvature *c* the value of r_1 in Figure E.2 is given by:

$$r_1 = \frac{1}{c} \quad \text{(E.22)}$$

The value of the angle between the line joining the center of the grain and the point contact of the grains and the line joining the center of the grain and the center of ther meniscus of radius r_1 is given by:

$$\text{angle} = \frac{R}{R + r_1} \quad \text{(E.23)}$$

The value of *H* is given by:

$$H = R \sin(\text{angle}) \quad \text{(E.24)}$$

The area of the wetting phase (blue area in Figure E.2) can be calculated as the area of the rectangle of sides 2*H* and 2*x*, that we called $Area_T$, where:

$$\text{Area}_T = 2\text{Hx} \tag{E.25}$$

minus the area of the circular segement in the grain ($Area_g$) and minus the area of the circular segment in the meniscus ($Area_m$). To calculate the area of the circular segment in the grain, we need to calculate firs the value of *x*, which is given by:

$$\text{x} = \text{R} - \sqrt{\text{R}^2 - \text{H}^2} \tag{E.26}$$

The area of the circular segment in the grain ($Area_g$) is then:

$$\text{Area}_\text{g} = \text{R}^2 \cos^{-1}\left(\frac{\text{R}-\text{x}}{\text{R}}\right) - \left(\text{R}-\text{x}\right)\sqrt{2\text{Rx}-\text{x}^2} \tag{E.27}$$

To calculate the area of the circular segment in the meniscus, we need to calculate firs the value of *z*, which is given by:

$$\text{z} = \text{r}_\text{l} - \sqrt{\text{r}_\text{l}^2 - \text{x}^2} \tag{E.28}$$

The area of the circular segment in the meniscus ($Area_m$) is given by:

$$\text{Area}_\text{m} = \text{r}_\text{l}^2 \cos^{-1}\left(\frac{\text{r}_\text{l}-\text{z}}{\text{r}_\text{l}}\right) - \left(\text{r}_\text{l}-\text{z}\right)\sqrt{2\text{r}_\text{l}\text{z}-\text{z}^2} \tag{E.29}$$

Therefore the area of the wetting phase ($Area_w$) is given by:

$$\text{Area}_w = \text{Area}_T - 2\text{Area}_g - 2\text{Area}_m \tag{E.30}$$

The length of the wetting-solid interface ($l_{w\text{-}s}$) is given by the length of the arc whose angle is equal to $2 \times angle$, where angle is given by equation (D.24). We are going to consider two circles of radius R contained in a rectangle of dimensions $2R \times 4R$. In this case we have 8 arcs of wetting-solid interface, therefore:

$$l_{w\text{-}s} = 8 \times R \times 2 \times \text{angle} \tag{D.31}$$

The length of the wetting-non-wetting interface ($l_{w\text{-}nw}$) is given by the length of the arc that the meniscus makes between the two grains. The angle (*beta*) is given by:

$$\text{beta} = 2\sin^{-1}\left(\frac{x}{r_1}\right) \tag{E.32}$$

and therefore $l_{w\text{-}nw}$ is given by:

$$l_{w\text{-}nw} = 8 \times R \times \text{beta} \tag{E.31}$$

where the 8 accounts for all the w-nw interfaces in the rectangle containing the two circles.

The length of the nw-s interface ($l_{nw\text{-}s}$) is calculated as:

$$l_{nw\text{-}s} = l_s - l_{w\text{-}s} \tag{E.32}$$

where l_s is the length of the total solid surface, given by :

$$l_s = 4\pi R^2 \tag{E.33}$$

The pore area of the system is given by:

$$\text{Pore Area} = \text{Total Area} - \text{Solid Area} = 8R^2 - 2\pi R^2 \tag{E.34}$$

The porosity based on the area is calculated as the ratio of *Pore Area* to *Total Area*. The wetting phase saturation, also based on the area, that we called S_{wA} is calculated as:

$$S_{wA} = \frac{4\,\text{Area}_w}{\text{Pore Area}} \tag{E.35}$$

where 4 accounts for the total wetting area in the system of two circles in radius R inside a rectangle of sides $2R$ and $4R$.

Appendix F: Digital Topology - Connectivity

Digital topology is used in algorithms that find the skeleton of an object. The Medial Axis (Sirjani and Cross, 1991) of a digitized object is a 26-connected or 6-connected centrally-located skeleton which preserves the original topology and geometry of the object. We have used the Medial Axis algorithm, via 3DMA-Rock software (Lindquist, 1994-2010) to find the skeleton of the contact line between three phases in porous media. In this appendix we introduce the concept of connectivity with simple examples.

A *pixel* is the smallest image area element and a *voxel* is the smallest image volume element. The term *Connected* essentially means "in one piece" and connected will be the original object before skeletonization. The following terms are commonly used in 2D and 3D:

- *4-connected* pixels in 2D share an edge (Figure F.1a)
- *8-connected* pixels in 2D share either an edge or a corner (Figure F.1b)
- *6-connected* voxels in 3D share a side,
- *18-connected* voxels in 3D share a side or an edge,
- *26-connected* voxels in 3D share a side, an edge or a corner

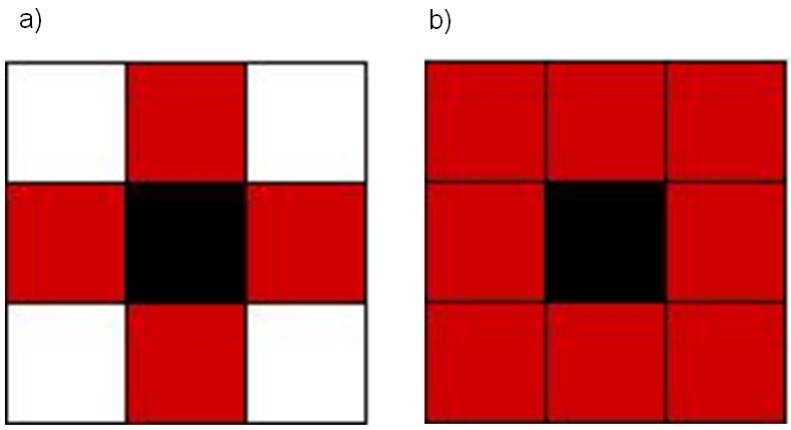

Figure F.1: 2D connectivity a) 4-neighborhood (red) of the center pixel (black) b) 8-neighborhood (red) of the center pixel (black)

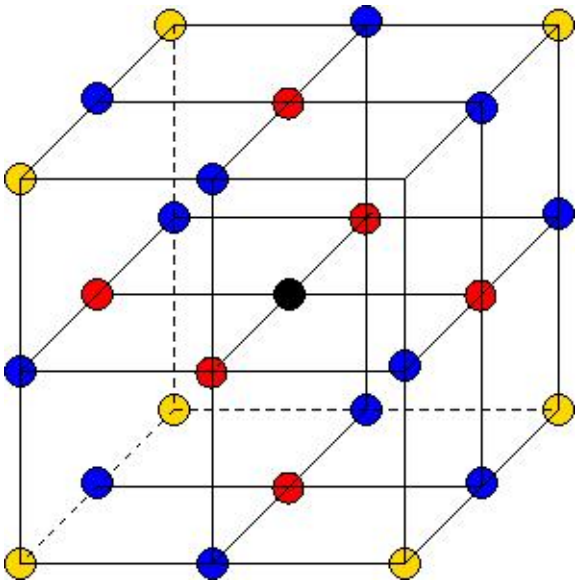

Figure F.2: 3D connectivity, where red dots indicate voxels sharing a side with the center, blue dots indicate voxels sharing an edge, and yellow dots indicate voxels sharing a corner

Therefore by choosing connectivity we define the boundaries of objects in an image. Different choices in connectivity will lead to different skeletons of the same object. In Figure F.3, if we choose the blue pixels to be 8 connected, they will represent one connected component of the blue phase. If they are chose to be 4-connected they will represent 4 individual components. If the blue pixels are assumed 8-connected and the white pixels are assumed 4-connected, then blue pixels represent the line that separates phases A and B.

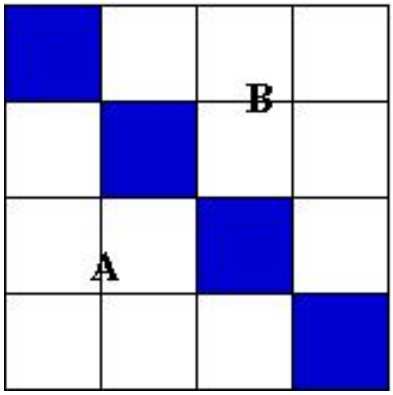

Figure F.3: Blue and white pixels in the figure can represent different scenarios depending on assumed connectivity.

Another simple example on connectivity decision is shown next. We know from math that two lines intersect at one point. In Figure F.4a we see two yellow phase lines intersecting at one pixel. However in the configuration of pixels in Figure F.4b we need 3 or 4 pixels to define the contact (for 8 and 4 connectivity respectively)

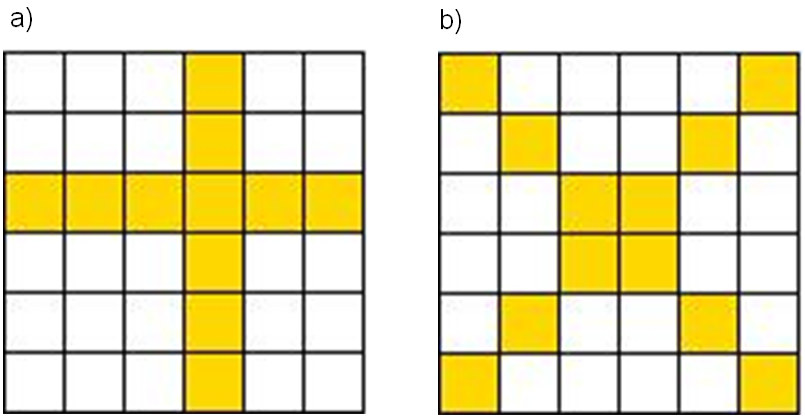

Figure F.4: Two cases of pixel representation of intersection of two lines. a) one pixel define the point contact. b) 3 or 4 pixels are needed to define the point contact.

For the case of a circle, shown in Figure F.5, depending on the cut-off value that we choose for connectivity, blue pixels may or may not be part of the digitized circle which is outlined in black.

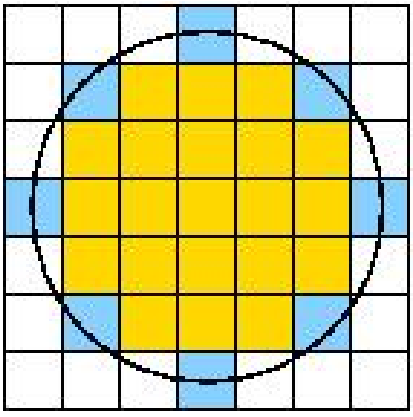

Figure F.5: Different choice in connectivity will include more or less pixels in the digitized image of a circle.

Appendix G: Surface Area Computation and Digitization

In this appendix we illustrate the effect of digitization and its effect on area computation error.

We tested digitization in a sample of 4 spheres whose analytical description is known. In this case the level set based surface area computation is fairly accurate, since the level set function is smooth as opposed to step like.

If the spheres are digitized, as is the case of the input from x-ray images, information is lost. However we have the option of "smoothing" digitized inputs. Figures G.1, G.2 and G.3 show the three scenarios just described for the case of 4 spheres of radius equal to 1 and a numerical spacing equal to 0.16 (computational grid and voxel size of the image).

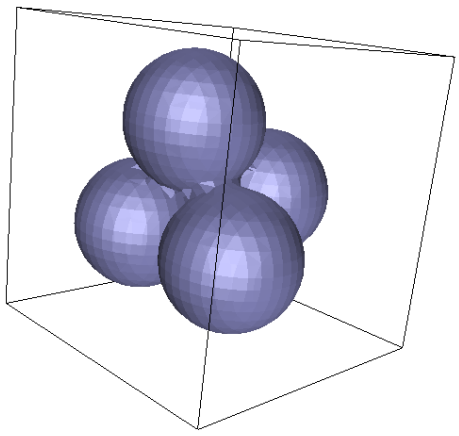

Figure G.1: Analytical information: resolution may be low (12.5 voxels across a diameter) but we have precise information on the distance to the sphere interface at each voxel center

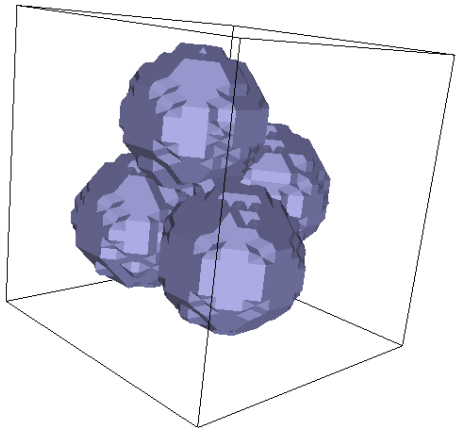

Figure G.2: Digitized information (segmented type): all the information that we have at a voxel is whether it is inside or outside of the sphere and the surface of the spheres shows “staircase effects”.

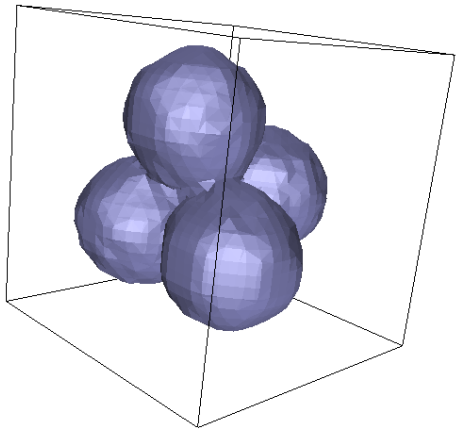

Figure G.3: Digitized information slightly smoothed, after segmented data is processed in the LSMPQS simulation (“reinitialize” routine)

In Figure G.4 we can see the absolute error in the calculation of the surface area when running the level set method in the porous media of know analytical geometry, in the digitized porous media and in the "smoothed" digitized porous media. The error for digitized information is consistent with marching cubes algorithm error (Dalla *et al*. 2002). In this algorithm, independently of how well the image is discretized, the error is going to be near 10% due to the "staircase" effect.

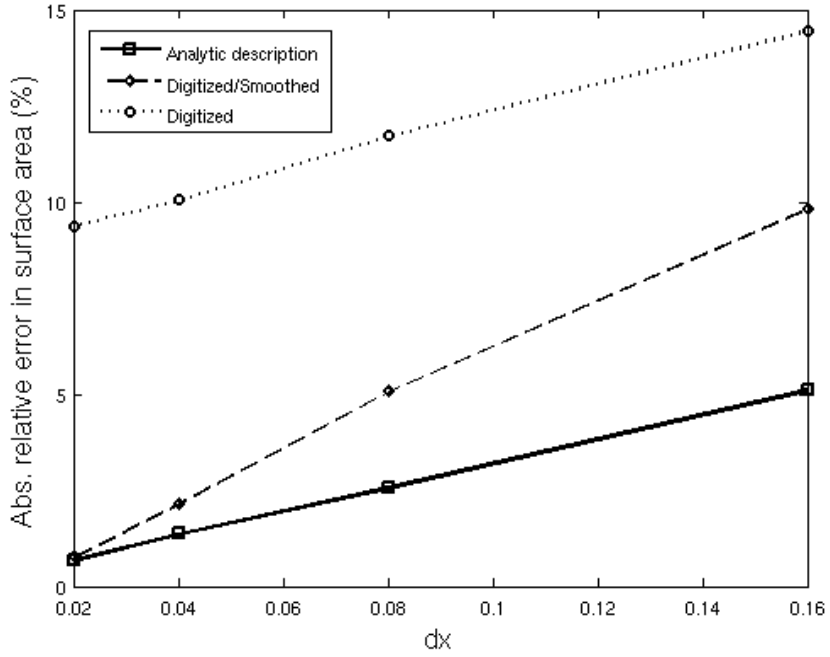

Figure G.4: Surface area error for level set based calculation

Appendix H: Effect of Spatial Configuration, Grain Radius and Presence of Cement in Contact Line Length

H.1. Contact Line Length in Slits of a Single Layer of Spheres

We simulated drainage in channels or slits filled with a single layer or randomly distributed spheres of the same size (Figure H.1) and calculated the contact line length in the same fashion as we did for the packs shown in Chapter 3 with the purpose of study n this case we can observe the influence of the particle distribution.

Figure H.3 shows contact line length versus wetting phase saturation for a packing of 91 (shown in Figure 3.5 in Chapter 3) and a packing of 99 spheres in a slit distribution. The contact line length for the slit is obviously larger than for the cubic packing, in part due to the "wall effects", i.e., the contact line associated with the walls of the container (Figure H.4) which is larger when compared with the volume of the pack than it is for the cubic packs but also due for the larger number of contact pendular rings at the end of drainage, shown in Figure H.2 (cf. Figure 3.8a in Chapter 3).

The geometric configuration of the spheres greatly affects the amount of contact line.

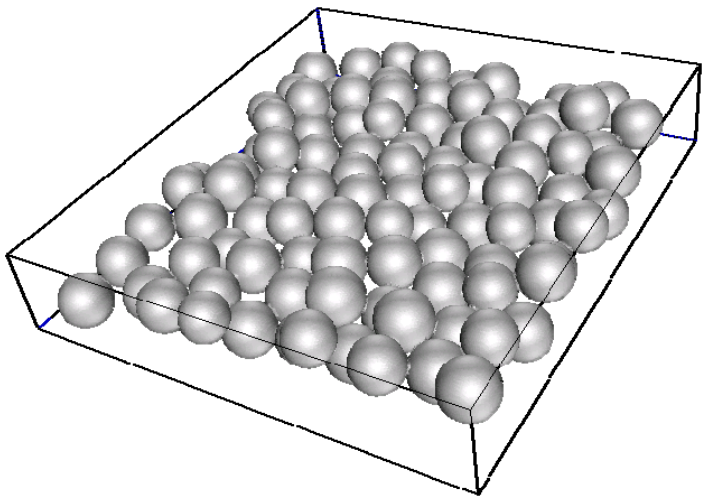

Figure H.1: Slit of 99 randomly distributed spheres of radius R. The dimensions of the slit are $22R \times 20R \times 2.5R$.

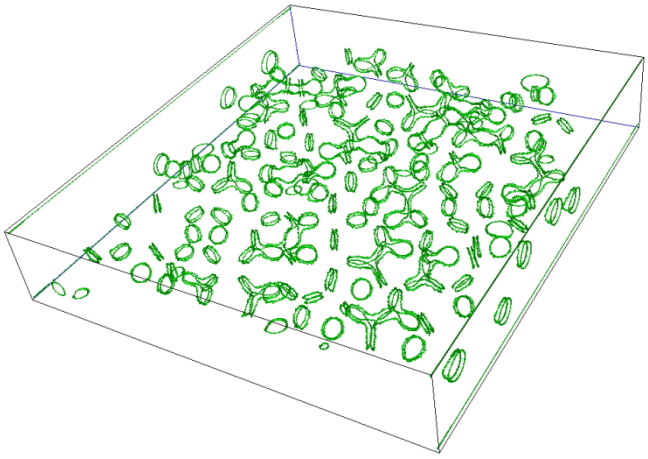

Figure H.2: Contact line configuration at the end of drainage ($S_w = 0.03$, curvature = 7.5).

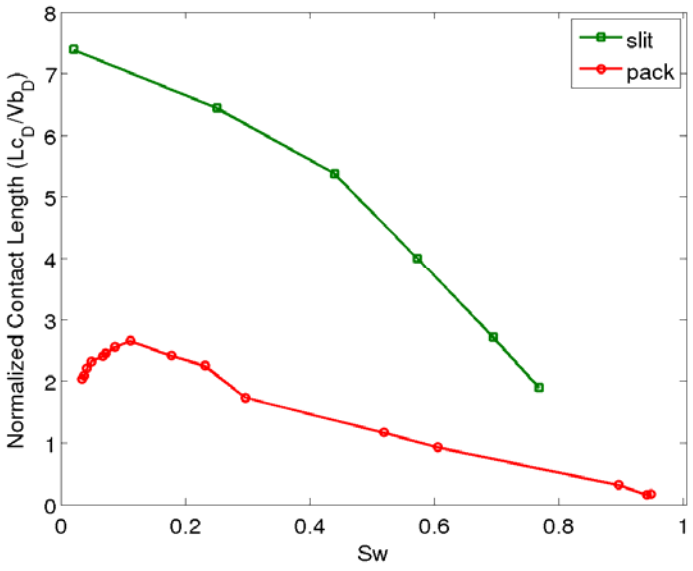

Figure H.3: Contact line *vs*. water saturation for a slit of 99 spheres and a cubic pack of 91 spheres of radius R for a voxel size $dx = 0.04R$.

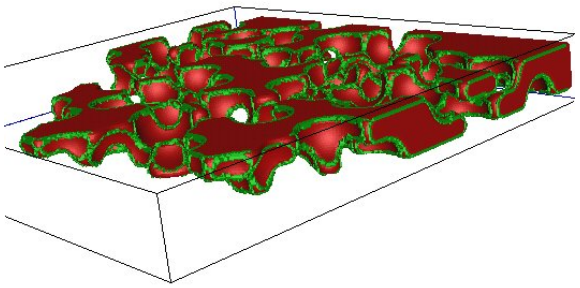

Figure H.4: Contact line configuration (green) and non-wetting phase (red) in a slit of spheres showing contact line associated to the walls.

H.2. EFFECT OF GRAIN SIZE

We simulate drainage and imbibition in a small pack of 22 spheres having a radius equal to R and in a pack with the same distribution of spheres but having a radius of $1.25R$. We also took the same volume for simulations. The packs are shown in Figures H.5 and H.6.

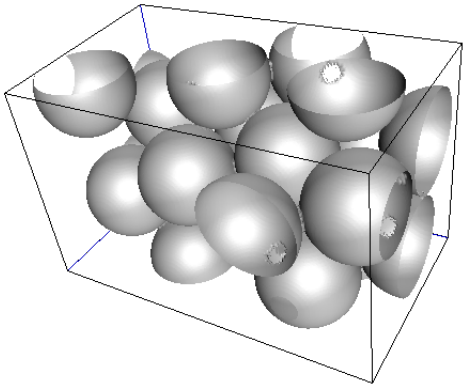

Figure H.5: Pack of 22 spheres of radius R contained in a cube of dimensions 113×188×120 where the voxel size is $dx = 0.04R$

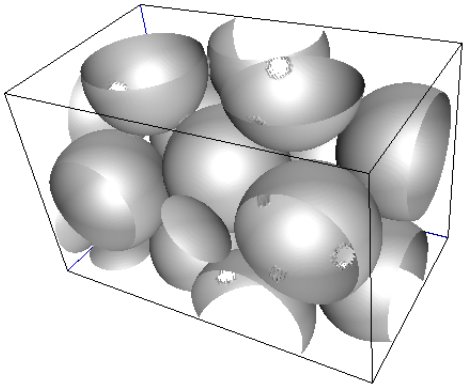

Figure H.6: Pack of 22 spheres of radius 1.25R contained in a cube of dimensions 113×188×120 where the voxel size is dx = 0.04R.

The configuration of the contact lines at the last step of drainage for both packs is shown in Figure H.7 and Figure H.8. The contact line lengths versus wetting phase saturation are shown in Figure H.9 and H.10.

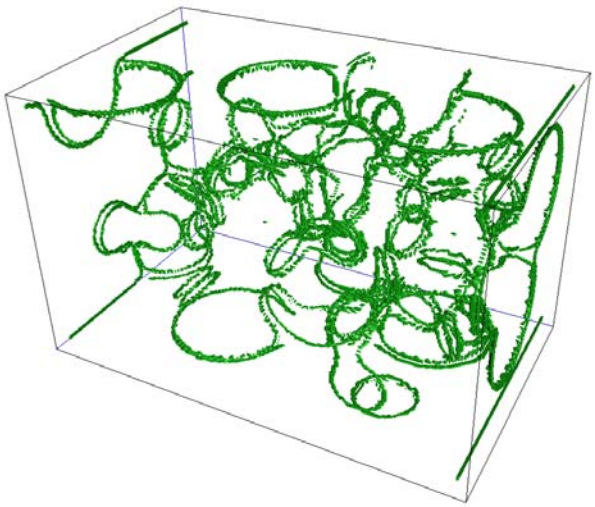

Figure H.7: Contact line configuration at the last step of drainage in a pack of spheres of radius equal to 1R. (S_w = 0.04, curvature = 8.5).

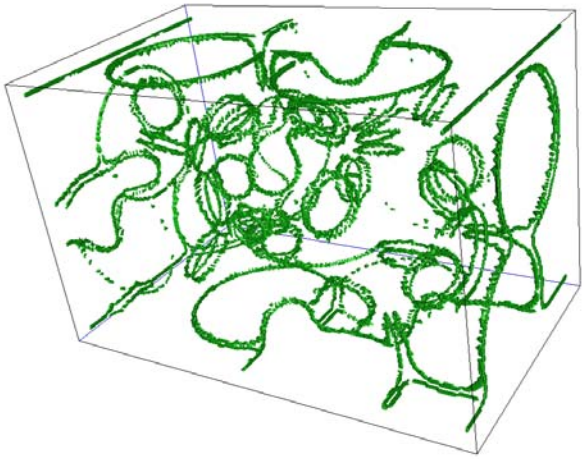

Figure H.8: Contact line configuration at the last step of drainage in a pack of spheres of radius equal to 1.25R. (S_w = 0.04, curvature = 8.9).

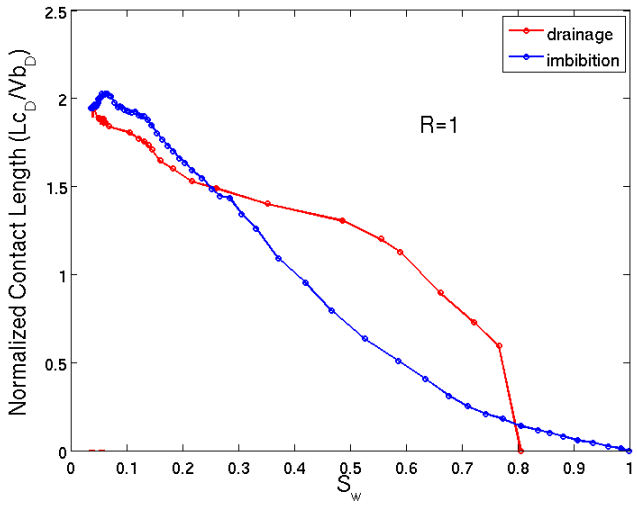

Figure H.9: Contact line length *vs.* wetting phase saturation for a computer generated pack of 22 spheres of radius R using a voxel size dx =0.04R.

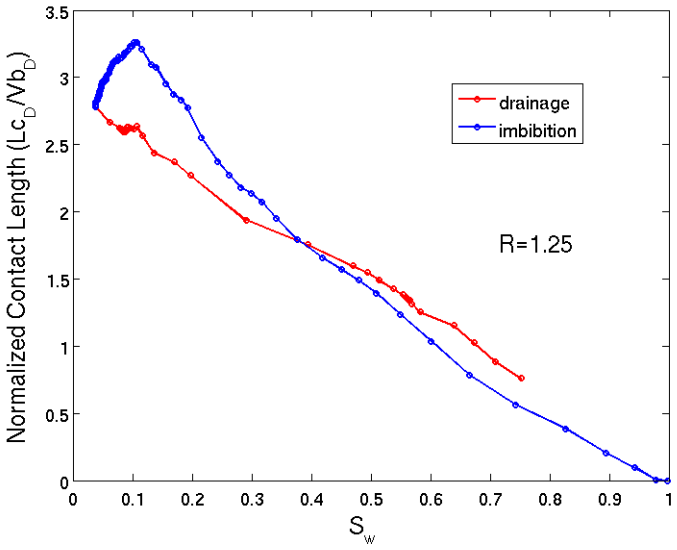

Figure H.10: Contact line length *vs.* wetting phase saturation for a computer generated pack of 22 spheres of radius R using a voxel size dx =0.04R.

The contact line length in this case is larger for the pack with larger particle size. The maximum value of contact line for the pack having spheres of size R is 2 which is

slightly smaller than the maximum observed for a larger pack with spheres of the same size and using the same resolution (cf. Figure 3.6).

The more noticeable difference in these results when compared with the results in sphere packs is the presence of hysteresis. We think this is caused by the amount of contact line that is associated to the walls of the pack. We recommend to "resize" the packs to remove the outer voxels where there is contact line associated to the wall, recalculate contact line length and check if the hysteresis disappears.

Bibliography

Adamson, W. and A.P. Gast: Electrical Aspects of Surface Chemistry, *in* Physical Chemistry of Surfaces, Chapter V, New York: Willey, 6th Edition (1997).

Baghdikian, S.Y., M.M. Sharma, and L.L. Handy: Flow of Clay Suspensions through Porous Media, Paper SPE 16257, *Proceedings of the SPE International Symposium on Oilfield Chemistry*, San Antonio, February 4-6, (1989).

Behseresht, J., S. Bryant, and K. Sepehrnoori: Infinite-Acting Physically Representative Networks for Capillarity-Controlled Displacements, *Society of Petroleum Engineers Journal*, 14 (4), 568-578, (2009).

Bellona, C., J.E. Drewes, P. Xu, and G. Amy: Factors Affecting the Rejection of Organic Solutes during NF/RO Treatment-a Literature Review, *Water Research*, 38, 2795-2809, (2004).

Berg, S., A.W. Cense, J.P. Hofman, and R.M.M. Smits: Two Phase Flow in Porous Media with Slip Boundary Condition, *Transport in Porous Media*, 74, 275-292 (2008).

Bird, R., W. Steward, and E. Lightfoot: Transport Phenomena, Wiley and Sons, New York, (2001).

Bowen, W.R. and T.A. Doneva: Atomic Force Microscopic Studies of Membranes: Effect of Surface Roughness on Double-Layer Interactions and Particle Adhesion, *Journal of Colloid and Interface Science*, 229, 544-549, (2000).

Bradford, S., and M. Bettahar: Concentration Dependent Transport of Colloids in Saturated Porous Media, *Journal of Contaminant Hydrology*, 82, 99-117, (2006).

Bradford, S. and F.J. Leij: Estimating Interfacial Areas for Multi-Fluid Soil Systems, *Journal of Contaminant Hydrology*, 27, 83-105, (1997).

Bradford, S., J. Simunek, M. Bettahar, M.T. van Genutchen, and S. Yates: Modeling Colloid Attachment, Straining and Exclusion in Saturated Porous Media, *Environmental Science and Technology,* 37, 2242-2250, (2003).

Bradford, S. and S. Torkzaban: Colloid Transport and Retention in Unsaturated Porous Media: A Review of Interface-, Collector-, and Pore-Scale Processes and Models, *Vadose Zone Journal*, 7(2), 667-681, (2008).

Bradford, S., S. Yates, M. Bettahar, and J. Simunek, Physical factors affecting the transport and fate of colloids in saturated porous media, *Water Resources Research*, 38 (12), 1327, paper 63, (2002).

Brant, J., J. Labille, J.-Y. Bottero, and M. Wiesner: Characterizing the Impact of Preparation Method on Fullerene Cluster Structure and Chemistry, *Langmuir*, 22 (8), 3878-3875, (2006).

Brant, J., J. Labille, J.-Y. Bottero, and M. Wiesner: Nanoparticle Transport, Aggregation, and Deposition, in Environmental Nanotechnology. Applications and Impacts of Nanomaterials, Chapter 7, Wiesner, M. R., and Bottero, J.-Y., eds., Mcgraw-Hill, (2007).

Bridge, J.W., A.L. Heathwaite, and S.A. Banwart: Measurement of Colloid Mobilization and Redeposition during Drainage in Quartz Sand, *Environmental Science and Technology*, 43, 5769-5775, (2009).

Bryant. S. and A. Johnson: Wetting Phase Connectivity and Irreducible Saturation in Simple Granular Media, *Journal of Colloid and Interface Science*, 263 (2), 572-579, (2003).

Bryant. S. and A. Johnson: Bulk and Film Contributions to Fluid/Fluid Interfacial Area in Granular Media, *Chemical Engineering Communications*, 191, 1660-1670, 2004, 263 (2), 572-579, (2003).

Bryant, S., Mellor, D., and Cade, C.: Physically Representative Network Models of Transport in Porous Media, *AIChE Journal*, 39(3), 387-396, (1993).

Buffle, J.: Complexation Reactions in Aquatic Systems: An Analytical Approach, pp. 242 and 332, Ellis Horwood, (1990).

Buyevich, Y.A., and S.K. Kapbsov: Segregation of a Fine Suspension in Channel Flow, *Journal of Non-Newtonian Fluid Mechanics*, 86, 157-184, (1999).

Cargill, G.S.: Radial Distribution Functions and Microgeometry of Dense Random Packings of Hard Spheres, *AIP Conference Proceedings*, 107 (1), 20-36, (1984).

Choi, S.K.: pH Sensitive Polymers for Novel Conformance Control and Polymer Flooding Applications, PhD Dissertation, The University of Texas at Austin (2007).

Crist, J.T., J.F. McCarthy, Y. Zevi, P. Baveye, J.A. Throop, and T.S. Steenhuis: Pore Scale Visualization of Colloid Transport and Retention in Partly Saturated Porous Media, *Vadose Zone Journal*, 3, 444-450, (2004).

Crist, J.T., Y. Zevi, J.F. McCarthy, J.A. Throop, and T.S. Steenhuis: Transport and Retention Mechanisms of Colloids in Partially Saturated Porous Media, *Vadose Zone Journal*, 4, 184-195, (2005).

Culligan, K.A., D. Wildenschild, B.S.B. Christensen, W.G. Gray, M.L. Rivers, and A.F.B. Tompson: Interfacial Area Measurements for Unsaturated Flow through a Porous Medium, *Water Resources Research*, 40, W12413, (2004).

Dalla, E., M. Hilpert, and C.T. Miller, Computation of the Interfacial Area for Two Fluids Porous Medium Systems, *Journal of Contaminant Hydrology*, 56, 25-48, (2002).

Davis, A., M. O'Neill, J. Dorrepal, and K. Ranger, Separation from the Surface of Two Equal Spheres in Stokes Flow, *Journal of Fluid Mechanics*, 77(4), 625-644, (1976).

Ding, Y., and D. Wen: Particle Migration in a Flow of Nanoparticle Suspensions, *Powder Technology*, 149, 84-92, (2005).

Eijkel, J.C.T., and A. van den Berg: Nanofluidics: What is it and what can we expect from it?, *Microfluid Nanofluid*, 1, 249-267, (2005).

Elimelech, M., J. Gregory, X. Jia, and R.A. Williams: Particle Deposition and Aggregation: Measurement, Modeling and Simulation, Boston: Butterworth-Heinemann, (1995).

Elimelech, M.: Effect of Particle Size on the Kinetics of Particle Deposition under Attractive Double-Layer Interactions, *Journal of Colloid and Interface Science*, 164(1), 190-199, (1994).

Elimelech, M.: Particle Deposition on Ideal Collectors from Dilute Flowing Suspensions: Mathematical Formulation, Numerical Solution, and Simulations, *Separation Technology*, 4, 186-212, (1994).

Espinasse, B., E.M. Hotze, and M.R. Wiesner: Transport and Retention of Colloidal Aggregates of C60 in Porous Media: Effects of Organic Macromolecules, Ionic Composition and Preparation Method, *Environmental Science and Technology*, 41, 7396-7402, (2007).

Faisal Anwar, A.H.M., M. Bettahar, and U. Matsubayashi: A Method for Determining Air-Water Interfacial Area in Variably Saturated Porous Media, *Journal of Contaminant Hydrology*, 43 (2), 129-146, (2000).

Finney, J., Random packings and the structure of simple liquids. I. The geometry of random close packing, *Proceedings of the Royal Society of London. Series A. Mathematical, Physical and Engineering Sciences*, 319, 479-493, (1970).

Foppen, J.W.A., A. Mporokoso, and J.F. Schijven: Determining Straining of Escherichia coli from Breakthrough Curves, *Journal of Contaminant Hydrology*, 76, 191-210, (2005).

Frimmel, F. H., F. von der Kammer, and H.C. Flemming: Colloidal Transport in Porous Media, Springer, (2007).

Gao, B., T.S. Steenhuis, Y. Zevi, V.L. Morales, J.L. Nieber, B.K. Richards, J.F. McCarthy, and J.Y. Parlange: Capillary Retention of Colloids in Unsaturated Porous Media, *Water Resources Research*, 44 (4), W04504, (2008).

Geilikman, M.B., D.E. Dria, and D.R. Stewart: Bean-up Guidelines for Sand-Control Completions, Paper SPE 95870, *Proceedings of the SPE Annual Technical Conference and Exhibition*, Dallas, Oct, 9-12, (2005).

Gladkikh, M. and S. Bryant: Prediction of Imbibition in Unconsolidated Granular Materials, *Journal of Colloid and Interface Science*, 288(2), 526-539, (2005).

Gladkikh, M. and S. Bryant: Prediction of Interfacial Areas during Imbibition in Simple Porous Media, *Advances in Water Resources*, 26 (6), 609-622, (2003).

Gray, W.: Thermodynamics and Constitutive Theory for Multiphase Porous-Media flow Considering Internal Geometry Constrains, *Advances in Water Resources*, 22 (5), 521-547, (1999).

Gray, W. and S.M. Hassanizadeh: Macroscale Continuum Mechanics for Multiphase Porous-Media Flow Including Phases, Interfaces, Common Lines and Common Points, *Advances in Water Resources*, 21 (4), 261-281, (1998).

Gray, W., A.F.B. Tompson and W.B. Soll: Closure Conditions for Two-Fluid Flow in Porous Media, *Transport in Porous Media*, 47 (1), 29-65, (2002).

Gruesbeck, C. and R.E. Collins: Entrainment and Deposition of Fine Particles in Porous Media, *Society of Petroleum Engineers Journal*, 22 (6), 847-856, (1982)

Gu, C.Y., and Q.F. Di: Slip Velocity Model of Porous Walls Absorbed by Hydrophobic Nanoparticles SiO_2, *Journal Hydrodynamics*, 19(3), 365-371, (2007).

Guzman, K.A.D., M.P. Finnegan and J.F. Banfield: Influence of Surface Potential on Aggregation and Transport of Titania Nanoparticles, *Environmental Science and Technology*, 40, 7688-7693, (2006).

Haines, W.B.: Studies in the Physical Properties of Soil. V. The Hysteresis Effect in Capillary Properties, and the Modes of Moisture Distribution Associated Therewith *Journal of Agricultural Science*, 20, 97-116, (1930).

Hall, W.A.: An Analysis of Sand Filtration, *Proceedings, American Society of Civil Engineers (Sanitary Engineering Division)*, SA3, paper 1276, 1-9, (1957).

Han, J., Y. Jin, and C.S. Willson: Virus Retention and Transport in Chemically Heterogeneous Porous Media under Saturated and Unsaturated Flow Conditions, *Environmental Science and Technology*, 40, 1547-1555, (2006).

Happel, J: Viscous Flow in Multiparticle Systems: Slow Motion of Fluids Relative to Beds of Spherical Particles, *AIChE Journal*, 4 (2), 197-201, (1958).

Hassanizadeh, M.S. and W.G. Gray: Mechanics and Thermodynamic of Multiphase Flow in Porous Media Including Interface Boundaries, *Advanced Water Resources,* 13 (4), 169-186, (1991).

Hassanizadeh, M.S. and W.G. Gray, Thermodynamic Basis of Capillary Pressure in Porous Media, *Water Resources Research*, 29 (10), 3389-3405, (1993).

Held, R.J. and M.A. Celia: Modeling Support of Functional Relationships between Capillary Pressure, Saturation, Interfacial Area, and Common Lines, *Advances in Water Resources*, 24, 325-343, (2001)

Herzig, J.P., D.M. Leclerc, and P. Le Goff. Flow of Suspensions through Porous Media-Application to Deep Filtration, *Industrial and Engineering Chemistry*, 62 (5), 8-35, (1970).

Hoek, E.M.V., and G.K. Agarwal: Extended DLVO Interactions between Spherical Particles and Rough Surfaces, *Journal of Colloid and Interface Science*, 298, 50-58, (2006).

Hunter, R.J.: Foundations of Colloid Science, New York: Oxford University Press, 2nd ed. (2001).

Israelachvili, J.: Intermolecular and Surface Force, London: Academic Press, 2nd ed. (1991).

Jha, R., Bryant, S. and Lake, L. Effect of Local Mixing on Dispersion, SPE 115961, *Proceedings of the 2008 SPE Annual Technical Conference and Exhibition*, Denver, CO, U.S.A., 21–24 September (2008).

Joekar-Niasar, V., M. Prodanovic, D. Wildenschild, and S.M. Hassanizadeh: Network Model Investigation of Interfacial Area, Capillary Pressure and Saturation Relationships in Granular Porous Media, *Water Resources Research*, 46, W06526, (2010).

Johnson, A: Theoretical Evaluation of Fluid/Fluid Interfacial Area during Drainage of a Porous Medium, MS Thesis, The University of Texas at Austin, (2001).

Kallay, N., and S. Žalac: Stability of Nanodispersions: A Model for Kinetics of Aggregation of Nanoparticles, *Journal of Colloid and Interface Science*, 253, 70-76, (2002).

Kaya, A., and Y. Yukselen: Zeta Potential of Clay Minerals and Quartz Contaminated by Heavy Metal, *Canadian Geotechnical Journal*, 42, 1280-1289, (2005).

Kim, H., P.S.C. Rao, and M.D. Annable: Determination of Effective Air-Water Interfacial Area in Partially Saturated Porous Media Using Surfactant Adsorption, *Water Resources Research,* 33 (12), (1997).

Kim, H., P.S.C. Rao, and M.D. Annable: Consistency of the Interfacial Tracer Technique: Experimental Evaluation, *Journal of Contaminant Hydrology*, 40 (1), 79-94, (1999).

Kinloch, C.H., S.A. Roberts, and A.H. Windle: A Rheological Study of Concentrated Aqueous Nanotube Dispersions, *Polymer*, 43, 7483-7491, (2002).

Kobayashi, M., F. Juillerat, P. Galletto, P. Bowen, and M. Borkovec: Aggregation and Charging of Colloidal Silica Particles: Effect of Particle Size, *Langmuir*, 21, 5761-5769, (2005).

Kumar, M.,T. Senden, M.A. Knackstedt, S.J. Latham, V. Pinczewski, R.M. Sok, A.P. Sheppard and M.L. Turner: Imaging of Pore Scale Distribution of Fluids and Wettability, *Petrophysics*, 50 (4), 311-321, (2009).

Lazouskaya, V., Y. Jin, and D. Or: Interfacial Interactions and Colloid Retention under Steady Flows in a Capillary Channel, *Journal of Colloid and Interface Science*, 303, 171-184, (2006).

Lazouskaya, V., and Y. Jin: Colloid Retention at Air-Water Interface in a Capillary Channel, *Colloid and Surfaces A: Physicochemical and Engineering Aspects*, 325, 141-151 (2008).

Lecoanet, H. and M.R. Wiesner: Velocity Effects of Fullerene and Oxide Nanoparticle Deposition in Porous Media, *Environmental Science and Technology*, 38, 4377-4382, (2004).

Lenhart, J.J. and J.E. Saiers, Transport of Silica Colloids through Unsaturated Porous Media: Experimental Results and Model Comparisons, *Environmental Science and Technology*, 36, 769-777, 2002.

Li, W., Y. Wang, K.D. Pennell, and L.M. Abriola: Investigation of the Transport and Deposition of Fullerene (C60) Nanoparticles in Quartz Sands under Varying Flow Conditions, *Environmental Science and Technology*, 42, 7174-7180, (2008).

Li, X., P. Zhang, C.L. Lin, and W.P. Johnson: Role of Hydrodynamic Drag on Microsphere Deposition and Re-entrainment in Porous Media under Unfavorable Conditions, *Environmental Science and Technology*, 39, 4012-4020, (2005).

Lindquist, W.B., S.M. Lee, W. Oh, A.B. Venkatarangan, H. Shin, and M. Prodanović: 3DMA-Rock (1994-2010), http://www.ams.sunysb.edu/~lindquis/3dma/3dma_rock/3dma_rock.html

Ma, S.X., G. Mason and N.R. Morrow: Effect of Contact Angle on Drainage and Imbibition in Regular Polygonal Tubes, *Colloids and Surfaces A: Physicochemical and Engineering Aspects*, 117 (3), 273-291, (1996).

Marlow, H.J., K.L. Duston, M.R. Wiesner, M.B.Tomson, J.T. Wilson and C.H. Ward: Microbial Transport through Porous Media: The Effects of Hydraulic Conductivity and Injection Velocity, *Journal of Hazardous Materials*, 28, 65-74, (1991).

Mason, G., and N.R. Morrow: Capillary Behavior of a Perfectly Wetting Liquid in Irregular Triangle Tubes, *Journal of Colloid and Interface Science*, 141 (1), 262-274, (1991).

Matthess, G., and A. Pekdeger, Survival and Transport of Pathogenic Bacteria and Viruses in Ground Water, in Ground Water Quality, Ward, C.H., Giger, W., McCarty, P., eds., John Wiley, New York, pp. 472-482, (1985).

Mayer, R.P. and R.A. Stowe: Mercury Porosimeter-Breakthrough Pressure for Penetration between Packed Spheres, *Journal of Colloid Science*, 20 (8), 891-911, (1965).

McCarthy, J.F., and J.M. Zachara: Subsurface Transport of Contaminants, *Environmental Science and Technology,* 23 (5), 496-502, (1989).

McClure, J.E., D. Adalsteinsson, C. Pan, W.G. Gray, and C.T. Miller: Approximation of Interfacial Properties in Multiphase Porous Medium Systems, *Advances in Water Resources*, 30 (3), 354-365, (2007).

Mellor, D., Random Close Packing (RCP) of Equal Spheres: Structure and Implications for Use as a Model Porous Medium, PhD Dissertation, Open University, Milton Keynes, UK, (1989).

Melrose, J.C: Wettability as Related to Capillary Action in Porous Media, *Society of Petroleum Engineers Journal*, 5 (3), 259-271, (1965).

Melrose, J.C. and G.C. Wallick: Exact Geometrical Parameters for Pendular Ring Fluids, *The Journal of Physical Chemistry*, 71, 3676-7, (1967).

Morrow, N.R.: Physics and Thermodynamics of Capillary Action in Porous Media, *Industrial and Engineering Chemistry*, 62 (6), (1970).

Motealleh, S., Mechanistic Study of Menisci Motion within Homogeneously and Heterogeneously Wet Porous Media, PhD Dissertation, The University of Texas at Austin, 2009.

Murray, C.B., C.R. Kagan, and M.G. Bawendi: Synthesis and Characterization of Monodipserse Nanocrystals and Closed-Packed Nanocrystal Assemblies, *Annual Review of Materials Science*, 30, 545–610 (2000).

Narter M. and M.L. Brusseau: Comparison of Interfacial Partitioning Tracer Tests and High Resolution Microtomography Measurements of Fluid-Fluid Interfacial Areas for an Ideal Porous Media, *Water Resources Research*, 46, W08602, (2010).

Osher, S. and J.A. Sethian: Fronts Propagating with Curvature-Dependent Speed: Algorithms Based on Hamilton-Jacobi Formulations, *Journal of Computational Physics*, 79, 12-49, (1988).

Pelley, A.J. and N. Tufenkji: Effect of Particle Size and Natural Organic Matter on the Migration of Nano and Microscale Latex Particles in Saturated Porous Media, *Journal of Colloid and Interface Science*, 321, 74-83, (2008).

Phillips, R.J., R.C. Armstrong, R.A. Brown, A.L. Graham, and J.R. Abbott: A Constitutive Equation for Concentrated Suspensions That Accounts for Shear-Induced Particle Migration, *Physics of Fluids, A: Fluid Dynamics*, 4, 30-40 (1992).

Priezjev, N.V.: Rate-Dependent Slip Boundary Conditions for Simple Fluids, *Physical Review E*, 75, 051605, (2007).

Princen, H.M.J.: Capillary Phenomena in Assemblies of Parallel Cylinders i: Capillary Rise between Two Cylinders, *Journal of Colloid and Interface Science*, 30 (1), 69-75, (1969a).

Princen, H.M.J.: Capillary Phenomena in Assemblies of Parallel Cylinders ii: Capillary Rise in Systems with More than Two Cylinders, *Journal of Colloid and Interface Science*, 30 (3), 359-371, (1969b).

Princen, H.M.J.: Capillary Phenomena in Assemblies of Parallel Cylinders iii: Liquid Columns between Horizontal Parallel Cylinders, *Journal of Colloid and Interface Science*, 34 (2), 171-184, (1970).

Prodanović, M: LSMPQS Software Manual, version 0.5, (2009). http://users.ices.utexas.edu/~masha/lsmpqs/index.html

Prodanović, M. and S.L. Bryant: A Level Set Method for Determining Critical Curvatures for Drainage and Imbibition, *Journal of Colloid and Interface Science*, 304 (2), 442-458, (2006).

Prodanović, M., S. Ryoo, A.R. Rahmani, R. Kuranov, C. Kotsmar, T.E. Milner, K.P. Johnston, S.L. Bryant, and C. Huh: Effects of Magnetic Fields on the Motion of Mutliphase Fluids Containing Paramagnetic Particles in Porous Media, SPE paper 129850 *Proceedings of the 2009 SPE Improved Oil Recovery Symposium*, Tulsa, OK, USA, April 24-28, (2010).

Pyrak-Nolte, L.J., D.D. Nolte, D. Chen, and N.J. Giordano: Relating Capillary Pressure to Interfacial Areas, *Water Resources Research*, 44 (6), W06408, (2008).

Quirke, N.: Adsorption and Transport at the Nanoscale, Boca Raton: CRC/Taylor and Francis (2006).

Rabani, E., B. Hetényi, B.J. Berne, and L.E. Brus: Electronic Properties of CdSe Nanocrystals in the Absence and Presence of a Dielectric Medium, *Journal of Chemical Physics*, 110(11), 5355-5369, (1999).

Rodriguez, E.: Straining of Small Particles in Porous Media, M.S. Thesis, The University of Texas at Austin, USA, (2006).

Rodriguez, E. and S.L. Bryant: Straining of Fine Particles in Gaps in Porous Media, SPE 110425, *Proceedings of the 2007 SPE Annual Technical Conference and Exhibition*, Anaheim, CA, November, 11-14, (2007).

Ryan, J.N., and Elimelech, M.: Colloid Mobilization and Transport in Groundwater, *Colloids and Surfaces A: Physicochemical and Engineering Aspects*, 107, 1-56, (1996).

Russell, W.B., D.A. Saville, and W.R. Schowalter: Colloidal Dispersions, Cambridge Univ. Press, (1991).

Saiers, J.E. and J.J. Lenhart: Ionic-Strength Effects on Colloid Transport and Interfacial Reactions in Partially Saturated Porous Media, *Water Resources Research*, 39 (9) 1256, (2003).

Saleh, N., H.Y. Kim, T. Phenrat, K. Matyjaszewski, R.D. Tilton, and G.V. Lowry: Ionic Strength and Composition Affect the Mobility of Surface–Modified Fe^0 Nanoparticles in Water-Saturated Sand Columns, *Environmental Science and Technology*, 42 (9), 3349-3355, (2008).

Sanchez-Reyes, J. and L.A. Archer: Interfacial Slip Violations in Polymer Solutions: Role of Microscale Surface Roughness, *Langmuir*, 19 (8), 3304-3312, (2003).

Schaefer, C.E., D.A. DiCarlo, and M.J. Blunt: Experimental Measurement of Air-Water Interfacial Area during Gravity Drainage and Secondary Imbibition in Porous Media, *Water Resources Research*, 36 (4), 885-890, (2000)

Schoch, R.B., J. Han and P. Renaud: Transport Phenomena in Nanofluidics, *Reviews of Modern Physics*, 80 (3), 839-883, (2008).

Schroth, M. H., M. Oostrom, R. Dobson and J. Zeyer: Thermodynamic Model for Fluid-Fluid Interfacial Areas in Porous Media for Arbitrary Drainage-Imbibition Sequences, *Vadose Zone Journal*, 7 (3), 966-971, (2008).

Sharma, M.M., and Y.C. Yortsos: Transport of Particulate Suspensions in Porous Media: Model Formulation, *AIChE Journal*, 33 (10), 1636-1643, (1987a).

Sharma, M.M., and Y.C. Yortsos: A Network Model for Deep Bed Filtration Processes, *AIChE Journal*, 33 (10), 1644-1653, (1987b).

Sharma, M.M., and Y.C. Yortsos: Fines Migration in Porous Media, *AIChE Journal*, 33 (10), 1654-1662, (1987c).

Shellenberger K. and B.E. Logan: Effect of Molecular Scale Roughness of Glass Beads on Colloidal and Bacterial Deposition, *Environmental Science and Technology*, 36, 184-189, (2002).

Sinyagin, A.Y., A. Belov, Z. Tang, and N.A. Kotov: Monte Carlo Computer Simulation of Chain Formation form Nanoparticles, *Journal of Physical Chemistry B*, 110, 7500-7507 (2006).

Sirivithayapakorn, S. and A. Keller: Transport of Colloids in Unsaturated Porous Media: A Pore Scale Observation of Processes during the Dissolution of Air-Water Interface, *Water Resources Research*, 39 (12), 1346, (2003).

Sokhan, V.P., D. Nicholson, and N. Quirke: Fluid Flow in Nanopores: An Examination of Hydrodynamic Boundary Conditions, *Journal of Chemical Physics*, 115 (8), 3878-3887, (2001).

Sorbie, K.S.: Polymer-Improved Oil Recovery. Boca Raton: CRC Press Inc., (1991).

Steenhuis, T.A., J.F. McCarthy, J.T. Crist, Y. Zevi, P. Baveye, J.A. Throop, R.L. Fehrman, A. Dathe and B.K. Richards: Reply to "Comments on 'Pore-Scale Visualization of Colloid Transport and Retention in Partially Saturated Porous Media"', *Vadose Zone Journal*, 4 (4), 957-958, (2005).

Thane, C.: Geometry and Topology of Model Sediments and their Influence in Sediment Properties, M.S. Thesis, The University of Texas at Austin, USA, (2006).

Thompson, S.S., M. Flury, M.V. Yates, and W.A. Jury: Role of the Air-Water-Solid Interface in Bacteriophage Sorption Experiments, *Applied Environmental Microbiology*, 64 (1), 304-309, (1998).

Tobiason, J.E., and C.R. O'Melia: Physicochemical Aspects of Particle Removal in Depth Filtration, *Journal of the American Water Works Association*, 80 (12), 54-64, (1988).

Torkzaban, S., S.M. Hassanizadeh, J.F. Schijven, and H.H.J.L. van den Berg: Role of Air-Water Interfaces on Retention of Viruses under Unsaturated Conditions, *Water Resources Research*, 42 (12), W12S14, (2006).

Tseng, W.J., and C.H. Wu: Aggregation, Rheology and Electrophoretic Packing Structure of Aqueous Al_2O_3 Nanoparticle Suspensions, *Acta Materialia*, 50 (15), 3757-3766, (2002).

Tufenkji, N., and M. Elimelech: Correlation Equation for Predicting Single-Collector Efficiency in Physicochemical Filtration in Saturated Porous Media, *Environmental Science and Technology*, 38 (2), 529-536, (2004).

Tufenkji, N., G.F. Miller, J.N. Ryan, R.W. Harvey, and M. Elimelech, Transport of *Cryptosporidium* Oocysts in Porous Media: Role of Straining and Physicochemical Filtration, *Environmental Science and Technology*, 38 (22), 5932-5938, (2004).

van Oss, C.J.: Interfacial Forces in Aqueous Media , Boca Raton: CRC Taylor & Francis, 2nd ed. (2006).

Wang, Y., Y. Li, J.D. Fortner, J.B. Huges, L.M. Abriola, and K. D. Pennell: Transport and Retention of Nanoscale C_{60} Aggregates in Water-Saturated Porous Media, *Environmental Science and Technology*, 42 (10), 3588-3594, (2008a).

Wang, Y., Y. Li, and K.D. Pennell: Influence of Electrolyte Species and Concentration on the Aggregation and Transport of Fullerene Nanoparticles in Quartz Sands, *Environmental Toxicology and Chemistry*, 27 (9), 1860-1867, (2008b).

Wan, J.M. and T.K. Tokunaga: Film Straining of Colloids in Unsaturated Porous Media: Conceptual Model and Experimental Testing, *Environmental Science and Technology*, 31 (8), 2413-2420, (1997).

Wan, J.M. and T.K. Tokunaga, Comments on "Pore-scale visualization of colloid transport and reaction in Partially Saturated Porous Media". *Vadose Zone Journal* 4, 954-956, 2005.

Wan, J.M and J.L. Wilson: Colloid Transport in Unsaturated Porous Media, *Water Resources Research*, 30, 857-864, (1994).

Willhite, G.P. and J.G. Dominguez *in* Improved Oil Recovery by Surfactant and Polymer Flooding, eds. Shah, D. O. and Shecter, R. S., Academic Press Inc., New York (1977).

Xu, S., B. Gao, J.E. Saiers: Straining of Colloidal Particles in Saturated Porous Media, *Water Resources Research*, 42 (12), W12S216, (2006).

Yao, K., M.T. Habibian, and C.R. O'Melia, Water and Waste Water Filtration: Concept and Applications, *Environmental Science and Technology*, 5(11), 1105-1112, (1971).

Zevi, Y., A. Dathe, J.F. McCarthy, B.K. Richards, and T.S. Steenhuis, Distribution of colloid particles onto interfaces in partially saturated sands, *Environmental Science and Technology*, 39, 7055-7064, (2005).

Zevi, Y., A. Dathe, B. Gao, B.K. Richards, and T.S. Steenhuis: Quantifying Colloid Retention in Partially Saturated Porous Media, *Water Resources Research*, 42 (12), W12S03, (2006).

Zevi, Y, A. Dathe, B. Gao, W. Zhang, B.K. Richards, and T.S. Steenhuis: Transport and retention of colloidal particles in partially saturated porous media: Effect of ionic strength, *Water Resources Research*, 45, W12403, (2009).

Vita

Elena Rodriguez-Pin was born in Oviedo, Spain, on December 1979. She holds a B.S. degree in Chemical Engineering from the University of Oviedo, Spain, awarded in July 2003. She enrolled as a graduate student in the Department of Petroleum and Geosystems Engineering at The University of Texas at Austin in September 2004, where she worked as a graduate research assistant under the supervision of Dr. Steven Bryant. Elena received her M.S. degree in Petroleum Engineering on December 2006. She worked as a summer intern for Object Reservoir in 2006 and for Chevron Corporation in 2008 and 2010.

Permanent email: elenarpin@gmail.com

This dissertation was typed by the author.